

**Bottom-Up Surface Self-Assembly of Polymer Colloids to Form Patterned Arrays**

by

Matthew Alan Ray

A Dissertation

Presented to the Graduate and Research Committee

of Lehigh University

in Candidacy for the Degree of

Doctor of Philosophy

in

Department of Chemistry

Lehigh University

December 4, 2006

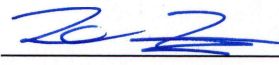
Approved and recommended for acceptance as a dissertation in partial fulfillment of the requirements for the degree of Doctor of Philosophy.


12/6/06  
Date

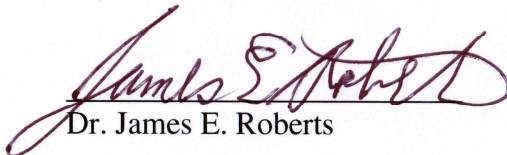
12/6/06  
Accepted Date

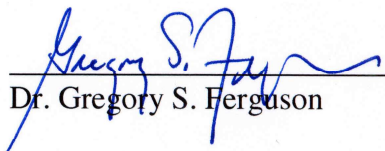
  
Dissertation Director

Committee Members:

  
Dr. Li Jia

  
Dr. Robert A. Flowers

  
Dr. James E. Roberts

  
Dr. Gregory S. Ferguson



## **Acknowledgements**

Special thanks go to my advisor, Dr. Li Jia, for giving advice and encouragement during the years I was under his leadership. I would like to thank Dr. Gregory Ferguson for his time and effort given in the revision process of this document. I would also like to thank my committee members, Dr. Robert Flowers and Dr. James Roberts, for taking part in the review of my work. I would like to thank the Lehigh University Department of Chemistry for providing me with the Amstutz Fellowship and Chemistry Department Fellowship, and the Dean of the College of Arts and Sciences as well as the Department of Chemistry for providing travel support. I would like to thank the Emulsion Polymers Institute for the many opportunities given to present my research work and for sponsoring me to attend the 2005 Gordon Conference on Polymer Colloids. I would also like to thank the Center for Optical Technologies for their sponsorship of my research work. Finally, I would like to thank my wife, Kelly, for her love and support, which have made this exercise worthwhile.

## **Copyrights**

The material contained in Chapter 2 has been published prior to submittal of this dissertation. The proper copyright permission was obtained from the journal before submittal of this document, with the publication cited at the beginning the chapter.

## Table of Contents

<b>Acknowledgements .....</b>	<b>iii</b>
<b>Copyrights.....</b>	<b>iv</b>
<b>List of Figures and Tables .....</b>	<b>ix</b>
<b>Abstract .....</b>	<b>1</b>
<b>Chapter 1: Fundamental Interactions .....</b>	<b>3</b>
1.1 Introduction .....	3
1.1.1 Historical Background.....	3
1.1.2 Overview of Self-Assembly Methods .....	4
1.2 The Self-Assembly Toolbox .....	5
1.2.1 van der Waals Interactions .....	7
1.2.2 Electrostatic Interactions .....	8
1.2.3 The DLVO Potential.....	10
1.2.4 Capillary Forces .....	15
1.3 The Building Blocks: Colloidal Particles.....	23
1.3.1 Reasons for Using Commercial Particles.....	25
1.3.2 Synthesis of Polymer Colloids .....	26
1.3.3 Particle Characterization .....	29
1.4 Summary .....	36
1.5 References and Notes .....	37
<b>Chapter 2: Dynamic Self-Assembly of Polymer Colloids to Form Linear Patterns .....</b>	<b>40</b>
2.1 Introduction .....	40
2.2 Experimental Methods .....	41
2.2.1 Particles .....	41

2.2.2	Patterning Method .....	42
2.2.3	Microscopy and Analysis .....	43
2.3	Results and Discussion.....	45
2.3.1	Line-Spacing Measurements .....	46
2.3.2	Linewidth Measurements .....	54
2.3.3	Optical Microscopy .....	57
2.3.4	Contact Angle Measurement .....	58
2.3.5	Self-Assembly Mechanism.....	64
2.3.6	Control Experiments.....	67
2.4	Conclusions .....	84
2.5	Acknowledgements .....	87
2.6	References and Notes.....	88
<b>Chapter 3:</b>	<b>Surface Self-Assembly of Polymer Colloids to Form Patterned Two-Dimensional Arrays .....</b>	<b>90</b>
3.1	Introduction .....	90
3.1.1	Background.....	91
3.1.2	Langmuir Particle Films .....	94
3.1.3	Interactions Unique to Surface Particles .....	97
3.1.4	Precedent for Transferred Particle Films.....	100
3.2	Experimental Methods .....	102
3.2.1	Particles .....	102
3.2.2	Substrate Functionalization .....	103
3.2.3	Transfer Method Development .....	108
3.2.4	Isotherm Plotting Options .....	109
3.2.5	Native Particle Films .....	110
3.2.6	Deposited Particle Films.....	111

3.2.7	Measurement of Particle-Interface Contact Angles ....	112
3.2.8	Surface Film Compression Methods .....	114
3.2.9	Substrate Transfer Processes .....	117
3.2.10	Microscopy and Methods of Pattern Analysis .....	120
3.3	Results and Discussion.....	124
3.3.1	Substrate Functionalization .....	124
3.3.2	Native Particle Films .....	131
3.3.3	Problems with the Native Film System.....	169
3.3.4	Deposited Particle Films.....	171
3.3.5	Transfer Completion.....	191
3.3.6	Comparison of Pattern Analysis Methods.....	194
3.3.7	Particle Surface Reconstruction .....	197
3.4	Conclusions .....	206
3.5	References and Notes .....	207
<b>Chapter 4:</b>	<b>Hierarchical Structures and Patterns .....</b>	<b>212</b>
4.1	Introduction .....	212
4.2	Experimental Results and Discussion .....	212
4.2.1	Thermal Annealing .....	213
4.2.2	Substrate Etching.....	213
4.2.3	Gold Nanoparticle Adsorption .....	225
4.2.4	SiO <sub>2</sub> Nanoparticle Adsorption.....	226
4.2.5	Formation of Silica Shells .....	232
4.2.6	Embedding Particle Arrays in PDMS .....	240
4.2.7	Nanopore Synthesis .....	246
4.2.8	Deposition onto Patterned Substrates.....	252
4.2.9	Microscopy and Analysis .....	254

4.3	Conclusions .....	257
4.4	References and Notes .....	258
<b>Appendix A: Langmuir Trough Method Development.....</b>		<b>260</b>
<b>Appendix B: Data Analysis Procedures for Select Methods .....</b>		<b>285</b>
<b>Appendix C: Useful Equations and Conversions .....</b>		<b>297</b>
<b>Biography .....</b>		<b>300</b>

## List of Figures and Tables

<b>Chapter 1: Fundamental Interactions .....</b>	<b>3</b>
<b>Figure 1.1</b> Debye Screening Length as a function of ionic concentration of univalent ions.....	11
<b>Figure 1.2</b> DLVO Interaction Potential as a function of separation distance .....	13
<b>Figure 1.3</b> DLVO Interaction Potential including hard sphere repulsion ....	14
<b>Figure 1.4</b> DLVO Interaction Potential as a function of low ionic concentration.....	16
<b>Figure 1.5</b> DLVO Interaction Potential as a function of high ionic concentration.....	17
<b>Figure 1.6</b> DLVO Interaction Potential as a function of particle surface potential .....	18
<b>Figure 1.7</b> DLVO Interaction Potential as a function of particle diameter .....	19
<b>Figure 1.8</b> Two- and three-dimensional particle arrays assembled by capillary forces.....	21
<b>Table 1.1</b> Latex particle properties .....	27
<b>Table 1.2</b> Results of the poly(styrene-co-vinylimidazole) latex synthesis.....	28
<b>Figure 1.8</b> SEM micrographs and particle size distributions of the poly(styrene-co-vinylimidazole) latex particles .....	30
<b>Figure 1.9</b> Zeta Potential plots for the Imidazole 258 and Sulfate 234 latexes .....	35
<b>Chapter 2: Dynamic Self-Assembly of Polymer Colloids to Form Linear Patterns .....</b>	<b>40</b>

<b>Figure 2.1</b>	Simple drying platform used to dry substrates at 10° tilt .....	44
<b>Figure 2.2</b>	Overview of the linear pattern and analysis procedures .....	47
<b>Figure 2.3</b>	Macroscopic appearance of the linear patterned region .....	48
<b>Figure 2.4</b>	Optical micrograph of the patterned region .....	49
<b>Figure 2.5</b>	Typical appearance of the linear pattern formed with the Imidazole 258 latex .....	50
<b>Figure 2.6</b>	Line spacing measurements .....	52
<b>Figure 2.7</b>	Linewidth measurements .....	55
<b>Figure 2.8</b>	Band pass spectrum of the green filter used for the contact angle measurements .....	60
<b>Figure 2.9</b>	Contact angle measurement by optical interference .....	61
<b>Figure 2.10</b>	Curve fitting of the line plot data .....	63
<b>Figure 2.11</b>	Line spacing as a function of contact angle .....	65
<b>Figure 2.12</b>	Schematic illustration of the ordering process .....	66
<b>Figure 2.13</b>	Negatively-charged Sulfonate 128 latex on glass .....	70
<b>Figure 2.14</b>	Negatively-charged Sulfate 176 latex on glass .....	72
<b>Figure 2.15</b>	Negatively-charged Sulfate 234 latex on glass .....	74
<b>Figure 2.16</b>	Negatively-charged Sulfate 357 latex on glass .....	76
<b>Figure 2.17</b>	Positively-charged Imidazole 258 latex on a positively-charged PDDA substrate .....	78
<b>Figure 2.18</b>	Substrate surface charge control experiments with the Imidazole 258 latex .....	80
<b>Figure 2.19</b>	Substrate surface charge control experiments with the Imidazole 391 latex .....	82
<b>Figure 2.20</b>	Pattern resulting from the deposition of the Amine 210 latex on glass .....	85



<b>Chapter 3: Surface Self-Assembly of Polymer Colloids to Form Patterned Two-Dimensional Arrays .....</b>	<b>90</b>
<b>Figure 3.1</b> Idealized stearic acid isotherm.....	93
<b>Figure 3.2</b> Schematic diagram of a particle trapped at an interface.....	96
<b>Figure 3.3</b> Detachment energy as a function of contact angle .....	98
<b>Figure 3.4</b> Detachment energy as a function of particle radius at a 90° particle-interface contact angle.....	99
<b>Figure 3.5</b> Schematic illustration of continuous and non-continuous particle patterns.....	101
<b>Figure 3.6</b> Particle-interface contact angle measurement method .....	113
<b>Figure 3.7</b> Particle halo fitting process .....	115
<b>Figure 3.8</b> Schematic illustration of the fluid-exchange procedure .....	121
<b>Figure 3.9</b> Kinetics of SAM formation with SPTCS at 25 °C .....	125
<b>Figure 3.10</b> Kinetics of SAM formation with TBAC on silicon at 25 °C....	127
<b>Figure 3.11</b> Kinetics of SAM formation with TMAC on silicon at 25 °C...	128
<b>Table 3.1</b> Properties of self-assembled monolayer substrates .....	129
<b>Figure 3.12</b> Macroscopic appearance of the crystalline grain like pattern ..	132
<b>Figure 3.13</b> Surface Pressure-Area Isotherm for the native film on 0.2 wt. % Imidazole 258 latex .....	135
<b>Figure 3.14</b> Surface Pressure-Distance Isotherm for the native Imidazole 258 latex film.....	136
<b>Figure 3.15</b> Native particle film on a sample of Imidazole 258 latex transferred to silicon substrates bearing SAMs derived from SPTCS.....	138
<b>Figure 3.16</b> Native particle films of Imidazole 258 latex particles transferred by the <u>LB</u> method to mirror finish stainless steel substrates ....	144

<b>Figure 3.17</b>	Native particle films of Imidazole 258 latex particles transferred by the <u>LS</u> method to mirror finish stainless steel substrates on the <u>first</u> compression cycle .....	147
<b>Figure 3.18</b>	Native particle films of Imidazole 258 latex particles transferred by the <u>LS</u> method to mirror finish stainless steel substrates on the <u>second</u> compression cycle.....	150
<b>Figure 3.19</b>	Substrate-dependent LB depositions .....	155
<b>Figure 3.20</b>	Surface-pressure- and substrate-dependent LS transfers .....	157
<b>Figure 3.21</b>	Angle- and rate-dependent transfer .....	162
<b>Figure 3.22</b>	Region of HCP monolayer partially distorted during the LB deposition process.....	166
<b>Figure 3.23</b>	Surface Pressure-Area Isotherms for the native surface film on 0.2 wt. % Imidazole 391 latex .....	168
<b>Figure 3.24</b>	LS transfer of the native surface film on 0.2 wt. Imidazole 391 latex to a mirror finish stainless steel substrate .....	170
<b>Figure 3.25</b>	Increase in surface pressure after drop-wise addition of IPA and suspensions in IPA.....	174
<b>Figure 3.26</b>	Optical micrograph of the distorted pattern that resulted from an LB transfer of a Sulfate 2700 latex film .....	176
<b>Figure 3.27</b>	Surface pressure-distance isotherm for the Sulfate 2700 latex.....	178
<b>Figure 3.28</b>	Isotherm coordinated LS transfers .....	179
<b>Figure 3.29</b>	Nearest Neighbor analysis of the micrographs shown in Figure 3.28 .....	187
<b>Figure 3.30</b>	Typical structures observed in the mesostructure region .....	188
<b>Figure 3.31</b>	Particles after solvent fixing as a function of solvent composition.....	193
<b>Figure 3.32</b>	Particle array after solvent fixing with acetone for 30 s .....	195

<b>Figure 3.33</b>	Optical micrograph of a hexagonal pattern of Sulfate 2700 latex particles.....	196
<b>Figure 3.34</b>	Laser diffraction pattern of a particle array with an 8 $\mu\text{m}$ spacing .....	198
<b>Figure 3.35</b>	Pattern resulting from a fast Fourier transform of the image in Figure 3.33 .....	199
<b>Figure 3.36</b>	Comparison of methods of analysis for the pattern shown in Figure 3.33 .....	200
<b>Figure 3.37</b>	Particle-(air-water) interface contact angle as a function of aging time in IPA.....	202
<b>Figure 3.38</b>	Calculated amount of particle surface exposed as a function of particle-interface contact angle.....	203
<b>Figure 3.39</b>	Interaction onset as a function of particle aging time in IPA ...	204

#### **Chapter 4: Hierarchical Structures and Patterns .....212**

<b>Figure 4.1</b>	Imidazole 258 particle patterns after thermal annealing.....	214
<b>Figure 4.2</b>	Negative etching using a particle pattern mask .....	217
<b>Figure 4.3</b>	Positive etching using a particle pattern mask.....	222
<b>Figure 4.4</b>	Particle size distribution analysis for the 15 nm diameter gold nanoparticles .....	227
<b>Figure 4.5</b>	Gold nanoparticles adsorbed onto a striped pattern of Imidazole 258 latex particles .....	228
<b>Figure 4.6</b>	Linear patterns of the Imidazole 258 latex after adsorbing $\text{SiO}_2$ nanoparticles .....	230
<b>Figure 4.7</b>	Linear patterns of the (A) Imidazole 258 and (B) Imiazole 391 latex after adsorbing Batch A Silica followed by calcination ..	233
<b>Figure 4.8</b>	Partially crushed calcined-silica nanoshells .....	235

<b>Figure 4.9</b>	Thermogravimetric Analysis (TGA) of the Imidazole 391 latex.....	238
<b>Figure 4.10</b>	Silica shells with a chimney .....	239
<b>Figure 4.11</b>	SiO <sub>2</sub> shells created on stainless steel .....	241
<b>Figure 4.12</b>	Patterned array of Imidazole 258 latex particles embedded in PDMS elastomer .....	243
<b>Figure 4.13</b>	Attempt to produce patterned SiO <sub>2</sub> nanopores embedded in PDMS .....	247
<b>Figure 4.14</b>	Experimental results of the nanopore synthesis.....	248
<b>Figure 4.15</b>	Schematic illustration of LS deposition onto patterned substrates.....	253
<b>Figure 4.16</b>	SEM Micrographs of an LS transfer onto a pre-patterned, chemically heterogeneous substrate .....	255
 <b>Appendix A: Langmuir Trough Method Development.....</b>		<b>260</b>
<b>Figure A.1</b>	Manual trough and the first generation dipper .....	261
<b>Figure A.2</b>	The mechanical trough .....	265
<b>Figure A.3</b>	Mechanical trough with the surface pressure transducer.....	266
<b>Figure A.4</b>	Drawings used for the fabrication of the mechanical trough....	267
<b>Figure A.5</b>	Surface area determination .....	275
<b>Figure A.6</b>	Surface pressure-area isotherm data treatment .....	281
 <b>Appendix B: Data Analysis Procedures for Select Methods .....</b>		<b>285</b>
<b>Figure B.1</b>	Indexed particle array laser diffraction pattern.....	292
<b>Figure B.2</b>	Families of particle lines responsible for producing the diffraction spots .....	293

## Abstract

Self-assembled particle arrays have received a significant amount of attention recently because of their interesting optical properties. In contrast to top-down self-assembly approaches, in which a pattern is imposed upon the system by such processes as microcontact printing or photolithography, bottom-up self-assembly relies upon the system to both define the pattern and assemble the individual elements. In this latter approach, fundamental parameters such as electrostatic and van der Waals interactions, as well as capillary forces are tuned to achieve the desired pattern. Two bottom-up particle self-assembly processes are discussed.

The first process involves drying a droplet containing a suspension of *positively charged* polymer particles on a flat *negatively charged* hydrophilic surface. This extremely simple method produces lines of polymer colloids with regular 1.5–4.5- $\mu\text{m}$  line spacings and smaller than 2- $\mu\text{m}$  linewidths over a broad surface area. The resulting patterns are at least an order of magnitude smaller in both linewidth and line spacing than similar approaches reported in the literature and follows a completely different mechanism. The second process involves the manipulation of polymer particle films trapped at an air-water interface. This modified Langmuir-Blodgett approach produces two-dimensional arrays of particles with hexagonal symmetry and tunable lattice constants. The key distinguishing feature in the present work is the ability to transfer patterned sub-monolayer interfacial particle films to a solid substrate. This transfer was achieved by tailoring the chemical functionality of the substrate surface to that of the polymer particle surface in order to promote rapid and strong adhesion with each

individual particle when the substrate is brought into contact with the interfacial particle film. By controlling the transfer geometry, the resulting pattern after deposition onto the substrate may be identical to that observed at the interface or, if desired, may be altered to produce a symmetry other than hexagonal. After assembling a patterned particle array, secondary processes, such as nanoparticle adsorption or substrate etching, may then be performed to increase the functionality and potential usefulness of the self-assembled system.

# Chapter 1

## Fundamental Interactions

### 1.1 Introduction

#### 1.1.1 Historical Background

According to The Royal Society and The Royal Academy of Engineering, “nanoscience is the study of phenomena and manipulation of materials at atomic, molecular, and macromolecular scales, where properties differ significantly from those at a larger scale,” and “nanotechnologies are the design, characterization, production, and application of structures, devices, and systems by controlling shape and size at nanometer scale.”<sup>1</sup> All chemistry could arguably be considered nanotechnology, and therefore both trace their philosophical origin to Democritus in ancient Greece, who first proposed the existence of the atom.<sup>2</sup> The current interest in nanotechnology traces its roots back to an influential speech given by Richard Feynman in 1959 at Caltech.<sup>3</sup> This speech, entitled “There’s Plenty of Room at the Bottom,” was a challenge to scientists worldwide to start thinking smaller not larger. Of course the repercussions of this speech reverberated across the next several decades in the electronics industry by the development of sophisticated photolithography processes. In contrast to this field, which could be accurately described as microfabrication, a separate field known as self-

assembly has experienced a period of rapid growth over the past decade and has become one of the main driving forces of the nanotechnology movement.

### 1.1.2 Overview of Self-Assembly Methods

Self assembly as a whole can be divided into two main categories, *top-down* and *bottom-up*. In top-down self-assembly, a pattern is imposed upon a system and the system assembles individual building blocks onto the pattern. This approach is typically related to traditional microfabrication in that the original pattern is made using traditional methods such as optical lithography. In some cases, the individual building blocks respond to a physically patterned topography, such as latex particles interacting with a substrate patterned with an array of holes.<sup>4,5</sup> In a second case, known as microcontact printing,<sup>6</sup> a polydimethylsiloxane (PDMS) stamp is prepared by curing the elastomer against a topographically patterned substrate. The stamp may then be “inked” with an organosilane compound,<sup>7</sup> or polyelectrolyte,<sup>8</sup> and stamped onto a suitable substrate producing a patterned chemically heterogeneous surface. This substrate may then be used to direct the assembly of individual building blocks onto particular regions of the substrate.<sup>9,10</sup>

In the second category, the bottom-up approach, the system is responsible for both defining the pattern as well as assembling the individual elements. In this approach, fundamental forces must be controlled in order to create the desired pattern. Common methods involve creating patterns during drying processes,<sup>11,12</sup> by interfacial phenomenon,<sup>13</sup> or by 2- and 3-dimensional confinement.<sup>14,15</sup> Even though the bottom-



up method can be quite challenging to predict and control, and often the patterns contain more defects than their top-down counterparts, it is perhaps more interesting because of the independent nature of the system. In this respect, the bottom-up approach more closely resembles the self-assembly processes that are observed in nature.

Two bottom-up particle self-assembly methods were investigated in this research. The first method, discussed in Chapter 2, deals with linear patterns that were self-assembled during the drying process of a dilute droplet of polymer colloids suspended in water on a glass slide or silicon wafer. The resulting patterns were controlled by the geometry of the droplet near the three-phase contact-line and the charge interactions between the suspended particles and the substrate. The second method, discussed in Chapter 3, deals with patterns of polymer colloids that self-assemble when trapped at an air-water interface. The patterns can be transferred intact to solid substrates using modified Langmuir-Blodgett and Langmuir-Schaeffer techniques. A number of proof-of-concept experiments are discussed in Chapter 4, which investigated the feasibility of using self-assembled particle arrays as a substrate or scaffolding on which to create systems of increased complexity by processes such as nanoparticle adsorption or particle mask lithography.

## **1.2 The Self-Assembly Toolbox**

Colloidal particles are a common recurring theme in self-assembly processes,<sup>16</sup> which is likely due to their ease of synthesis, controllable surface chemistry, and the

ability to produce them monodispersely over a wide range of particle sizes. Colloidal particles can be synthesized with sizes ranging from a few nanometers for colloidal gold to several hundreds of microns for polymer colloids synthesized by suspension polymerization. Since the use of colloidal particles is so prevalent in self-assembly processes, it is important to have a good understanding of the physical interactions that can be utilized in order to control their behavior.

Colloidal particles can interact *via* a variety of interactions, predominantly *Coulombic* and *van der Waals* forces. These interactions are the two main forces in DLVO theory (discussed in **Section 1.2.3**), which provides a framework for describing colloidal interaction and stability. Another key force in colloidal self-assembly is the *capillary force*. Capillary forces can arise between particles at a liquid interface or particles confined to a solid surface bridged by a liquid layer. In order for capillary forces to operate, a three-phase contact line must exist at the particle surface. These forces can be quite strong, and in many cases dominate interparticle behavior. *Steric interactions* can be utilized to maintain inter-particle separations. This interaction is inherently entropic in nature because particle repulsion is driven by the relaxation of particle chains compressed between two particles. The polymer chains attempt to regain an equilibrium state by pushing the particles apart. *Hydrogen bonding* and even *covalent bonding* can also play a part in particle self-assembly, but these interactions have typically not been systematically utilized. For a more thorough treatment of the topics discussed, a variety of excellent resources are available.<sup>17, 18, 19</sup>

## 1.2.1 van der Waals Interactions

**1.2.1.1 Between Two Molecules.** Van der Waals (vdW) forces are typically fairly weak and short-ranged interactions. They account for the melting point and boiling point of nonpolar molecules such as alkanes, but they are still quite weak compared to the Columbic forces in ionic solids that can result in melting points several orders of magnitude higher. For small molecules, the vdW interaction potential,  $U_{vdW}$ , may be simplified to

$$U_{vdW} = \frac{-\lambda}{r^6} \quad (1.1)$$

in which  $\lambda$  is a molecule specific constant, and  $r$  is the molecular separation distance.<sup>18</sup>

**1.2.1.2 Between Two Particles.** The vdW attraction between two particles is the summation of all the individual attractive molecular interactions between the two particles, which results in a significant “long-ranged” force. The vdW attractive interaction energy,  $V_A$ , between two spherical particles with the same diameter can be approximated by

$$V_A = -\frac{a \cdot A}{12 \cdot H_0} \quad (1.2)$$

in which  $a$  is the particle radius,  $A$  is the Hamaker constant for the interparticle interaction, and  $H_0$  is the closest separation distance between the two spheres.<sup>19</sup> For identical particles interacting across a vacuum, the Hamaker constant is defined by the bulk particle material. However, if the particles are interacting through a continuous phase such as water, the Hamaker constant for the interaction,  $A_{121}$ , is equal to

$$A_{121} = (\sqrt{A_{11}} - \sqrt{A_{22}})^2 \quad (1.3)$$

in which  $A_{11}$  and  $A_{22}$  are the Hamaker constants for the particle material, and the continuous phase respectively. For the system described in this work, polystyrene particles in water, the Hamaker constants are approximately  $A_{11} = 9 \times 10^{-20}$  J and  $A_{22} = 6 \times 10^{-20}$  J, respectively, which results in a total interaction constant  $A_{121} = 3 \times 10^{-21}$  J. This value should be used in **Equation 1.2** above.<sup>19</sup>

## 1.2.2 Electrostatic Interactions

**1.2.2.1 Between Two Ions.** The Coulombic force on single ions takes on the form,

$$F_C = \frac{q_1 \cdot q_2}{4\pi\epsilon_r\epsilon_0x^2} \quad (1.4)$$

in which  $F_C$  is the Coulombic force,  $q_1$  and  $q_2$  are the charges of the two ions,  $\epsilon_r$  is the relative permittivity of the medium (also known as the dielectric constant),  $\epsilon_0$  is the permittivity of a vacuum ( $\epsilon_0 = 8.854 \times 10^{-12}$  C<sup>2</sup>/J·m), and  $x$  is the separation distance between the two ions.<sup>18</sup> Naturally, when the ions are of the same charge, the force is positive and therefore repulsive, and when the ions bear the opposite charge, the force is negative and therefore attractive.

**1.2.2.2 Between Two Particles.** A polymer latex particle or an inorganic nanoparticle can be viewed as a complex ion having multiple charges with most of the charges confined to the particle's surface. Because ions on the surface of adjacent

particles are no longer able to interact as single ions, but rather as ensembles of ions, a more complex description of the interaction is needed. The presence of the charged particle surface creates a disturbance in the equilibrium state of ions in the continuous phase. A layer of ions with opposite charge tightly binds to the surface of the particle creating what is referred to as the Stern layer. The ions making up the Stern layer do not readily exchange with ions in the surrounding media.<sup>17</sup> Outside of the Stern layer lies a region called the diffuse layer which still has a higher concentration of counterions than those found at equilibrium in the continuous phase, but ions found here are able to exchange with those in the surrounding medium. The combination of the Stern layer and the diffuse layer is called the double layer. When two colloidal particles approach each other, their double layers interact, resulting in an attractive or repulsive force. The repulsive Coulombic interaction energy,  $V_R$ , between two spherical double layers can be approximated by

$$V_R = \frac{\epsilon_r \epsilon_0 a \psi_0^2}{2} \ln(1 + e^{-\kappa H_0}) \quad (1.5)$$

in which  $\psi_0$  is the surface potential of the particles, and  $\kappa$  is the Debye reciprocal length.<sup>19</sup> The true surface potential of a particle is very difficult to measure precisely because of the tightly bound stern layer. However, the zeta potential is readily measured by electrophoretic mobility measurements. The zeta potential is the potential at an imaginary plane in the double layer called the shear or slipping plane and can be significantly lower in magnitude than the true surface potential. This plane represents the points at which particular ions are no longer permanently associated with the

particle as it moves through solution. Zeta potential measurements are very sensitive to the ionic concentration of the continuous phase and there is no way to directly correlate zeta potential with the true surface potential because the exact position of the shear plane is not measurable. Nonetheless, the zeta potential is a very useful parameter in describing colloidal stability, as it represents the effective surface charge. An important parameter in describing the length scale over which particles are able to interact is the *Debye Length*,  $1/\kappa$ , which can be approximated by

$$\frac{1}{\kappa} = \frac{N}{\sqrt{C}} \quad (1.6)$$

in which C is the molar concentration of electrolyte in the continuous phase and N is equal to 0.304 for a 1:1 electrolyte (NaCl), 0.176 for a 2:1 electrolyte (CaCl<sub>2</sub>), and 0.152 for a 2:2 electrolyte (MgSO<sub>4</sub>).<sup>17</sup> This length, which is defined as the distance at which the magnitude of the electric field surrounding a particle decreases to 1/e (or 0.3679) of its surface value, is highly dependent on the concentration and valence of the ions in the continuous phase. A plot showing the Debye length as a function of the concentration of univalent ions is shown in **Figure 1.1**.

### 1.2.3 The DLVO Potential

When the attractive vdW interaction is combined with the repulsive electrostatic interaction for particles of like charge a total interaction potential is produced that can be repulsive at long range but attractive at short range. The so-called DLVO potential, named after Derjaguin, Landau, Verwey, and Overbeek who developed the theory,

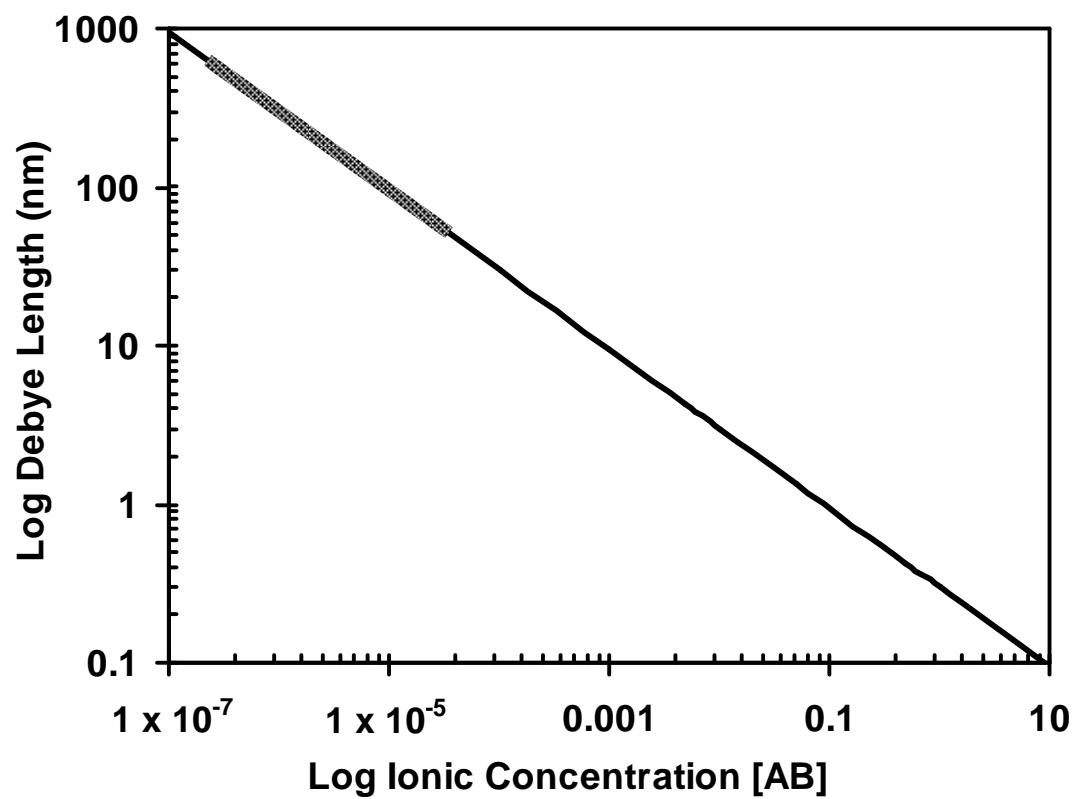


**Figure 1.1** *Debye Screening Length as a function of ionic concentration of univalent ions. Most highly cleaned latexes would likely fall into the shaded region.*

describes this complex behavior. The total potential,  $V_T$ , for two identical spherical particles can be approximated by combining **Equation 1.2** and **Equation 1.5** to produce

$$V_T = \frac{\epsilon_r \epsilon_0 a \psi_0^2}{2} \ln(1 + e^{-\kappa H_0}) - \frac{a \cdot A}{12 \cdot H_0} \quad (1.7)$$

which gives a valid approximation of the inter-particle interaction at distances on the order of  $0.4 \cdot a$  (**Figure 1.2**).<sup>19</sup> **Equation 1.7** does not include the hard sphere potential, also known as the Born repulsion, which accounts for the interaction when the particles come into physical contact with each other.<sup>19</sup> Based on the assumption that the particles are incompressible hard spheres, the interaction potential becomes infinite when the separation distance is zero. The hard sphere potential,  $V_{HS}$ , can be approximated by,

$$V_{HS} = \left( \frac{2 \cdot a}{d_s} \right)^n \quad (1.8)$$

in which  $d_s$  is the center-to-center particle separation distance and  $n$  is an integer.<sup>17</sup> The effect of including  $V_{HS}$  in the total potential is qualitatively shown in **Figure 1.3**. Three main regions exist in a typical DLVO plot: the vdW primary minimum at short distance, which accounts for irreversible coagulation; the primary maximum caused by electrostatic repulsion, which accounts for colloidal kinetic stability; and in some cases (i.e., large diameter or intermediate ionic strength) the secondary minimum, which accounts for reversible flocculation because particles are attracted by a potential of several kT yet still held apart by the electrostatic barrier. The primary minimum is typically so deep that it is not necessary to know the exact depth of the potential well. For this reason, the hard sphere potential is usually omitted from DLVO calculations.



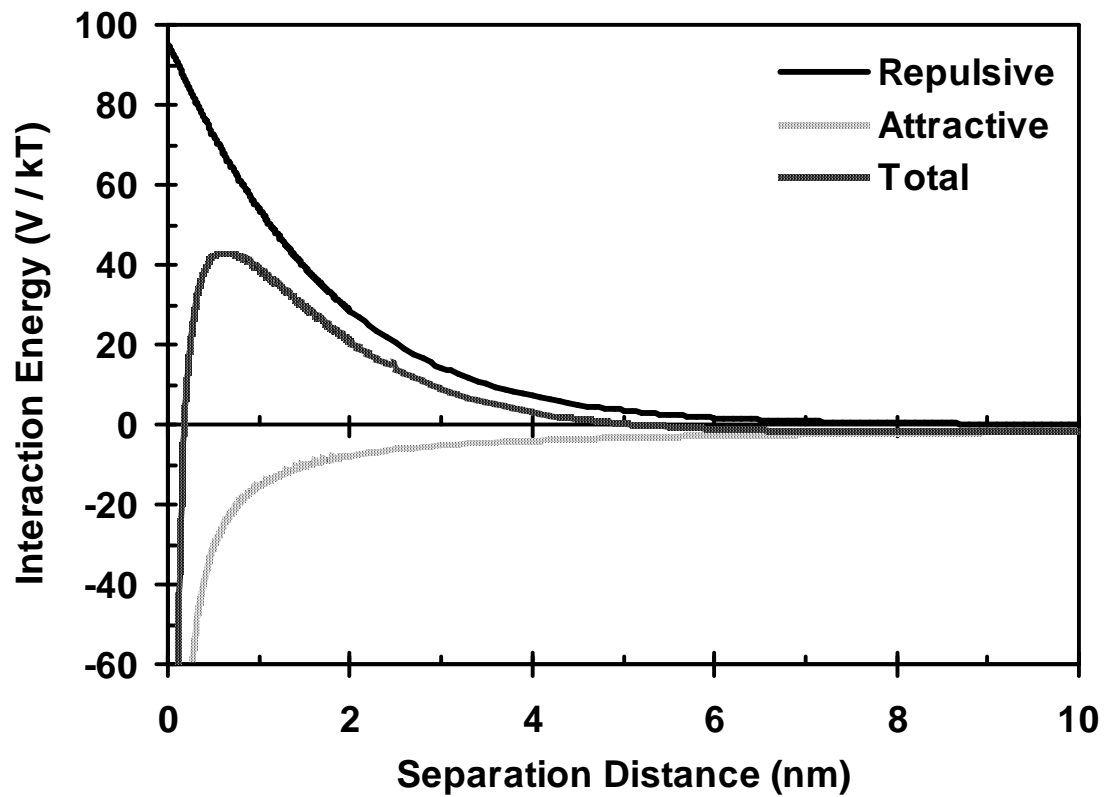


**Figure 1.2** *DLVO Interaction Potential as a function of separation distance. The bottom curve shows the vdW attractive potential (Equation 1.2) with  $A = 3 \times 10^{-21}$  J, and  $a = 250$  nm. The upper solid curve shows the electrostatic repulsion (Equation 1.5), with  $\psi = 80$  mV and  $C = 50$  mM. The middle shaded line shows the sum of the two potentials (Equation 1.7).*

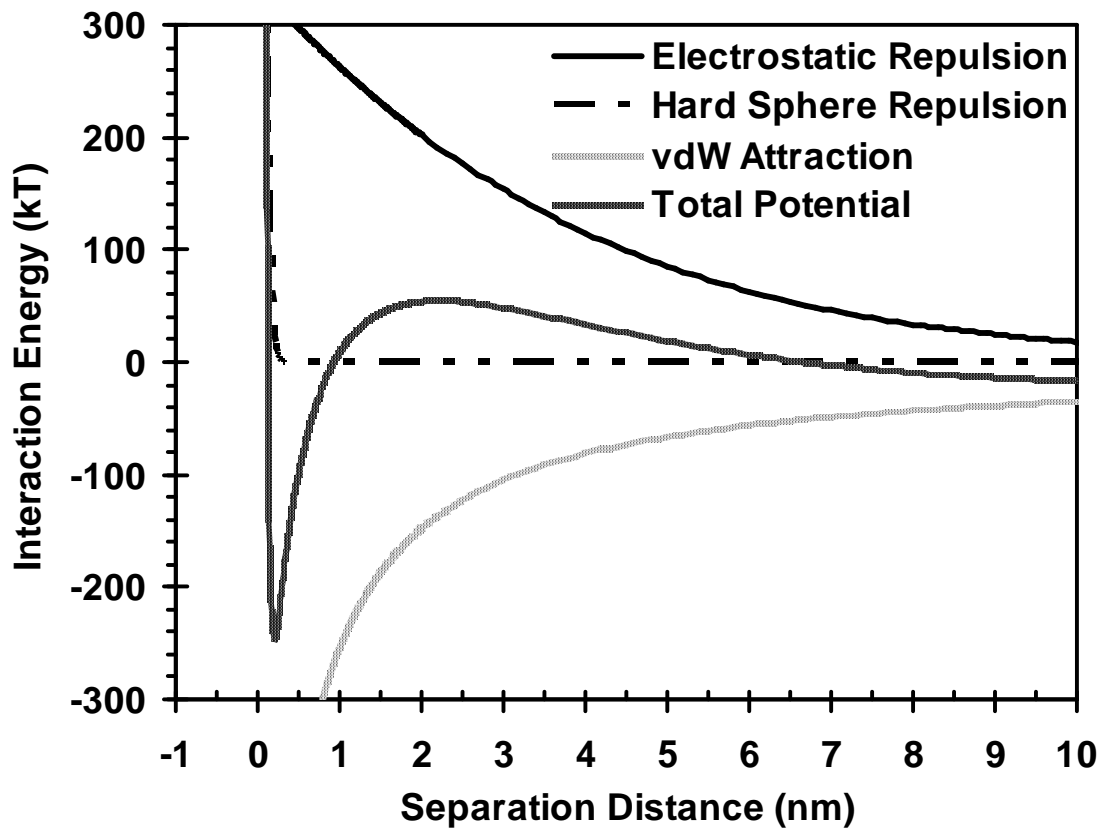


**Figure 1.3** *DLVO Interaction Potential including hard sphere repulsion.* By combining *Equations 1.7 and 1.8*, a more complete description of the total interaction potential is given. Because the primary vdW minimum is so deep, resulting in irreversible coagulation, the hard sphere repulsion is typically omitted from calculations.

The interactions between a particle and a charged flat surface are qualitatively quite similar to those described above even though the mathematical form of the potential is altered to accommodate the different geometry.<sup>19</sup>

Derjaguin-Landau-Verwey-Overbeek theory is not meant to be an exhaustive quantitative treatment, but rather to provide useful guidelines for understanding colloidal behavior. As the ionic strength of the continuous phase is increased, the height of the electrostatic barrier and the interparticle repulsion distance are decreased, until finally no barrier exists and the particles are freely pulled into the vdW minimum (**Figures 1.4 and 1.5**). As the surface potential of the particles is increased, the height of the electrostatic barrier is increased while maintaining a similar interaction distance (**Figure 1.6**). As the particle diameter is increased, the height of the electrostatic barrier increases and the secondary minimum becomes deeper (**Figure 1.7**). Of course, if the two particles (or a particle and a substrate) are oppositely charged, the sign of the electrostatic barrier is reversed and the total interaction potential is attractive at all distances, resulting in rapid heterocoagulation (or adsorption).

#### **1.2.4 Capillary Forces**

Capillary forces play a role in particle systems wherever an air-liquid-particle three-phase contact-line is present. These systems can exist at the air-bulk latex interface as well as during drying. Capillary forces can have a remarkably constructive effect on a drying suspension of colloidal particles if a three-dimensional minimum volume or two-dimensional minimum area structure is desired. In such systems, the

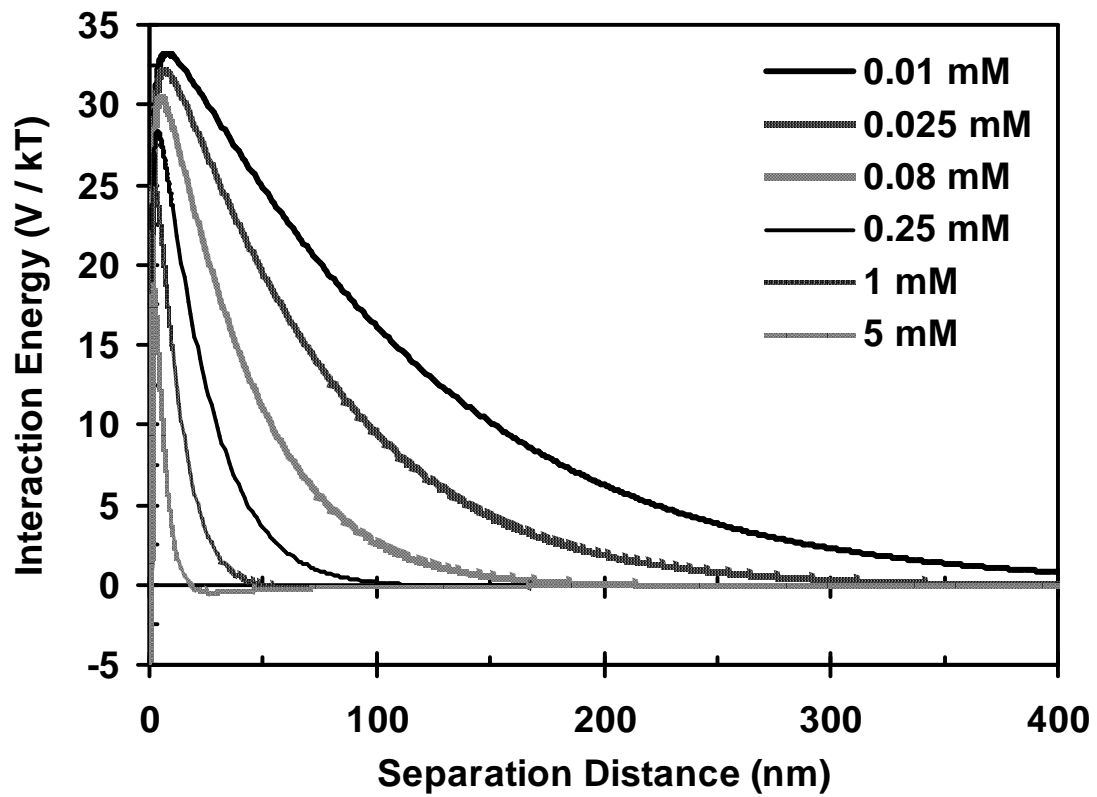


**Figure 1.4** *DLVO Interaction Potential as a function of low ionic concentration.*

*Equation 1.7* was plotted with  $A = 3 \times 10^{-21}$  J,  $a = 250$  nm,  $\psi = 50$  mV, and  $C$  was varied as shown above.

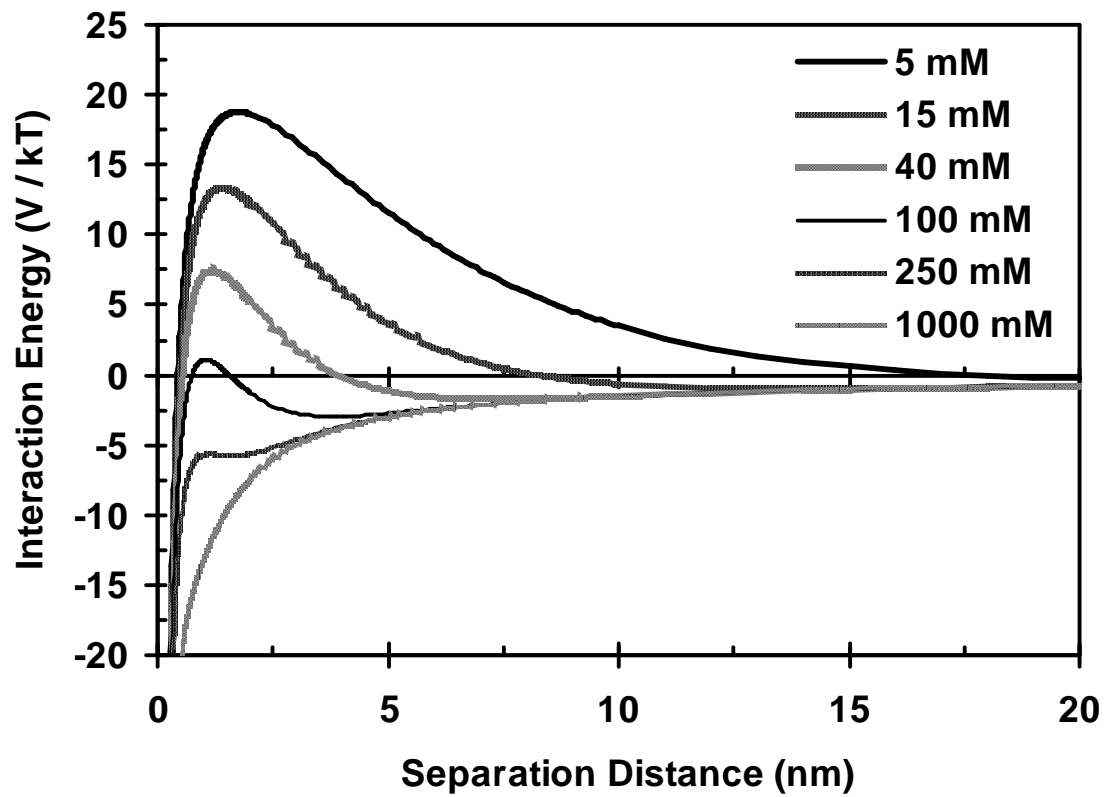


**Figure 1.5** *DLVO Interaction Potential as a function of high ionic concentration.*

*Equation 1.7* was plotted with  $A = 3 \times 10^{-21}$  J,  $a = 250$  nm,  $\psi = 50$  mV, and  $C$  was varied as shown above.

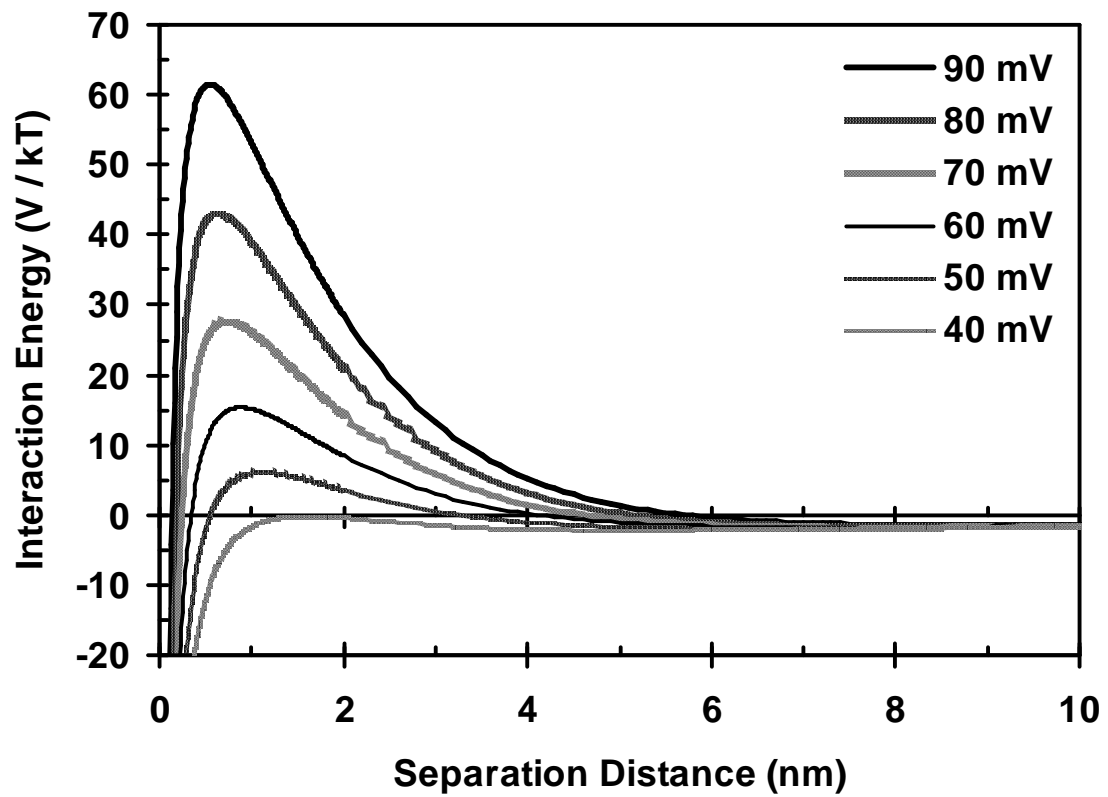


**Figure 1.6** *DLVO Interaction Potential as a function of particle surface potential.*

*Equation 1.7* was plotted with  $A = 3 \times 10^{-21}$  J,  $a = 250$  nm,  $C = 50$  mM, and  $\psi$  was varied as shown above.

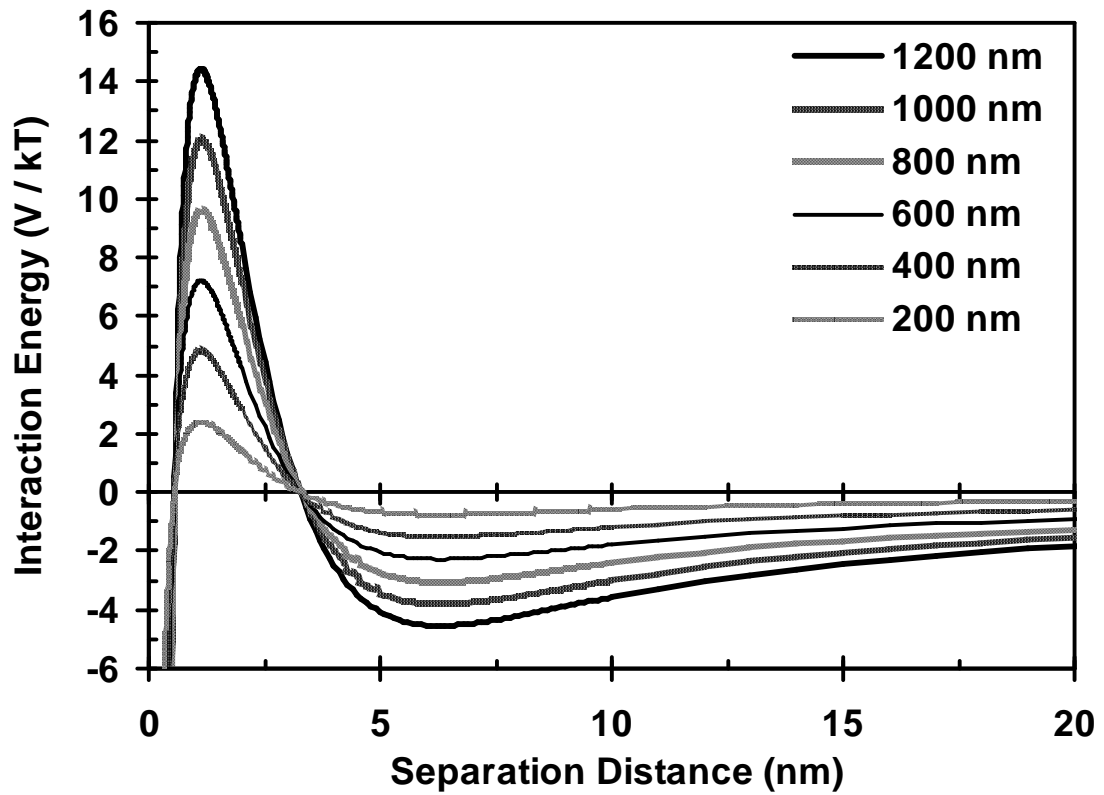


**Figure 1.7** *DLVO Interaction Potential as a function of particle diameter.*

*Equation 1.7* was plotted with  $A = 3 \times 10^{-21}$  J,  $\psi = 50$  mV,  $C = 50$  mM, and  $a$  was varied as half of the diameter values shown above.

magnitude of the capillary force exceeds the strength of the inter-particle electrostatic repulsion which plays the role of directing individual particles into lattice positions as the available volume or area is decreased during the drying process. To maintain a maximum separation distance, particles adopt a hexagonal close-packed arrangement creating a three-dimensional crystalline array for a concentrated suspension or a two-dimensional crystalline array for a dilute suspension drying on an appropriate substrate (**Figure 1.8**). Extensive research in the area of two-dimensional self-assembly by capillary forces has been reported by Nagayama et. al.<sup>20, 21, 22</sup>

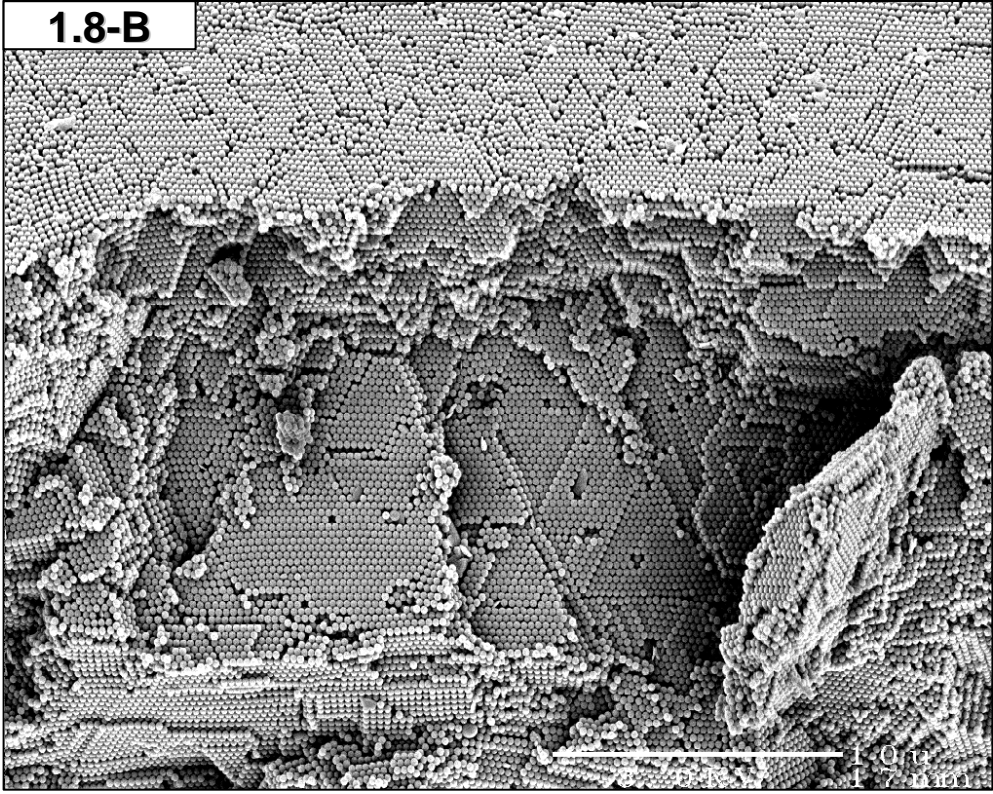
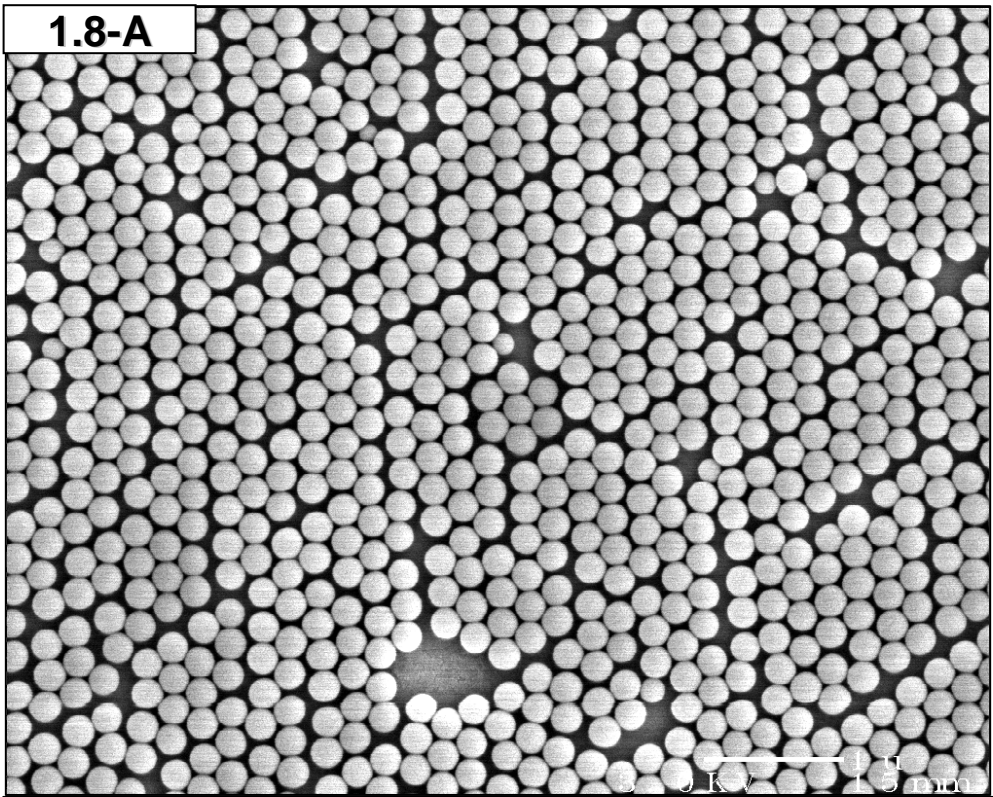
If a minimum volume or area structure is not desired, capillary forces can be quite destructive. In the case of a well-spaced array of individual particles adhered to a substrate, the capillary force can exceed the adhesive interaction between the particles and the substrate and squeeze the particles into small disordered clusters if water is allowed to dry across the substrate. The magnitude of the capillary force is governed by the surface tension of the liquid, the particle separation distance, and the curvature of the bridging meniscus between particles or between a particle and the substrate. Two sources give rise to the capillary force, known as the pressure effect and the surface tension effect. The pressure effect is governed by the Laplace equation,

$$\Delta P = \gamma_l \left( \frac{1}{R_1} + \frac{1}{R_2} \right) \quad (1.9)$$

in which  $\Delta P$  is the change in pressure from the gas phase above and the interior of the meniscus,  $\gamma_l$  is the surface tension of the liquid, and  $R_1$  and  $R_2$  are the orthogonal radii of curvature of the meniscus.<sup>18</sup> The surface tension effect has been extensively studied by



**Figure 1.8** *Two- and three-dimensional particle arrays assembled by capillary forces. (A) The result of drying one drop of 0.02 wt. % Sulfate 234 latex on glass. (B) The result of drying one drop of 1.0 wt. % Imidazole 258 latex on a silicon wafer. Notice the distinct hexagonal packing in both instances.*



Kralchevsky et. al., and a number of exhaustive derivations have appeared in the literature.<sup>23,24</sup> The lateral capillary force,  $F_c$ , between two identical particles at a solid interface partially immersed in a liquid film can be expressed as,

$$F_c = 2\pi \cdot \gamma_l \cdot r_c^2 \left( \frac{\sin^2(\varphi)}{L} \right) \quad \text{if} \quad r_c \ll L \ll \sqrt{\frac{\gamma_l}{(\Delta\rho)g}} \quad (1.10)$$

in which  $r_c$  is the radius of the three-phase contact line at the particle surface,  $\varphi$  is the mean slope angle of the meniscus at the contact line with respect to horizontal,  $L$  is the center to center particle separation distance,  $\Delta\rho$  is the difference between the mass densities of the liquid and gas phases, and  $g$  is acceleration due to gravity.<sup>25</sup> For micron-sized and smaller particles, the surface tension effect is many orders of magnitude larger than the pressure effect.

### 1.3 The Building Blocks: Colloidal Particles

Colloidal polymer particles are typically produced by heterogeneous polymerization in which water, monomer, stabilizer, and initiator are mixed together and heated for several hours. Such polymerizations are capable of producing particles with a very narrow size distribution over a wide range of particle size.<sup>19</sup> Vinyl-based monomers and free-radical initiators are almost exclusively used in this process and the stabilizer can simply be a detergent such as sodium dodecylsulfate, though some systems utilize polymeric steric stabilizers, or surfactant co-surfactant mixtures. In the initial stages of the reaction, an emulsion forms composed of surfactant stabilized monomer droplets suspended in the continuous phase. Emulsions can be divided into

three main categories, macro-, mini-, and microemulsions, depending on the size of the droplets. Macroemulsions have droplet diameters in the range of 1-100  $\mu\text{m}$  and are stable for seconds to hours; miniemulsions have droplet diameters in the range of 0.05-0.5  $\mu\text{m}$  (50-500 nm) and are stable for hours to months; and microemulsions have droplet diameters in the range of 0.01-0.1  $\mu\text{m}$  (10-100 nm) and are stable for months to many years.<sup>26</sup> Heterogeneous polymerizations can be divided into four main categories: emulsion, inverse emulsion, dispersion, and suspension.<sup>27</sup> Emulsion polymerizations typically produce hydrophobic particles in the 0.1 – 1  $\mu\text{m}$  size range. Inverse emulsion polymerizations begin as a water-in-oil emulsion with water-soluble monomer dissolved in water droplets that are suspended in a hydrocarbon continuous phase and produce hydrophilic particles in the 0.05-0.3  $\mu\text{m}$  size range. Dispersion polymerizations begin as a homogeneous monomer solution in a carefully chosen solvent-stabilizer system such that the resulting polymer precipitates to form particles in the 0.01-10  $\mu\text{m}$  size range. Suspension polymerizations begin as an oil-in-water emulsion, but the monomer droplets are much larger than those in emulsion polymerization. The coarse droplets are kept in suspension by proper application of shear and produce particles in the 100-10,000  $\mu\text{m}$  size range. A sub-type of emulsion polymerization known as surfactant-free emulsion polymerization was used to synthesize several of the latexes used in this research work. In this method, the surfactant is replaced by a water soluble co-monomer which co-polymerizes with the hydrophobic monomer to form a stabilizing layer at the particle surfaces. This method

is advantageous for surface chemistry studies since the resulting particles do not need to be rigorously cleaned to remove surfactant.

### 1.3.1 Reasons for using Commercial Particles

Monodisperse polystyrene latex particles are commercially available from a variety of sources<sup>28</sup> in a wide range of sizes, between 0.1 and 100  $\mu\text{m}$ . Therefore, fully characterized latex particles with the desired diameter, size distribution, surface functional group identity, and charge density may simply be purchased. Latex particle synthesis is not a particularly difficult task, as the polymerizations are typically performed as one pot reactions with no rigorous attention to cleanliness or contamination. However, the synthetic, purification, and characterization procedures can be quite time-consuming. Since the goals of this project did not focus on the synthesis of monodisperse latex particles, but rather to use them as building blocks to create self-assembled arrays, particles were only synthesized when the desired size and surface chemistry were not available commercially. In this way, the focus could remain on the experiments of interest.

Poly(styrene-*co*-vinylimidazole) latex particles with an average diameter of 258 nm (*Imidazole 258 latex*) and poly(styrene-*co*-styrenesulfonate) latex particles with an average diameter of 128 nm (*Sulfonate 128 latex*) were obtained from the Emulsion Polymers Institute (EPI) at Lehigh University.<sup>29</sup> The particles, which had been prepared by surfactant-free emulsion co-polymerization<sup>30</sup> and purified by ultracentrifugation and serum replacement, were used as received. Sulfate functionalized polystyrene latex

particles with average diameters of 176, 234, and 357 nm (*Sulfate 176, 234, and 357 latexes*) were obtained from Dow (Batches LS-1045-E, LS-1047-E, and LS-1010-E respectively), and used as received. Sulfate functionalized polystyrene latex particles with an average diameter of 2.7  $\mu\text{m}$  (*Sulfate 2700 latex*) and amine functionalized latex particles with an average diameter of 210 nm (*Amine 210 latex*) were obtained from Interfacial Dynamics Inc. (IDC, 1-2600 Batch 619,1 and 6-200 Batch 2101-HMD-1 respectively), and used as received. Most of the latex samples were supplied with a known diameter and size distribution measured by transmission electron microscopy (TEM), and surface charge density measured by titration. The surface area per functional group on the particle surface, known as the parking area, can be easily calculated from the titration data. **Table 1.1** is a summary of the properties and sources of the particles used in this project.

### 1.3.2 Synthesis of Polymer Colloids

Surfactant-free emulsion co-polymerization of styrene and vinylimidazole was carried out by placing 45.0 mL of DI water (Millipore,  $>15\text{ M}\Omega$ ), and appropriate amounts of 2,2'-azobis(2-amidinopropane) dihydrogen chloride (V50) initiator (Aldrich, 97%, used as received), styrene (Aldrich,  $\geq 99\%$ , distilled before use), and finally 1-vinylimidazole (Aldrich,  $>99\%$ , used as received) into a 100-mL glass bottle. The amounts of the reagents used are shown in **Table 1.2**. The bottles were purged with nitrogen, tightly capped and placed into a bottle polymerization unit (Atlas LP2 Computer Controlled Dyeing System) for 21 hours at  $70^\circ\text{C}$ . After the reaction, the

Styrene Latex (Group + $D_{(nm)}$ )	$D_N$ ( $\mu\text{m}$ )	$\sigma$ ( $\mu\text{m}$ )	PDI	CV (%)	Charge Density ( $\mu\text{C}/\text{cm}^2$ )	Parking Area ( $\text{\AA}^2/\pm$ )	Zeta Potential (mV)	Source
<b>Positive</b>								
Imidazole 258	0.258		1.003		+20.0	80.25	+31.6	EPI
Imidazole 391	0.372	0.042	1.032	11			+31.6	Synth.
Amine 210	0.210	0.010		4.8	+94.2	17	+17.6	IDC
(COOH)*					-7.1	225		
<b>Negative</b>								
Sulfonate 128	0.128		1.014		-66.2	24.2	-71.2	EPI
Sulfate 176	0.176	0.002		1.3				DOW
Sulfate 234	0.234	0.003		1.1			-54.2	DOW
Sulfate 357	0.357	0.006		1.6				DOW
Sulfate 2700	2.700	0.073		2.7	-8.9	179		IDC

\*The Amine 210 latex particles have carboxylic acid groups at the surface as well.

**Table 1.1** *Latex particle properties.* This table shows the number-average particle diameter ( $D_N$ ), the standard deviation of the average particle size ( $\sigma$ ), the polydispersity index (PDI), the coefficient of variation (CV), the particle charge density measured by conductometric titration, the surface group parking area calculated from the charge density, the zeta potential measured as described in **Section 1.3.3**, and the source of the particles.

<b>Batch</b>	<b>Styrene</b>		<b>Vinylimidazole</b>		<b>Initiator</b>		<b>Yield (%)</b>	<b>D<sub>n</sub> (nm)</b>	<b>PDI</b>
	<b>Weight (g)</b>	<b>Mol %</b>	<b>Weight (g)</b>	<b>Mol %</b>	<b>Weight (g)</b>	<b>Conc. (mM)</b>			
<b>A</b>	3.5	67.8	1.5	32.2	0.061	5	96.8	295	1.039
<b>B</b>	3.5	67.8	1.5	32.2	0.122	10	99.7	263	1.213
<b>C</b>	3.58	68.3	1.5	31.7	0.183	15	99.7	217	1.467
<b>D</b>	5	74.6	1.54	25.4	0.061	5	88.9	338	1.038
<b>E</b>	5	75.1	1.5	24.9	0.122	10	98.0	332	1.367
<b>F</b>	5	73.9	1.6	26.2	0.183	15	99.3	273	1.082
<b>G</b>	5	81.9	1	18.1	0.061	5	98.1	372	1.032
<b>H</b>	5	81.9	1	18.1	0.122	10	99.5	289	1.326
<b>I</b>	5	81.9	1	18.1	0.183	15	99.6	259	1.406
<b>J</b>	5	81.9	1	18.1	0.244	20	99.8	242	1.527

**Table 1.2** *Results of the poly(styrene-co-vinylimidazole) latex synthesis. Batch G was selected since it produced particles with properties closest to the desired results.*



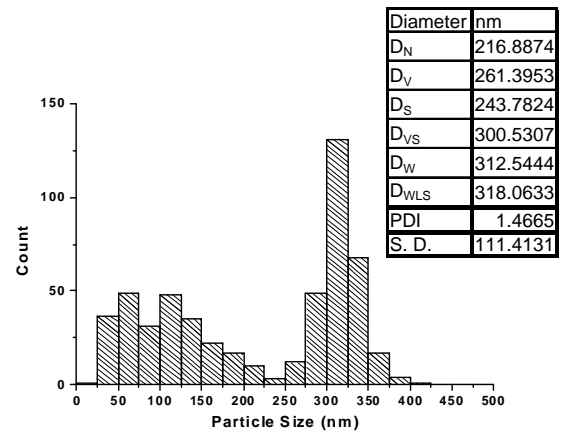
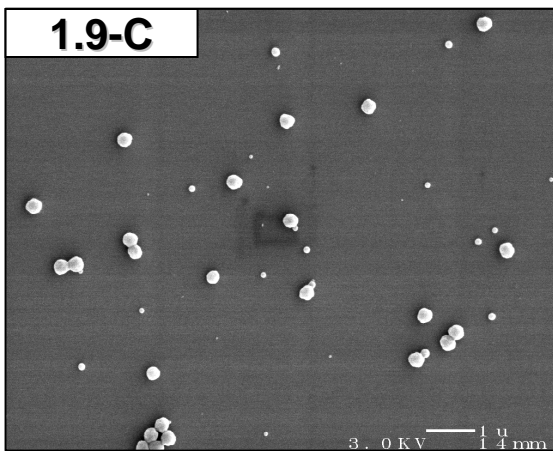
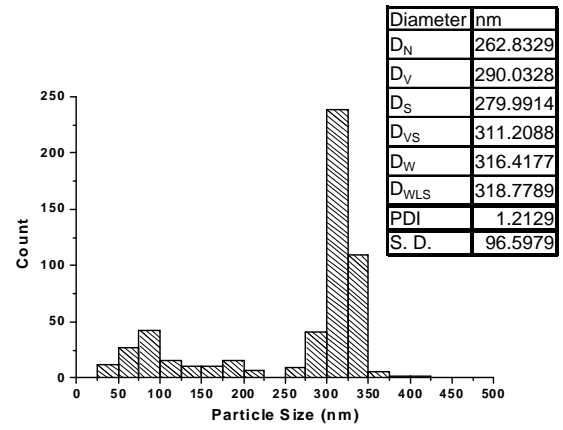
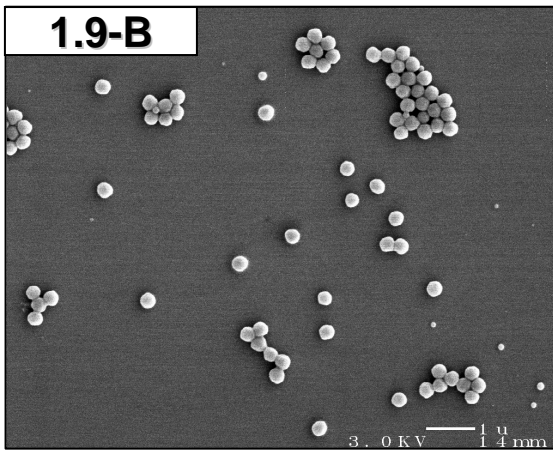
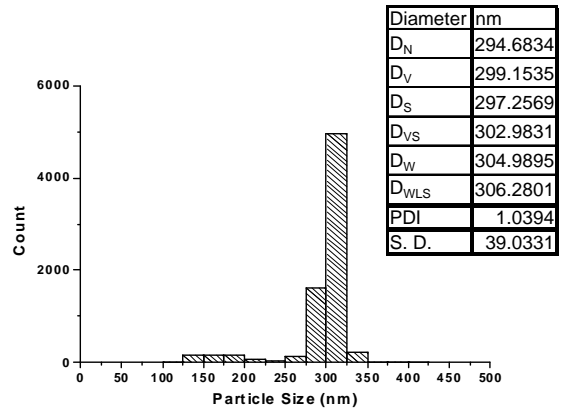
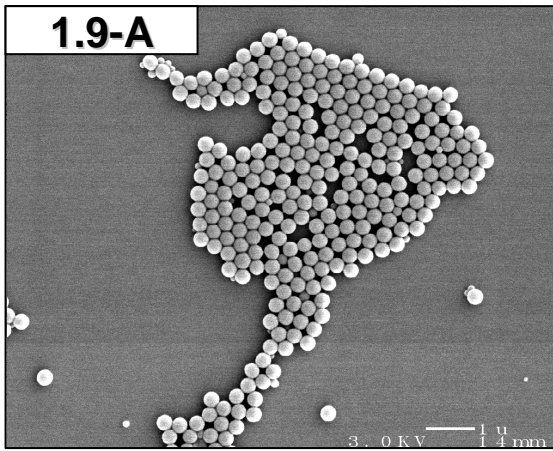
bottles were allowed to cool to room temperature and the yields of the reactions were determined gravimetrically. Small samples of each latex were diluted and analyzed by scanning electron microscopy (SEM). Particle size distribution measurements were made from the SEM micrographs, and the results are shown in **Figure 1.9**. A detailed description of how the particle size measurements were performed is given in **Appendix B.1**. Batch G was selected because it produced results that were the closest to the target particle properties. The latex was purified by repeated centrifugation cycles with deionized water. Even though the calculated average was 372 nm, the particle self-assembly processes were driven by the size of the major distribution which was 391 nm. For this reason batch G will be referred to as the *Imidazole 391 latex*.

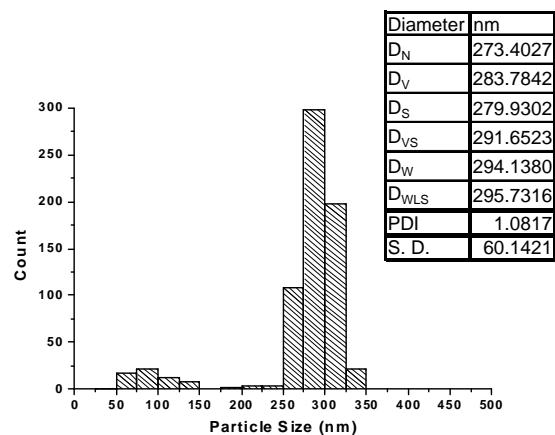
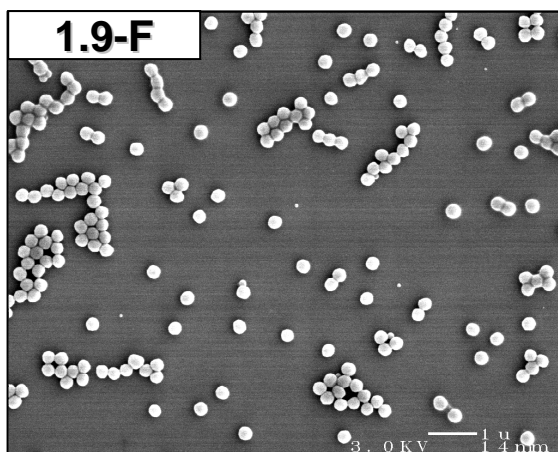
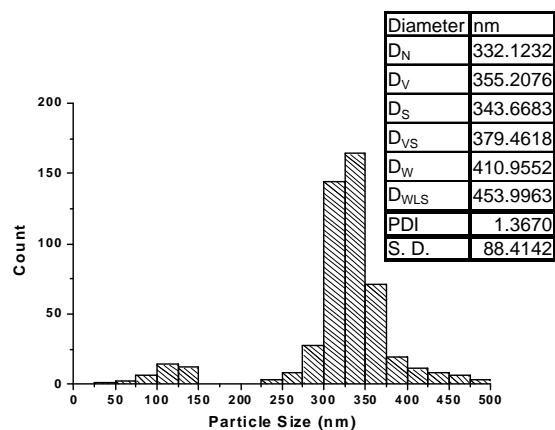
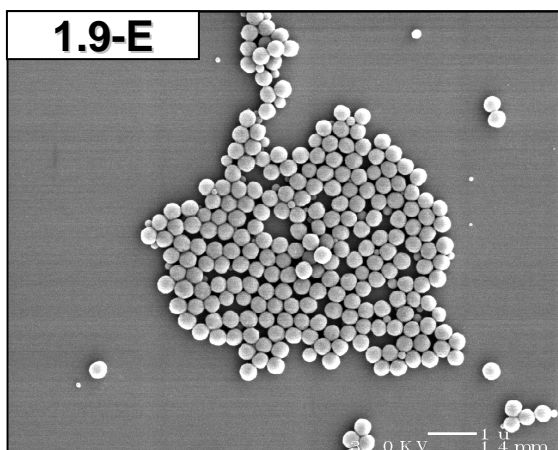
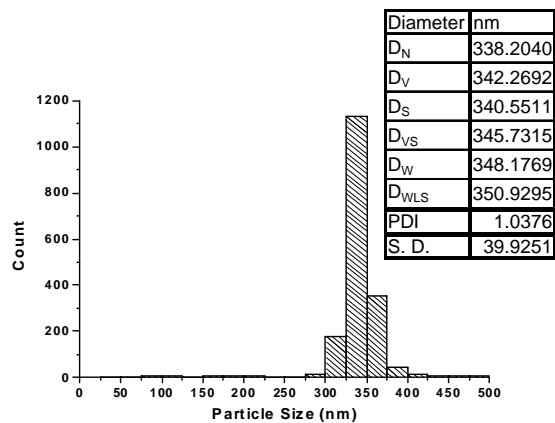
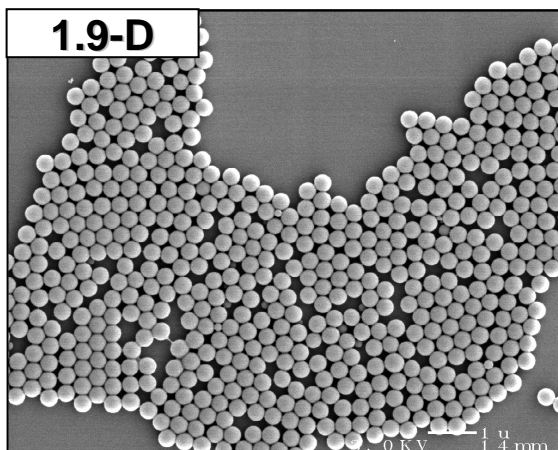
### **1.3.3 Particle Characterization**

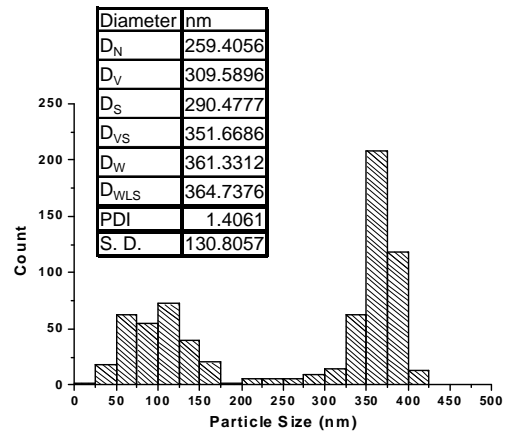
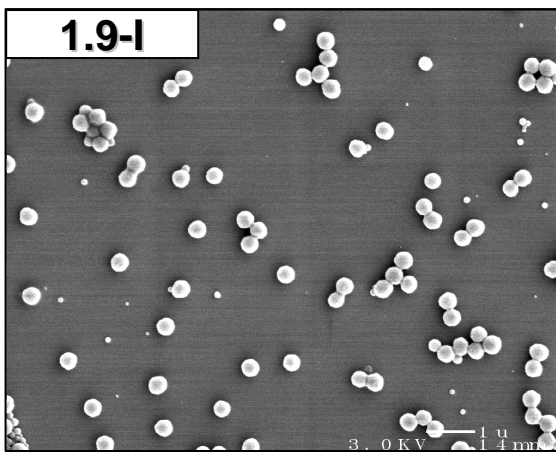
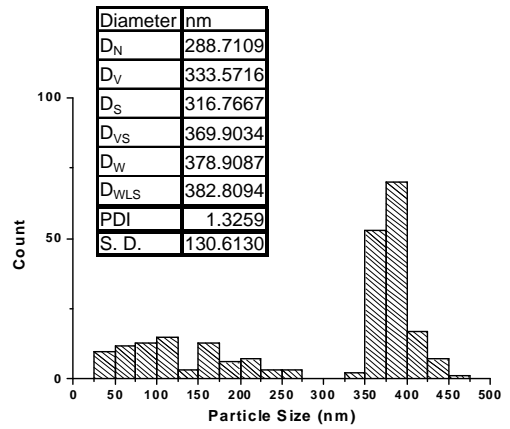
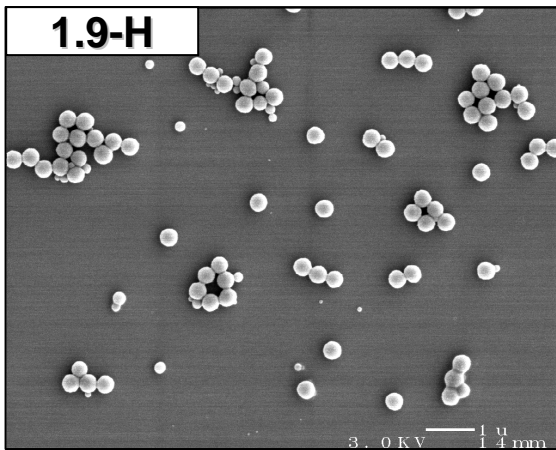
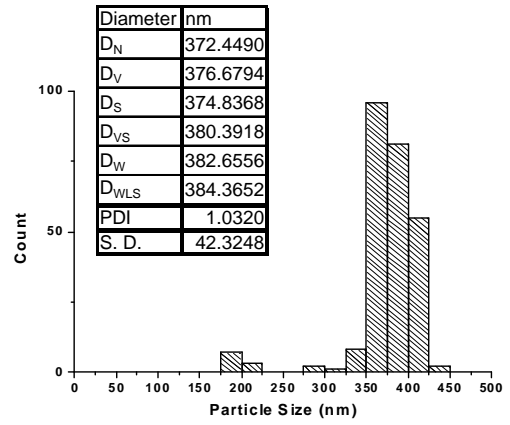
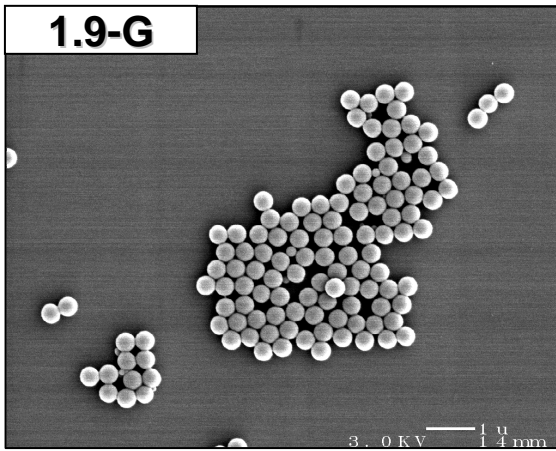
The zeta potential of several of the particles used in this research work were measured. For these measurements, latex samples were highly diluted with deionized water until the sample appears only slightly turbid. The measurements were made using a PenKem model 501 Lazer Zee Meter or a Coulter Delsa 440 SX, and the results are shown in **Table 1.1**. An example of the data measured with the Delsa is shown in **Figure 1.10**.

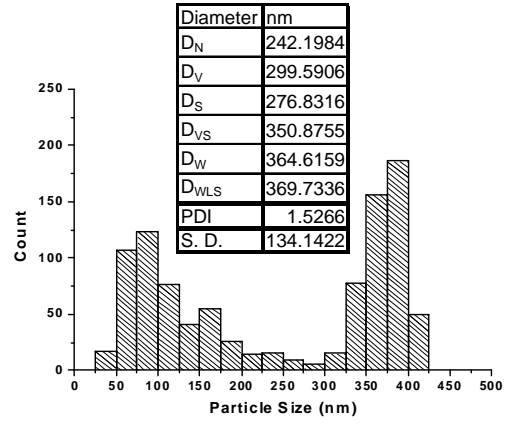
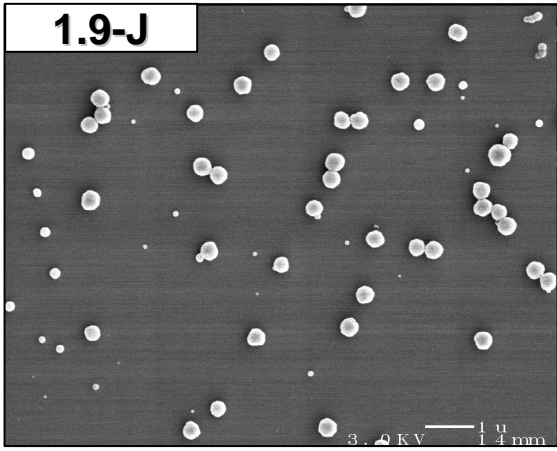
Elemental analysis was performed on the Imidazole 258 latex. This latex was synthesized at 30 mol % vinylimidazole loading, however, not all of the monomer was incorporated into the final latex. Much of the monomer forms water soluble imidazole rich polymer and oligomers which were removed from the final latex during cleaning.

**Figure 1.9** *SEM micrographs and particle size distributions of the poly(styrene-co-vinylimidazole) latex particles. The figure letters correspond to the batch letters in Table 1.2.*









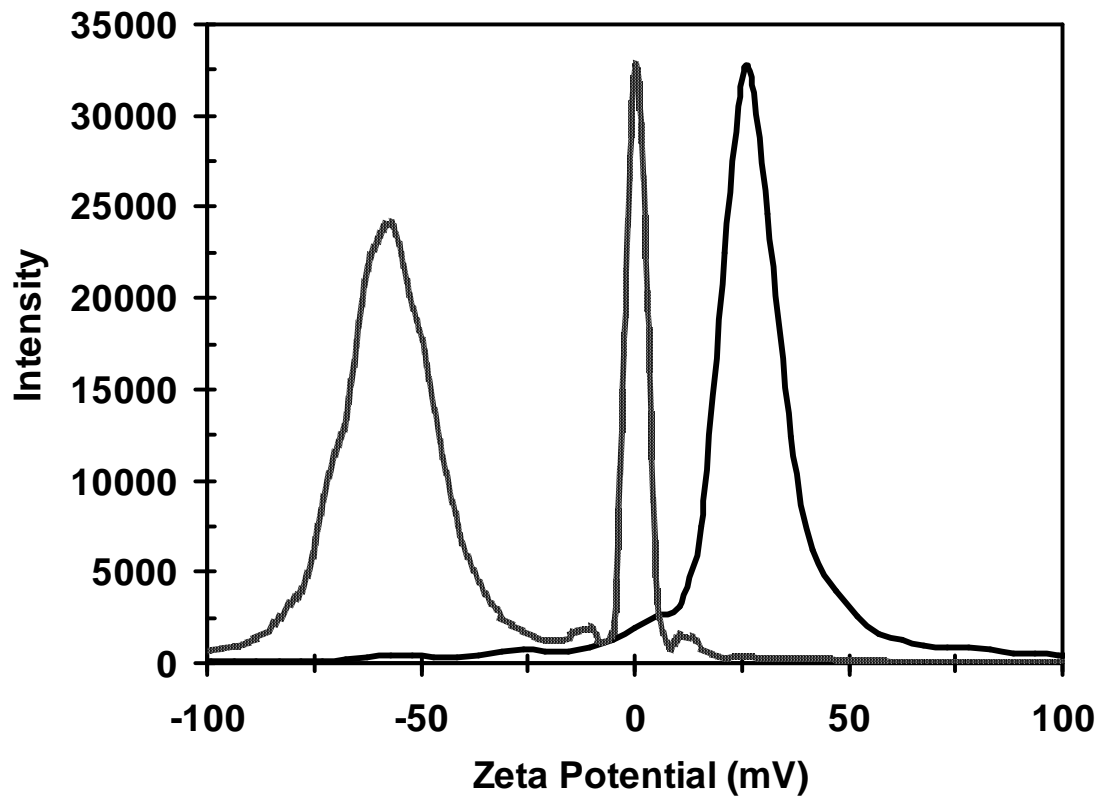


**Figure 1.10** *Zeta Potential plots for the Imidazole 258 and Sulfate 234 latexes. The positively-charged Imidazole 258 latex had a zeta potential of +31.6 mV and the negatively-charged Sulfate 234 latex produced a value of -54.2 mV. The peak at 0 mV is an artifact caused by the incident beam.*

Two, 1.0- mL latex samples were dried under vacuum, producing approximately 20 mg of dry latex each. The samples were sent to Galbraith Laboratories, Inc. for elemental analysis. Sample 1 contained 90.36 % C, 8.15 % H, and 1.25 % N, and sample 2 contained 90.32 % C, 8.03 % H, and 1.25 % N. Two samples were sent to ensure experimental reproducibility. The confidence limits for this analysis were reported as 0.28 % for C, 1.26 % for H, and 0.39 % for N, so both runs were well within the consistent range. The latex contained 4.2 wt % polyvinylimidazole based on nitrogen analysis, which was likely confined to the surface of the particles forming an extended polyelectrolyte layer.<sup>31</sup> This layer allowed the particles to strongly adsorb onto surfaces because the electrolyte layer was deformable, allowing for a larger particle-interface contact area.

## **1.4 Summary**

Bottom-up self-assembly approaches can be used to create ordered structures by carefully utilizing fundamental interactions. Existing theory provides a framework for understanding and designing systems to self-assemble colloidal particles using electrostatic, vdW, and capillary forces. Such systems provide an attractive alternative to top-down approaches because of their simplicity. Polymer colloids are a well suited medium to perform self-assembly processes because of the ability to produce them in a wide size range with a high degree of monodispersity and due to the versatility of their surface functionality. These factors provided the motivation to pursue the investigations described in the following chapters.



## 1.5 References and Notes

---

- <sup>1</sup> *Nanoscience and Nanotechnologies: Opportunities and Uncertainties*. Report on Nanotechnologies; The Royal Society and The Royal Academy of Engineering: London, UK, 29 July 2004. Available: <http://www.nanotec.org.uk/finalReport.htm>. Accessed: 11 November 2006.
- <sup>2</sup> Oldershaw, R. L. *Speculations Sci. Technol.* **1998**, 21, 37-44.
- <sup>3</sup> Feynman, R. P. *Eng. Sci.* **1960**, 23, 22-36.
- <sup>4</sup> Yin, Y.; Lu, Y.; Gates, B.; Xia, Y. *J. Am. Chem. Soc.* **2001**, 123, 8718-8729.
- <sup>5</sup> Ye, Y. H.; Badilescu, S.; Truong, V. V. *Appl. Phys. Lett.* **2001**, 79, 872-874.
- <sup>6</sup> Jackman, R.; Wilbur, J.; Whitesides, G. M. *Science*, **1995**, 269, 664-666.
- <sup>7</sup> Palacin, S.; Hidber, P. C.; Bourgoïn, J. P.; Miramond, C.; Fermon, C.; Whitesides, G. M. *Chem. Mater.* **1996**, 8, 1316-1325.
- <sup>8</sup> Zheng, H.; Rubner, M. F.; Hammond, P. T. *Langmuir*, **2002**, 18, 4505-4510.
- <sup>9</sup> Kaltenpoth, G.; Himmelhaus, M.; Slansky, L.; Caruso, F.; Grunze, M. *Adv. Mater.* **2003**, 15, 1113-1118.
- <sup>10</sup> Aizenberg, J.; Braun, P. V.; Wiltzius, P. *Phys. Rev. Lett.* **2000**, 84, 2997-3000.
- <sup>11</sup> Adachi, E.; Dimitrov, A.S.; Nagayama, K. *Langmuir* **1995**, 11, 1057-1060.
- <sup>12</sup> Deegan, R.D.; Bkajin, O.; Dupont, T.F.; Huber, G.; Nagel, S.R.; Witten, T.A. *Nature* **1997**, 389, 827-829.
- <sup>13</sup> Aveyard R.; Clint, J.H.; Nees, D.; Paunov, V.N. *Langmuir*, **2000**, 16, 1969-1979.
- <sup>14</sup> Kamenjicki, M.; Asher, S. A. *Macromolecules*, **2004**, 37, 8293.

- 
- <sup>15</sup> Kumacheva, E.; Garstecki, P.; Wu, H.; Whitesides, G. M. *Phys. Rev. Lett.* **2003**, *91*, 128301-1—12830-4.
- <sup>16</sup> Xia, Y.; Gates, B.; Yin, Y.; Lu, Y. *Adv. Mater.* **2000**, *12*, 693-713.
- <sup>17</sup> Israelachvili, J.N. *Intermolecular and Surface Forces*; Academic Press: Orlando, FL, 1985.
- <sup>18</sup> Adamson, A.W.; Gast, A.P. *Physical Chemistry of Surfaces*, 6<sup>th</sup> Edition; Wiley: New York, NY, 1997.
- <sup>19</sup> Fitch, R. M. *Polymer Colloids: A Comprehensive Introduction*; Academic Press: San Diego, CA, 1997.
- <sup>20</sup> Nagayama, K. *Colloids Surf. A*, **1996**, *109*, 363-374.
- <sup>21</sup> Adachi, E.; Dimitrov, A.S.; Nagayama, K. *Langmuir* **1995**, *11*, 1057-1060.
- <sup>22</sup> Dushkin, C.D.; Lazarov, G.S.; Kotsev, S.N.; Yoshimura, H.; Nagayama, K. *Colloid Polym. Sci.*, **1999**, *277*, 914-930.
- <sup>23</sup> Kralchevsky, P. A.; Nagayama, K. *Adv. Colloid Interface Sci.* **2000**, *85*, 145-192.
- <sup>24</sup> Kralchevsky, P. A.; Nagayama, K. *Particles at Fluid Interfaces and Membranes*; Elsevier: Amsterdam, 2001, pp. 517-590.
- <sup>25</sup> Denkov, N. D.; Velev, O. D.; Kralchevsky, P. A.; Ivanov, I. B.; Yoshimura, H.; Nagayama, K. *Langmuir*, **1992**, *8*, 3183-3190.
- <sup>26</sup> Sudol, E.D.; El-Asser, M.S. In *Emulsion Polymerization and Emulsion Polymers*; Lovell, P.A. and El-Asser, M.S., Eds. Wiley: West Sussex, England, 1997, pp 699-722.

- 
- <sup>27</sup> El-Asser, M.S. In *An Introduction to Polymer Colloids*; Candau, F. and Ottewill, R.H., Eds. Kluwer: Dordrecht, The Netherlands, 1990, pp 1-34.
- <sup>28</sup> Xia, Y.; Gates, B.; Yin, Y.; Lu, Y. *Adv. Mater.* **2000**, 12, 693-713.
- <sup>29</sup> H. Kim, Sample VZ-01, *GRPR No. 61*, p. 115, **2004**; and Sample 36-01, *GRPR No. 60*, p. 112, **2003**.
- <sup>30</sup> Tauer, K.; Deckwer R.; Kühn, I.; Schellenberg, C. *Colloid Polym. Sci.* **1999**, 277, 607-626.
- <sup>31</sup> Candau, F.; Ottewill, R. H.; Eds. *An Introduction to Polymer Colloids*; Kluwer: Dordrecht, The Netherlands, 1990, pp 130.

## Chapter 2

# Dynamic Self-Assembly of Polymer Colloids to Form Linear Patterns

*Portions of this chapter were reprinted with permission from Langmuir 2005, 21, 4786-4789.<sup>1</sup> Copyright 2005 American Chemical Society.*

### 2.1 Introduction

Dewetting is a process that has drawn lasting scientific interest because of its role in areas such as inks and surface coatings.<sup>2</sup> The events of surface pinning and convective flow during the dewetting process of a droplet of a colloidal suspension on a flat surface have received renewed interest because they can be harnessed as an extremely simple way for surface patterning.<sup>3</sup> A variety of patterns generated by this process have been observed on mica and glass.<sup>4, 5, 6, 7</sup> The patterns generally lack a regular repeating distance and individual pattern elements exceed a length scale of 10  $\mu\text{m}$ . In all of the previous studies, the substrate surface and the colloidal particles both had a negative surface charge and, therefore, electrostatically repelled each other. Theoretical studies of evaporating droplets on flat surfaces simply treated particle deposition as a passive process by discounting the surface-particle interactions.<sup>8, 9, 10, 11</sup> This lack of information on particle substrate interactions during drying processes

prompted our investigation of systems with substrate surface and particles of opposite charge. Drying a dilute droplet of *positively charged* polymer particles on a flat *negatively charged* hydrophilic surface resulted in the deposition of lines of particles with regular line-spacing over a broad surface area (greater than  $0.5 \text{ cm}^2$ ). The mechanism of the dynamic self-assembly process is also discussed.

The main objectives of this project were: 1. The use of polymer latex particles as nano-building blocks to self-assemble ordered structures using the processes of drying and dewetting, and 2. To understand the dynamic self-assembly mechanisms that produce patterns during dewetting, as well as to highlight the crucial role that Coulombic forces play in these processes.

## **2.2 Experimental Methods**

### **2.2.1. Particles**

Poly(styrene-co-vinylimidazole) latexes (*Imidazole 258 and 391*, obtained from the Emulsion Polymers Institute (EPI) at Lehigh University, and synthesized as outlined in Chapter 1 respectively) were diluted to appropriate sample concentrations with Milli-Q water ( $>15 \text{ M}\Omega$ ). The pH of the dilute suspensions in water was approximately 8 (Vernier Logger Pro pH Meter, the pH readings were unstable, likely due to the particulate nature of the sample). The imidazole groups on the surface of the particles ionize at this pH and bear a positive charge. As a result, the zeta potentials of the particles were measured (PenKem model 501 Lazer Zee Meter) and found to be  $+31.6 \pm 2.4 \text{ mV}$  (standard deviation, 12 measurements) for the 258-nm particles and  $+31.6 \pm 3.5$

mV (standard deviation, 25 measurements) for the 391-nm particles. The linear patterns formed over a particle concentration range of between 0.005 and 0.2 wt % solids. Experiments run above and below this range did not result in patterns. Several experiments were also performed using amine-functionalized polystyrene latex particles (*Amine 210 latex*, obtained from Interfacial Dynamics Corporation), which had a zeta potential of  $+17.6 \pm 3.0$  mV.

For control experiments of the particle charge poly(styrene-*co*-styrenesulfonate) latex particles with an average diameter of 128 nm (*Sulfonate 128 latex*, obtained from EPI), and sulfate functionalized latex particles with an average diameters of 176, 234, and 357 nm were used (*Sulfate 176, 234, and 357 latex*, obtained from DOW). The zeta potentials of two of the particles were measured and found to be  $-71.2 \pm 9.7$  mV (standard deviation, 6 measurements) for the Sulfonate 128 latex, and  $-54.2 \pm 1.7$  mV (standard deviation, 12 measurements) for the Sulfate 234 latex. The properties and sources of all the latexes used in this research are summarized in **Table 1.1**.

### 2.2.2 Patterning Method

Silicon wafer and glass substrates were cleaned with concentrated sulfuric acid, thoroughly rinsed with deionized water, and blown dry with a nitrogen jet prior to use. The pattern was formed by placing a single drop ( $\sim 38$   $\mu$ L) of suspension onto a 12-mm x 12-mm glass or silicon substrate. The substrate was immediately tilted in different directions to allow the drop to completely wet the surface. Once the surface was completely wetted, the substrate was typically placed at an angle of  $10^\circ$  with respect to

the benchtop and allowed to dry in a covered Petri dish at room temperature as shown in **Figure 2.1**. Typical drying times were 2-3 h.

For control experiments of the substrate surface charge, PDDA [poly(diallyldimethylammonium chloride), MW 200-350 k, Aldrich, 20 wt % in water] was used to switch the surface charge from negative to positive. To accomplish this, cleaned glass substrates were dipped into 5.0 wt % PDDA for 30 min, thoroughly rinsed with deionized water, and blown dry with a nitrogen jet. These substrates were then used in the procedure as outlined above.

### **2.2.3 Microscopy and Analysis**

The particle patterns were analyzed with scanning electron microscopy (JEOL, 6300f). All of the scanning electron microscope (SEM) samples were sputter-coated with a thin layer of gold palladium alloy (Polaron E5100 SEM coating unit) to make the surface conductive. Video and color digital images of the ordering process were recorded by a CCD camera attached to the optical microscope (Olympus, BH2). For this procedure the entire microscope was tilted to  $\sim 10^\circ$ , and the same sample preparation procedure was used except that the substrate was placed on the microscope stage to dry. The repeat distance of the striped pattern was analyzed by two-dimensional Fast Fourier Transform (FFT). Fourier transform image analysis was performed using Scion Image for Windows release Beta 4.0.2. By measuring the distance between the center, defined as pixel # (256, 256) in a 512 x 512 pixel image, and the prominent points in the transformed image, the periodicity in the original image can be calculated. The distance

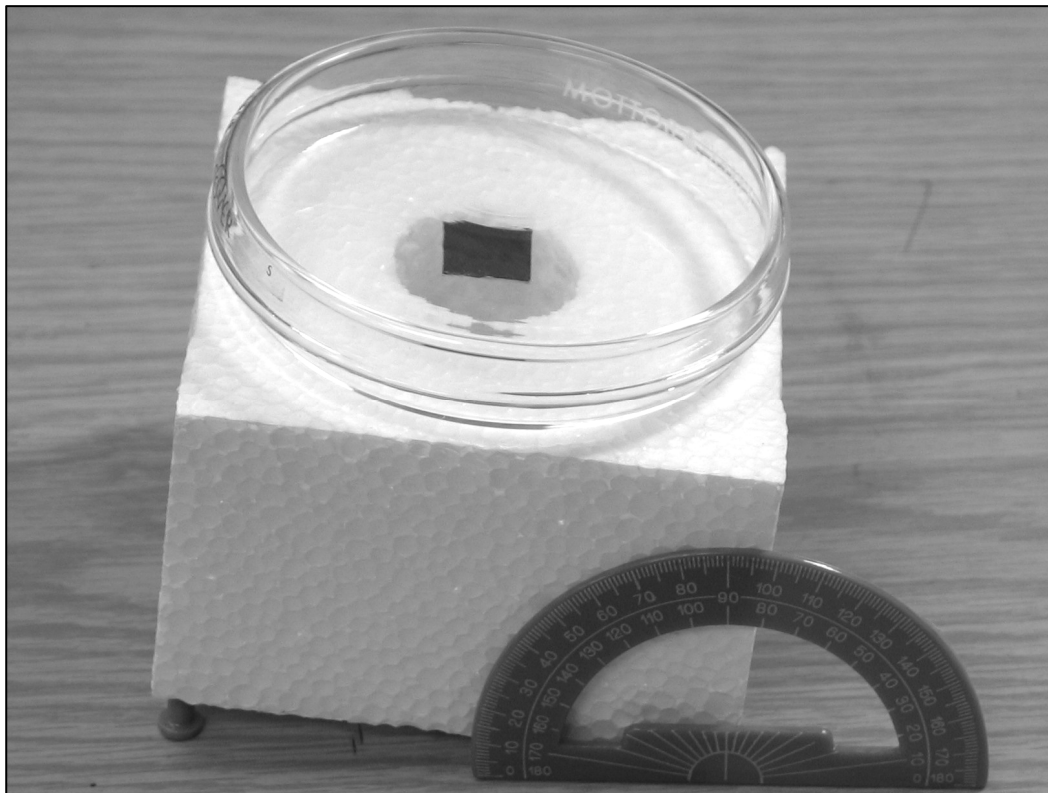


**Figure 2.1** *Simple drying platform used to dry substrates at 10° tilt. The block was shimmed to 10° with respect to the bench top using push pins. After placing the particle suspension on the substrate, the sample was placed into the Petri dish and allowed to dry while covered as shown above.*



in the transformed image can be related to the distance in the original image using the equation  $d = 512/r$ , in which  $d$  is the center-to-center line spacing in the original image and  $r$  is the distance in pixels from the center of the transformed image to the center of the prominent points. Laser diffraction patterns were obtained by illuminating samples at normal incidence with a 5mW helium-neon laser (Hughes) and projecting the resulting diffraction patterns onto a screen at a projection length of 25 cm. Images of the diffraction patterns were taken using a digital camera (Cannon, G3). Zeta potential measurements were performed using a PenKem model 501 Lazer Zee Meter or a Coulter Delsa 440 SX.

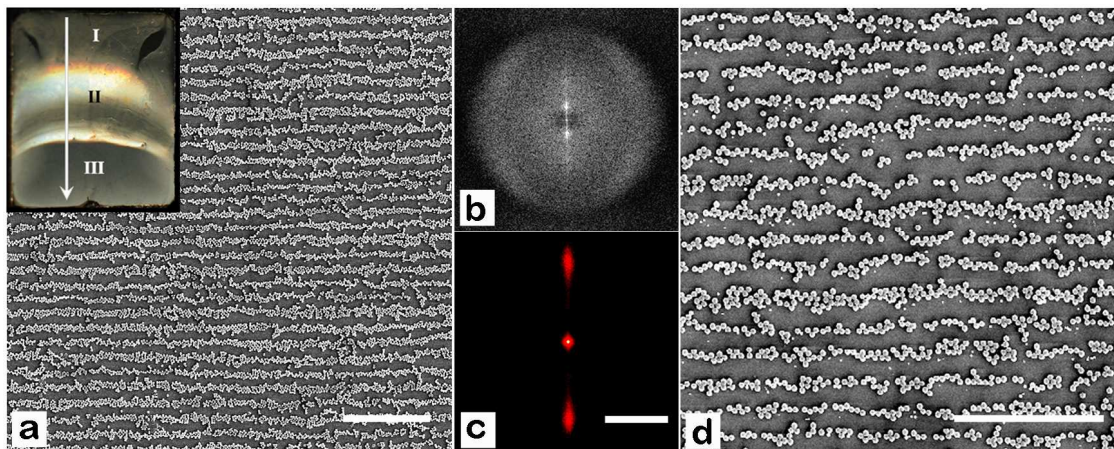
### **2.3 Results and Discussion**

For this study, poly(styrene-*co*-vinylimidazole) latex particles with average diameters of 258 and 391 nm and narrow distributions were the main system investigated. The particles were substantially positively charged under our experimental conditions, as indicated by zeta-potential measurements. It has been previously reported that SiO<sub>2</sub> surfaces in contact with water ionize and bear a negative charge density of roughly -0.32 mC/m<sup>2</sup>.<sup>12</sup> The surfaces of the silicon wafers and glass slides used in this investigation were presumed to have a surface charge similar to this literature value. The self-assembly process was studied by simply placing a drop of a colloidal suspension (typically at 0.02 wt %) on a substrate and allowing the wetted surface to dry. Initially, in a given run, the contact line pinned on the edge of the substrate, which resulted in a region of randomly absorbed colloidal particles (**Figure**

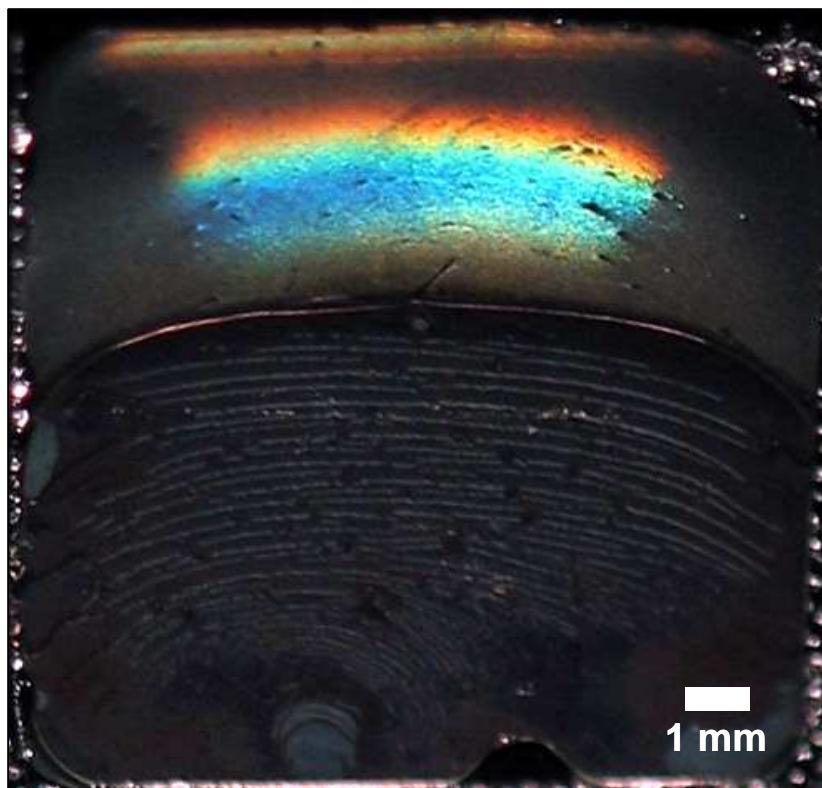
2.2, inset region I). After a sufficient decrease in drop volume due to evaporation, the contact line became dislodged from the edge of the substrate, rapidly advanced a few millimeters, and then began to move in very regular increments. This process resulted in deposition of lines of particles *parallel* to the air-substrate-liquid contact line with regular spacing (**Figure 2.2**, inset region II). The patterned array diffracts light, giving the surface an iridescent appearance, as shown in **Figure 2.3**. The alternating regions of different refractive index at the surface (**Figure 2.4** and **Figure 2.5**) cause the array to behave as a diffraction grating. Macroscopic directionality of the linear pattern running all the way across the width of the substrate was achieved by placing the substrate at a small tilt angle with respect to the horizontal benchtop. If the substrate was left flat, the pattern was in the form of concentric circles.

### 2.3.1 Line-Spacing Measurements

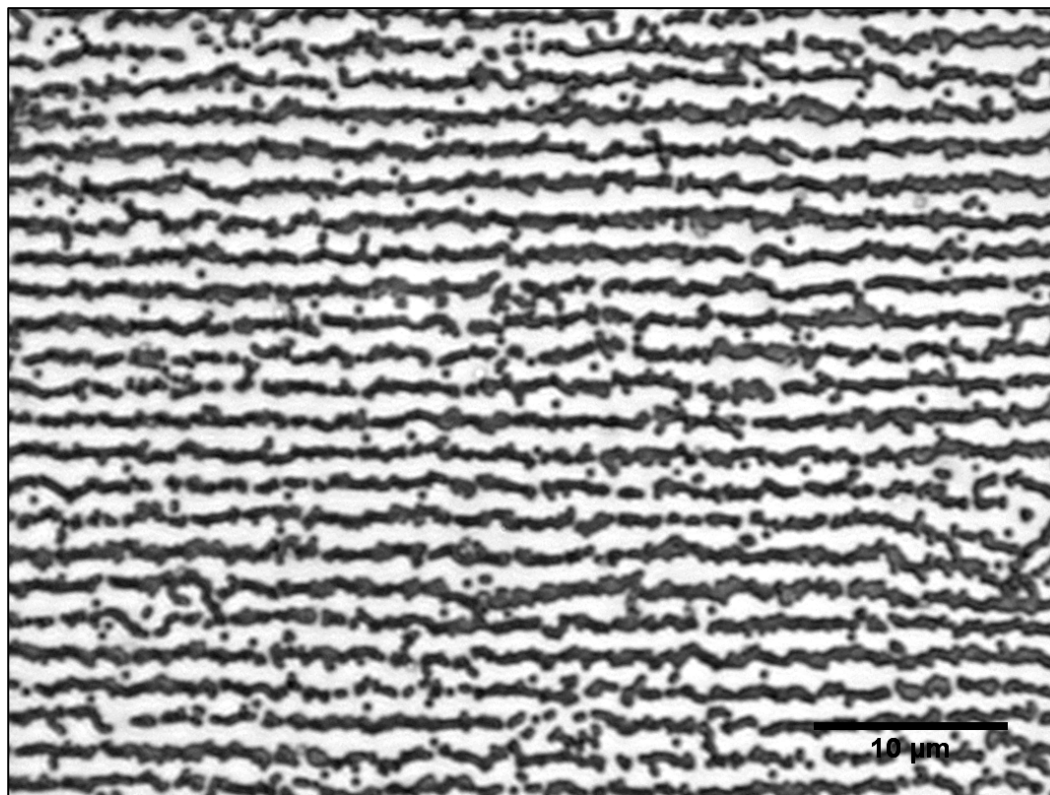
The center-to-center line spacing of the pattern was determined by two-dimensional FFT of the SEM images (**Figure 2.2-b**).<sup>13</sup> As the pattern begins at the end of region I (as described in **Section 2.3.3**), the line spacing is wide and gradually decreases to become roughly constant throughout the rest of region II (**Figure 2.6**). Region III (**Figure 2.2**, inset region III) is characterized by randomly adsorbed particles or an area of close-packed particle monolayers and multilayers, depending on the initial droplet concentration. The end of regular line formation at the junction between regions II and III is likely caused by the concentration of particles in the droplet going below or above (depending on the initial droplet concentration) the range for pattern formation by



**Figure 2.2** *Overview of the linear pattern and analysis procedures. (a) SEM micrograph of the linear array found in inset region II by patterning Imidazole 258 latex particles on glass. Scale bar: 10  $\mu\text{m}$ . The inset (12 mm wide) shows the three regions observed with a typical sample. The arrow indicates the direction in which the liquid receded during the drying process. (b) Fast Fourier transform (FFT) of the linear pattern in micrograph a. The intense spots were used to measure the center-to-center line spacing and the halo is caused by the particle diameter. (c) Laser diffraction pattern of a similar patterned region.  $\lambda$ , 632.8 nm; projection length, 25 cm; Scale bar, 10 cm. (d) SEM micrograph of the linear array formed by patterning Imidazole 391 latex particles on glass. Scale bar: 10  $\mu\text{m}$ .*

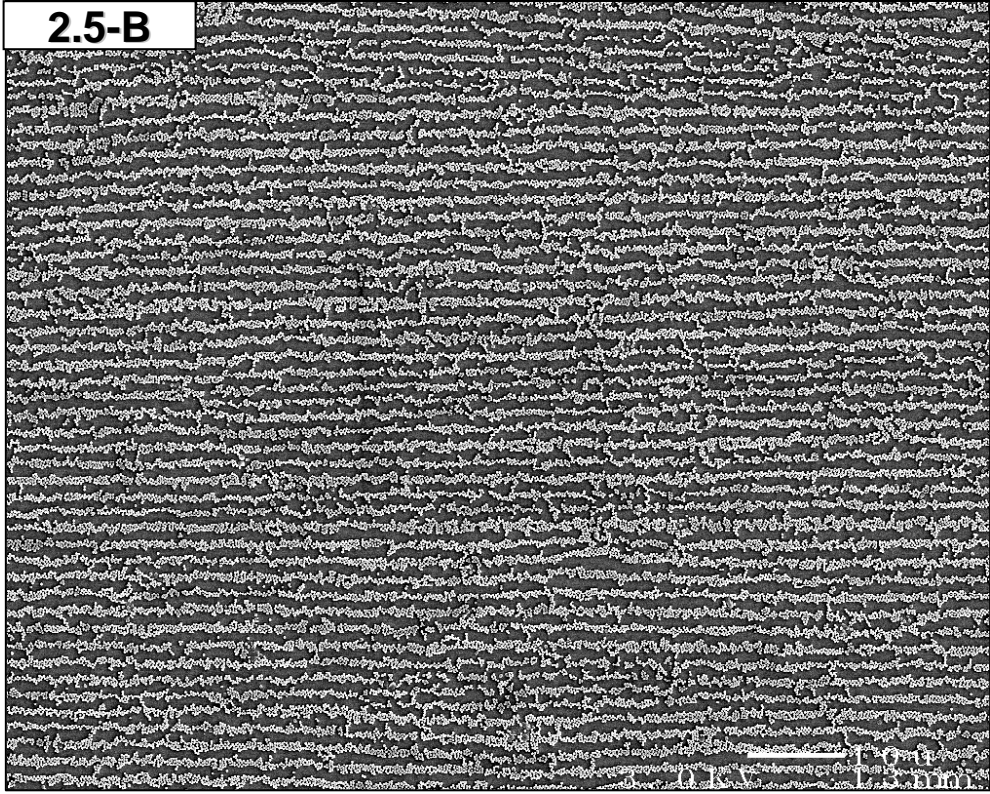
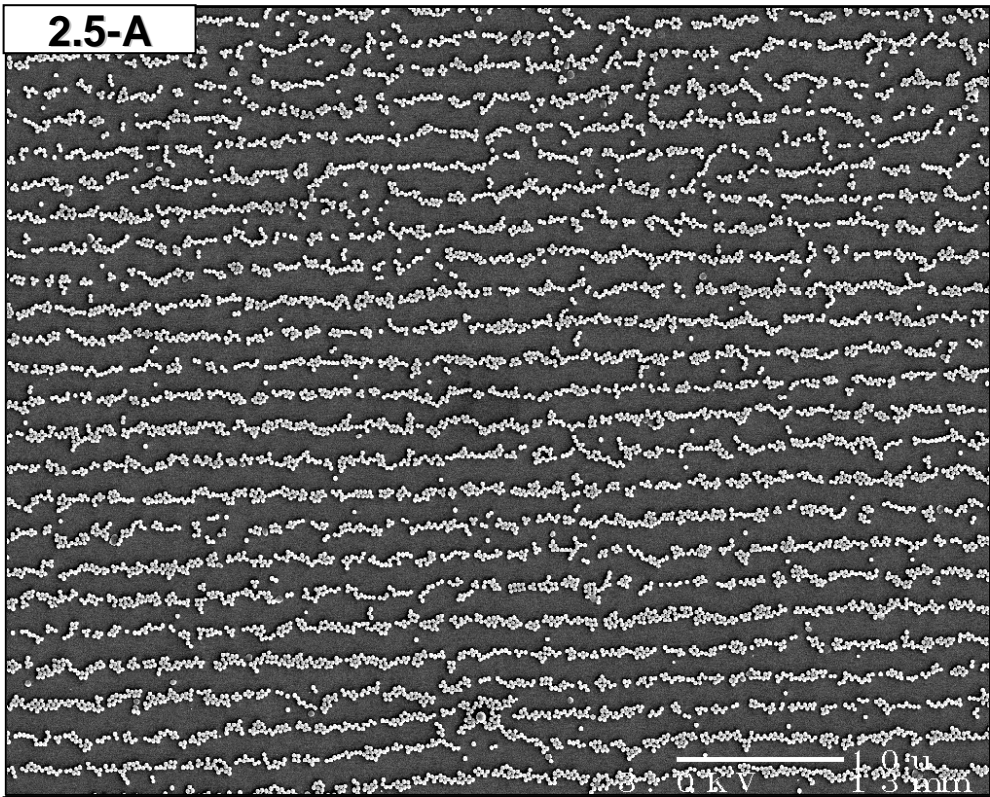


**Figure 2.3** *Macroscopic appearance of the linear patterned region. When illuminated by white light, the linear pattern behaves like a diffraction grating as shown above.*



**Figure 2.4** *Optical micrograph of the patterned region. Since the individual particle diameter of the Imidazole 258 latex is smaller than the wavelength of visible light, individual particles cannot be sharply resolved. Instead, a line of particles behave as a continuous band. The alternating regions of different refractive index are the cause of the optical diffraction. Scale Bar: 10  $\mu\text{m}$ .*

**Figure 2.5** *Typical appearance of the linear pattern formed with the Imidazole 258 latex. The following two micrographs show different regions of the same sample prepared by drying a single drop of 0.02 wt % Imidazole 258 latex on clean glass and allowing it to dry at 10 ° tilt. Scale Bars: 10 μm.*





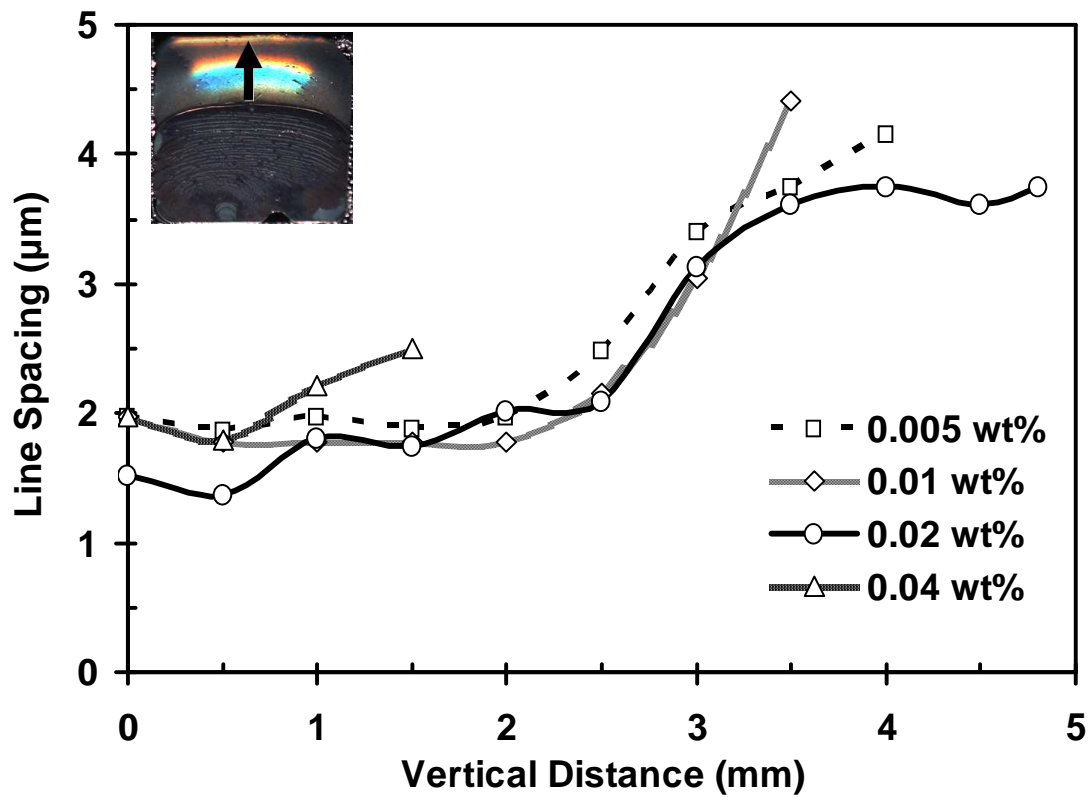


**Figure 2.6** *Line spacing measurements. The change in line spacing with the progression of the drying process for the Imidazole 258 latex particle system on glass at different initial concentrations. The origin was placed in the center of the boundary between region II and region III and measurements were taken at 500- $\mu\text{m}$  intervals while moving toward region I, as shown in the inset.*



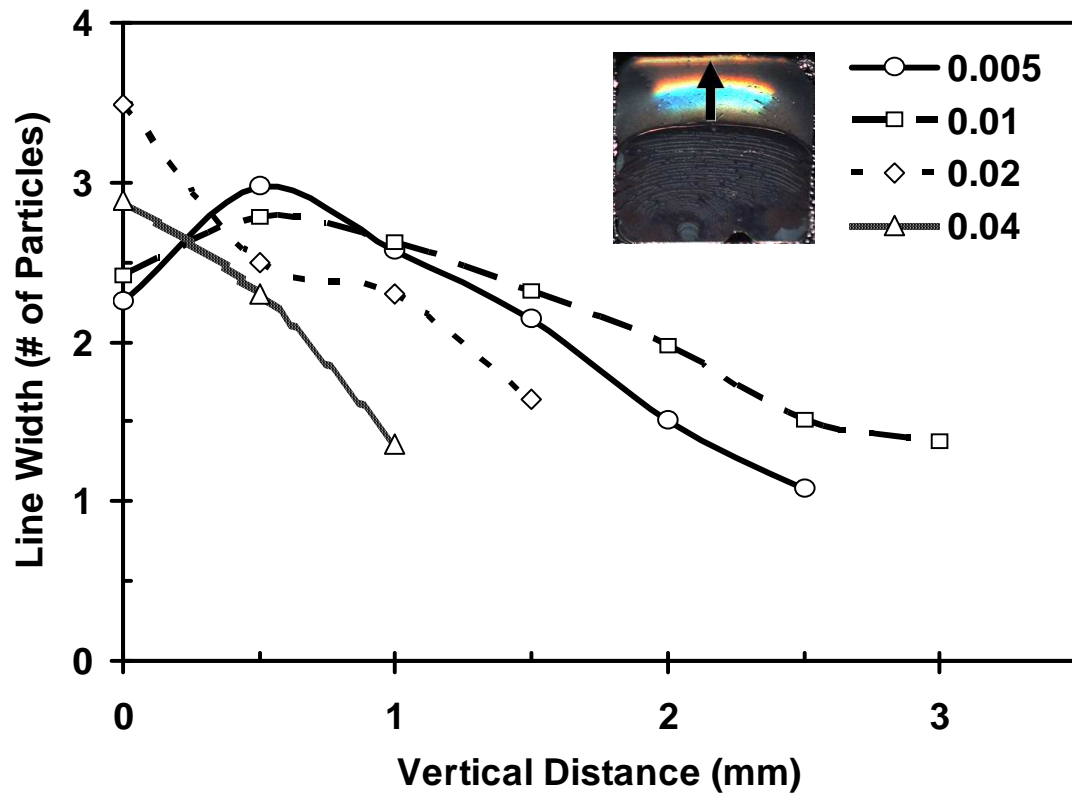
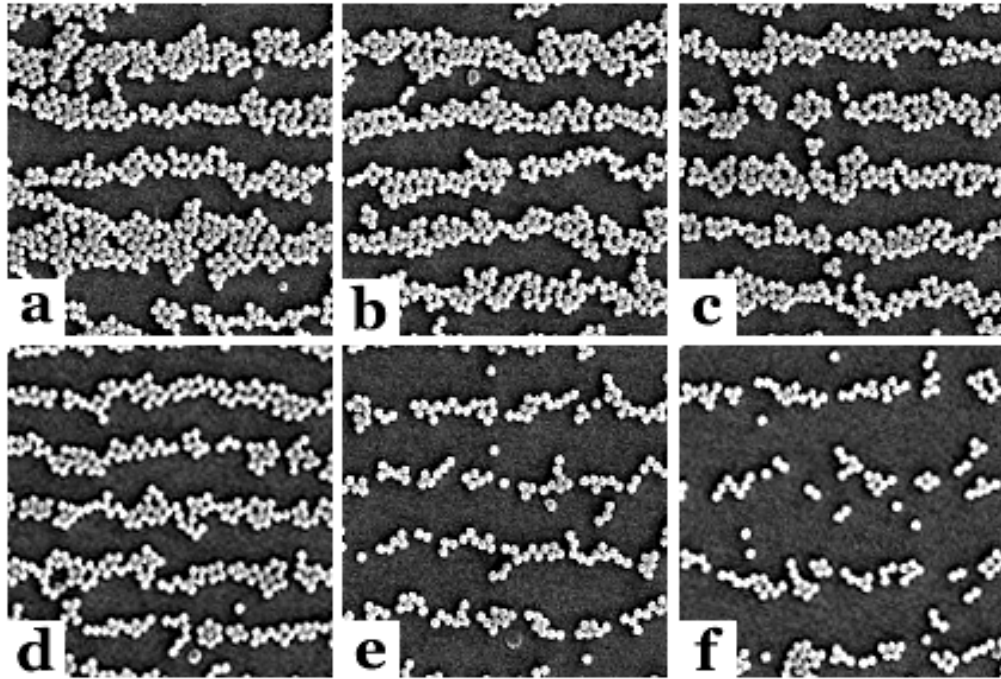
particle deposition or solvent evaporation. The optimal initial concentration ranges from 0.005 to 0.02 wt % particle solids. Within this range, the largest area of region II is observed on the substrate. The upper limit of initial concentration for line formation is approximately 0.2 wt % particle solids. Since the particle suspension concentrations used in these experiments were quite dilute, random sequential adsorption (RSA) of oppositely charged colloids onto the charged substrate<sup>14, 15</sup> occurred very slowly compared to the ordering process and, therefore, did not significantly interfere. Surface coverage measurements were taken to investigate the rate of RSA compared to the ordering process. Even though it typically took 2-3 hours for the substrate to completely dry, the ordered portion of the substrate (region II) was usually dry in approximately 30 minutes. At this point, the suspension concentration of the droplet presumably drops below the critical limit for sustaining the ordering process for samples starting in the optimum concentration range (0.005-0.02 wt % solids), because region III was observed to have a low coverage of randomly adsorbed particles. A control experiment was performed to investigate the degree of particle RSA that occurs during the critical initial stages of the ordering process. Surface coverage measurements were taken by placing a substrate vertically into a sample of 0.008 wt % Imidazole 258 latex for 3 and 10 minutes. The substrate was then removed, gently rinsed with DI water and blown dry with a nitrogen jet. The surface coverage was then measured by SEM. The 3-minute sample resulted in a surface coverage of  $15 \pm 2$  particles per  $100 \mu\text{m}^2$  (standard deviation, 5 measurements), or  $\theta = 0.008$ . The 10-minute sample resulted in a surface coverage of  $22 \pm 3$  particles per  $100 \mu\text{m}^2$  (standard

deviation, 5 measurements), or  $\theta = 0.011$ . These measurements show that RSA occurs very slowly during the ordering process and therefore does not significantly interfere. However, when the experiment was repeated using a sample of 0.2 wt % latex, which is the approximate upper limit of pattern formation, RSA occurred much more quickly. The 3-minute sample resulted in a surface coverage of 226 particles per  $100 \mu\text{m}^2$ , or  $\theta = 0.118$  and the 10-minute sample resulted in a surface coverage of 418 particles per  $100 \mu\text{m}^2$ , or  $\theta = 0.219$ . This surface coverage could be quite disruptive to pattern formation and is one of the probable explanations for the existence of the upper limit.

### 2.3.2 Linewidth Measurements

The linewidths within region II were examined by counting and averaging the number of particles in individual lines (**Figure 2.7**). At low initial concentrations (0.005 and 0.01 wt %), the individual linewidth gradually increased, reached a maximum, and then decreased before the linear pattern rather abruptly faded into region III which contained only sparse randomly adsorbed particles. At intermediate initial concentrations near 0.02 wt %, the individual linewidth more rapidly increased (and for some samples became an area of nearly continuous hexagonal close packed (HCP) monolayer after which individual linewidths re-emerged), and then gradually decreased before the appearance of Region III, once again containing sparse randomly adsorbed particles. At high initial concentrations at or above 0.04 wt %, the individual linewidth rapidly increased and then became a monolayer at the edge of region III which contained HCP monolayers and multilayers. These changes in the linewidth were likely

**Figure 2.7 Linewidth measurements.** Sequence of micrographs of a sample prepared by depositing 1 drop of 0.01 wt % Imidazole 258 latex on a clean glass substrate and allowing the substrate to dry at 10° tilt. Images are taken in sequence moving upwards across the sample in 0.5 mm steps from the boundary of regions II and III, which is in the opposite direction from which the particles were deposited (see plot inset). a. 0.5 mm, b. 1.0 mm, c. 1.5 mm, d. 2.0 mm, e. 2.5 mm, f. 3.0 mm. Each micrograph panel is 10 x 10 μm. Linewidth data from this sample as well as samples with other initial concentrations are shown below. These measurements were taken by drawing a line perpendicular to the particle line array and counting the number of particles making up the width of each particle line at the intersection point. Multiple measurements were averaged to give the data points.



caused by the changing particle concentration within the droplet due to two concurrent events, solvent evaporation and particle deposition.

### 2.3.3 Optical Microscopy

The pattern formation process was monitored by optical microscopy with the substrate at a tilt angle of  $10^\circ$ . The contact line initially receded quickly, in part due to gravity shaping the drop on the tilted surface, resulting in region I. After advancing several millimeters, self-pinning<sup>4</sup> occurred (pinning of the contact line caused by material deposited from within the droplet itself), and the region bearing the linear pattern started to appear. There was no clear transition between regions I and II; instead, the ordered lines emerged from the disorder in a smooth gradient. During the formation of a single line in region II, the contact line was temporarily pinned at a certain position. A point of the contact line then receded to the next position, which immediately triggered the recession of the entire line to the next position. The motion occurred with a regular period of  $5 \pm 2$  s (standard deviation, 126 measurements) during the ordering process for the Imidazole 258 latex. The observed “stick-slip” behavior was remarkably similar to the classic dewetting study by Oliver, Huh, and Mason using a phonograph record blank as the substrate.<sup>16, 17</sup> Compared to pattern initiation, the end of the line-formation process happened abruptly with the appearance of region III.

Optical microscopy indicated that the deposition of the lines of particles parallel to the contact line was due to both the convective particle flow<sup>11</sup> within the evaporating droplet and the “stick-slip” motion of the contact line. The remaining critical question

was what caused the “stick-slip” motion to occur in such regular steps on a substrate without linear surface features. To answer this question, several variables thought to affect the periodicity of the linear pattern were examined: suspension concentration, substrate tilt angle, and the evaporation rate. Varying the initial colloidal suspension concentration had no obvious effect on the center-to-center line spacing. The line spacing was also independent of the substrate tilt angle between 0 and 30°. Variation of the evaporation rate by covering the drying substrate in a Petri dish or leaving it exposed to the ambient environment exerted no obvious effect on the line spacing either, though a faster drying rate resulted in more defects bridging the adjacent lines. The only observed change of line spacing resulted from the progress of the drying process (**Figure 2.6**). The line spacing was wide at the beginning of region II and gradually decreased to become roughly constant throughout the rest of that region.

#### **2.3.4 Contact Angle Measurement by Optical Interference**

A careful examination of the change of the liquid height profile close to the contact line during the evaporative dewetting process provided important insights. First, the liquid height profile was accurately measured by optical interference microscopy using a monochromatic light source.<sup>18</sup> The contact angles at specific positions as the contact line moved down the substrate were calculated from the height profiles. A green band pass filter with a FWHM range of 502-568 nm and a band center of 535 nm was placed into the microscope’s illuminating light beam path. The optical properties of the filter were analyzed using a UV-VIS scanning spectrophotometer

(Shimadzu, UV-2101PC), and the spectrum is shown in **Figure 2.8**. The wavelength of the band center was used for all calculations. Line-plot analysis of the interference bands in the resulting optical micrographs was performed with Image J release 1.32j.<sup>19</sup> After a given micrograph was calibrated, a line-plot in grey value was measured perpendicular to the contact line, which produced a damped sinusoidal curve (**Figure 2.9**). The damping was caused by the increased amount of scattering losses from latex particles in the medium as the height profile increased. The centers of the bright and dark bands were then easily measured using the local max and min values of the curve.<sup>20, 21, 22</sup> The line plot can be fitted with the equation,<sup>23, 24</sup>

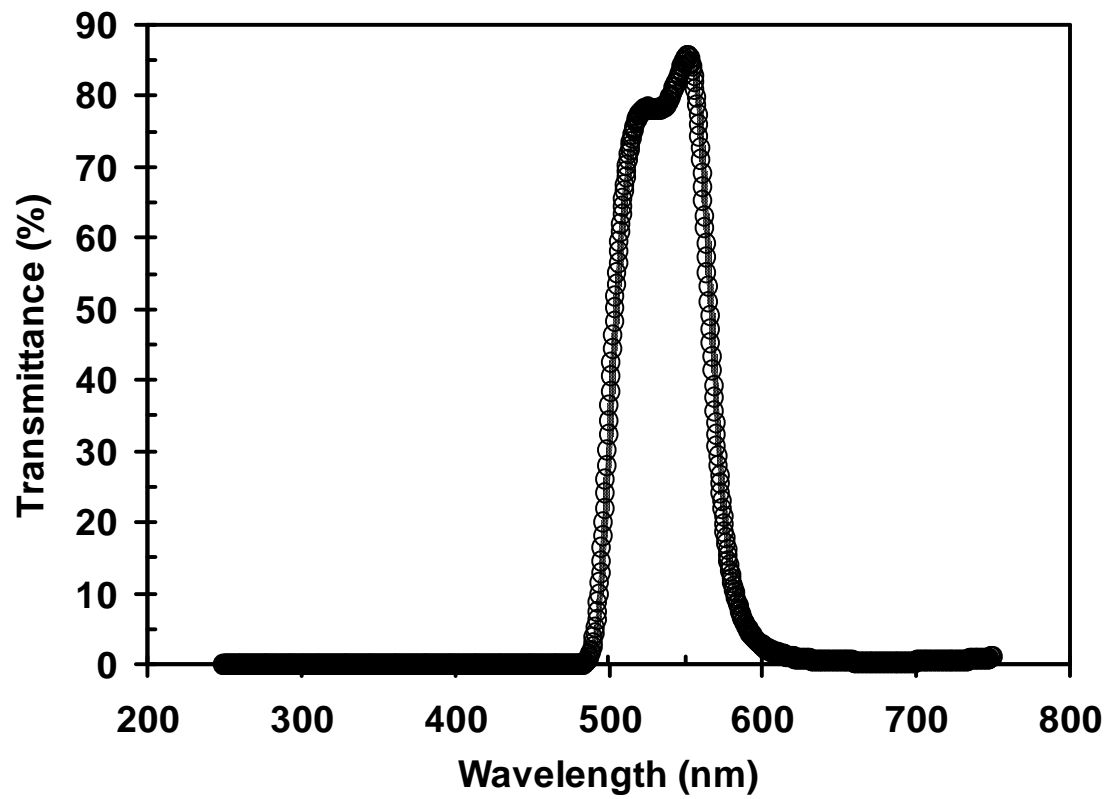
$$y = A \cdot e^{-\gamma \cdot x} \cos(\omega \cdot x + \varphi) + B \quad (2.1)$$

in which  $y$  is the gray value,  $A$  is the amplitude,  $\gamma$  is the decay constant,  $x$  is the perpendicular distance from the contact line,  $\omega$  is the angular frequency,  $\varphi$  is the phase constant, and  $B$  is the baseline offset. Rigorous treatment of the data would require that each line plot be fitted with this equation, as shown in **Figure 2.10**, and the local max and min be calculated from the roots of the derivative. However, this exhaustive treatment produced nearly identical results as approximating the value from the plot. For this reason, we used the second, simpler method.

Optical interference takes place according to the equation,<sup>25</sup>

$$h_l = \frac{m \cdot \lambda}{4 \cdot n_l} \quad (2.2)$$

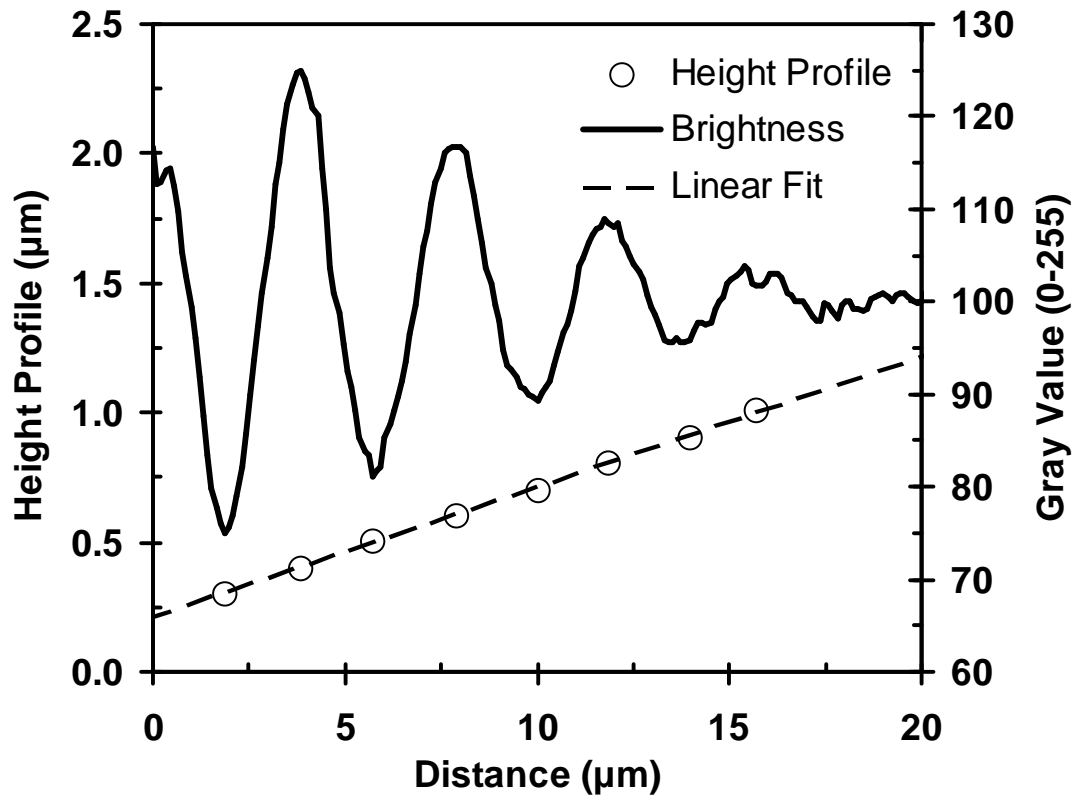
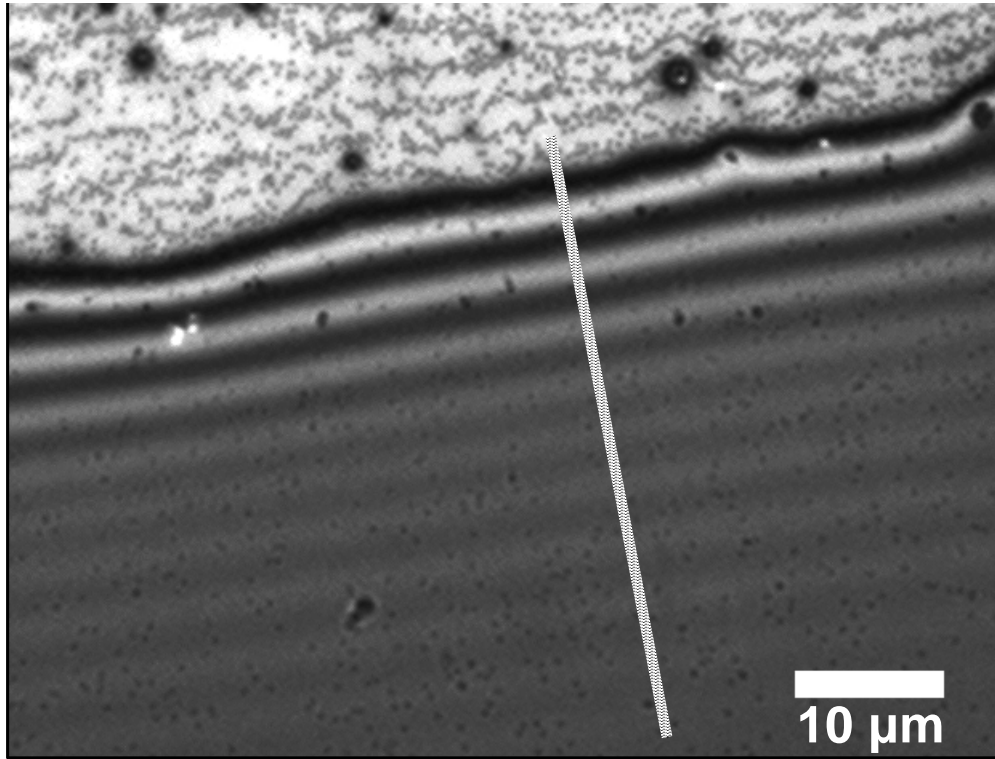
in which  $h_l$  is the height of the liquid layer,  $m$  is a positive integer,  $\lambda$  is the wavelength of the incident beam, and  $n_l$  is the refractive index of the material comprising the liquid



**Figure 2.8** *Band pass spectrum of the green filter used for the contact angle measurements. The filter has a FWHM range of 502-568 nm and a band center of 535 nm.*



**Figure 2.9** *Contact angle measurement by optical interference. The top image shows a grayscale optical micrograph of three-phase line during the ordering process illuminated with 535nm light. Scale bar: 10  $\mu\text{m}$ . The graph below shows the gray scale line plot taken perpendicular to the three phase line (line used seen in image) and the drop height profile approaching the three phase line. The linear fit of the height profile data produces the equation  $y = 0.0503 + 0.2084x$  with  $R^2 = 0.9996$ . The inverse tangent of the slope produces a contact angle value of  $2.88^\circ$ .*



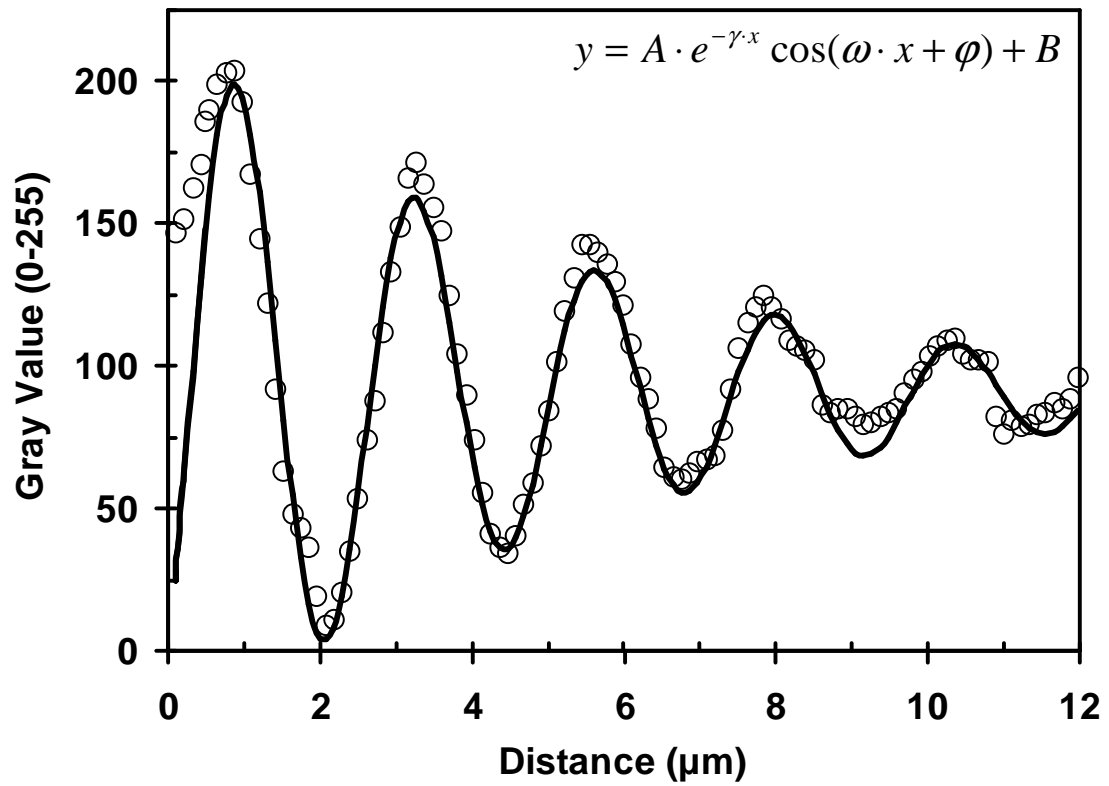


**Figure 2.10** *Curve fitting of the line plot data. The data are fit with the equation shown above with  $A = 128.7$ ,  $\gamma = 0.1927$ ,  $\omega = 2.650$ ,  $\varphi = 3.909$ , and  $B = 90.27$ .*

layer. Constructive interference takes place if  $m$  is an even number, and destructive interference takes place if  $m$  is odd. The linear height profile can be constructed by least-square fitting of the height data (**Figure 2.9**), and the contact angle was easily calculated as the inverse tangent of the slope of the linear fit. FFT analysis of the optical micrographs was then performed to measure the line spacing just above the contact line region where a given contact angle was measured. The correlation between the contact angle and the line spacing is shown in **Figure 2.11**.

### **2.3.5 Self-Assembly Mechanism**

The decrease of the line spacing with the increase of the contact angle allows the following mechanism for the formation of the linear pattern to be proposed. After the ordering process is initiated, the contact line is pinned on the back edge of the previously formed line at a height lower than one particle diameter (**Figure 2.12**). Because the contact angle is quite small, the liquid layer does not reach the height of one particle diameter until moving back one to a few  $\mu\text{m}$  from the contact line. Convective flow rushes particles into the wedge-shaped liquid layer, and at the location with the wedge thickness equal to, or perhaps slightly larger than, the particle diameter, the particles are arrested by the surface and become immobile due to attractive forces. As the deposition process continues down the substrate, one line at a time, the contact angle gradually increases as the contact line approaches the bulk drop resting at the bottom of the substrate. As a result, the particles are able to approach closer to the previous line where the drop edge is pinned, resulting in closer line spacing. By

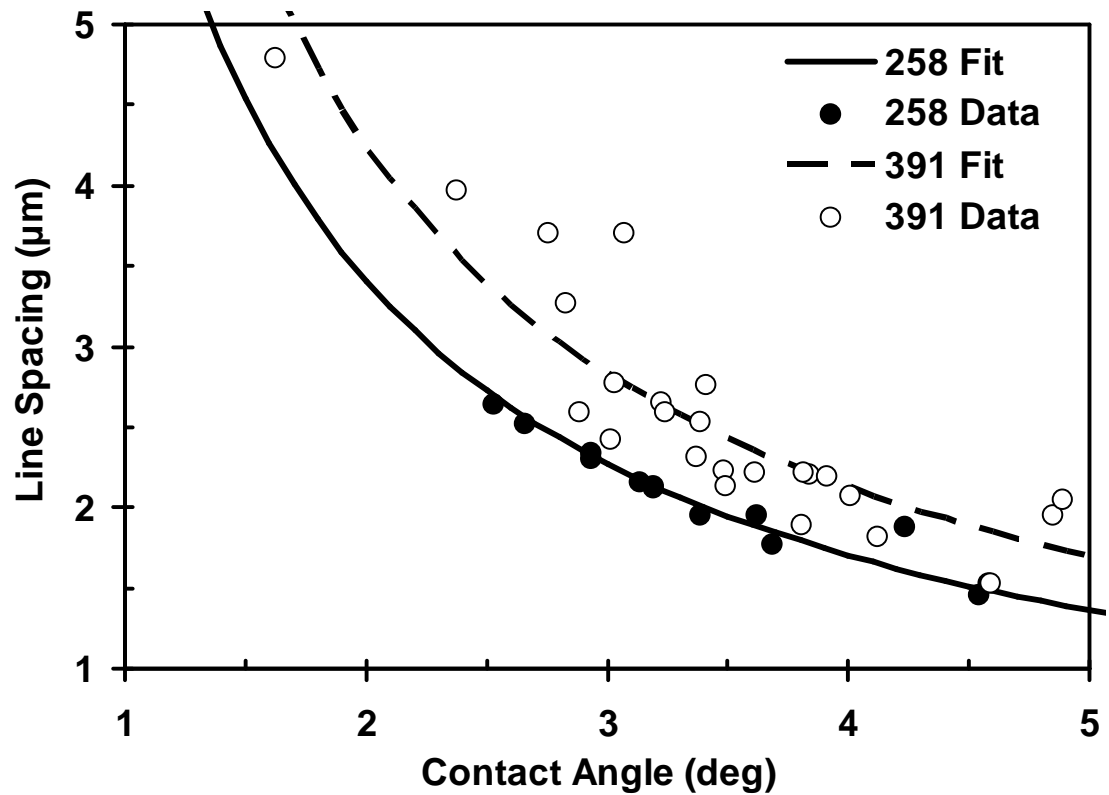


**Figure 2.11** *Line spacing as a function of contact angle. Effect of the contact angle on the line spacing of 258 and 391 nm particle patterns on glass fitted with the equation  $y = (D-h)/\tan(x)$  in which  $y$  is the line spacing from the FFT data,  $D$  is the particle diameter,  $h$  is the height of the three phase line at the pinning site, and  $x$  is the contact angle.*

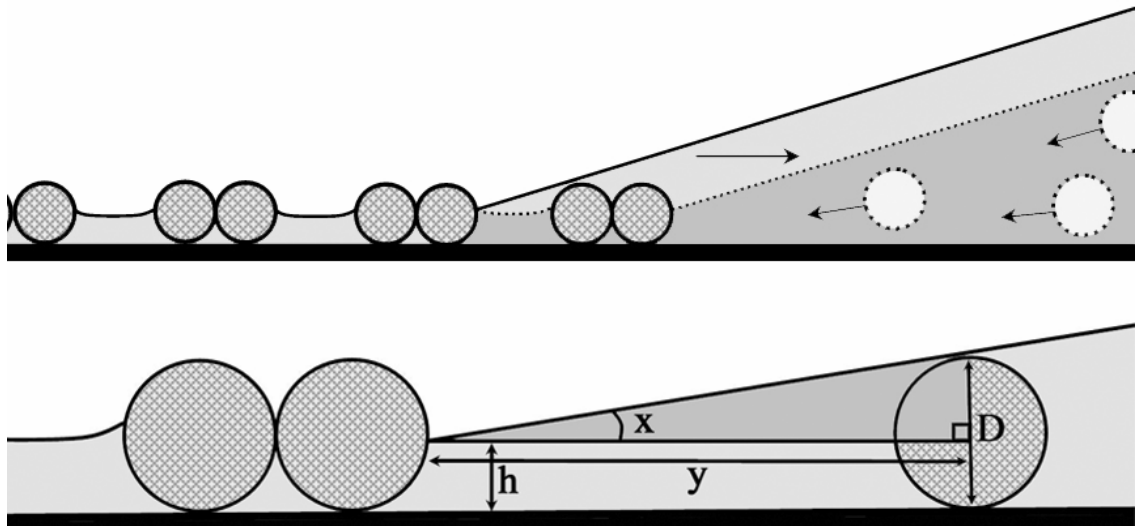


**Figure 2.12** *Schematic illustration of the ordering process. Top: The contact line pins on the back edge of the previously formed particle line. The advancing particles are forced into contact with the substrate at a fixed distance from the front due to the wedge shaped geometry. This line is the next pinning site as the self-propagating assembly mechanism moves down the substrate driven by the decreasing volume of the drying drop. Bottom: Geometry used to describe the ordering process.*

assuming that a given particle will become pinned when it encounters the liquid height equal to its diameter, the above model predicts the geometric relationship,

$$y = \frac{(D - h)}{\tan(x)} \quad (2.3)$$

in which  $y$  is the line spacing in  $\mu\text{m}$ ,  $D$  is the particle diameter in micrometers,  $h$  is the pinning height in micrometers on the back of the previous line, and  $x$  is the contact angle in degrees. The data resulting from the contact angle and FFT spacing analysis for both the Imidazole 258 and 391 latex particles can be fitted with this equation (**Figure 2.11**). The curve fit produces an  $h$  value of 139 nm for the 258 nm particle data and 243 nm for the 391 nm particle data. These height values are consistent with what would be expected if the contact line were being pinned on the backside of a ridge one diameter high.<sup>2</sup> Essentially, a grooved surface similar to the classic phonograph record example was assembled one line at a time.<sup>16, 17</sup> The “groove” behind the contact line is assembled immediately before the contact line retracts and pins upon it. Once the first particle row forms, the order reproduces itself as the contact line propagates down the surface of the substrate. Thousands of lines are deposited during a typical experiment.

### 2.3.6 Control Experiments

The deposition of negatively charged particles on negatively charged glass surfaces to form HCP particle bands has been rather extensively studied by Nagayama et al.<sup>5, 8, 9</sup> As control experiments, some of their results were reproduced. Further, when the surface charge of the substrate was switched from negative to positive by adsorbing

a layer of PDDA, both the 258 and 391 positive particles again formed wide HCP particle bands with irregular band spacings similar to the negative particles on the negative surface. It is instructive to review previous studies on the formation of HCP bands of negatively charged latex particles on negatively charged surfaces formed by evaporative processes in comparison with the present case.<sup>4, 5, 6, 7</sup> In these reports, bands with widths ranging from 10 to 200  $\mu\text{m}$  with irregular inter-band distances are formed. According to Nagayama's model, particles are injected *past the contact line into the wetting film* by convective flow. The negative particles are laterally mobile in the wetting film until incorporated into the HCP lattice by capillary forces. No line or band is assembled behind the contact line before the contact line slips. In the positive-on-negative case, the particles stop and are *laterally immobile before they are able to reach the contact line*. The differences between the same-charged systems and the oppositely charged systems clearly show, without excluding the possible roles of other attractive force, that the Coulombic attraction is critical for the linear pattern formation.

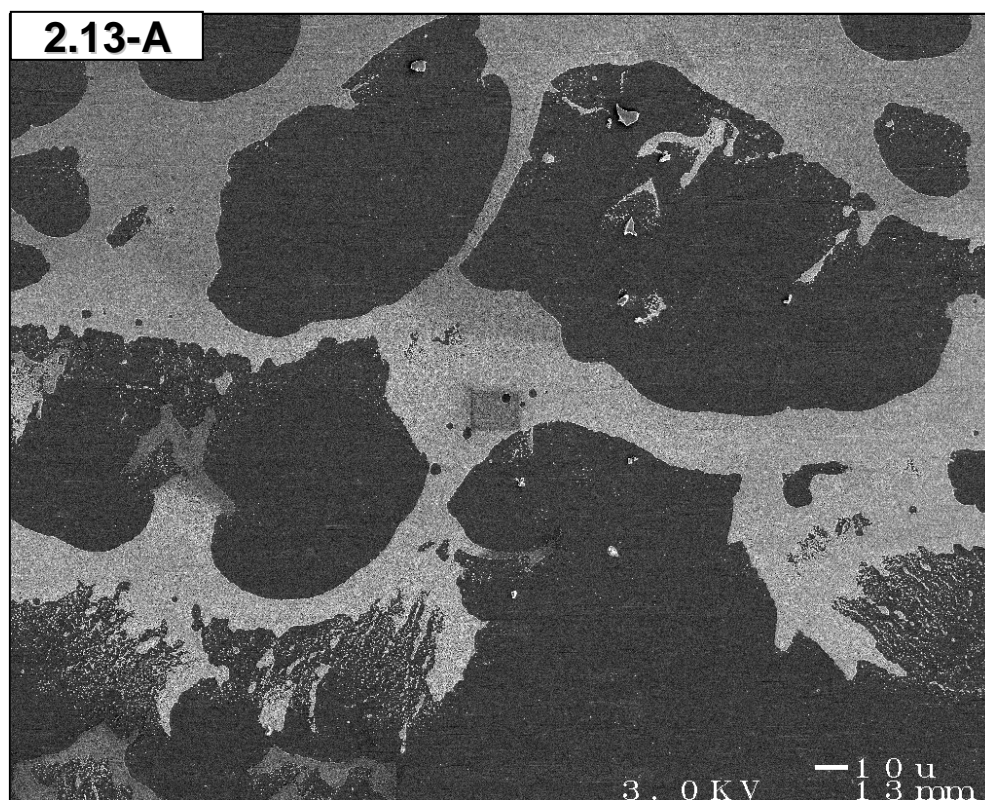
In order to demonstrate the importance of the particle substrate interaction, control experiments were performed in which the particles and the substrate were of opposite charge. Negatively charged particles with various diameters and surface chemistries were used to establish that these variables did not affect the deposition mode. Alternatively, the substrate surface charge was switched using a positively-charged polyelectrolyte or adsorbed particle layer to further investigate the charge interactions.

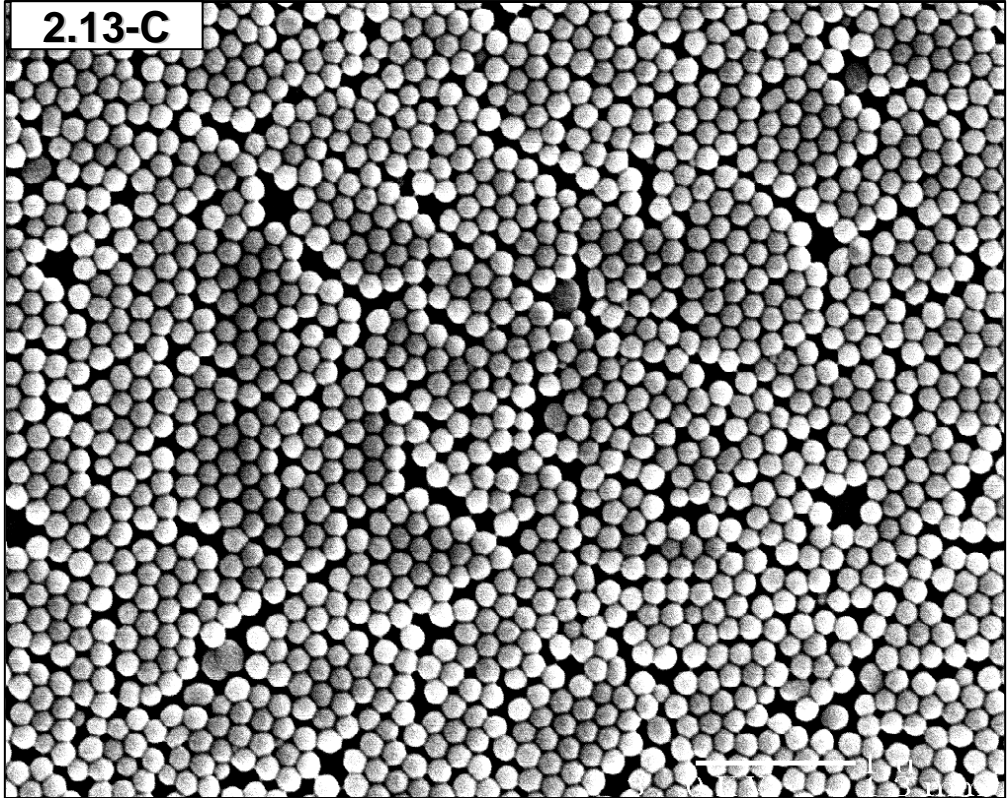
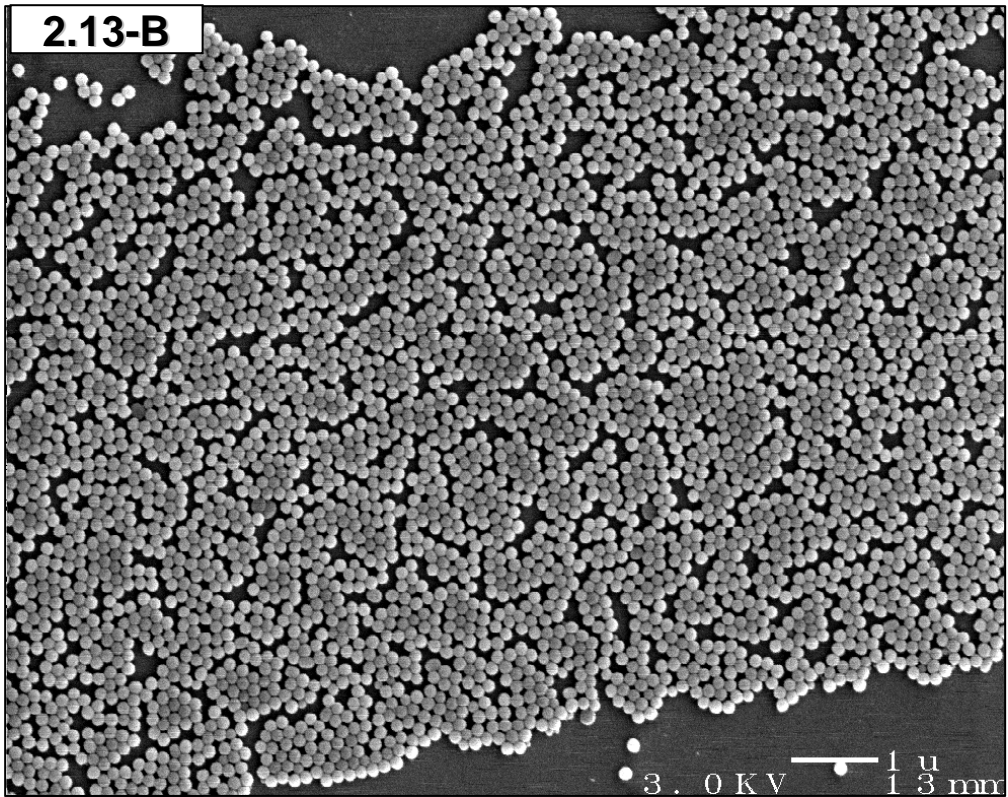


**2.3.6.1 Particle Charge.** The sample shown in **Figure 2.13** was prepared by depositing one drop of 0.03 wt % Sulfonate 128 latex onto a clean glass substrate and allowing the substrate to dry at 10° tilt. Wide HCP particle bands with irregular spacing resulted. The experiment was repeated using one drop of 0.02 wt % Sulfate 176, 234, and 357 latex particles and the results of this experiment are shown in **Figure 2.14**, **Figure 2.15**, and **Figure 2.16** respectively. Wide HCP particle bands with irregular spacing resulted in every case, with no obvious effect caused by increasing the particle diameter.

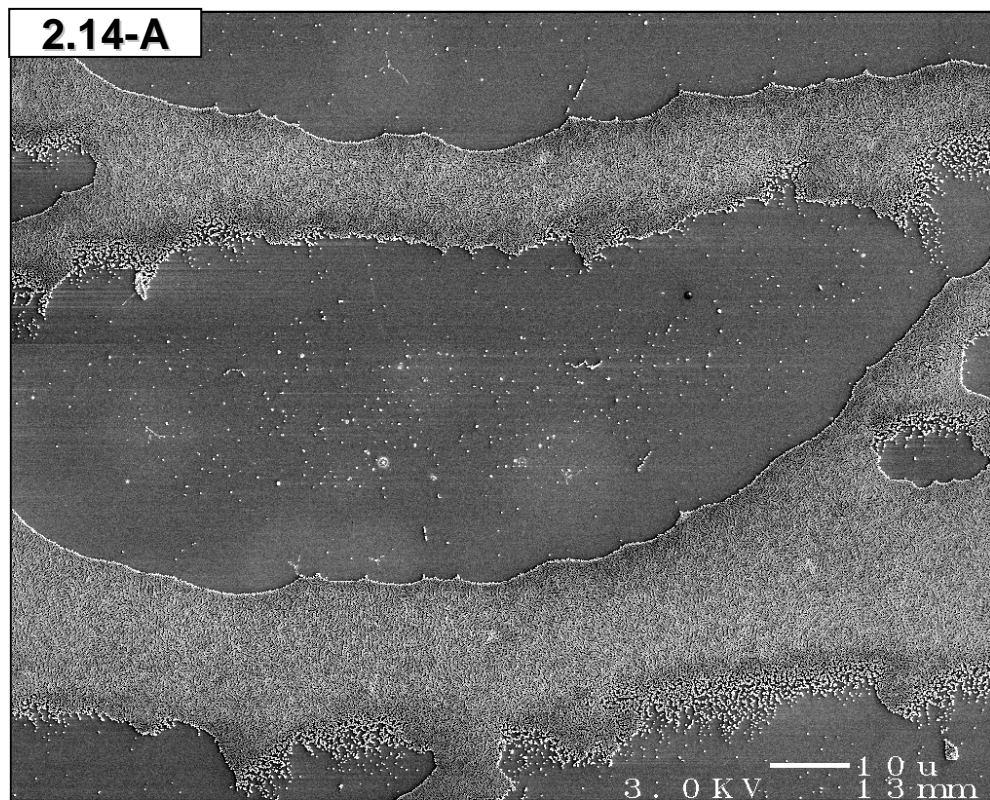
**2.3.6.2 Surface Charge.** The sample shown in **Figure 2.17** was prepared by placing one drop of 0.02 wt % Imidazole 258 latex on a glass substrate that had been treated with PDDA, rendering the surface positively-charged, and drying at 10° tilt. Micrographs of the resulting pattern bear a striking resemblance to the negative-on-negative patterns shown in **Figure 2.13** through **Figure 2.16**. When the substrate has the same charge as the particles, irregularly spaced wide bands result. A side by side comparison of the effect of surface charge is shown in **Figure 2.18**. The sample shown in **-A** was prepared by depositing Imidazole 258 latex on a clean glass, and **-B** was prepared on a PDDA-treated substrate. As can be seen, the first sample resulted in thin well-spaced particle lines, while the second produced thick irregularly spaced bands. The experiment was repeated, except the respective samples were prepared using Imidazole 391 latex particles as seen in **Figure 2.19**. Once again, switching the surface charge disrupted the linear pattern-forming process and resulted in wide particle bands.

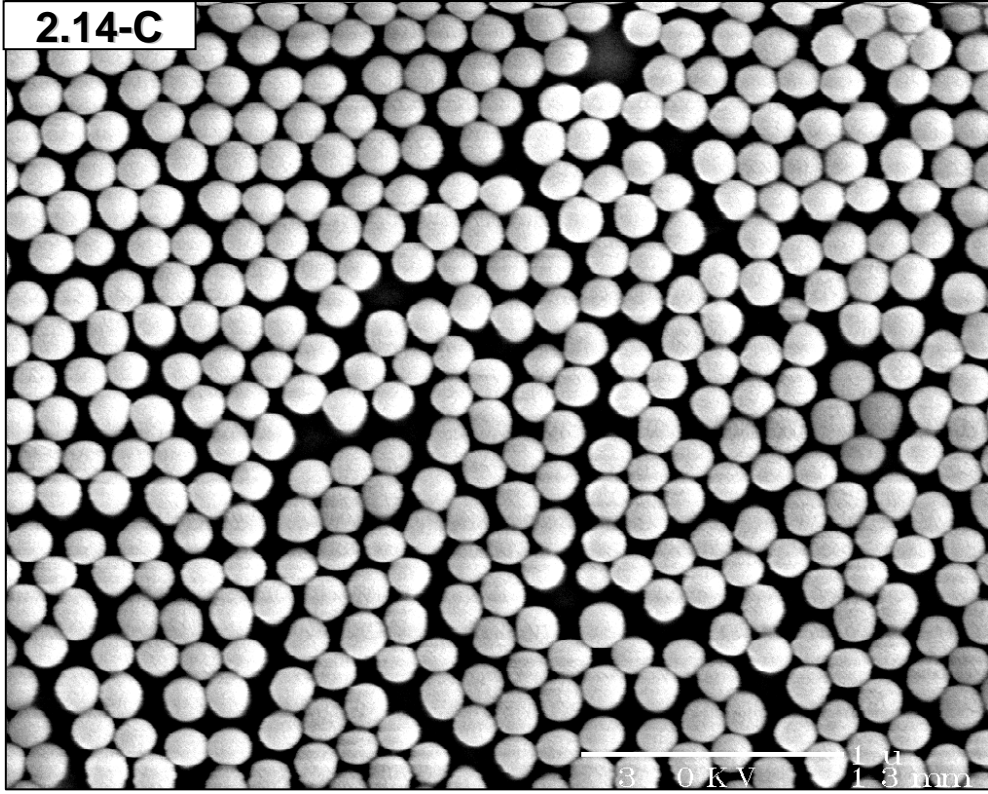
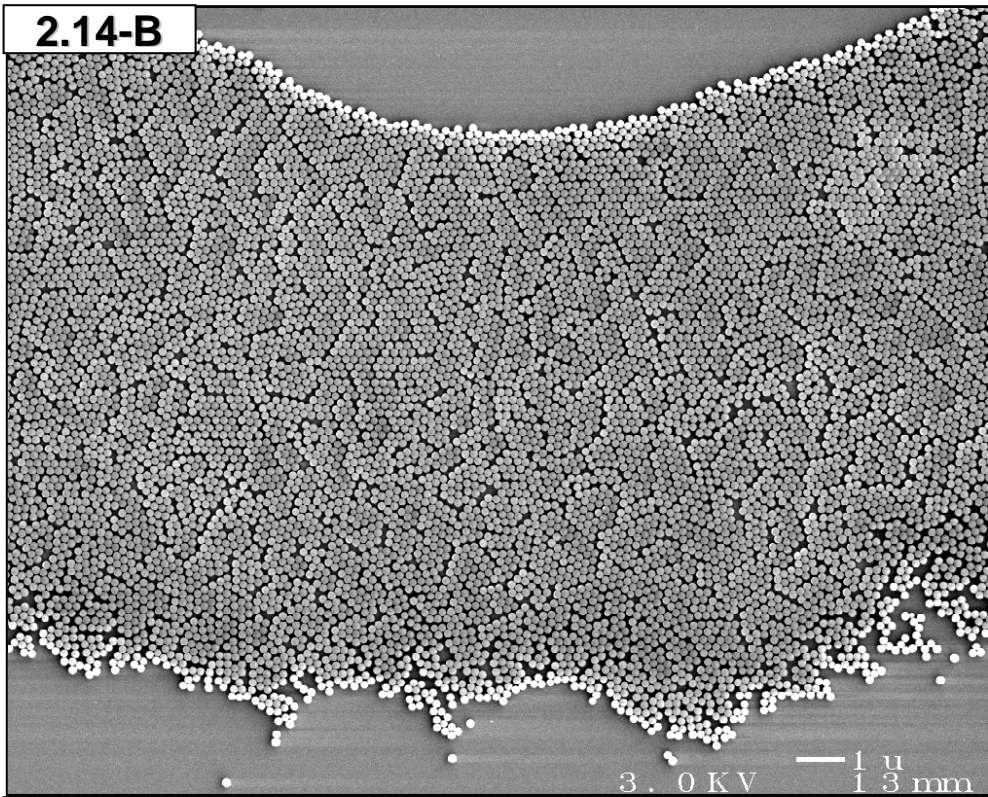
**Figure 2.13** *Negatively-charged Sulfonate 128 latex on glass. The following set of micrographs, increasing in magnification, show the result of depositing one drop of 0.03 wt % Sulfonate 128 latex on a negatively-charged glass surface and allowing it to dry at 10° tilt. Scale Bars: 10, 1, and 1 μm respectively.*





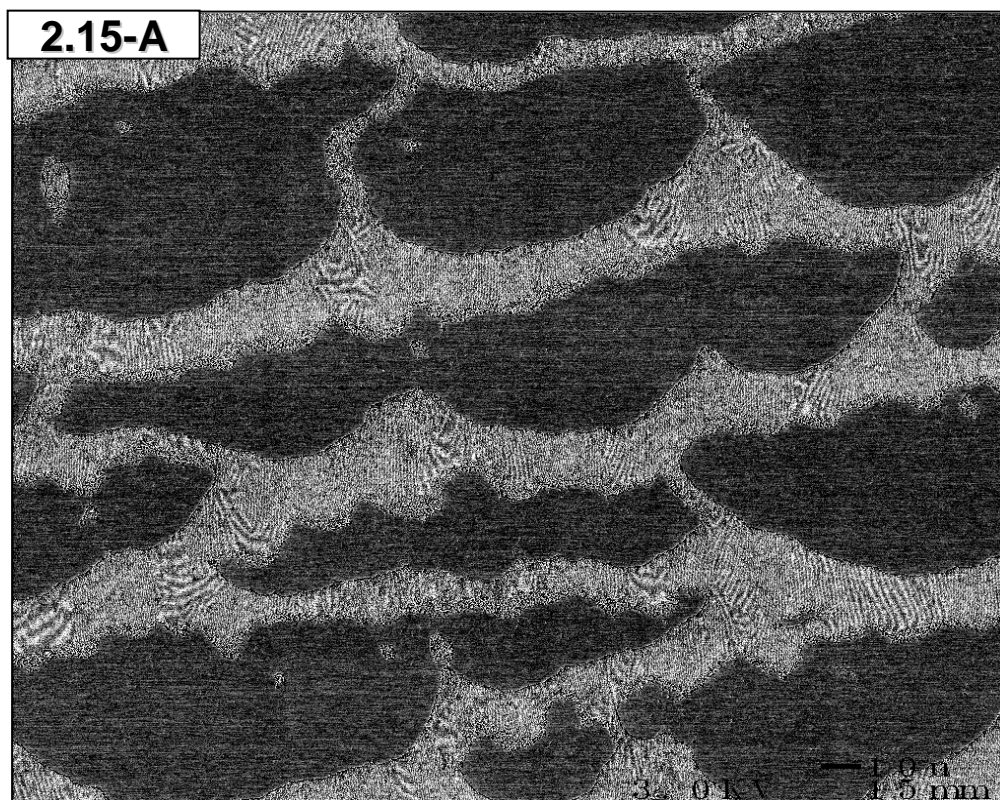
**Figure 2.14** *Negatively-charged Sulfate 176 latex on glass. The following set of micrographs, increasing in magnification, show the result of depositing one drop of 0.02 wt % Sulfate 176 latex on a negatively-charged glass surface and allowing it to dry at 10° tilt. Scale Bars: 10, 1, and 1 μm respectively.*

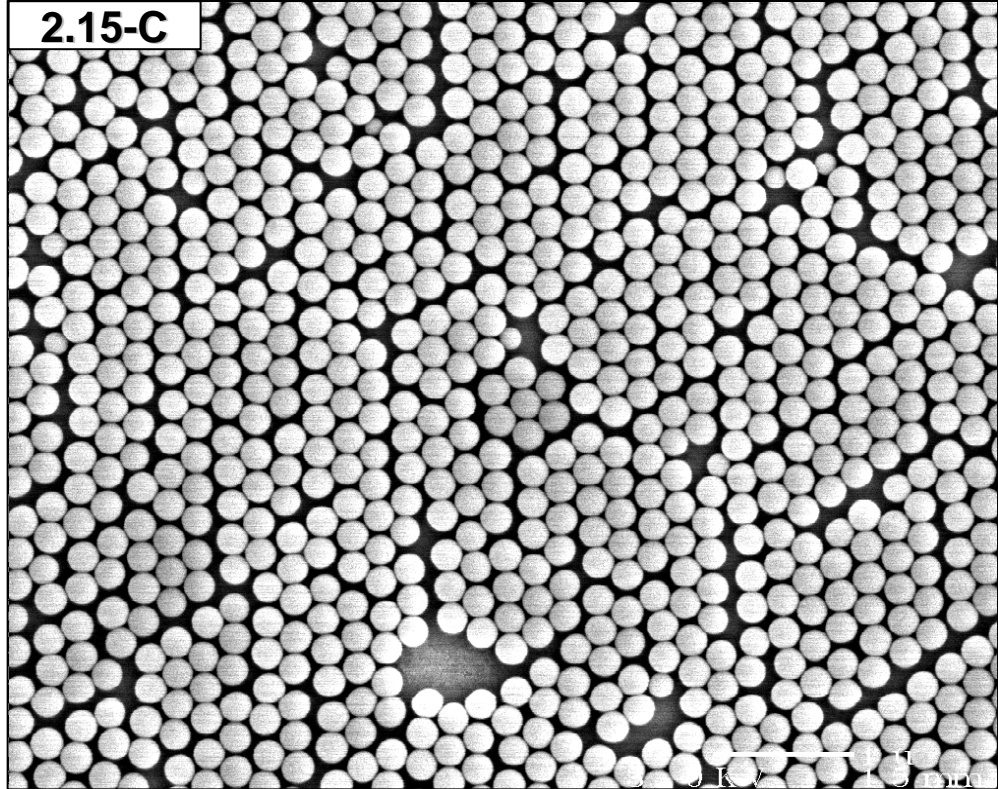
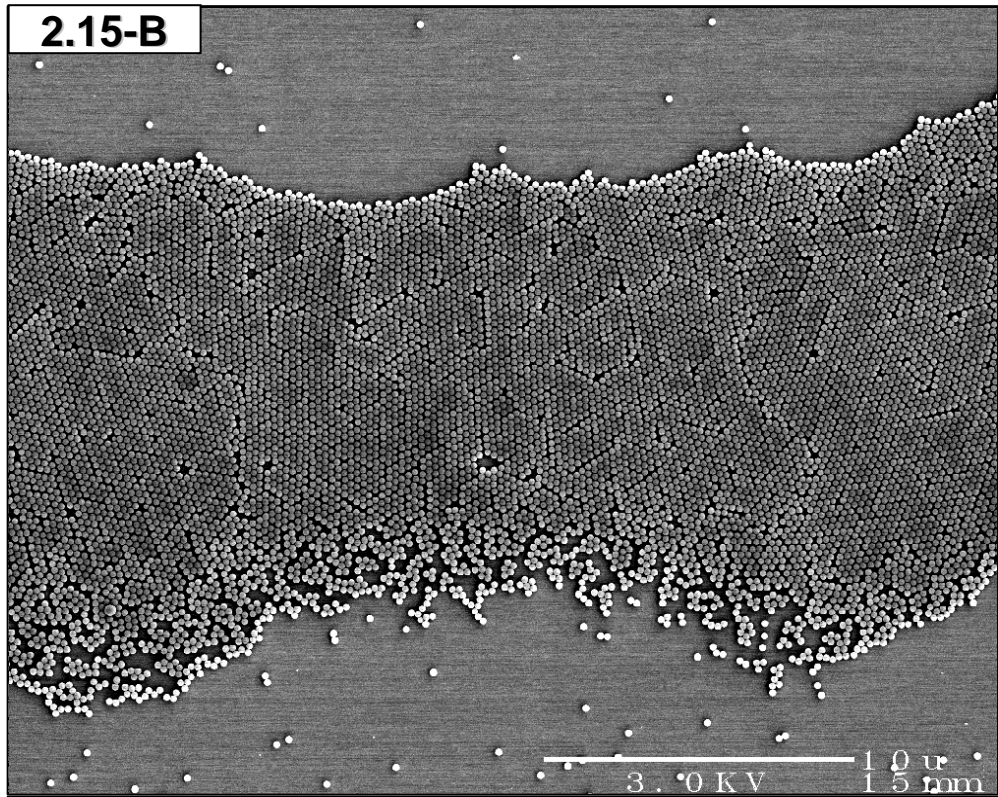




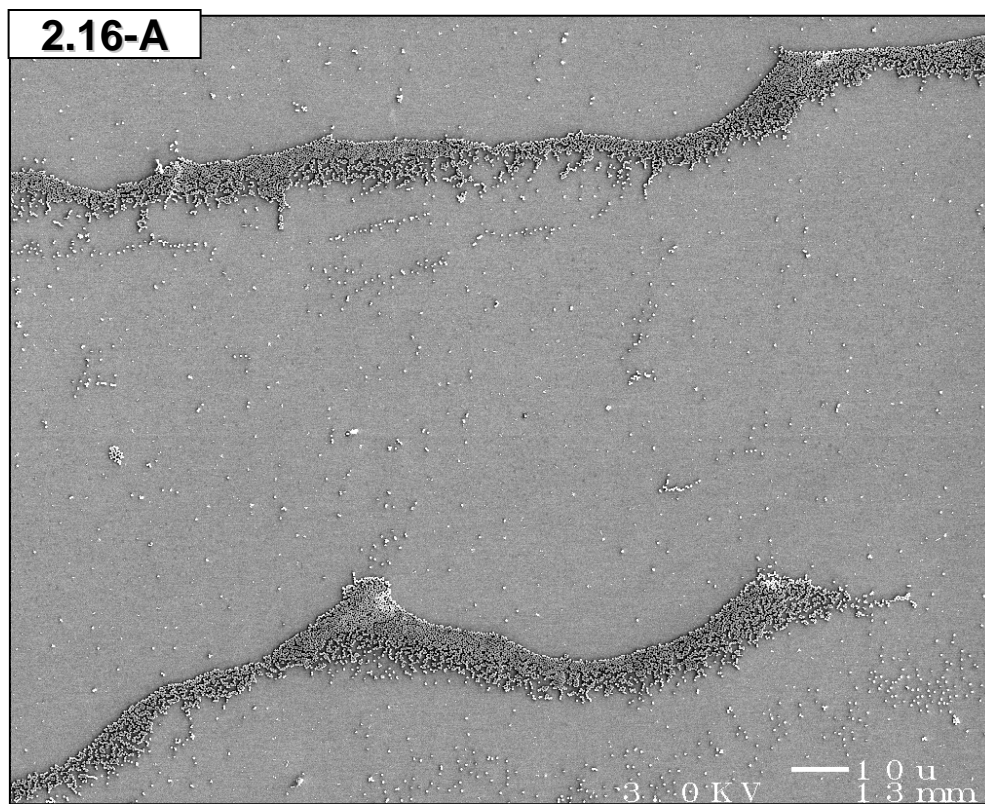


**Figure 2.15** *Negatively-charged Sulfate 234 latex on glass. The following set of micrographs, increasing in magnification, show the result of depositing one drop of 0.02 wt % Sulfate 234 latex on a negatively-charged glass surface and allowing it to dry at 10° tilt. Scale Bars: 10, 10, and 1 μm respectively.*

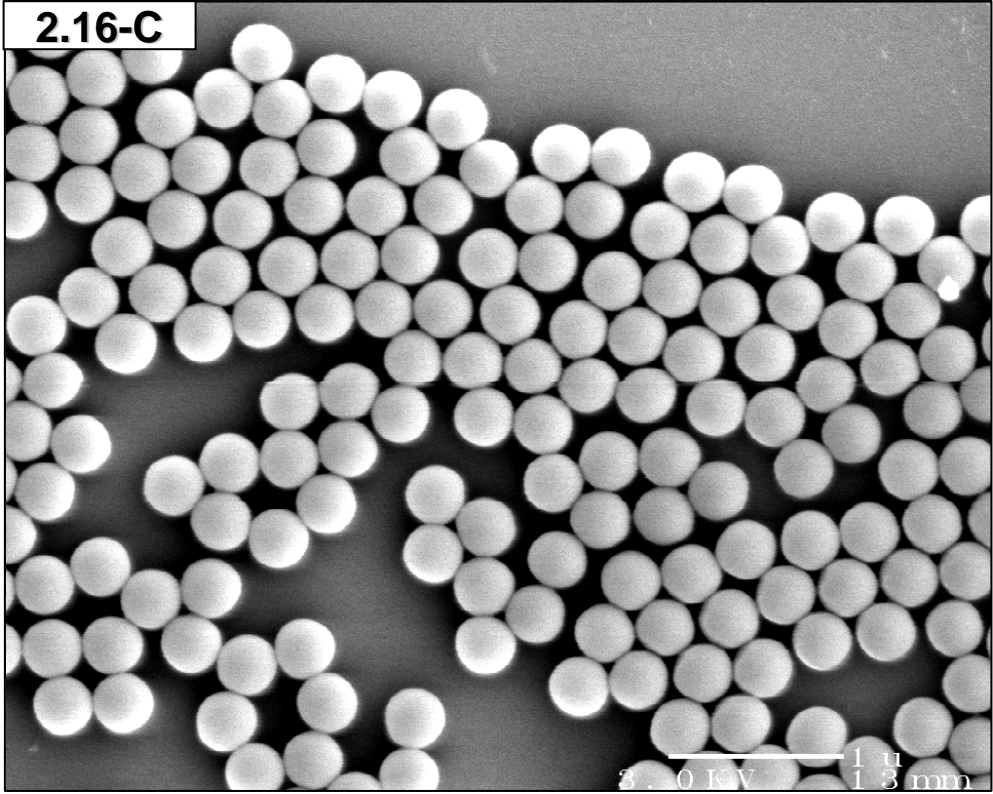
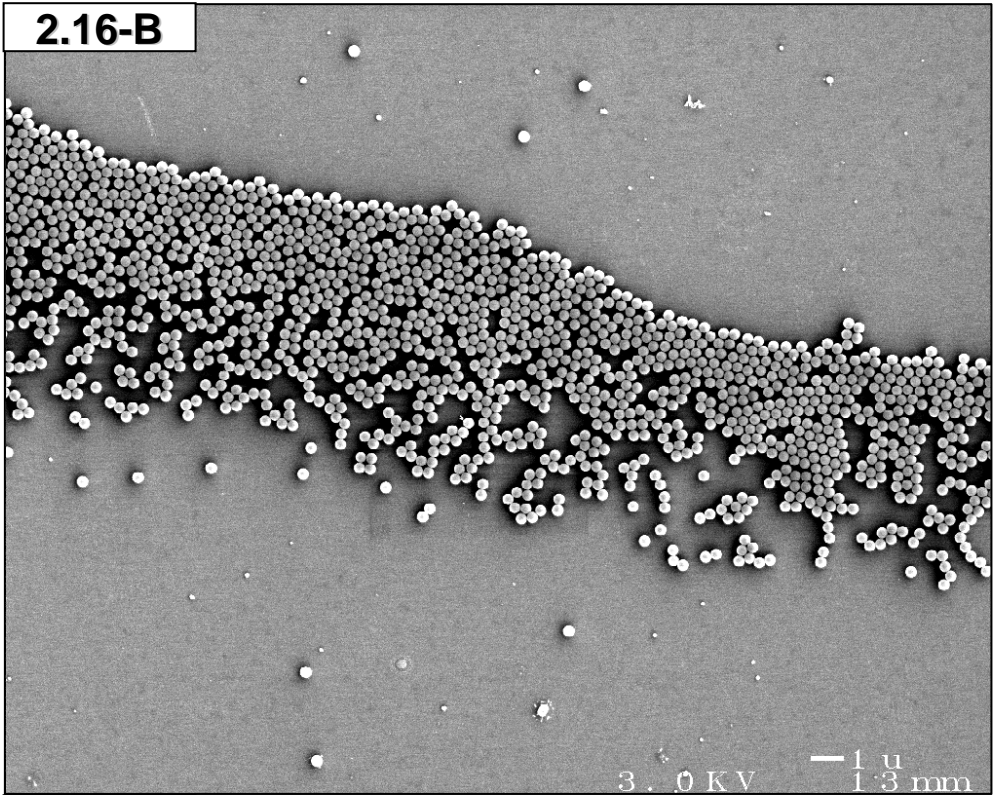




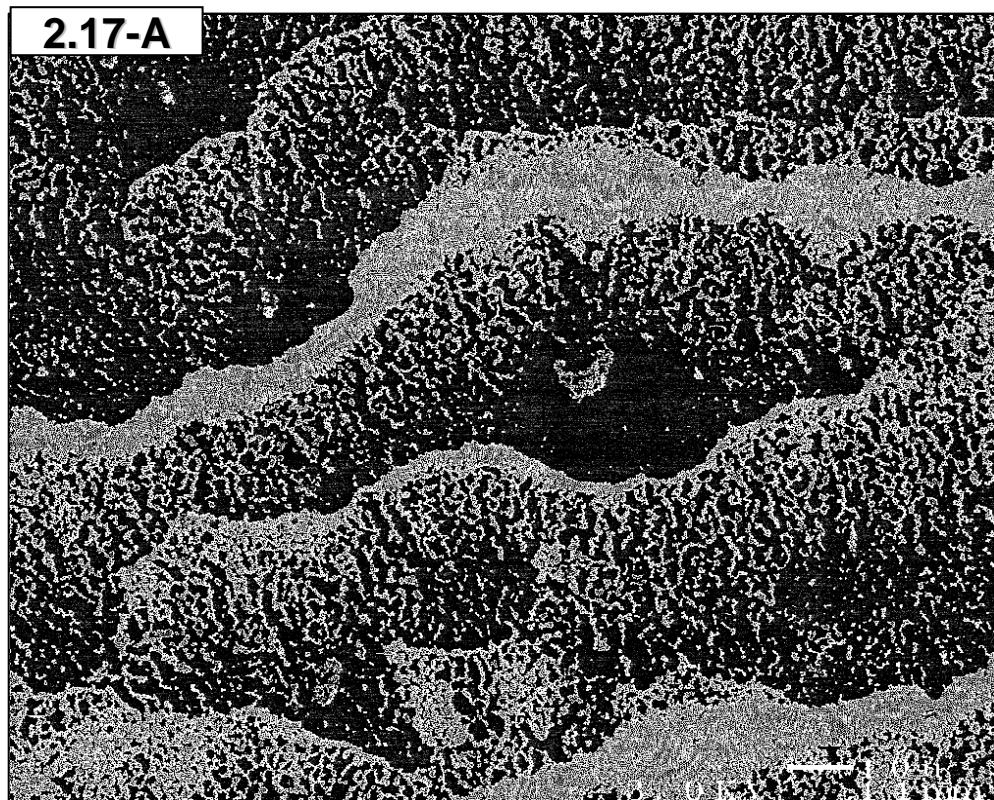
**Figure 2.16** *Negatively-charged Sulfate 357 latex on glass. The following set of micrographs, increasing in magnification, show the result of depositing one drop of 0.02 wt % Sulfate 357 latex on a negatively-charged glass surface and allowing it to dry at 10° tilt. Scale Bars: 10, 1, and 1 μm respectively.*







**Figure 2.17** *Positively-charged Imidazole 258 latex on a positively-charged PDDA substrate. The following set of micrographs are of a sample prepared by depositing one drop of 0.02 wt % positively-charged 258 nm latex particles on a positively charged PDDA surface. Scale Bars: 10, 10, 1  $\mu$ m respectively.*



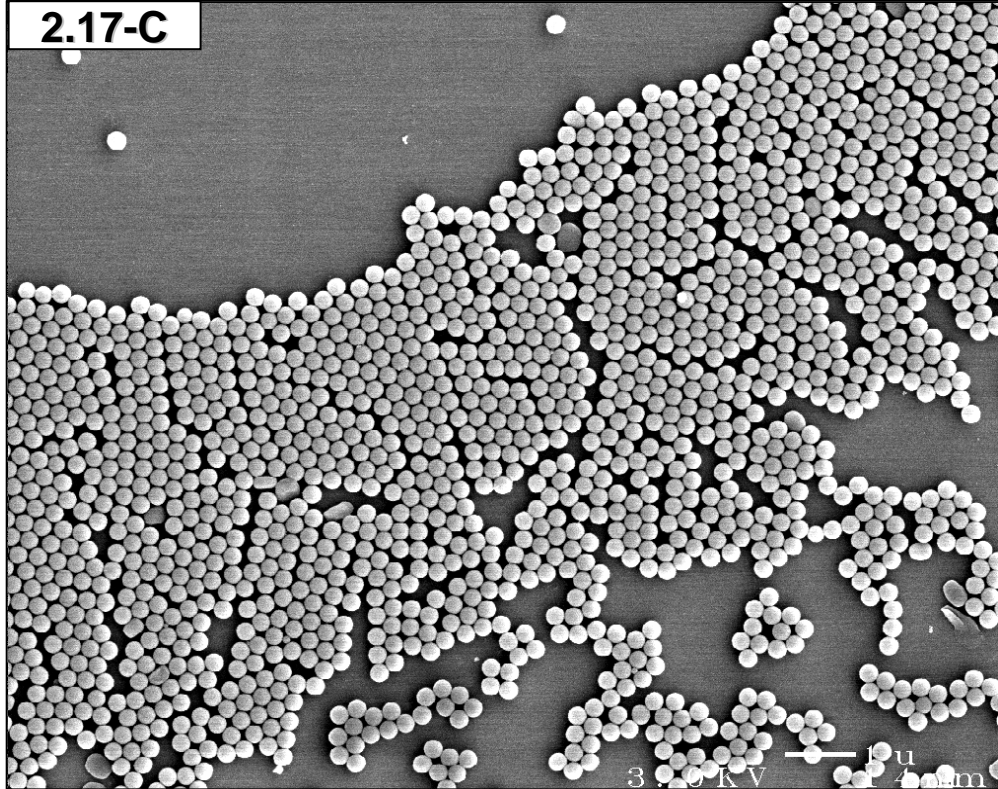
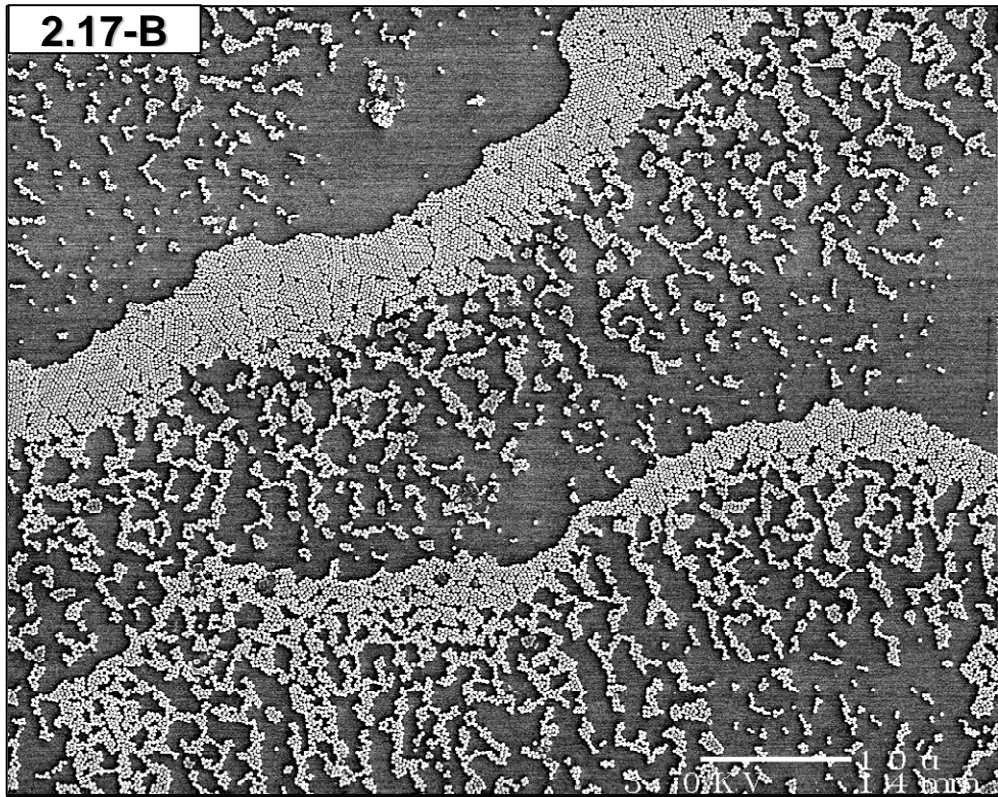
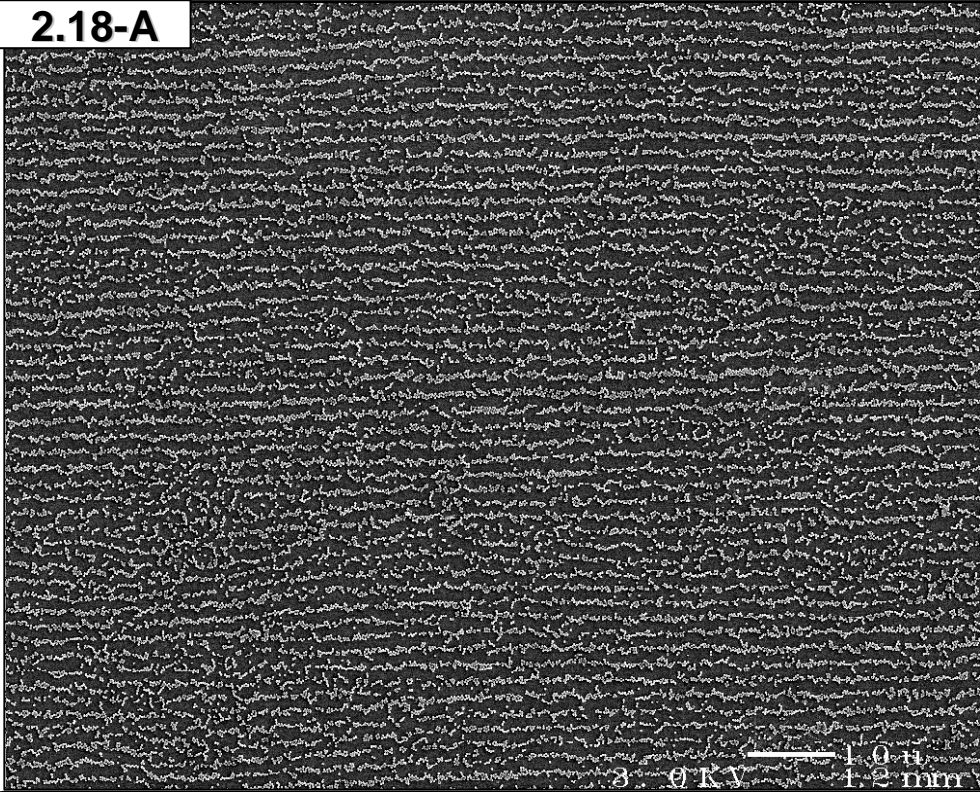


**Figure 2.18** *Substrate surface charge control experiments with the Imidazole 258 latex. The following set of micrographs show the result of depositing one drop of 0.02 wt % positively-charged Imidazole 258 nm latex on (A) glass and (B) an adsorbed layer of PDDA polyelectrolyte on glass. Scale Bars: 10  $\mu$ m.*



**2.18-A**



**2.18-B**

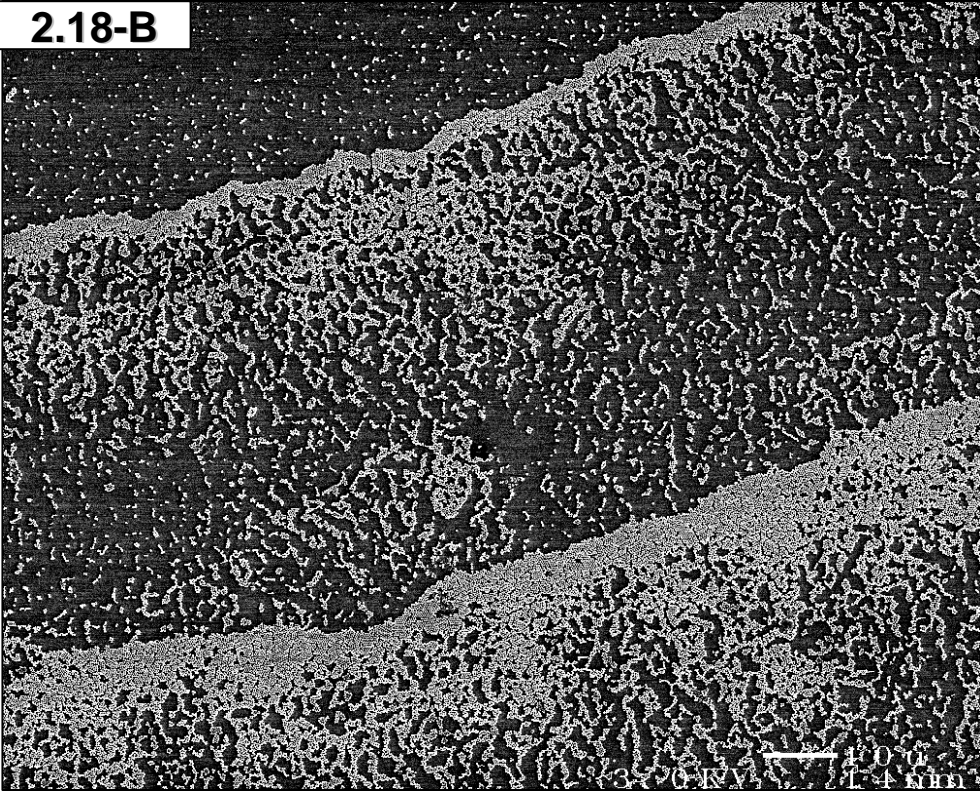
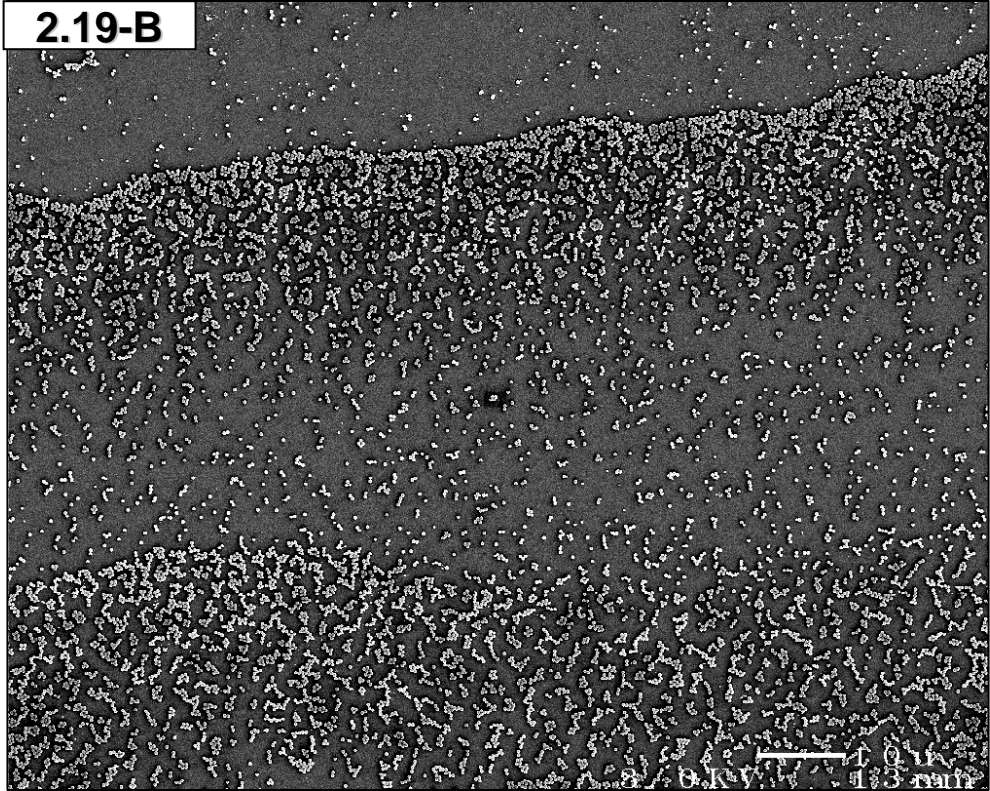
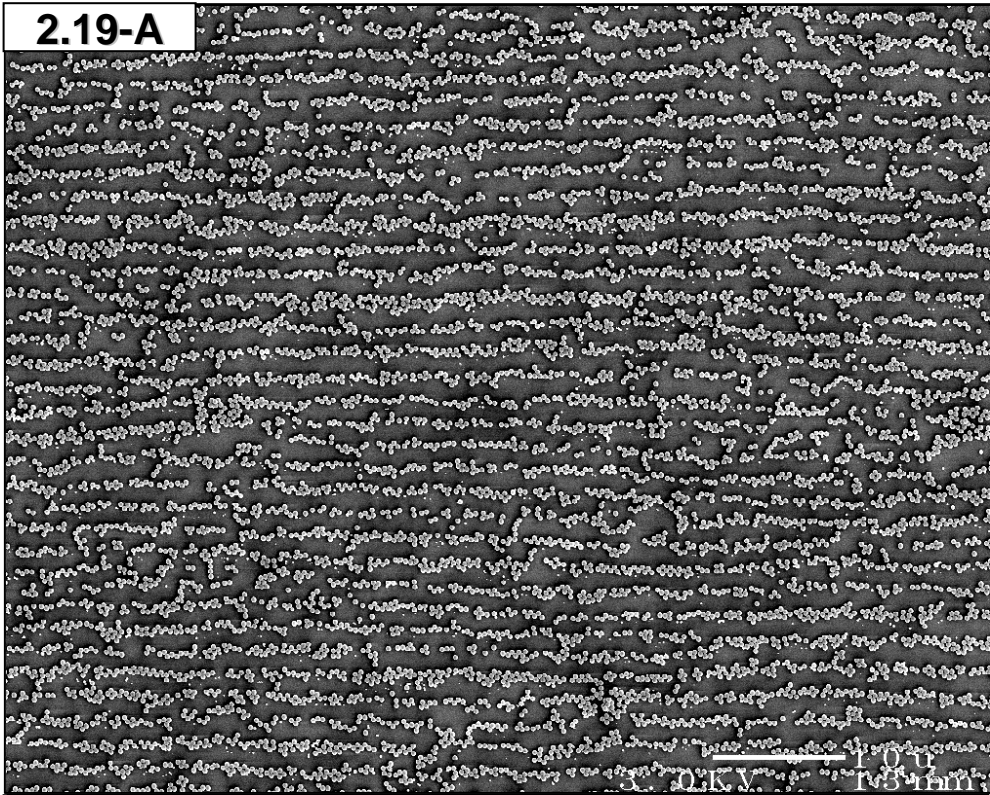


**Figure 2.19** *Substrate surface charge control experiments with the Imidazole 391 latex. The following set of micrographs show the result of depositing one drop of 0.02 wt % positively-charged Imidazole 391 latex on (A) glass and (B) an adsorbed layer of PDDA polyelectrolyte on glass. Scale Bars: 10  $\mu\text{m}$ .*



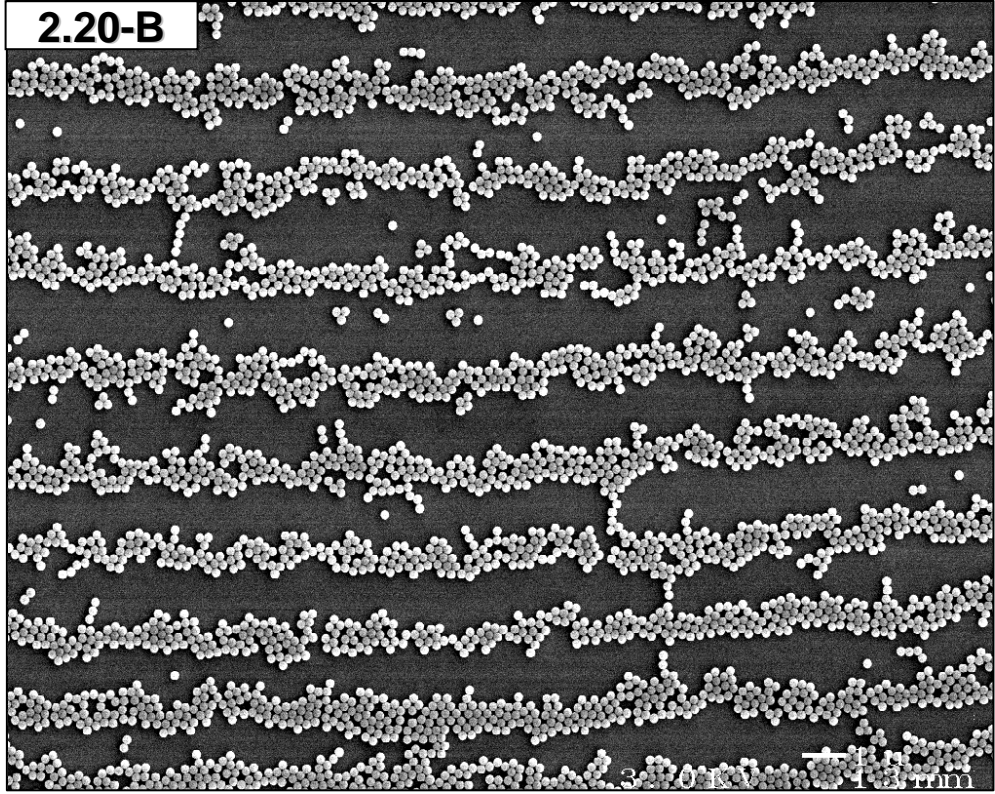
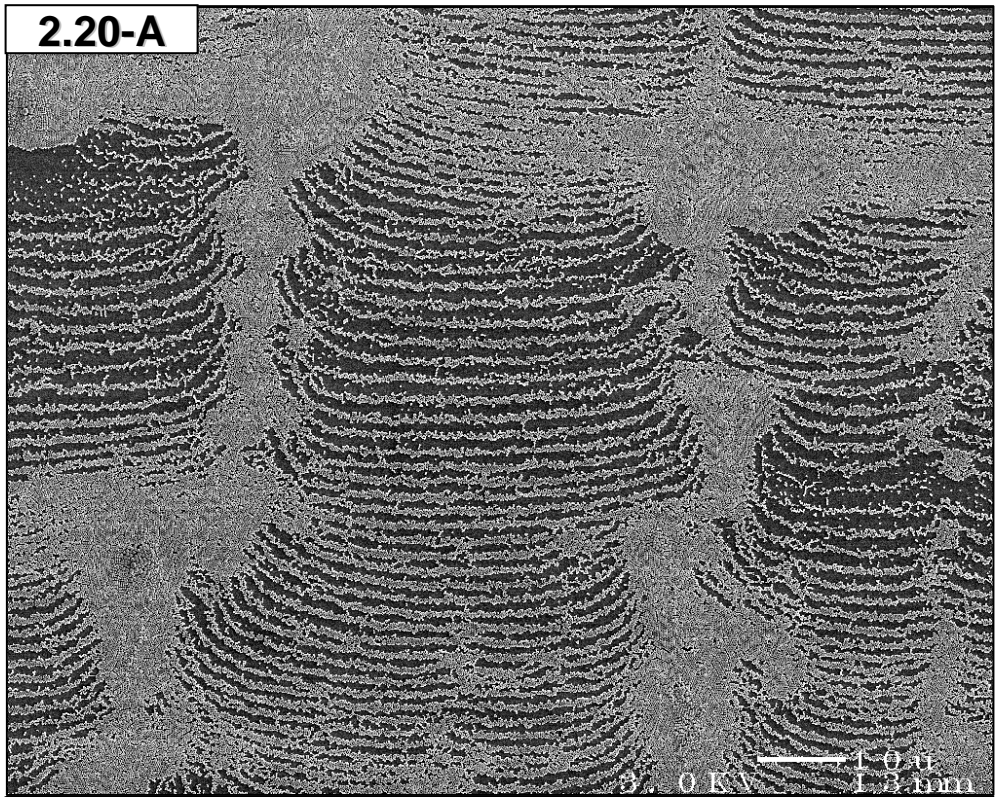
**2.3.6.3 Amine Functionalized Particles.** As another example of a positive-on-negative system, the experiment was repeated using the Amine 210 latex. The particles were diluted to 0.02 wt % with DI water and one drop of the suspension was placed onto a clean glass substrate and allowed to dry at 10° tilt. The resulting pattern was not identical to the Imidazole particle case, but did show related structures. The pattern could be characterized by two major deposition modes, vertical pillars bridged by the linear pattern. The pillars, which have been previously observed by others,<sup>4</sup> are formed when the three phase line ceases to be linear and takes on a festooned appearance.<sup>26</sup> Particles collect in the points of the festoon, and as the contact line recedes, particles are continuously fed into this area to form a pillar. The arcs connecting the pillars assemble particle lines in an identical fashion to the Imidazole case. Because the liquid wedge is exceptionally thin in the bridging area, the particle lines are separated by exceptionally wide line spacings as seen in **Figure 2.20**. Even though the Amine latex did not produce the same linear pattern as the Imidazole latexes, the deposition mode still followed a positive-on-negative motif distinctly different from the negative-on-negative cases discussed above.

## 2.4 Conclusions

A dynamic self-assembly process is reported that involves drying a droplet containing a suspension of *positively charged* polymer particles on a flat *negatively charged* hydrophilic surface. This extremely simple method produces lines of colloidal particles with regular 1.5–4.5- $\mu\text{m}$  line spacings and smaller than 2- $\mu\text{m}$  linewidths over a



**Figure 2.20** *Pattern resulting from the deposition of the Amine 210 latex on glass.*  
*The following two micrographs show the pattern prepared by drying a single drop of 0.02 wt % Amine 210 latex on clean glass and allowing it to dry at 10 ° tilt. Scale Bars: 10 and 1 μm respectively.*



broad surface area. The ordered region diffracts light to display an iridescent appearance and generates first-order diffraction spots when illuminated by a He–Ne laser. Using optical microscopy, a periodic stick-slip motion of the three-phase contact line is observed during the drying process. This periodic motion is related to the periodic deposition of particles. We propose that the simultaneous deposition of particles at a fixed distance (i.e., line spacing) behind the previous line of particles where the contact line is pinned, is in turn responsible for the periodic stick-slip motion. The key feature distinguishing this method from others found in the literature is the attractive interaction between the particles and the substrate which, coupled with the geometry of the contact line region, instigates the periodicity of the particle deposition process.

## **2.5 Acknowledgements**

We thank the Center of Optical Technologies at Lehigh University for financial support and EPI student Hyungsoo Kim for kindly allowing the use of two of his latex samples in this research work.

## 2.6 References and Notes

- 
- <sup>1</sup> Ray, M. A.; Kim, H.; Jia, L. *Langmuir*, **2005**, *21*, 4786-4789.
- <sup>2</sup> de Gennes, P.G. *Rev. Mod. Phys.* **1985**, *57*, 827-863.
- <sup>3</sup> Deegan, R.D.; Bkajin, O.; Dupont, T.F.; Huber, G.; Nagel, S.R.; Witten, T.A. *Nature*, **1997**, *389*, 827-829.
- <sup>4</sup> Deegan, R.D. *Phys. Rev. E*, **2000**, *61*, 475-485.
- <sup>5</sup> Nagayama, K. *Colloids Surf. A*, **1996**, *109*, 363-374.
- <sup>6</sup> Micheletto, R.; Fukuda, H.; Ohtsu, M. *Langmuir*, **1995**, *11*, 3333-3336.
- <sup>7</sup> Abkarian, M.; Nunes, J.; Stone, H.A. *J. Am. Chem. Soc.* **2004**, *126*, 5978-5979.
- <sup>8</sup> Adachi, E.; Dimitrov, A.S.; Nagayama, K. *Langmuir*, **1995**, *11*, 1057-1060.
- <sup>9</sup> Dushkin, C.D.; Lazarov, G.S.; Kotsev, S.N.; Yoshimura, H.; Nagayama, K. *Colloid Polym. Sci.* **1999**, *277*, 914-930.
- <sup>10</sup> Hu, H.; Larson, R.G. *J. Phys. Chem. B*, **2002**, *106*, 1334-1344.
- <sup>11</sup> Fischer, B.J. *Langmuir*, **2002**, *18*, 60-67.
- <sup>12</sup> Behrens, S.H.; Grier, D.G. *J. Chem. Phys.* **2001**, *115*, 6716-6721.
- <sup>13</sup> Gonzalez, R.C.; Woods, R.E. *Digital Image Processing*; Prentice: Upper Saddle River, NJ, 2002.
- <sup>14</sup> Johnson, C.A.; Lenhoff, A.M. *J. Colloid Interface Sci.* **1996**, *179*, 587.
- <sup>15</sup> Evans, J.W. *Rev. Mod. Phys.* **1993**, *65*, 1281.
- <sup>16</sup> Oliver, J.F.; Huh, C.; Mason, S.G. *J. Adhesion*, **1977**, *8*, 223-234.
- <sup>17</sup> Huh, C.; Mason, S.G. *J. Colloid Interface Sci.* **1977**, *60*, 11-38.

- 
- <sup>18</sup> Hadjiishi, A.; Dimova, R.; Denkov, N.D.; Ivanov, I.B, Borwanker, R. *Langmuir*, **1996**, *12*, 6665-6675.
- <sup>19</sup> Image J software may be obtained free of charge from <http://rsb.info.nih.gov/ij/>
- <sup>20</sup> Gokhale, S. J.; Plawsky, J. L.; Wayner, P. C. *J. Colloid Interface Sci.* **2003**, *259*, 354-366.
- <sup>21</sup> Hull, D. *Acta Mater.* **1997**, *45*, 233-244.
- <sup>22</sup> Hull, D. *Fractography: Observing, Measuring, and Interpreting Fracture Surface Topography*; Cambridge: New York, **1999**, pp 280-281.
- <sup>23</sup> Serway, R. A. *Physics for Scientists and Engineers with Modern Physics, Fourth Edition*; Saunders: Philadelphia, 1996, pp 377-378.
- <sup>24</sup> Holzwarth, G. Using Excel to Fit a Damped Sinusoid to Experimental Data. [http://www.wfu.edu/physics/cel/excel\\_fitting.htm](http://www.wfu.edu/physics/cel/excel_fitting.htm) (accessed Oct 2006).
- <sup>25</sup> Serway, R. A. *Physics for Scientists and Engineers with Modern Physics, Fourth Edition*; Saunders: Philadelphia, 1996, pp 1106-1107.
- <sup>26</sup> Poulard, C.; Benichou, O.; Cazabat, A. M. *Langmuir*, **2003**, *19*, 8828-8834.

## Chapter 3

# Surface Self-Assembly of Polymer Colloids to Form Patterned Two-Dimensional Arrays

### 3.1 Introduction

Particles trapped at a liquid interface behave quite differently than those in suspension. Although surface particles still undergo Brownian motion, the range of the motion is decreased because the particles are confined to the two-dimensional plane of the interface. Most latex samples spontaneously form a partial monolayer of particles at air-liquid interfaces. The number of particles at the interface depends largely on the surface properties of the particles, the concentration of the latex, and the concentration of other materials in the latex such as surfactants. Once at the interface, particles become irreversibly trapped after the particle-interface contact angle exceeds more than a few degrees. Since surface particles partially protrude above the interface into the vapor-phase, which typically has a significantly lower dielectric constant, they are able to interact over much longer distances than would otherwise be possible in the aqueous subphase. For particles of like-charge, these long range interactions cause the particles to assume a configuration of minimum repulsion, which results in a hexagonal close-packed (HCP) lattice at sufficient surface concentrations. Such particle arrays have

previously been observed and reported at both air-water and alkane-water interfaces. This research reported here has focused on developing methods to transfer interfacial particle patterns to solid substrates, which enables them to be useful for secondary processes.

### **3.1.1 Background**

An ancient Japanese art form called Suminagashi involved spreading pigment particles at an air-water interface, producing beautiful swirling patterns that were then transferred to a piece of rice paper brought into contact with the surface of the water.<sup>1</sup> This art form, which is remarkably similar to the Langmuir-Schaefer monolayer transfer process, has been practiced in Japan since the 12<sup>th</sup> century A.D. and was likely developed from a similar method that originated in China over 2000 years ago.<sup>2</sup> The first reported scientific study of interfacial phenomenon appearing in the academic literature was published by Benjamin Franklin, whose observations on the effect of spreading a thin layer of oil on a pond were reported to the Royal Society of London in 1774.<sup>1</sup> The first systematic study of a material trapped at an air-water interface was conducted by Agnes Pockels in her kitchen. Her results on the behavior of soap films were recognized as significant by Lord Rayleigh and published in *Nature* in 1891.<sup>3</sup> The greatest advances in this area, however, were the innovations of Irving Langmuir who constructed a trough capable of making detailed studies of interfacial films.<sup>4</sup>

The Langmuir trough was first developed to study small molecule amphiphiles at an air-water interface. In the traditional experiment, a solution of a fatty acid in a

suitable solvent (i.e., stearic acid in chloroform), was spread at a clean air-water interface. After evaporation of the solvent, the surface pressure of the resulting interfacial film was then monitored while decreasing the surface area available to the monolayer by closing one or more movable barriers. The data, when plotted as a function of surface area, contains detailed information about the two-dimensional phase of the material at the interface and is called a *surface pressure-area isotherm*.

When a surface film is compressed, the individual molecules (or particles) comprising the film typically go through gas-like, liquid-like, and solid-like phases at constant temperature. As this behavior is comparable to the transitions observed during the isothermal compression of a three-phase gas (such as carbon dioxide, which is capable of changing phase at constant temperature by varying the pressure), the resulting plot was called a surface pressure-area ( $\pi$ -A) isotherm (**Figure 3.1**). The steep increase above the liquid-solid transition indicates that the molecules comprising the film are completely close packed. By extrapolating the linear portion of the solid region of the isotherm to the x-axis, and dividing the total surface area by the number of molecules added to the interface, the molecular cross-sectional area can be measured. This experiment revealed that fatty acid molecules aligned vertically at an interface since the cross-sectional area was widely independent of the acid chain length.

The Langmuir trough also provides a way to transfer the thin films created at the air-water interface onto solid substrates. Katherine Blodgett pioneered this work along with Langmuir to develop suitable transfer methods. In the Langmuir-Blodgett (**LB**) transfer method,<sup>5</sup> a substrate is pushed through the interfacial film in a perpendicular



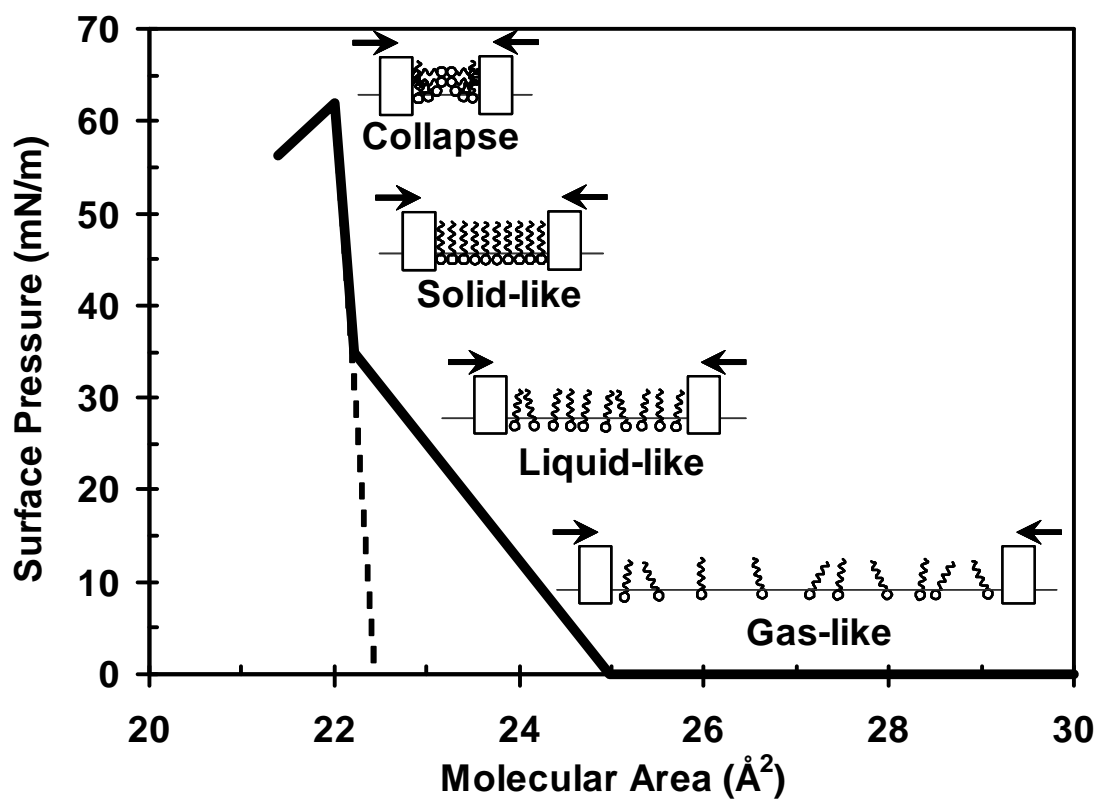


**Figure 3.1** *Idealized stearic acid isotherm.* The plot schematically shows the isotherm features corresponding to the gas-like, liquid-like, and solid-like phases. Further compression of the solid-like film results in film collapse. By extrapolating the solid-like region to the baseline, the molecular head group area of the amphiphile can be measured. Figure after reference 1.

geometry while maintaining constant surface pressure, causing the interfacial film to fold and adhere to the substrate. Multiple layers can be deposited by repeated transfers to the same substrate, resulting in a film of precisely controlled thickness. The resulting films first found use as antireflective coatings.<sup>5</sup> An alternate deposition method, known as the Langmuir-Schaefer (**LS**) method,<sup>6</sup> utilizes a different geometry in which a substrate is brought into contact with the interfacial film in a parallel fashion. These small molecule transfer methods rely heavily on hydrophobic-hydrophilic interactions to repeatedly transfer and build up alternating layers of fatty acids onto a single substrate.

### **3.1.2 Langmuir Particle Films**

Latex particle films trapped at an air-water interface were first studied and reported by H. Schuller.<sup>7</sup> Various related studies at air-water<sup>8, 9, 10</sup> and alkane-water<sup>11,12,13</sup> interfaces have since been conducted. One of the main interests of these early studies was to adapt the Langmuir trough method to measure the average particle diameter of spread latex particles in a way analogous to measuring the molecular cross-sectional area.<sup>14</sup> In a typical experiment, 50 to 200  $\mu\text{L}$  of latex suspension in a spreading solvent such as methanol, ethanol, or isopropyl alcohol, were injected at the interface or deposited in a drop-wise fashion. After being allowed to equilibrate, the area of the surface film was then compressed at a rate typically near 2.5%/min,<sup>13</sup> but rates as slow as 0.001%/min have been reported.<sup>10</sup> Surface pressure area isotherms were recorded during compression of the surface film, and in several studies, optical

micrographs were taken at various points on the isotherm in order to correlate the surface pressure with the physical arrangement of the particles.

Particles at an air-water interface tend to behave like surfactant molecules.<sup>15</sup> In most cases, a particle will protrude above the interface, and rest at a depth governed by the particle-interface equilibrium contact angle as seen in **Figure 3.2**. In the case of micron sized or smaller particles, in which the effect of gravity is negligible, the interface near a spherical particle does not distort in order to achieve an equilibrium contact angle, instead, the particle simply raises or lowers until the angle is achieved.

It has been repeatedly reported in the literature that particle alcohol suspensions do not spread efficiently at an air-water interface, and that a low concentration of electrolyte is needed in the subphase to prevent a significant fraction of the particles from transferring into the subphase.<sup>7, 12</sup> Curiously, it has elsewhere been reported that highly ordered particle arrays could in fact be created at an air-water interface in the absence of electrolyte, with no mention of any difficulties.<sup>10</sup> Highly ordered particle films have also been created by spreading particles in alcohol suspension at an alkane-water interface in the absence of electrolyte. Particle films at an octane-water interface have been extensively studied by Aveyard et. al.,<sup>12, 13</sup> and this system was reported to yield superior particle films when compared to those formed at an air-water interface. The increase in surface capture efficiency and higher degree of order was attributed to the higher particle-interface contact angle at the alkane-water interface.

Particles can become quite strongly attached to an interface depending on the wetting characteristics of the particle and the surface tension of the interface. The

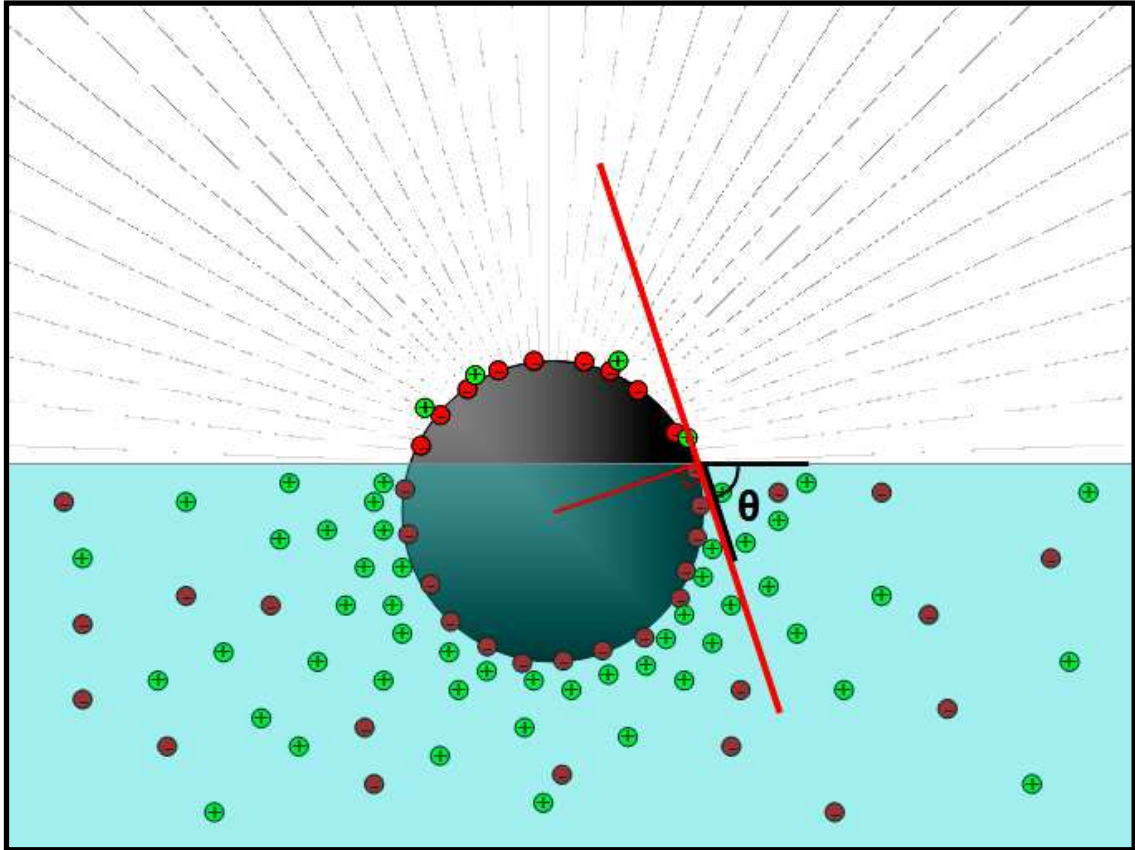


**Figure 3.2** *Schematic diagram of a particle trapped at an interface. The submerged portion of the particle behaves in accordance with DLVO theory via double layer repulsion and vdW attraction, while the upper portion exposed to the low dielectric medium can induce long range monopolar and dipolar interactions due to the absence of charge screening. The particle makes a well defined contact angle,  $\theta$ , with the interface. Diagram after Aveyard et. al.<sup>12</sup>*

energy required to remove a particle from an interface and transfer it to the subphase,  $E$ , is given by the equation,<sup>15</sup>

$$E = \pi \cdot r^2 \gamma_{\alpha\beta} (1 - \cos \theta)^2 \quad (3.1)$$

in which  $r$  is the particle radius,  $\gamma_{\alpha\beta}$  is the interfacial surface tension, and  $\theta$  is the particle-interface contact angle. To calculate the energy needed to remove the particle into the super-phase, the sign of the cosine term is inverted. The solution to this equation is plotted as a function of  $r$  and of  $\theta$  in **Figure 3.3** and **Figure 3.4**, respectively. As can be seen, interfacial particle attachment is a thermally irreversible process after the contact angle exceeds only a few degrees.

### 3.1.3 Interactions Unique to Surface Particles

Particles trapped at an interface can experience long range attractive<sup>16, 17</sup> and repulsive<sup>9, 13, 18</sup> forces that do not operate on particles in the bulk latex, though despite considerable research, these interactions are still not fully understood. Since air has a dielectric constant of 1 in contrast to that of water (80), electrostatic interactions are able to occur through air over length scales much longer than would be possible in water.<sup>9, 19</sup> Experimental evidence suggests that the long range *repulsive* force originates from charged surface groups that are only partially charge compensated on the portion of the particle's surface that protrudes out of the aqueous phase into the superphase, which is typically a low dielectric medium such as air or oil.<sup>20</sup> Dipolar interactions could also contribute to the repulsive force through the low dielectric medium.<sup>18</sup> As a result, repulsive interactions are observed between surface particles over tens of

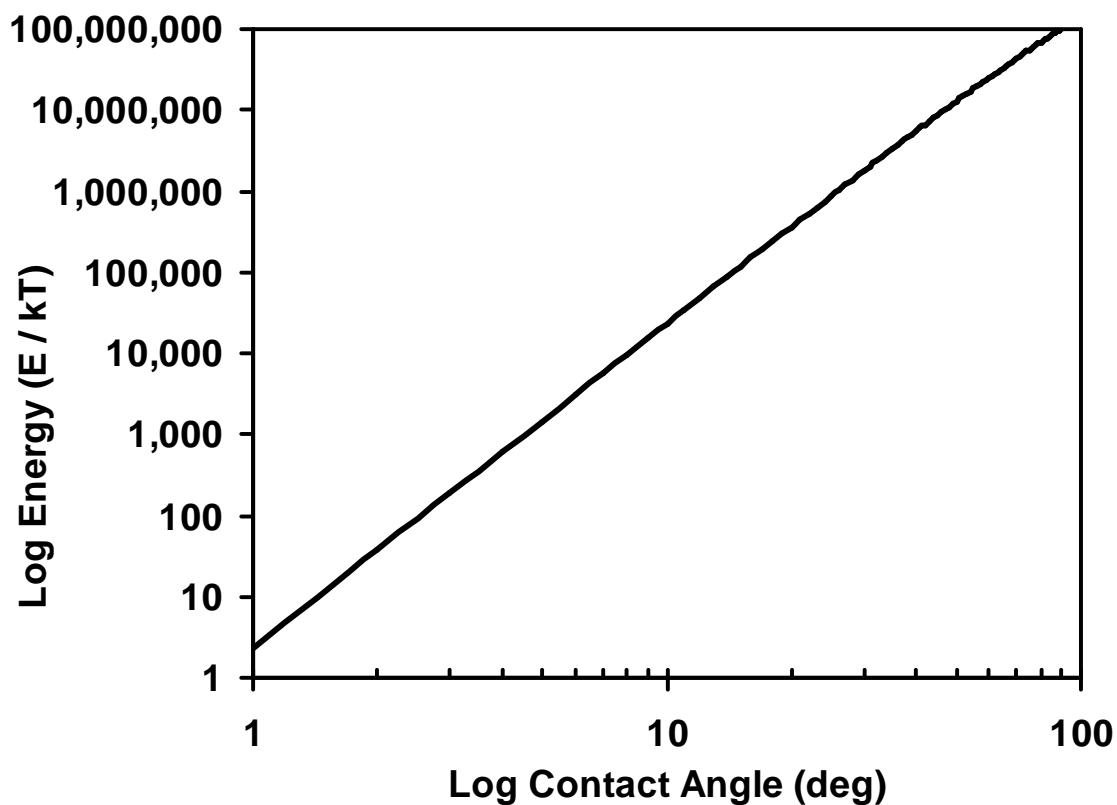


**Figure 3.3** *Detachment energy as a function of contact angle. This plot shows the energy required, as multiples of  $kT$ , to move a  $2.7 \mu\text{m}$  diameter particle from the interface back into the water subphase. Interfacial particle attachment is thermally irreversible after the contact angle exceeds only a few degrees.*

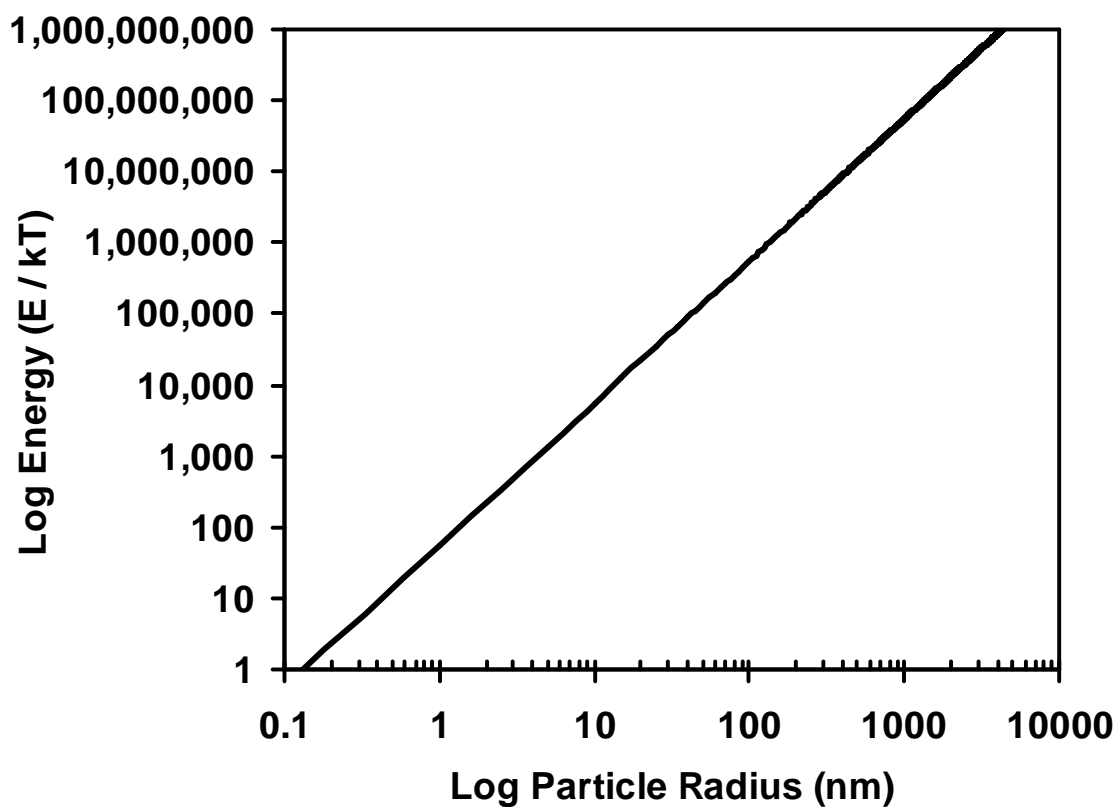


**Figure 3.4** *Detachment energy as a function of particle radius at a 90° particle-interface contact angle. This plot shows the energy required, in multiples of  $kT$ , to move a particle with a 90° interfacial contact angle back in to the subphase. When the particle diameter approaches molecular dimensions, attachment becomes reversible.*

microns, instead of tens to hundreds of nanometers as observed in bulk subphases. The origin of the long range *attractive* interaction is less well understood. Current theory<sup>17</sup> suggests that the attraction is caused by capillary forces resulting from slight deformations of the air-water interface in the vicinity of each particle. These deformations are believed to be caused by the mismatch in dielectric constant above and below the particle, though this theory is still under debate.<sup>21</sup> Particles respond to these long range forces and self-assemble into ordered arrays at the interface.

### 3.1.4 Precedent For Transferred Particle Films

Fully compressed particle films,<sup>22, 23, 24</sup> and aggregated particle networks,<sup>25</sup> have been successfully transferred to solid substrates using Langmuir techniques. In these examples, the individual particles in the film were in contact with one another, giving the film structure and cohesive strength. The transfer of sub-monolayer particle films to solid substrates has always resulted in a loss of order, producing a random particle film after transfer.<sup>26, 27, 28</sup> No method currently exists to transfer non-continuous particle patterns *intact* to solid substrates.<sup>29</sup> The transfer and immobilization of such two-dimensional sub-monolayer HCP crystals with lattice constants larger than the particle diameter is especially challenging because the particles are not physically touching each other and can easily be moved out of their lattice positions. As a result, the variety of patterns that have been observed at air-water interfaces have not been able to be captured and used for secondary processes. This problem was the focus of this research.



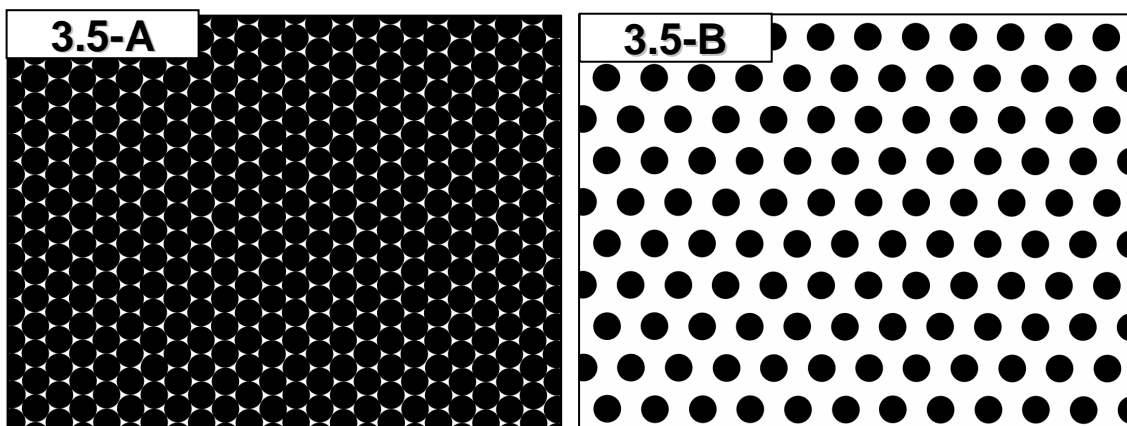


**Figure 3.5** *Schematic illustration of continuous and non-continuous particle patterns. (A) This illustration demonstrates the appearance of a continuous particle film that has been fully compressed, forming a HCP particle monolayer. Because the particles are touching, the film has cohesive strength and can be transferred intact to a substrate. (B) This illustration demonstrates the appearance of a non-continuous particle film that has not been fully compressed, but the particles still form a hexagonal lattice due to electrostatic repulsion. This type of pattern is difficult to transfer to a substrate since the particles are not touching each other and therefore can be easily moved from their lattice positions.*

## 3.2 Experimental Methods

### 3.2.1 Particles

**3.2.1.1 Positively Charged Latex.** Positively charged poly(styrene-co-vinylimidazole) latex particles with an average diameter of 258 nm (Imidazole 258 latex) synthesized by surfactant-free emulsion polymerization were obtained from the Emulsion Polymers Institute. The particles had a narrow PDI of 1.003 and a surface charge density of  $20 \mu\text{C}/\text{cm}^2$  (measured by conductometric titration), corresponding to an average surface area per single functional group (also known as a parking area) of  $80.3 \text{ \AA}^2/\text{N}^+$ . The latex was purified by serum exchange and ultracentrifugation and was used as received. The latex, originally supplied at 2.48 wt %, was diluted with deionized water (Milli-Q, 15 M $\Omega$ ) to 0.2 wt % and experiments were conducted using the native latex surface film. In addition, several experiments were performed using an analogous 391-nm latex (Imidazole 391 latex) synthesized and characterized as described in **Section 1.3.2.1**.

**3.2.1.2 Negatively Charged Latex.** Sulfate functionalized polystyrene latex particles with an average diameter of 2.7  $\mu\text{m}$  (Sulfate 2700 latex) were purchased from Interfacial Dynamics Inc. (Product Number: 1-2600, Batch Number 619,1). The particles were prepared by surfactant-free emulsion polymerization and had a surface charge density of  $8.9 \mu\text{C}/\text{cm}^2$  corresponding to a parking area of  $179 \text{ \AA}^2/\text{SO}_4^-$ . The particles, which were supplied as an 8.3 wt % suspension in water, were purified by at least 4 centrifugation-re-dispersion cycles in isopropyl alcohol (IPA). To accomplish

this, 0.5 g of stock suspension was placed into a 4-in test tube and diluted with approximately 10 mL of IPA. The suspension was then centrifuged at 2500 rpm for 4 min. The clear supernate was decanted and the particles were re-suspended in ~10 mL of fresh IPA using vortexing and sonication. The latex was finally diluted with IPA to 3.0 wt %. Empirically, IPA was found to be a superior spreading solvent to methanol or ethanol.

### **3.2.2 Substrate Functionalization**

**3.2.2.1 Substrate Preparation.** Silicon wafers with a diameter of 5 in (donated by Agere Systems, Inc.) were scored and snapped into 1 inch squares. These substrates were additionally scored into 0.25 inch squares or 0.125 inch squares to be separated after substrate functionalization. The substrates were swabbed with an ethanol-soaked Kimwipe® to remove silicon dust produced by the scoring process. The substrates were then placed vertically into freshly prepared piranha solution (a 70:30 solution of concentrated sulfuric acid and 30% hydrogen peroxide) in a glass Coplin staining jar and kept under solution until use. *Caution: Piranha solution is a strong oxidizer that reacts violently with organic material and should be handled carefully.* Substrates were then removed, rinsed with at least 100 mL of deionized water dispensed from a squirt bottle and dried with a nitrogen jet. Contact-angle measurements were taken using a Rame-Hart Inc. NRL C.A. Goniometer (model# 100-00 115) using a Gilmont volumetric syringe to dispense buffered water at pH 7. The buffer was prepared by dissolving 3.40 g of  $\text{KH}_2\text{PO}_4$  and 0.58 g of NaOH in 500 mL of deionized water.

Piranha-cleaned silicon substrates had an advancing contact angle (ACA) of  $13 \pm 2^\circ$  (standard deviation, 19 measurements) and a receding contact angle (RCA) too small to measure. The average thickness of the native oxide layer remaining on the wafers after cleaning was determined by ellipsometry using a Rudolph Research Auto EL-III Automatic Ellipsometer with a HeNe Laser source at a wavelength of 632.8 nm and an angle of incidence of  $70^\circ$ . Using ellipsometer program 211 with a lower refractive index value of 1.46,<sup>30</sup> the native oxide layer thickness of the cleaned silicon wafer substrates was found to be  $16.0 \pm 0.4 \text{ \AA}$  (standard deviation, 33 measurements).

**3.2.2.2 Negatively-Charged SAM Substrates.** Negatively charged hydrophobic self-assembled monolayers (SAMs) were prepared by allowing clean silicon substrates to react with 2-(4-chlorosulfonylphenyl)-ethyltrichlorosilane (SPTCS), which was purchased from Gelest as a 50 wt % solution in toluene and used as received. Several methods have previously appeared in the literature for preparing SPTCS SAMs.<sup>31, 32, 33, 34</sup> These reports were used as a starting point to develop the method outlined below. The SPTCS stock solution was stored under dry nitrogen, and air-free handling techniques were used because SPTCS rapidly cross-condenses when exposed to moisture. Twenty-five mL of anhydrous toluene and 10 drops of the SPTCS stock solution were placed into a glass Coplin staining jar under a nitrogen purge. Six to eight 25-mm x 25-mm square glass or silicon substrates (pre-scored into four 12.5-mm x 12.5-mm square sections to reduce handling after functionalization) were then placed vertically into the solution. The top of the jar was covered with parafilm and a

slight positive pressure of nitrogen was maintained in the jar. The substrates were allowed to react for 30 min, after which they were sequentially rinsed with toluene, THF, deionized water, and finally blown dry with a nitrogen jet. The substrates were then separated into 12.5-mm x 12.5-mm square sections and stored in a Petri dish until use. The kinetics of SPCTS SAM formation were measured by immersing a substrate into the reaction solution for 1 s, 1 min, 1 h, and 20 h, and measuring the contact angle and ellipsometric thickness.

**3.2.2.3 Mirror-Finish Stainless Steel Substrates.** Samples of mirror-finish stainless steel, obtained from Pacific Plus International, Inc., were donated by members of the Lehigh University Department of Electrical Engineering. The 500- $\mu\text{m}$  thick, type 304, stainless steel had a polishing grade CMP (chemical mechanical polish) super #8 mirror with a protective polyvinylchloride (PVC) film on the mirrored side. The steel was cut into 1 cm squares and, after removing the protective PVC film, was used as a transfer substrate without further treatment. Empirically, the steel substrates behaved quite similarly to the SPTCS SAM substrates. The steel substrates were characterized by contact angle measurement and X-ray Photoelectron Spectroscopy (XPS, Scienta ESCA300, Uppsala, Sweden) to determine if a polymeric surface coating was present on the mirror surface of the steel. A substrate with the protective PVC film freshly removed was analyzed for C, O, Fe, Cr, and Ni. The surface of the substrate was then scratched while under vacuum in the spectrometer and re-analyzed.

**3.2.2.4 Non-Charged Hydrophobic SAM Substrates.** Non-charged hydrophobic SAMs were prepared by allowing clean silicon or glass substrates to react with octadecyltrichlorosilane (OTS, Gelest). Twenty-five mL of anhydrous toluene and 3 drops of OTS were placed into a Petri dish at room temperature. Four pre-scored substrates were placed into the solution and allowed to react for 30 min. The substrates were then removed, rinsed with toluene, tetrahydrofuran, and deionized water, and finally blown dry with a nitrogen jet. The substrates were then separated into smaller sections and stored in a Petri dish.

**3.2.2.5 Positively-Charged SAM Substrates.** Positively charged SAMs with varying degrees of hydrophobicity were prepared by allowing clean glass or silicon substrates to react with ammonium functionalized trimethoxy silanes, all purchased from Gelest and used as received. The silanes were N-(trimethoxysilylethyl)benzyl-N,N,N-trimethylammonium chloride (NBENZ) supplied as a 60% solution in MeOH, (3-trimethoxysilylpropyl)diethylenetriamine (TRIN) supplied neat at 95% purity, tetradecyldimethyl(3-trimethoxysilylpropyl)-ammonium chloride (TDAC) supplied as a 50% solution in MeOH, N-trimethoxy-silylpropyl-N,N,N,-tri-n-butylammonium chloride (TBAC) supplied as a 50% solution in MeOH, and N-trimethoxysilylpropyl-N,N,N-trimethylammonium chloride (TMAC) supplied as a 50% solution in MeOH. No particular precaution against airborne moisture was taken, as trimethoxysilanes are much less susceptible to cross-polymerization than trichlorosilanes, especially when

dissolved in methanol. Several literature methods were used as starting points for method development.<sup>31, 35, 36</sup>

Fifteen mL of methanol and 15 drops of positively charged trialkoxysilane stock solution were placed into a 9-cm diameter glass Petri dish. Typically, four 25-mm x 25-mm square substrates were placed into the solution and allowed to rest face up on the bottom of the dish. The solution was then heated to 60 °C with the dish loosely covered. The methanol was allowed to evaporate partially and concentrate the silane solution while being careful not to allow the surface of the substrates to become dry. After approximately 2.5 h (or an amount of time sufficient to evaporate enough methanol to endanger the substrate surfaces of becoming dry), an additional 15 mL of methanol were added and heating was continued. After a total heating time of 3.5 to 4 h, the heat was removed, additional methanol was added to bring the total volume to ~25 mL, and the samples were allowed to cool to room temperature and typically to sit overnight. The substrates were then removed, rinsed with methanol followed by water, and finally blown dry with a nitrogen jet. The substrates were then separated into smaller sections and stored in a Petri dish until use. The resulting SAMs were characterized by contact angle measurements and ellipsometry.

Room-temperature kinetics were measured for TBAC and TMAC SAM formation. Twenty-five mL of methanol and 5 drops of silane stock solution were placed into a Petri dish along with 8, 12-mm x 12-mm silicon substrates. The substrates were removed from the reaction solution at various times, rinsed with methanol

followed by deionized water and blown dry with a nitrogen jet. The substrates were then characterized by contact angle measurements and ellipsometry.

### 3.2.3 Transfer Method Development

A number of iterative improvements were made during the method development process. They are described here in the order in which they were made. Initial experiments were carried out in 20-mL scintillation vials containing 10 mL of 0.2 wt % Imidazole 258 latex. The suspension was sonicated and vortexed, followed by dipping a SPTCS SAM silicon or a mirror-finish steel substrate vertically through the latex-air interface in a LB geometry. The substrate was then removed, rinsed with DI water, and blown dry with a nitrogen jet. Initially, all samples were manually transferred by holding the substrate in self-closing tweezers and slowly lowering it through the interface. This method will be referred to as the *Vortex Process*.

In order to increase the reproducibility of the transfer process, a crude dipping apparatus that was capable of linear dipping rates between 10 and 50 mm/s was constructed, as described in **Appendix A.1**. This apparatus will be referred to as the *First Generation Dipper*. A 25-mL manually operated Langmuir trough was constructed as described in **Appendix A.2**. Surface pressure-area isotherms collected by this trough were somewhat crude, however, several critical initial experiments were performed making this apparatus a significant stepping stone toward understanding the particle self-assembly systems. This apparatus will be referred to as the *Manual Trough*. A precise stepper-motor-controlled dipping apparatus that was capable of



dipping at variable rates and angles was constructed as described in **Appendix A.4**.

This apparatus will be referred to as the *Second Generation Dipper*.

A suitable mechanized small-volume Langmuir trough was not commercially available. Since investigations were to be carried out on bulk latex samples, and since only a limited supply of the particles was available, small trough dimensions were necessary. The smallest size commercially available was a 150-mL trough from NIMA, and the size as well as the cost was prohibitive. For these reasons, a 50-mL, computer-controlled Langmuir trough was designed and fabricated, as described in **Appendix A.5**. This apparatus will be referred to as the *Mechanical Trough*.

### 3.2.4 Isotherm Plotting Options

Pressure-area isotherms can be plotted in several ways. When the exact number of particles at the interface is unknown, the data can only be plotted as a function of the trough area. Although this approach gives a qualitative description of the particle behavior at the interface, it fails to describe the system on a per-particle basis. If the number of particles placed at the surface is known, the data may be plotted in the traditional fashion, as a function of area available per particle, also known as the *reduced area*,  $A_r$ . An additional, and perhaps more descriptive, method was typically used in this research: the data were plotted as a function of the theoretical particle separation distance,  $d_s$ . This distance can be calculated by the simple expression,

$$d_s = \sqrt{\frac{A_r}{\sin(60^\circ)}} \quad (3-2)$$

and is based on the assumption that the particles are spread evenly across the entire surface into a hexagonal array after deposition. This assumption only rigorously holds after the particles are close enough to experience long range repulsion and closer than the long range secondary minimum if one exists. The data plotted in this fashion allow direct comparison with the other methods used for pattern analysis, such as nearest-neighbor and fast-Fourier-transform analysis. This method also emphasizes the subtle changes in slope of the isotherm, which indicate two-dimensional phase transitions.

### **3.2.5 Native Particle Films**

The following method was typically used for the positively charged latexes such as Imidazole 258 and 391. The positively charged latexes were not stable as alcohol suspensions, and therefore could not be successfully spread at an interface by traditional methods. In fact, the Imidazole particles became unstable and coagulated after adding only a few percent of ethanol to the aqueous suspensions. Instead, the particle films which spontaneously formed at the air-water interface on 0.2 wt % latex, known as native surface films, were investigated. The latexes were rapidly agitated by vortexing and sonication before each experiment, which had the effect of enriching the number of particles at the air-latex interface. In addition, the number of particles at the interface could be further increased by bubbling nitrogen through the bulk latex in the trough. By creating new latex-air interface in the bulk, particles could ride the bubbles to the surface and be deposited at the interface. After compressing the surface film to the desired compression ratio, a substrate transfer could be performed as described above.

Even though the experiments were qualitatively reproducible, the number of particles comprising the native surface film was not constant or reproducible from run to run. Since the exact number of particles at the interface was unknown, quantitative measurements were not possible.

### **3.2.6 Deposited Particle Films**

The following method was typically used for latexes such as Sulfate 2700 that were stable in alcohol suspension. The latex of interest was first cleaned by repeated centrifugation re-dispersion cycles in IPA to remove water and residual impurities, and finally was suspended at around 3 wt % in IPA. The exact final concentration was determined gravimetrically. An appropriate amount (5-100  $\mu\text{L}$ ) of suspension was placed at a clean deionized water-air interface with a 100- $\mu\text{L}$  glass SGE microsyringe connected to a KD Scientific syringe pump (model# 100). If done properly, with the tip of microsyringe needle in contact with the interface, very few particle clusters were formed, and transfer of particles to the subphase was suppressed. In this manner, the number of particles at the interface was known and could be used to predict particle spacing at a particular compression ratio. Since the surface tension of alcohol is significantly lower than that of water, the alcohol suspension readily spreads at the air-water interface and evenly deposits the particles across the air-water interface when the alcohol evaporates or dissolves into the subphase.

### 3.2.7 Measurements of Particle-Interface Contact Angles

Measurements of particle-interface contact angles were performed using a two-particle method. First, the 2.7- $\mu\text{m}$  negatively-charged Sulfate 2700 latex particles were spread at the interface using the method outlined in the preceding section. Several drops of positively-charged Imidazole 258 latex particles at 0.2 wt % in water were then slowly added to the surface with a pipette and allowed to equilibrate for several hours. Langmuir-Schaefer transfers of the resulting surface film were then performed using silicon substrates bearing TBAC SAMs. The transferred films were imaged by SEM at a tilt angle of  $60^\circ$ , as shown in **Figure 3.6**. The micrographs were analyzed using Microsoft PowerPoint because this program conveniently allowed an ellipse of known major and minor axis, and major axis angle to be superimposed on the images.<sup>37</sup> The micrograph proportions were adjusted to compensate for tilting distortion (the vertical or horizontal aspect ratio was adjusted until the larger particles could be circumscribed by a perfect circle), and a best-fit ellipse was drawn that intersected the centers of the particles comprising the halo around each of the larger particles. A concentric ellipse was then drawn inside of the halo, fit to approximate the contact-line around the larger particle. If  $a$  is half of the length of the major-axis of the contact-line fit ellipse, and  $r$  is equal to the radius of the larger particle, the interfacial particle contact angle is defined by,

$$\theta = \sin^{-1}\left(\frac{a}{r}\right) \quad (3.3)$$

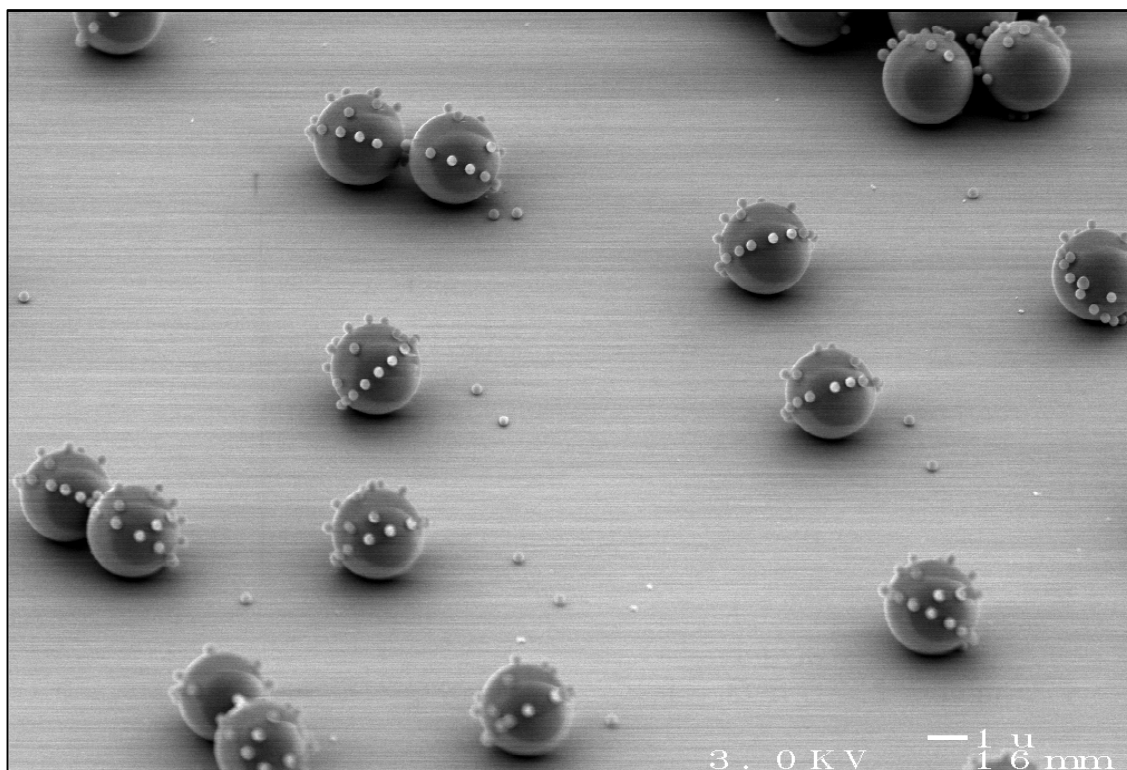


**Figure 3.6** *Particle-interface contact angle measurement method.* The larger particles were first placed at an air-water interface followed by the smaller oppositely-charged particles resulting in heterocoagulation in the plane of the interface. Some of the smaller particles transferred to the subphase and became attached to the submerged portion of the larger particle. The surface film was then transferred to a TBAC SAM silicon substrate and imaged by SEM. As a result of the transfer, the portion of the particles that had been submerged faced upward. Scale Bar: 1  $\mu\text{m}$ .

as seen in **Figure 3.7-A**. In the special case in which the minor-axis of the contact-line ellipse was exactly coincident with direction of viewing, the angle could be measured directly from the image, as shown in **Figure 3.7-B**. This method gives an accurate measurement of the particle-interface contact angle based on the assumption that attachment of the smaller particles does not significantly change the vertical position of the larger particles. This assumption is reasonable based on the fact that the smaller particles attach in a straight line around the larger particle. Since the smaller particles attach sequentially, one would expect a jagged line to result if the attachment of the smaller particles sequentially changed the position of the larger particle.

### **3.2.8 Surface-Film Compression Methods**

Three surface-film compression methods were used during the course of this project and are described below in order of increasing complexity.

**3.2.8.1 Vortex Compression.** Initially, for the early LB experiments, surface films were compressed during the vortexing procedure. The area of the latex-air interface for a latex sample in a 20-mL scintillation vial (Fisher Brand, true volume 25 mL) at rest is approximately equal to the interior cross sectional area of the vial which is  $491 \text{ mm}^2$ . Typically 10 mL of 0.2 wt % latex was placed into the vial and when the latex sample was vortexed, the area of the latex-air interface was increased as the liquid was forced up the wall of the vial by centrifugal force. The area of the latex-air interface during this procedure could be approximated as the wall of a cylinder and was

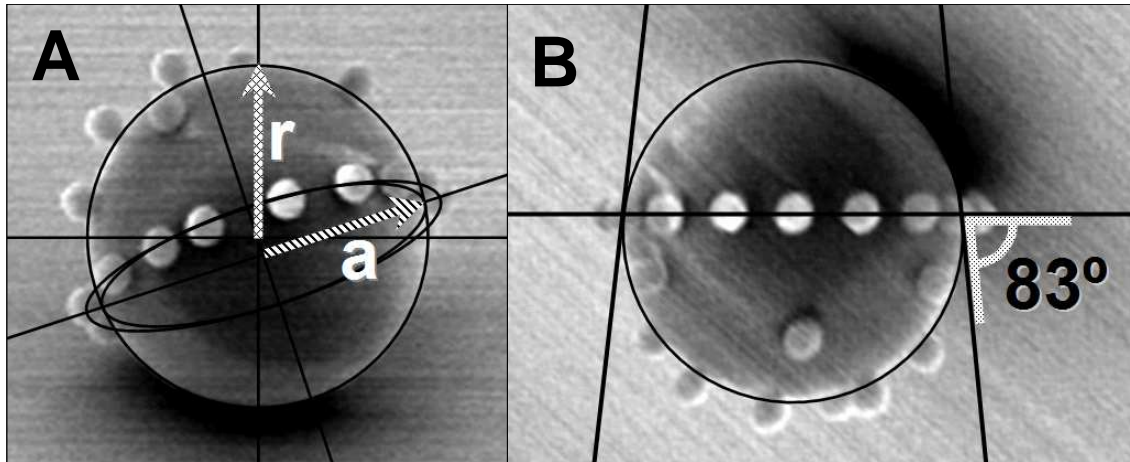


**Figure 3.7 Particle halo fitting process.** (A) An ellipse was superimposed on the micrograph and fit to intersect the center of each of the smaller particles. A second concentric ellipse was placed inside the first and approximates the points of contact. The interfacial contact angle can then be calculated using the ratio of the major axis of the second ellipse,  $a$ , to the particle radius,  $r$ , using **Equation 3.3**. (B) If the particle halo was oriented in a plane coincident with the viewing direction, the contact angle can be directly measured as shown.

approximately equal to  $3016 \text{ mm}^2$ . Surprisingly, even though the inner cylindrical latex-air interface was quite turbulent during the vortexing procedure, a significant number of latex particles became entrapped at this newly formed interface. Upon stopping the vortexing, the surface area returned to the resting state cross sectional area, which represents a surface film compression ratio of approximately 84%. Highly compressed particle films were formed by this simple method for particles having a high propensity for surface enrichment such as the Imidazole 258 latex. This method will be referred to as *Vortex Compression*.

**3.2.8.2 Compression at Constant Surface Area.** This simple method allowed for a higher degree of control, and yielded more reproducible results, compared to the vortex method. A polystyrene Petri dish (Fisher Brand) with an inner diameter of 86 mm was half filled with deionized water. The resulting air-water interface had an area of  $5809 \text{ mm}^2$ . A known amount of latex suspended in isopropyl alcohol was then deposited at the interface using a microsyringe. Since the total surface area was constant, due to the rigid walls of the container, compression of the particle film was achieved by adding more particles to the interface. Since the area of the interface and the exact concentration of the suspension were known, any desired degree of compression could be achieved. However, at high compression ratios, partial clustering was observed due to the inability of the nearly complete monolayer to accommodate and redistribute the additional influx of particles. This method will be referred to as *Constant-Area Compression*.



**3.2.8.3 Compression at Constant Particle Number.** This method offered the highest degree of control of the three methods discussed because the compression could be precisely performed at a constantly known ratio and rate, and because the process was reversible by simply reversing the barrier. In addition, this method allowed the collection of a quantitative surface pressure-area isotherm, which gave valuable information about the two-dimensional phase of the system at every point in the compression history. This method was used to examine both native and deposited latex particle films prepared as discussed above. The surface films could be compressed to any desired amount by movable barriers. This method will be referred to as *Langmuir Trough Compression*.

### **3.2.9 Substrate Transfer Processes**

**3.2.9.1 Langmuir-Blodgett (LB) Transfers.** To perform a manual LB transfer, an appropriate substrate held by self-locking tweezers was vertically lowered slowly by hand through the interface after the surface film had achieved a desired state. Since the rate and angle of the manual method was not rigorously reproducible, mechanical LB transfers were typically performed using one of the dipping apparatuses described above.

**3.2.9.2 Langmuir-Schaefer (LS) Transfers.** To perform mechanical LS transfers, a substrate holder was constructed from copper wire to fit the mechanical dipping apparatuses that would hold the substrates in a parallel geometry and allow

simultaneous transfer onto two substrates. Particle films transferred by this method often had large void areas in the center of the substrate where an air bubble had been trapped. This behavior was not observed using manual LS transfers, which surprisingly gave more reproducible results. Consequently, for this geometry, manual transfers were typically performed. To affect a manual LS transfer, an appropriate substrate was fixed to the end of a 60-mm x 3-mm-diameter stainless steel dipping rod using double-sided tape. Once the surface film was placed in a desired state, the substrate was slowly lowered manually in a parallel geometry into contact with the surface film. For particle films of the Imidazole 258 and 391 latex particles, the substrate was then removed from the interface, rinsed with DI water, and blown dry with a nitrogen jet. This retracting method proved to be too harsh for particle films of the Sulfate 2700 latex, for which two methods were developed for retracting the substrate from the interface as outlined below.

**3.2.9.3 Alternate Withdrawal Method.** After contacting the interfacial film, the substrate was lifted away from the interface and given a single sharp shake in the lateral direction using wrist action to flick off any excess water clinging to the substrate. If any droplets still remained, they were wicked away with the corner of a Kimwipe®. Particle arrays of the Sulfate 2700 latex transferred by this method showed disordered, streaked regions where water droplets moved across the surface. To circumvent this dewetting problem, an additional method was developed. After contacting the interfacial film, the substrate was lowered further into the subphase and carefully

detached from the dipping rod using forceps which caused the substrate to come to rest face down at the bottom of the trough. Once all of the desired transfers had been made for a given run, the remaining interfacial particle film was removed by suction and the trough was refilled with deionized water. The substrates were then carefully turned face up underwater using forceps. A cover glass slip with dimensions slightly larger than the substrate was floated at the air-water interface. Using forceps with a 45° curved tip, the substrate was raised directly beneath the floating cover slip and then raised out of the liquid with the cover slip on top of it protecting the particle array in-between with a thin liquid layer. By following this procedure the transferred particle film was not subjected to destructive capillary forces which can completely destroy the transferred patterned array. The array could then be imaged through the cover-slip using optical microscopy.

**3.2.9.4 Fluid-Exchange and Solvent-Fixing Procedures.** Even though the particle pattern can be imaged while underwater, the array must be transferred into air to undergo further processing. Two methods were used to complete the transfer process, by either significantly lowering the capillary force during drying or by increasing the particle-substrate adhesion. These methods were designed to prevent the particles in the transferred array from ever being in contact with an air-water-particle contact line. In the first approach, the cover glass was removed while the substrate was completely submerged in ethanol. The lower capillary force generated by ethanol, due to its lower surface tension, leaves the pattern nearly undisturbed during the drying process. However, if particles in the array were within approximately one particle

diameter of each other, some destructive capillary forces were still observed. This method is shown schematically in **Figure 3.8**.

Alternatively, to increase the adhesive interaction between the particles and the substrate, a solvent fixing method was employed. After removing the substrate covered by a cover slip from the trough subphase, the substrate was placed into a 6-cm diameter watch glass. An appropriate solvent or solvent mixture was then placed into the watch glass, completely immersing the substrate. The cover glass was then removed allowing the solvent to come into contact with the patterned array. After a desired amount of time, the substrate was rinsed with DI water or IPA and allowed to dry. By carefully choosing the right solvent and exposure time, the degree of particle deformation could be controlled. By increasing the particle-substrate contact area, the adhesive force is increased, rendering the array resistant to destructive capillary forces.

### **3.2.10 Microscopy and Methods of Pattern Analysis**

**3.2.10.1 Imaging and Analysis.** Optical microscopy was performed using an Olympus BH2 optical microscope fitted with a PAXcam CCD camera. Scanning electron microscopy was performed using a JEOL 6300f SEM. Optical and scanning electron micrographs were processed using ImageJ<sup>38</sup> version 1.34s for pattern analysis and particle counting and Spatial Analysis Utilities<sup>39</sup> version 1.0.f for nearest-neighbor measurements. A detailed description of the nearest-neighbor analysis method is given in **Appendix B.2**. Atomic force microscopy was performed using a Digital Instruments

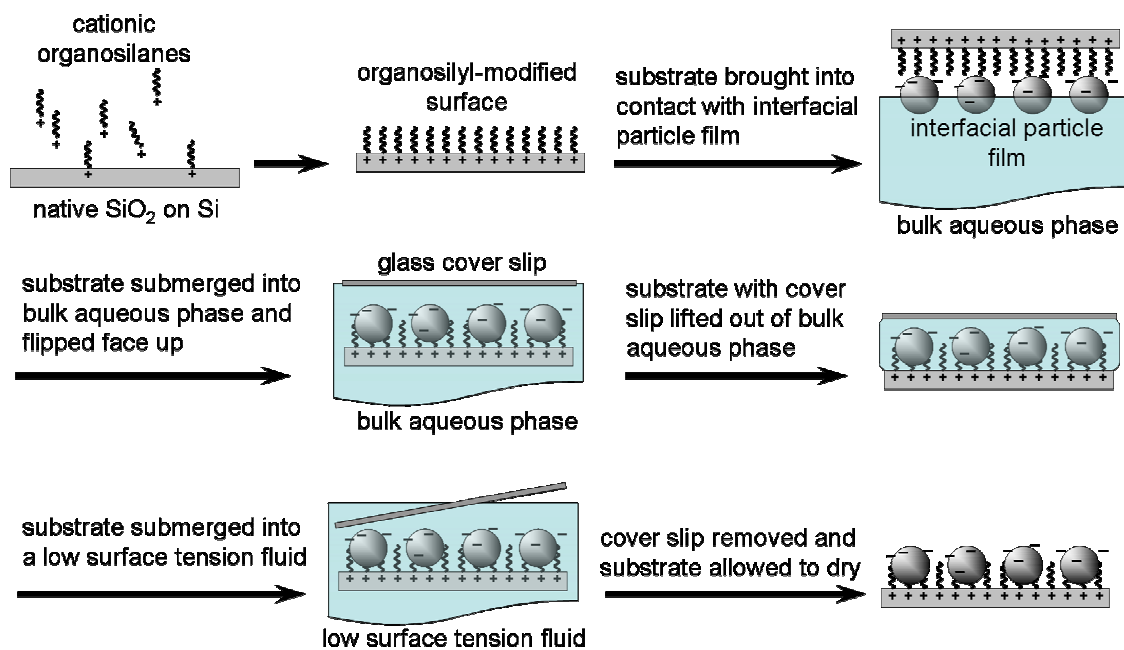


**Figure 3.8** *Schematic illustration of the fluid-exchange procedure. This method was used to transfer non-continuous interfacial particle films intact onto silicon substrates.*

Nanoscope E, LFM-2. AFM micrographs were processed using WSxM<sup>40</sup> version 4.0 develop 8.6 analysis software.

**3.2.10.2 Laser Diffraction.** In addition to giving information about the inter-particle spacing, laser diffraction also gave information about the grain size of individual crystallites comprising the particle pattern. A diffraction pattern with sharp spots indicates that the crystalline grain producing the diffraction pattern is the same size or larger than the spot size of the laser. A laser diffraction apparatus was set up using a 5-mW Helium-Neon laser (Hughes) with a wavelength of 633 nm and a spot diameter of approximately 1 mm. The laser tube was clamped to a ring stand and adjusted so that the beam was normal to the benchtop. In transmission mode, which was used for patterns on transparent substrates, a clear stage was placed at a known distance from the tabletop, and the diffraction pattern was projected onto a piece of paper. The distance between the plane of the pattern and the screen surface below, known as the projection length, was typically set to 25 cm. This distance must be known in order to calculate the diffraction angle for points in the diffraction pattern. In reflection mode, which was used for patterns on opaque reflective substrates such as silicon, a screen with a small hole in the center was placed a known distance *above* the patterned substrate. The laser beam was directed through the hole and onto the sample, and the resulting diffraction pattern was reflected onto the screen. For this geometry, a projection length of 10 cm was typically used. Diffraction patterns were recorded using

a digital camera (Kodak, P850) or recorded manually. The distances in the particle lattice could be calculated using the diffraction grating equation,

$$d = \frac{m \cdot \lambda}{\sin(i) + \sin(\theta)} \quad (3.4)$$

in which  $d$  is the spacing of a particular set of particle lines in the pattern,  $m$  is the order of diffraction,  $\lambda$  is the wavelength of the incident beam,  $i$  is the angle of incidence of the incoming beam (which in the current apparatus was always set to 0), and  $\theta$  is the diffraction angle for a particular diffraction spot. A more detailed description of how inter-particle spacings were measured by this method is given in **Appendix B.3**.

**3.2.10.3 Fast-Fourier-Transform Analysis.** Fast-Fourier-transform (FFT) analysis was also used to extract particle-spacing data, as well as information about the lattice orientation within particular crystalline grains. Scanning electron and optical micrographs were analyzed by FFT using ImageJ or Scion Image software. Fast-Fourier-transform analysis produces results that are nearly identical to laser diffraction. The benefit of using FFT over laser diffraction lies in the ability to simply extract data from micrographs instead of performing the tedious diffraction experiments.

### 3.3 Results and Discussion

#### 3.3.1 Substrate Functionalization

Although a large body of experimental data exist in the literature for trichlorosilane SAMs such as OTS, available data for trialkoxysilane SAMs are less complete.<sup>41</sup> Trichlorosilanes react with hydroxyl-bearing surfaces very rapidly to produce an organosiloxane monolayer. A wide variety of functional silanes are commercially available from companies such as Gelest. Many of these compounds are not available as trichlorosilanes because cross reactions and self-polymerizations would render them unstable. For this reason, trialkoxy-derivatives are often used. These reagents have a much slower reaction rate compared to their trichloro-counterparts. A number of methods have been reported in the literature on preparing monolayers from alkoxy-silane, however, there does not seem to be a consensus on the best method to follow. In fact, many authors seem to use similar methods for both trichloro- and trialkoxy-silanes as if there were no difference between the two. As a result, the examples found in the literature were used only as a starting point for developing the following SAM adsorption methods.

**3.3.1.1 Kinetics for Trichlorosilanes 25 °C.** The kinetics of formation for SPTCS monolayers were probed by measuring the advancing and receding contact angles and the ellipsometric thickness at several time intervals. The resulting plots are shown in **Figure 3.9**. The curve reached a limiting value after reacting for several min. Based on these results, the reaction was typically allowed to proceed for 30 minutes,



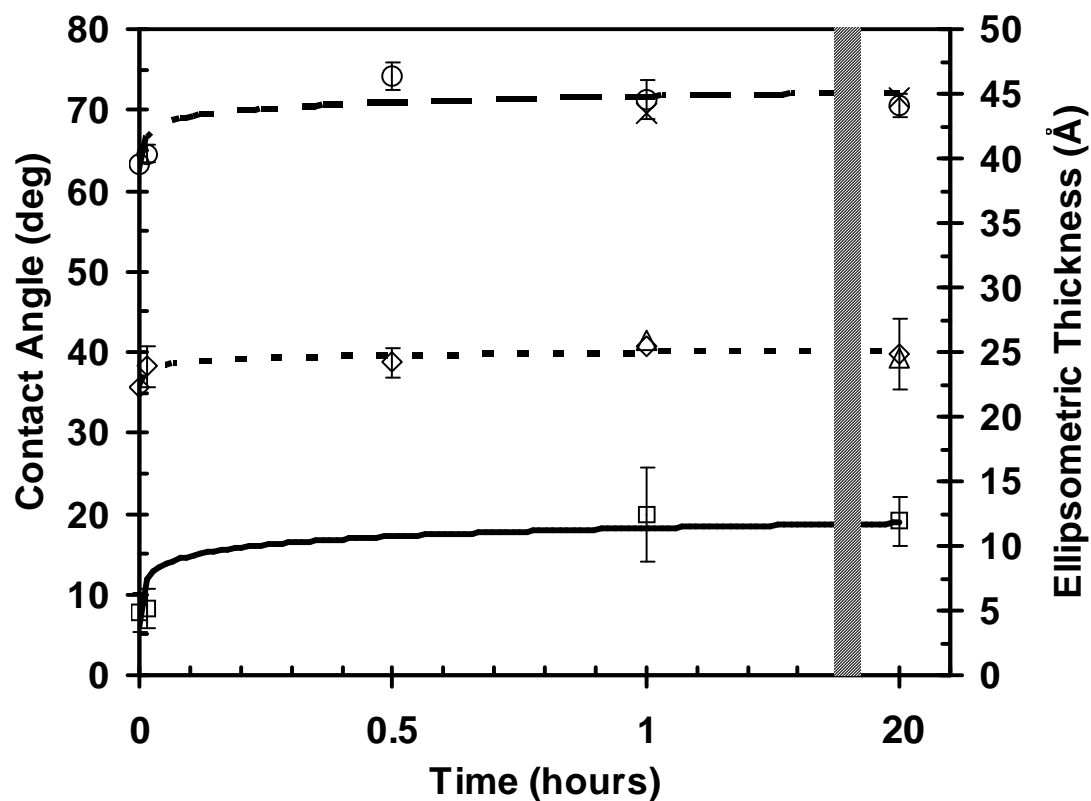


**Figure 3.9** Kinetics of SAM formation with SPTCS at 25 °C. (○) advancing contact angle, silicon substrate, (×) advancing contact angle, glass substrate, (◇) receding contact angle, silicon substrate, (△) receding contact angle, glass substrate, (□) ellipsometric thickness, silicon substrate. The lines are added as guides to the eye.

which produced SAMs with characteristics within experimental error of the limiting values.

**3.3.1.2 Kinetics for Trialkoxysilanes at 25 °C.** The kinetics of SAM formation from TMAC and TBAC at 25 °C were probed. At approximately 1 wt % (15 drops of stock solution in 25 ml) it took several days to reach a limiting contact angle and ellipsometric thickness. The kinetics plots are shown in **Figure 3.10** and **Figure 3.11**. Similar kinetic curves were obtained for SAM formation from TDAC and NBENZ.

**3.3.1.3 Kinetics for Trialkoxysilanes at 60 °C.** After the limiting values were known, a rapid preparation procedure, described in the experimental section above, was developed that produced contact angle and ellipsometric measurements within experimental error of values found in the slower room-temperature experiments. A number of different SAMs were prepared by this method to find the one best suited to promote rapid adhesion with negatively charged latex particles at an air-water interface. SAMs derived from TBAC and TDAC performed the best for sequestering Sulfate 2700 latex films, with TDAC slightly outperforming TBAC (based on qualitative observations of the difference in resistance of transferred particle films to lateral capillary forces). A summary of the SAM substrate properties used in this research work is shown in **Table 3.1**. The goal of this research work was not to produce perfect siloxane monolayers, but rather to produce chemically functionalized substrates capable

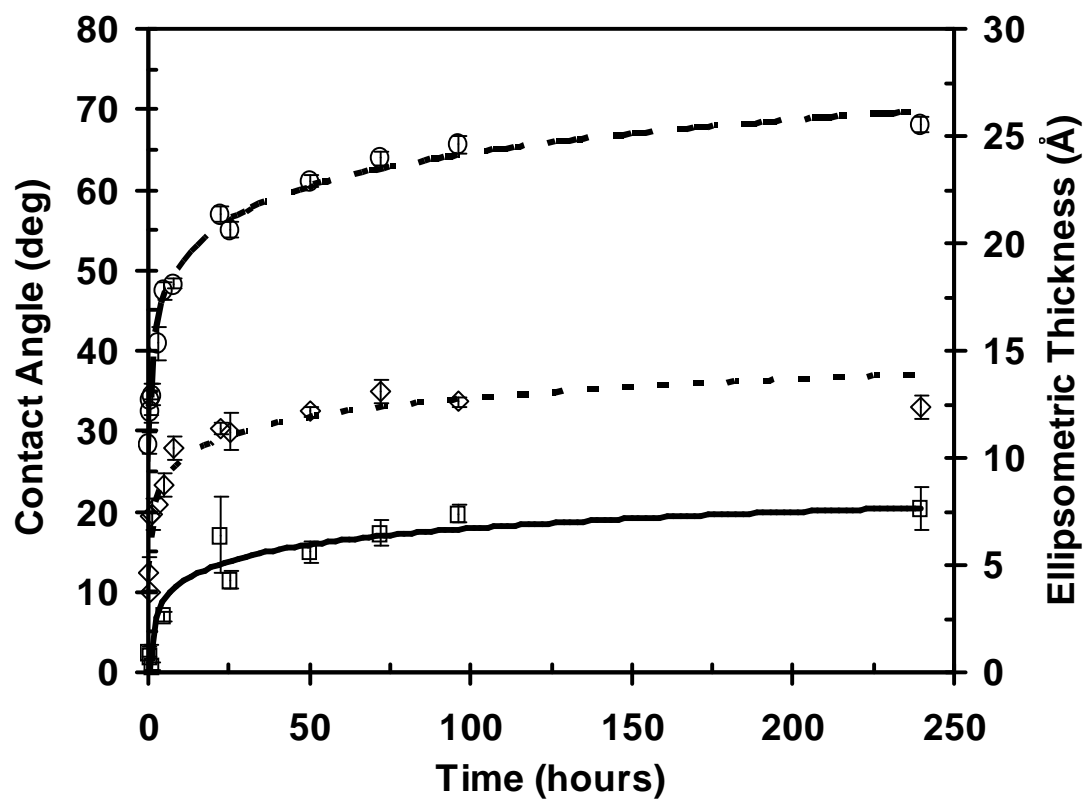


**Figure 3.10** *Kinetics of SAM formation from TBAC on silicon at 25 °C.*

(○) *advancing contact angle*, (◇) *receding contact angle*, (□) *ellipsometric thickness*.

*The lines are added as guides to the eye.*

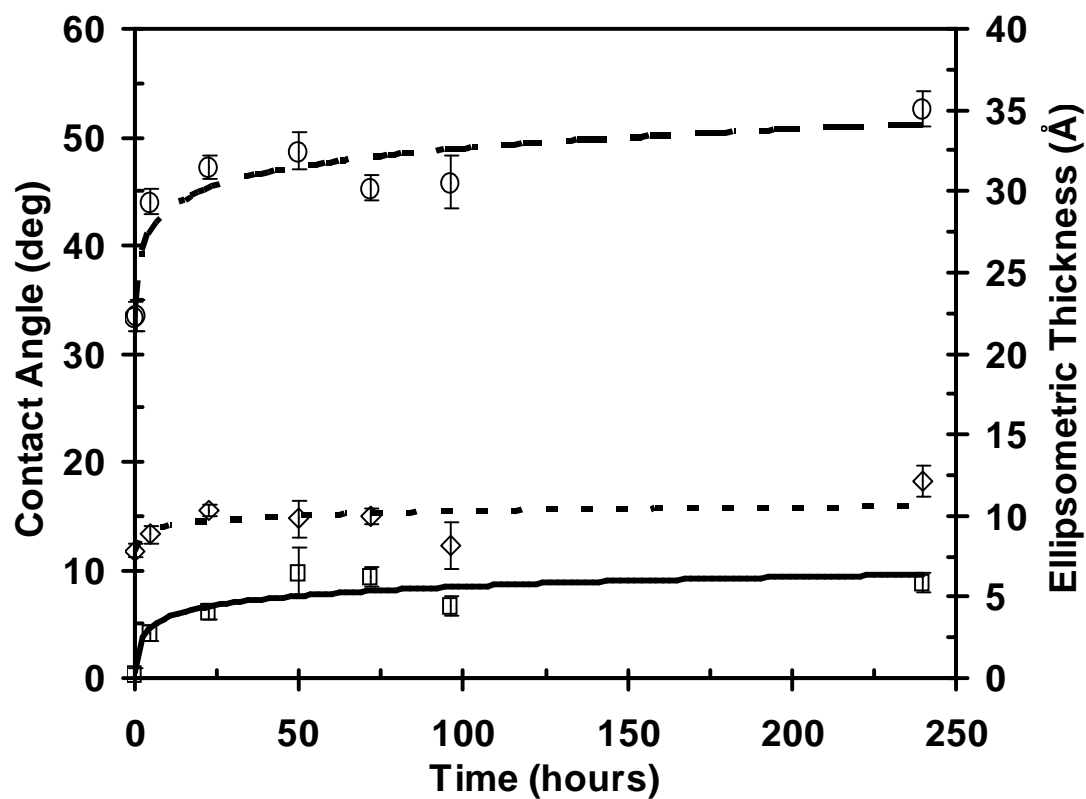


**Figure 3.11** *Kinetics of SAM formation from TMAC on silicon at 25 °C.*

(○) *advancing contact angle*, (◇) *receding contact angle*, (□) *ellipsometric thickness*.

*The lines are added as guides to the eye.*

SAM	±	Contact Angle		Ellipsometric Thickness (Å)
		<i>Advancing</i>	<i>Receding</i>	
TRIN	+	38 ± 2°, 14	10 ± 1°, 4	11 ± 1, 8
TMAC	+	49 ± 2°, 16	15 ± 2°, 6	7 ± 2, 8
NBENZ	+	59 ± 1°, 12	13 ± 1°, 2	11 ± 1, 8
TBAC	+	66 ± 3°, 16	34 ± 2°, 6	10 ± 2, 10
TDAC	+	78 ± 2°, 16	49 ± 1°, 8	10 ± 1, 8
SPTCS	-	71 ± 1°, 24	40 ± 3°, 16	12 ± 2, 20

**Table 3.1** *Properties of self-assembled monolayers. All of the positively-charged SAMs were allowed to react at 60 °C except for TMAC which was allowed to react at 25 °C. Negatively-charged SPTCS SAMs were prepared as described in the text. The silane abbreviations are explained in Section 3.2.2. Contact angle measurements were taken using buffered water at pH 7. The mean value, standard deviation, and number of measurements are reported for each entry.*

of adhering to particle monolayers. For this reason, the substrate surface properties were not further characterized.

**3.3.1.4 Stainless Steel Substrates.** Stainless steel substrates provided an attractive alternative to the use of SAMs derived from SPTCS because they could be used directly and required no substrate preparation. After removal of the protective PVC film from the mirrored surface, the substrates could be used in both LB and LS geometries to produce nearly identical results to the negatively charged SPCTS SAMs on silicon substrates. Freshly deprotected stainless-steel substrates had an advancing contact angle (ACA) of  $101 \pm 3^\circ$  (standard deviation, 10 measurements) and a receding contact angle (RCA) of  $38 \pm 6^\circ$  (5 measurements). The ACA seemed quite high for a metallic surface, which suggested that a thin polymer film could be present at the surface. After rinsing the substrate with toluene, acetone, isopropyl alcohol, and methanol and drying the substrate with a nitrogen jet, the ACA dropped to  $95 \pm 2^\circ$  (6 measurements) and the RCA remained at  $38 \pm 3^\circ$  (4 measurements). A freshly deprotected substrate was buffed gently with 000 steel wool, rinsed with water and dried with a nitrogen jet, which caused the ACA to drop to  $35 \pm 3^\circ$  (11 measurements) and the RCA to  $10 \pm 4^\circ$ . Allowing the buffed substrate to sit in air for 2 days brought the ACA back up to  $57 \pm 3^\circ$  (14 measurements), and the RCA to  $13 \pm 1^\circ$ ; and allowing the substrate to sit in air for 3 weeks brought the ACA up to  $61 \pm 2^\circ$  (16 measurements) and the RCA up to  $15 \pm 1^\circ$ . The increase in contact over time in air was likely caused by the re-growth of the physisorption of organic contaminants at the surface. These

data are consistent with our inference that a thin polymer film existed at the surface of the stainless steel substrates. To further investigate this possibility, XPS was performed on one of the freshly deprotected substrates. Strong carbon and oxygen peaks were observed, which could be greatly diminished by scratching the substrate while in the spectrometer and reanalyzing. No chlorine peaks were observed, which suggests that the protective PVC film was isolated from the steel surface by an adhesive layer. Inquiries were made to the steel manufacturer concerning the presence of polymer film, but no reply was received. Nevertheless, the data strongly suggest that the mirrored steel was covered by a thin organic film.

### **3.3.2 Native Particle Films.**

**3.3.2.1 Positive Particle System.** Initially, experiments were conducted to prepare densely packed particle monolayers at the substrate-latex interface by random sequential adsorption from bulk suspension. After deposition, the patterned substrates displayed an angle dependent iridescent appearance, as shown in **Figure 3.12-A** and **-B**. Surprisingly, some of the particle arrays exhibited a two-dimensional crystalline grain like structure, as shown in **Figure 3.12-C** and **-D**. At first, we believed that the particles were sequentially adsorbing in an ordered fashion. Under certain conditions oriented flocculation can occur,<sup>42</sup> and it seemed reasonable that oriented adsorption could occur as well. However, when this hypothesis was tested by varying the latex concentration and the “adsorption” time, a similar degree of surface coverage was always produced.

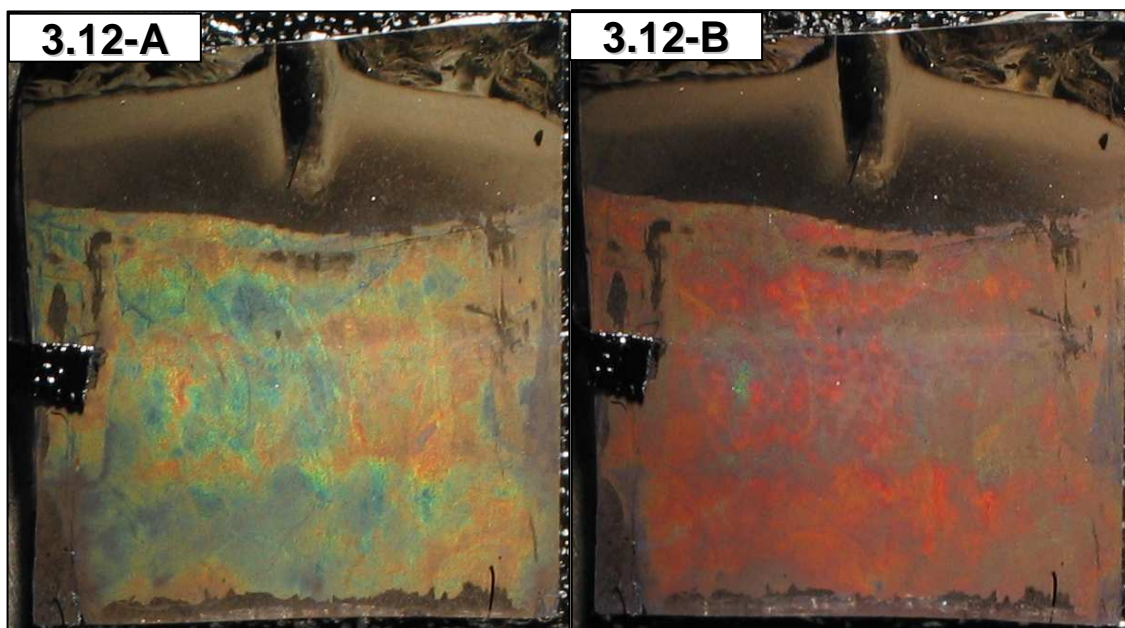
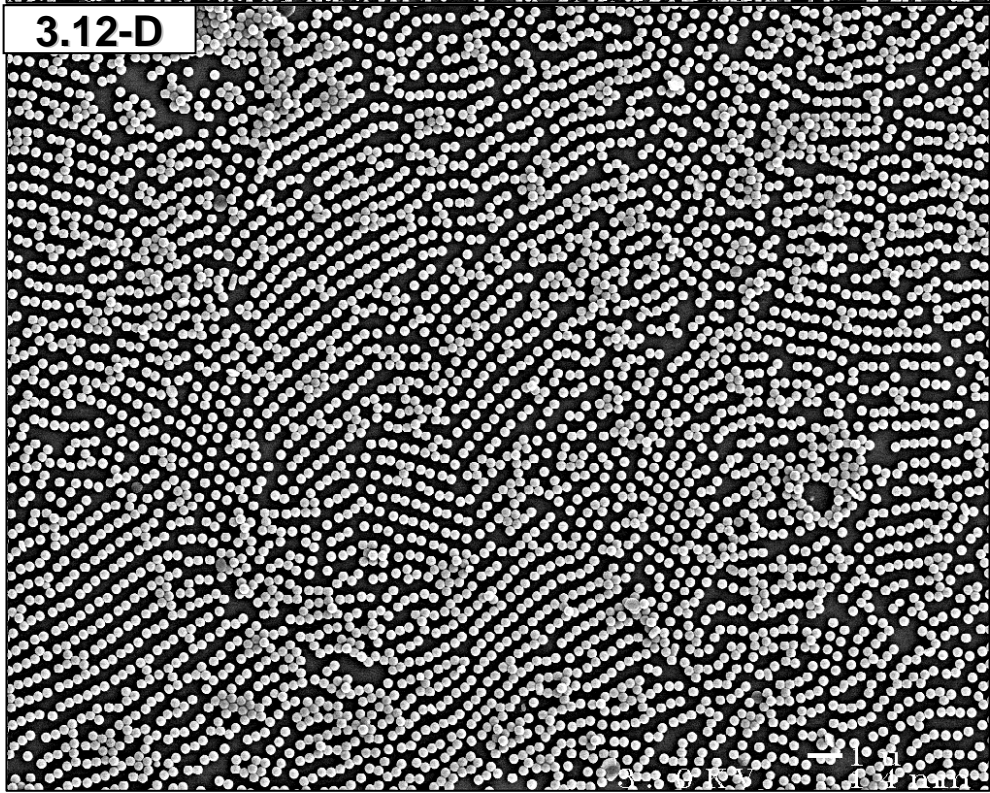
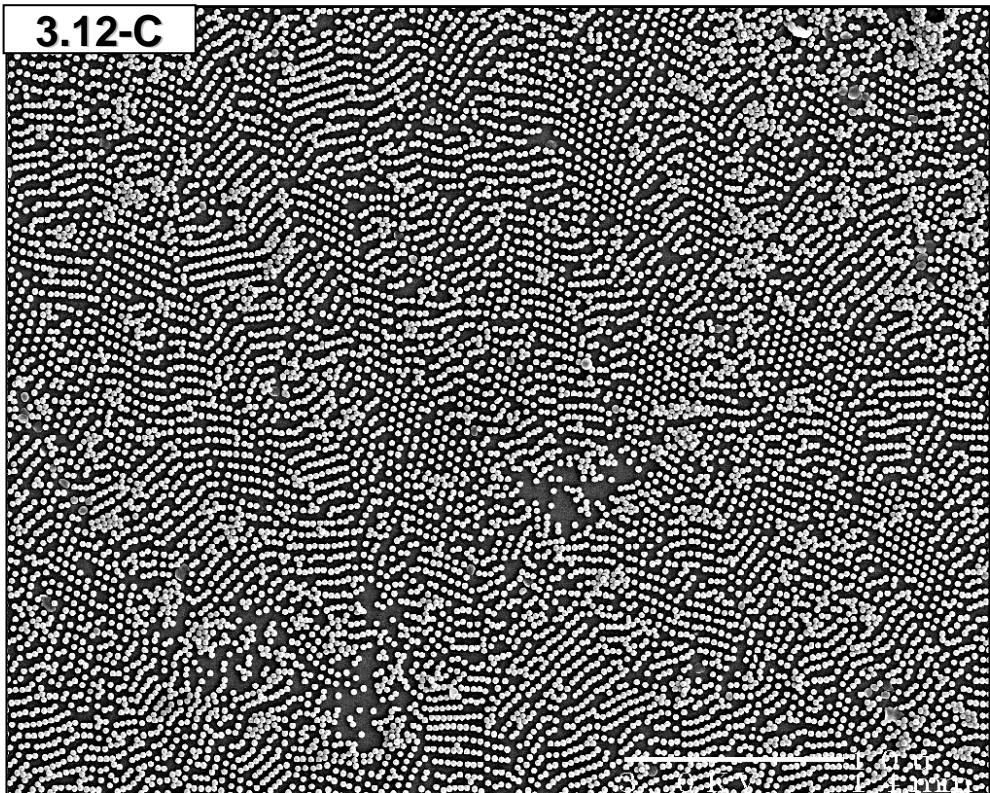


**Figure 3.12** *Macroscopic appearance of the crystalline grain like pattern. (A and B) Images taken at different viewing angles while illuminated with white light, notice the angle dependent coloration caused by diffraction. The sample shown was prepared by performing an LB transfer of the native surface film on 0.2 wt % Imidazole 258 latex onto a SPTCS SAM on a silicon substrate. (Following page, C and D) SEM micrographs of the patterned region, showing a distorted hexagonal pattern. Scale Bars: (C) 10  $\mu\text{m}$  and (D) 1  $\mu\text{m}$ .*





Apparently, an ordered particle film was being transferred from the latex-air interface to the substrate when it was first dipped into the latex.

**3.3.2.2 Imidazole 258 Latex Isotherm.** The surface pressure-area isotherm for the native surface film on a sample of 0.2 wt % Imidazole 258 (positively-charged latex) was recorded. After being vortexed and sonicated, approximately 50 mL of the latex was placed into the mechanical trough. The initial film area was 6000 mm<sup>2</sup> and was compressed at a rate of 11.8 %/min. Since the number of particles comprising the surface film was unknown, the isotherm was first plotted as a function of the trough surface area or compression ratio (**Figure 3.13**). After the solid-phase transition was recorded, which occurs when the particle separation distance is equal to the particle diameter, the isotherm could then be plotted as a function of separation distance assuming an HCP particle monolayer was formed (**Figure 3.14**). According to the isotherm data, the Imidazole 258 latex particles did not begin to significantly interact with each other until they approached within 100 nm of each other. The micrographs in the following sections can be correlated with the isotherm, based on the surface pressures at which the samples were taken. However, they cannot be directly compared based on the compression ratio for reasons discussed in **Section 3.3.3**.

**3.3.2.3 Deposition on SAMs derived from SPTCS.** Native particle films on samples of the 0.2 wt % Imidazole 258 latex were readily transferred to negatively-charged substrates bearing SAMs derived from SPTCS. A systematic comparison

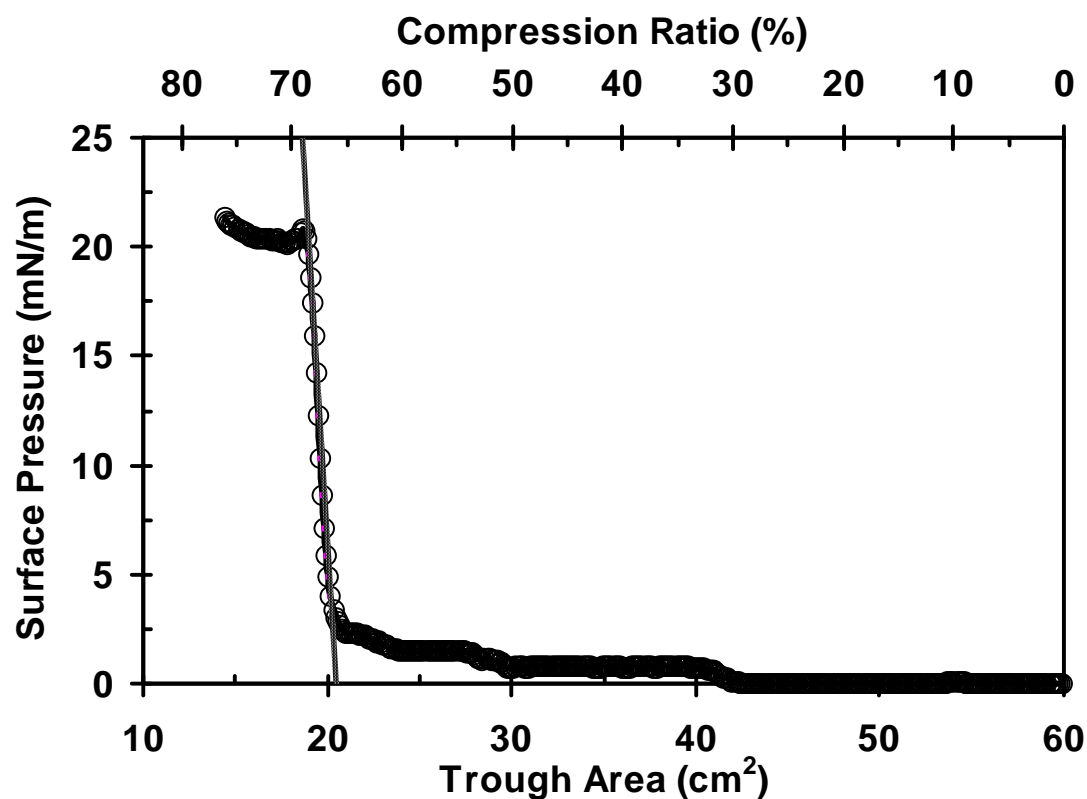


**Figure 3.13** *Surface Pressure-Area Isotherm for the native film on a sample of 0.2 wt % Imidazole 258 latex. The isotherm is plotted both as a function of the trough area and the surface film compression ratio. By extrapolating the solid transition to the area axis, which produced the equation  $y = -13.61x + 278.1$ ,  $R^2 = 0.9918$ , the number of particles at the surface can be calculated from the HCP packing area and was found to be  $3.544 \times 10^{10}$ .*

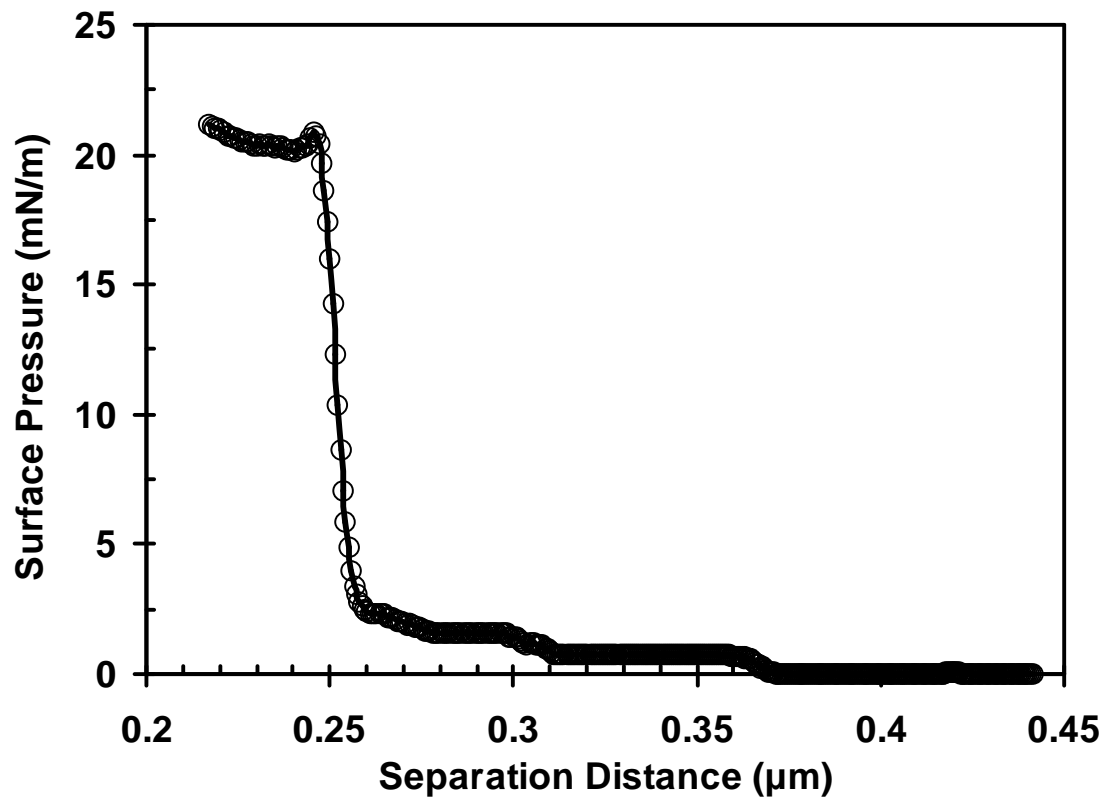


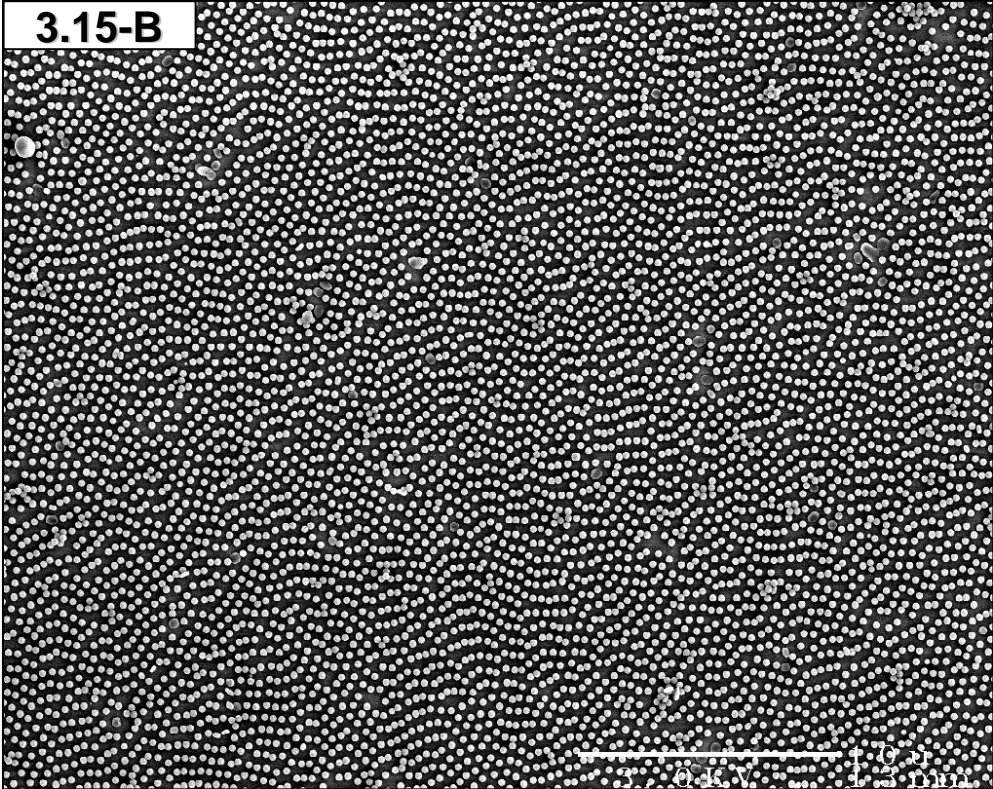
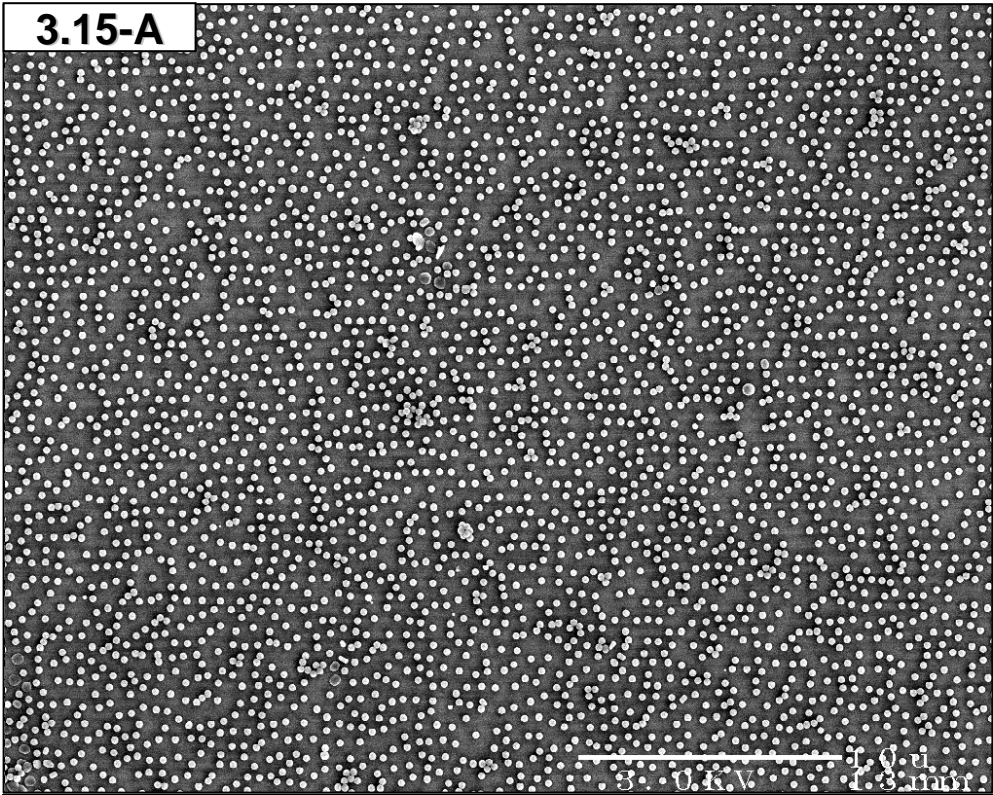
**Figure 3.14** *Surface Pressure-Distance Isotherm for the native Imidazole 258 latex film.* By assuming that the solid-phase transition occurs at a separation distance equal to the particle diameter (0.258 μm), the particle separation distance at all points can be approximated. The particles do not detectably interact with each other until they are approximately 100 nm apart.

between the LB and LS deposition methods was performed using the mechanical trough and the second-generation dipper. The surface film area was compressed at a rate of 45.1 %/min. Samples were taken at compression ratios of 20, 30, 40, and 50 %, at a rate of 13.6 mm/s. The results of the experiment are shown in **Figure 3.15**.

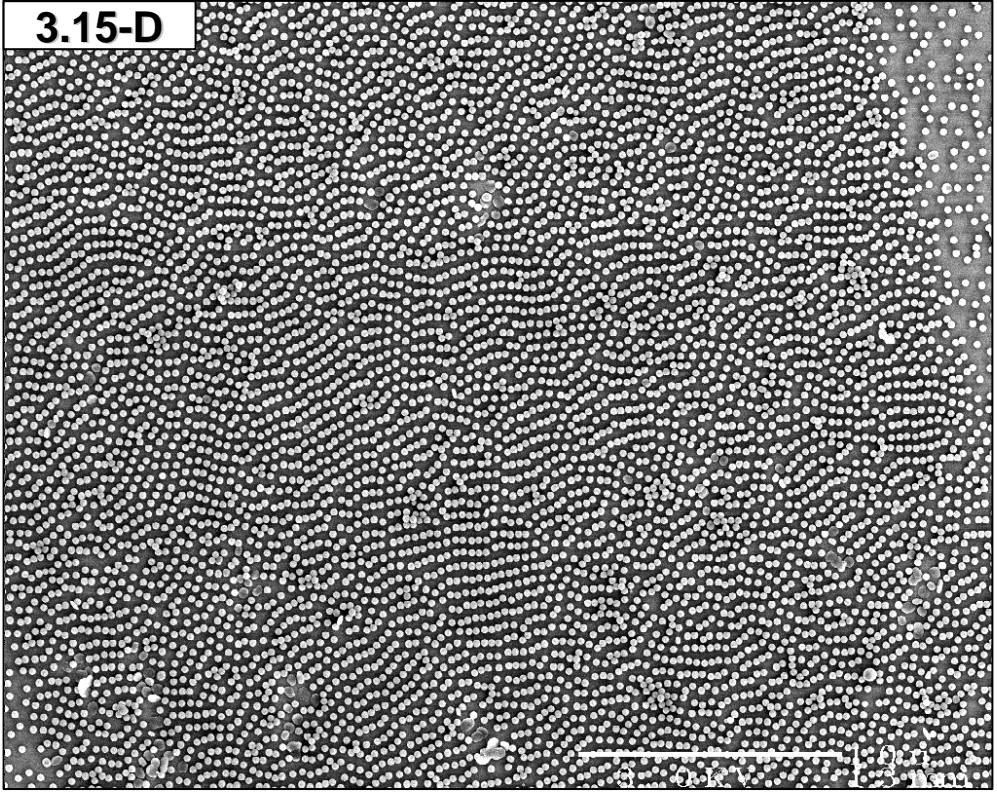
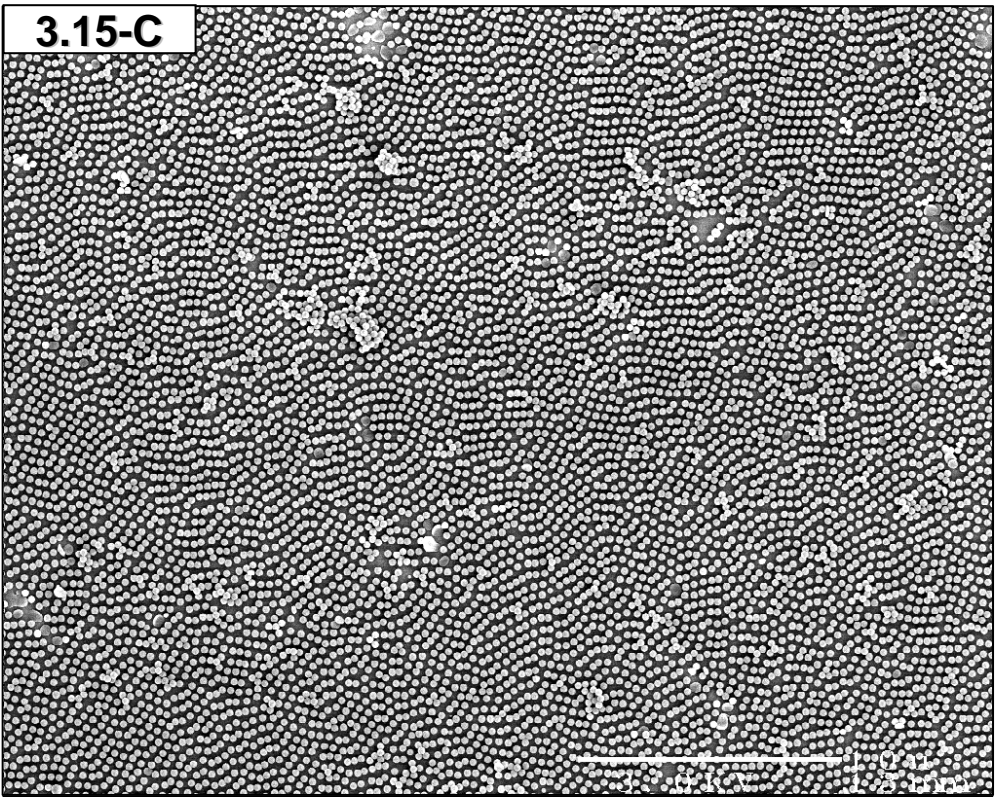
Empirically, the compression ratios for this experiment should be shifted upward by 10-20% for comparison with the isotherm in **Figure 3.13**. The pattern after transfer can only be as good as the original pattern at the interface. At low compression, the particles were in a gas-like state as seen in **Figure 3.15-A** and **-E**. As the film was compressed, the particle spacing decreased until finally a complete HCP monolayer formed as seen in **Figure 3.15-H**. The LB-transferred pattern in **Figure 3.15-D** has a distorted appearance because it was stretched by shear forces during the deposition procedure, as discussed in **Section 3.3.2.6**. The LS-transfer method preserves the hexagonal symmetry from the interface by approaching in a parallel geometry resulting in the simultaneous transfer of the entire film.

**3.3.2.4 Deposition on Stainless Steel Substrates.** Native particle films on samples of the Imidazole 258 latex were also transferred to mirror-finish stainless steel substrates, with results remarkably similar to the substrates bearing SAMs derived from SPTCS. A sample of 0.2 wt % latex was placed into the manual trough after vortexing and sonication, and transfers were performed at compression ratios of 0, 20, 40, 60, 80, and 88 %. The barrier was manually closed, compressing the film surface area at a rate of approximately 2.5 %/s. LB samples were taken at a rate of  $22.5 \pm 0.5$  mm/s using the

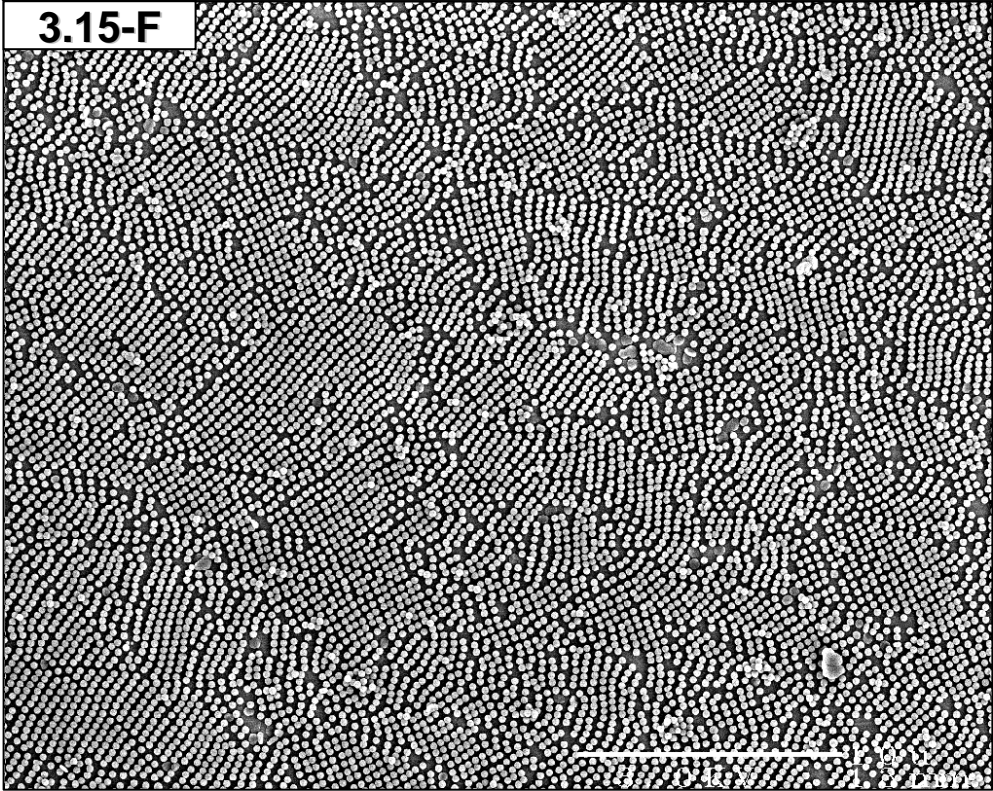
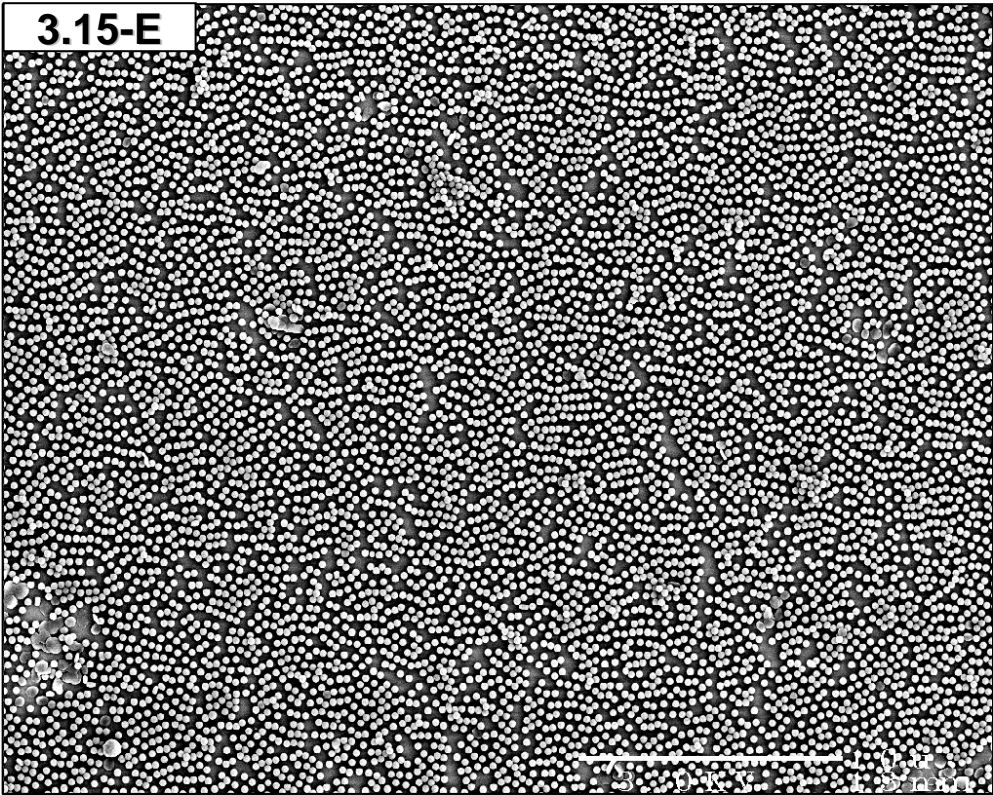
**Figure 3.15** *Native particle film on a sample of the Imidazole 258 latex transferred to silicon substrates bearing SAMs derived from SPTCS. The transfer geometry and compression ratio at transfer were: (A) LB at 20%, 0 mN/m, (B) LB at 30%, 0 mN/m, (C) LB at 40%, 0 mN/m, (D) LB at 50%, 0.8 mN/m, (E) LS at 20%, 0 mN/m, (F) LS at 30%, 0 mN/m, (G) LS at 40%, 0.8 mN/m (H) LS at 50%, 3.1 mN/m. Scale Bars: 10  $\mu\text{m}$ .*

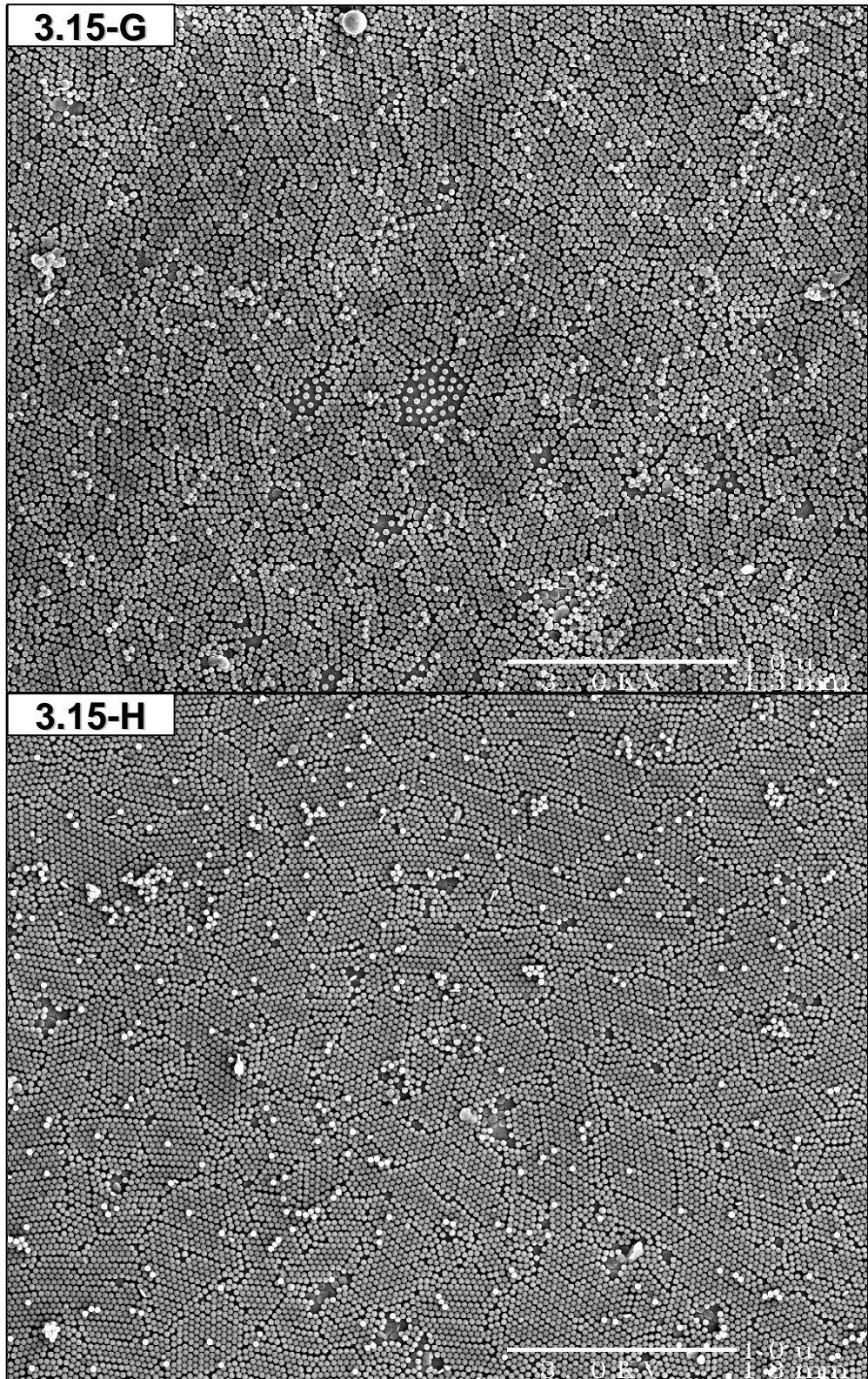










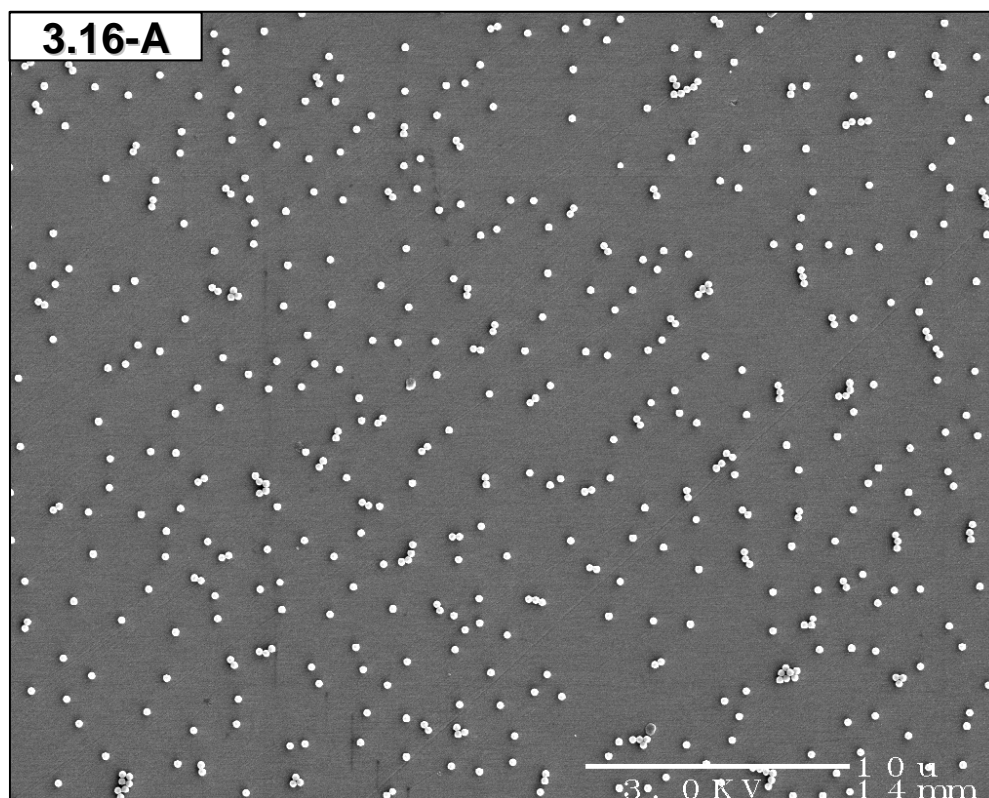


first-generation dipper, and LS samples were taken manually. After deposition, all samples were rinsed with deionized water and blown dry with a nitrogen jet. SEM micrographs of both types of transferred-particle films are shown in **Figure 3.16** and **Figure 3.17**.

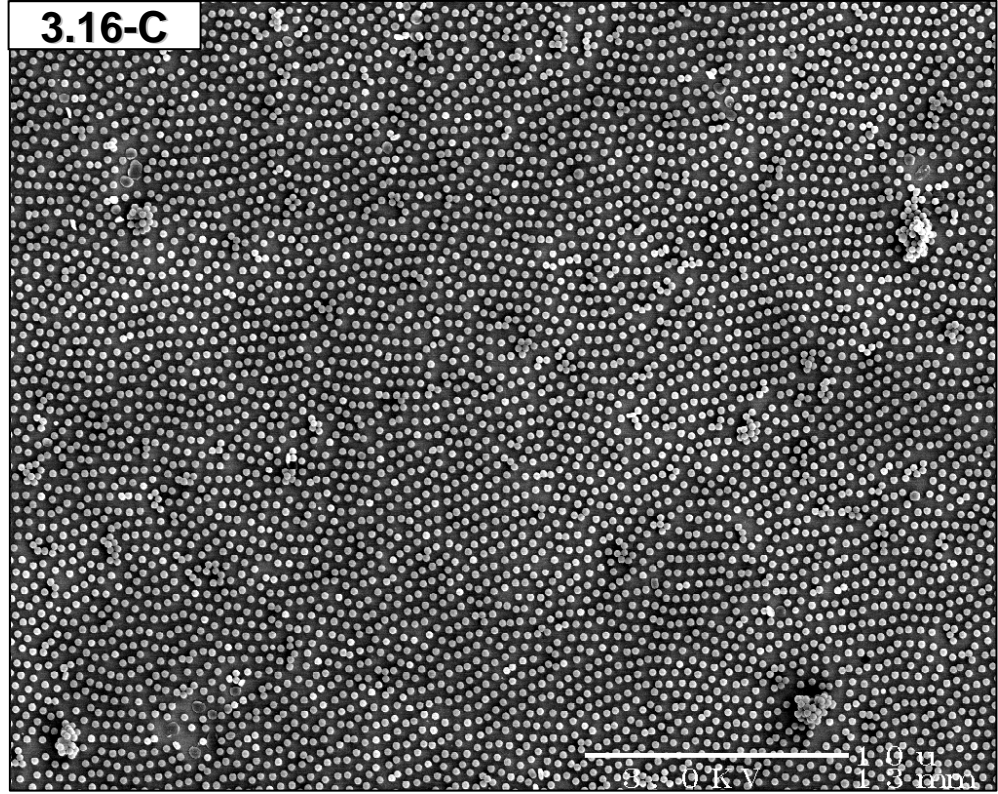
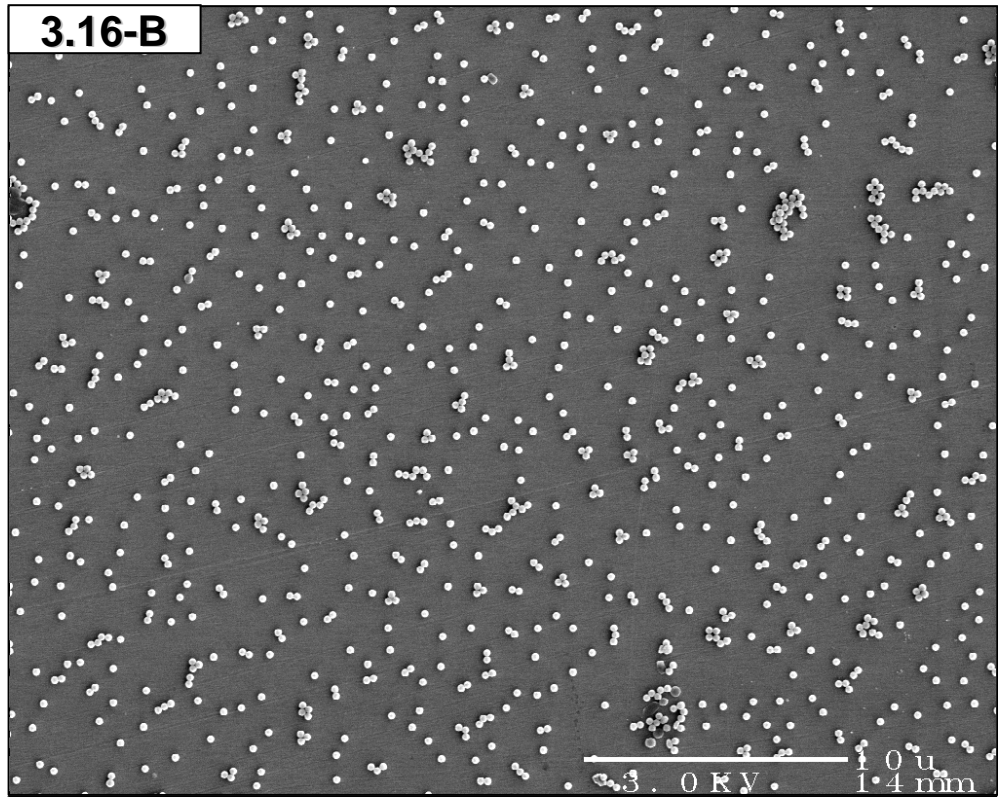
In a similar experiment, LS transfers were performed during the *second* compression cycle of the surface film. A fresh surface film was first compressed to a ratio of 80 %, and the barriers were then fully opened. LS transfers were taken at 20-% intervals on the second compression cycle. Films transferred at low compression exhibited a much higher degree of order than those observed in the first cycle LS films (**Figure 3.18**). We believe this result to be caused by a “memory” effect, wherein the hexagonal arrangement from being compressed during the first cycle partially remained in the second compression cycle. The surface film in this run was compressed an additional 8 %, which pushed it above collapse as seen in **Figure 3.18-F**. After re-expansion of the collapsed film, an LS sample was taken (**Figure 3.18-G**), which revealed fused rafts of particles, demonstrating the irreversibility of film collapse.

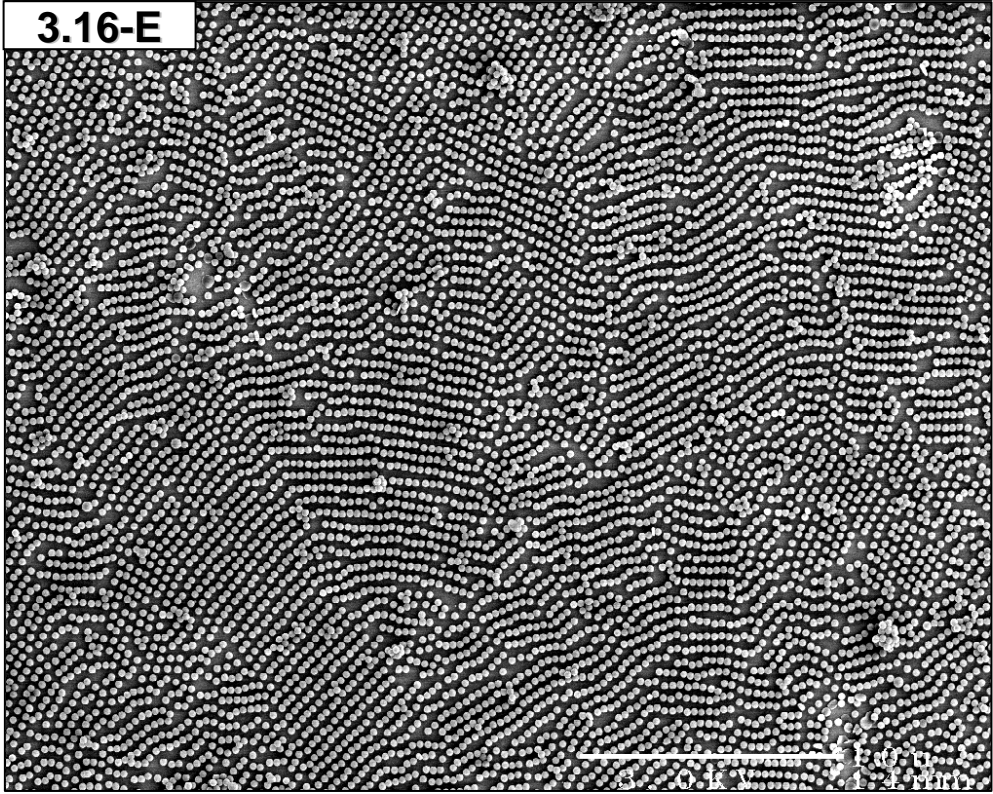
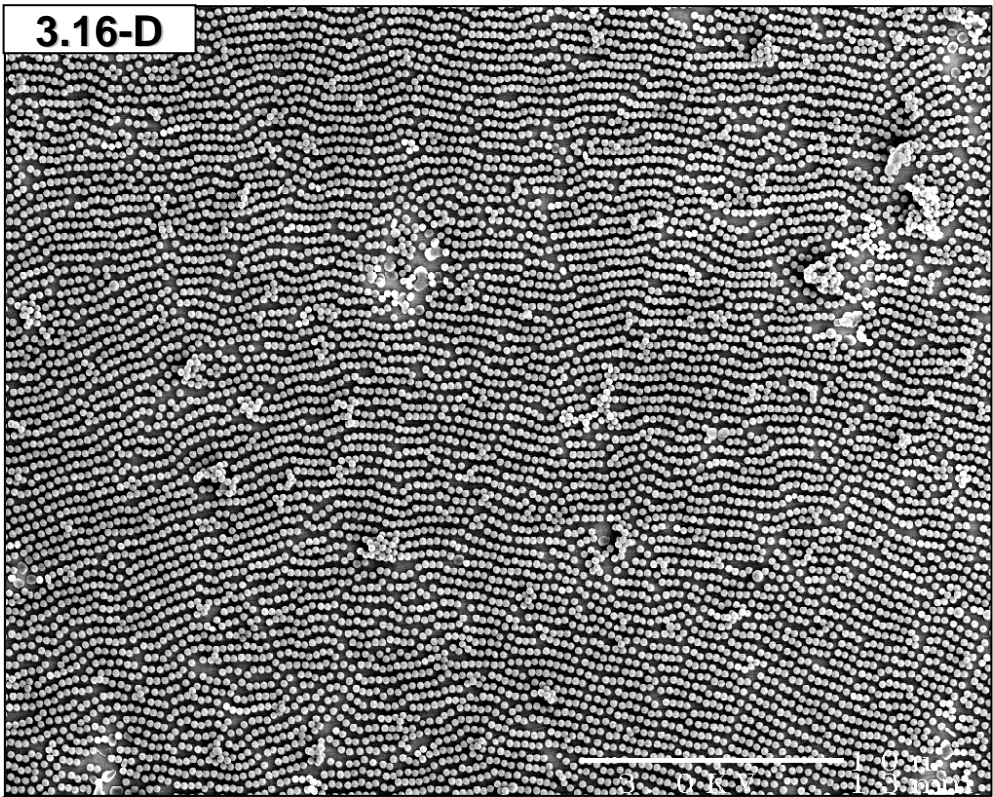
**3.3.2.5 Deposition on SAMs derived from OTS.** Native particle films on the Imidazole 258 latex were also successfully transferred to silicon substrates functionalized with SAMs derived from octadecyltrichlorosilane (OTS). These SAMs likely had a greatly reduced effective surface charge, compared to that of native SiO<sub>2</sub>, because of the intervening C<sub>18</sub> low dielectric layer. Macroscopically, the transferred particle films had a shimmering silver appearance, instead of the typically observed

**Figure 3.16** *Native particle films of Imidazole 258 latex particles transferred by the LB method to mirror-finish stainless steel substrates. Transfers were performed on the first compression cycle at compression ratios of: (A) 0%, (B) 20%, (C) 40%, (D) 60%, and (E) 80%. Scale Bars: 10  $\mu$ m.*

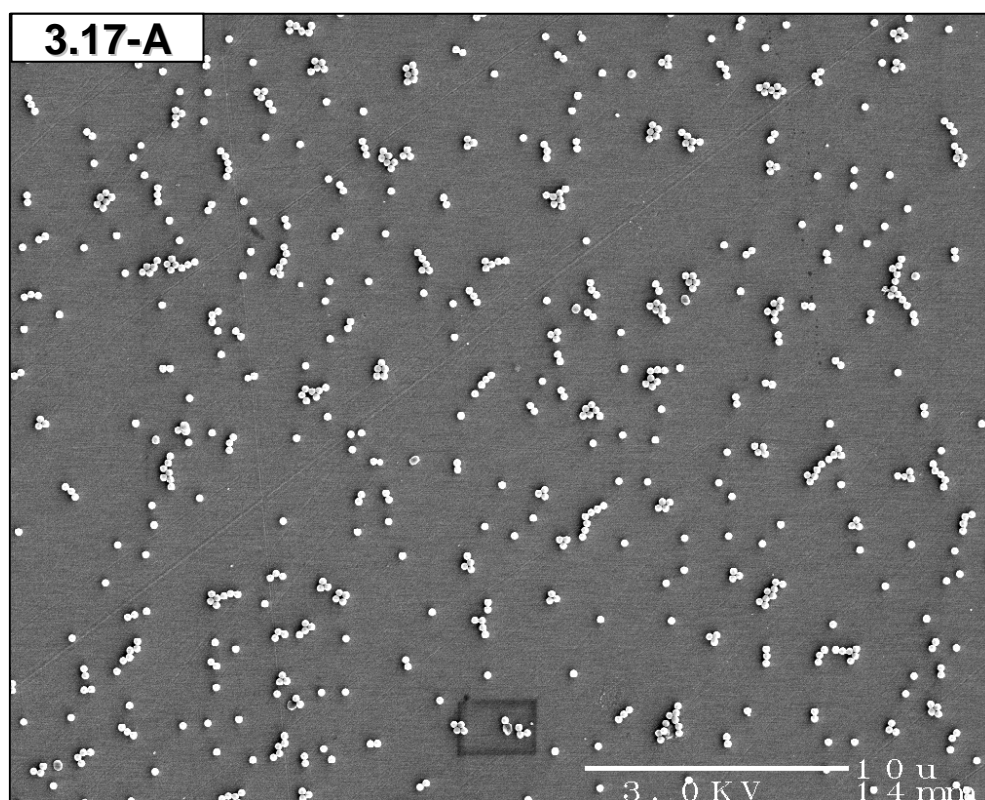




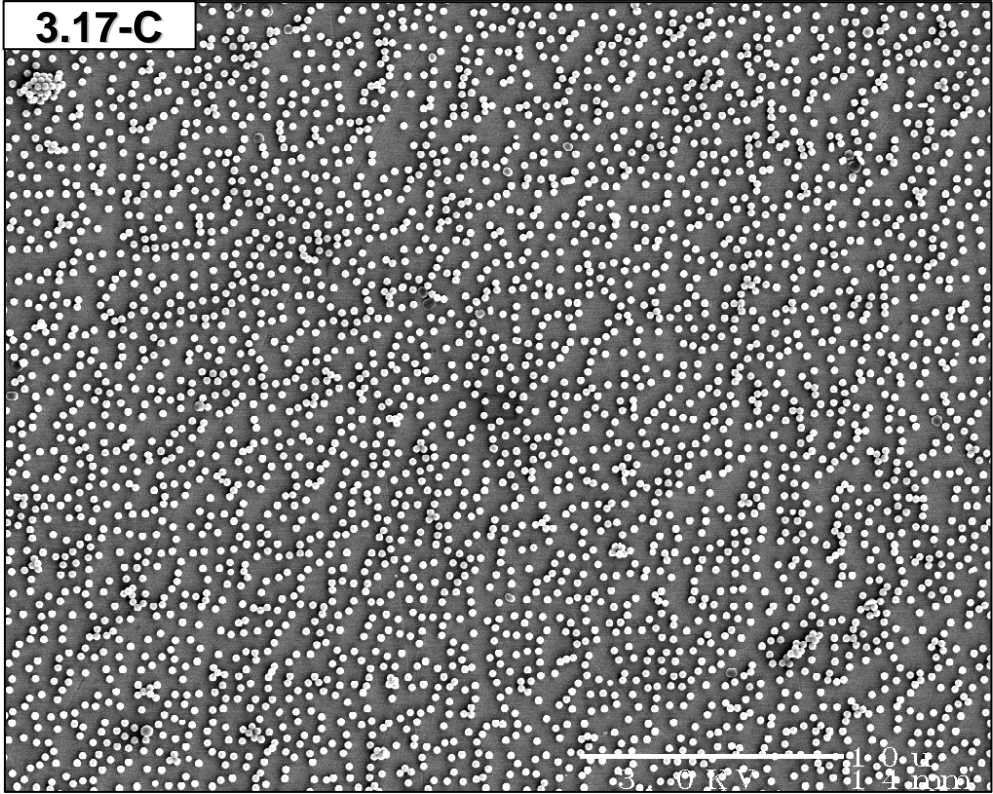
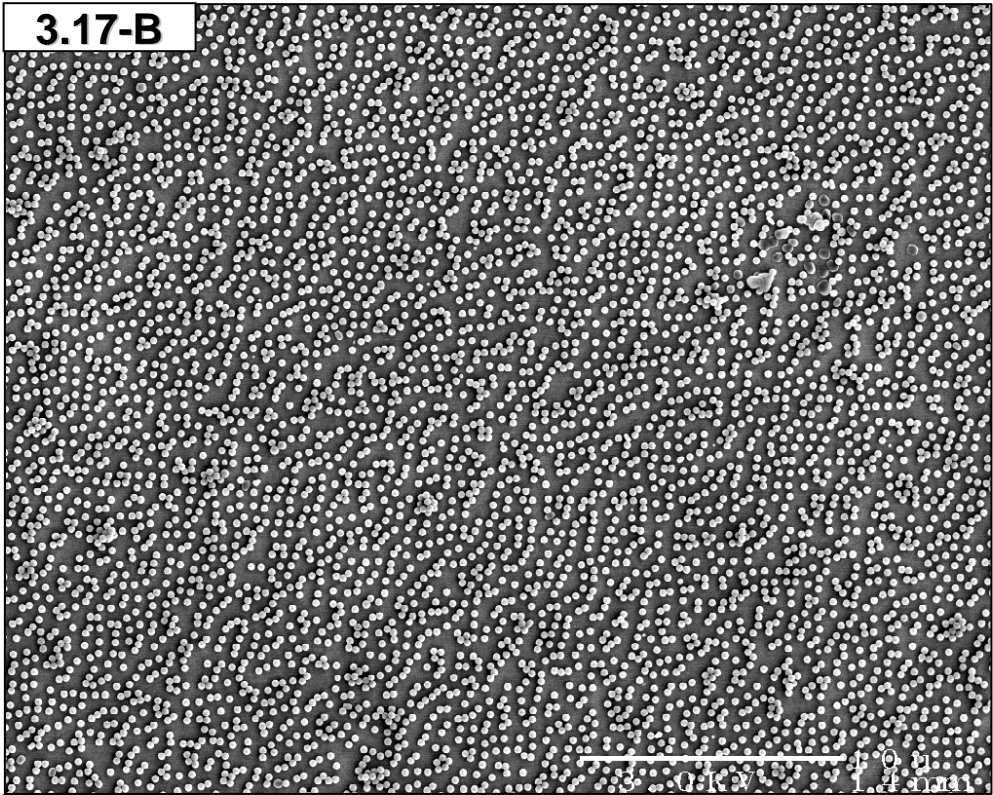




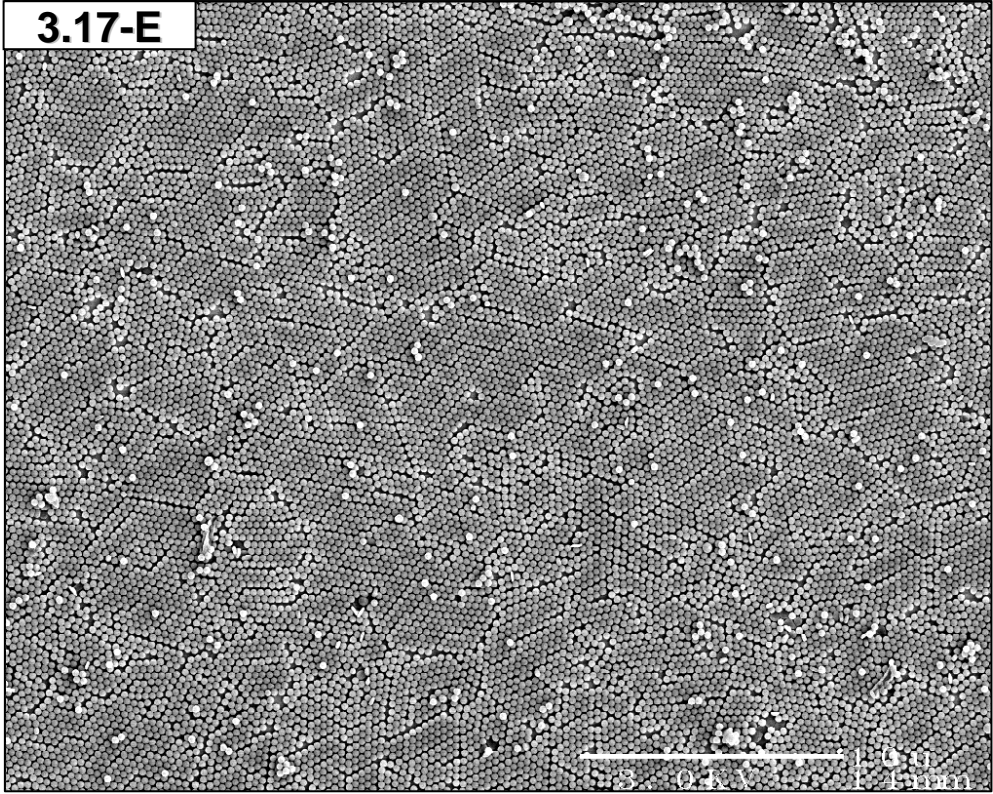
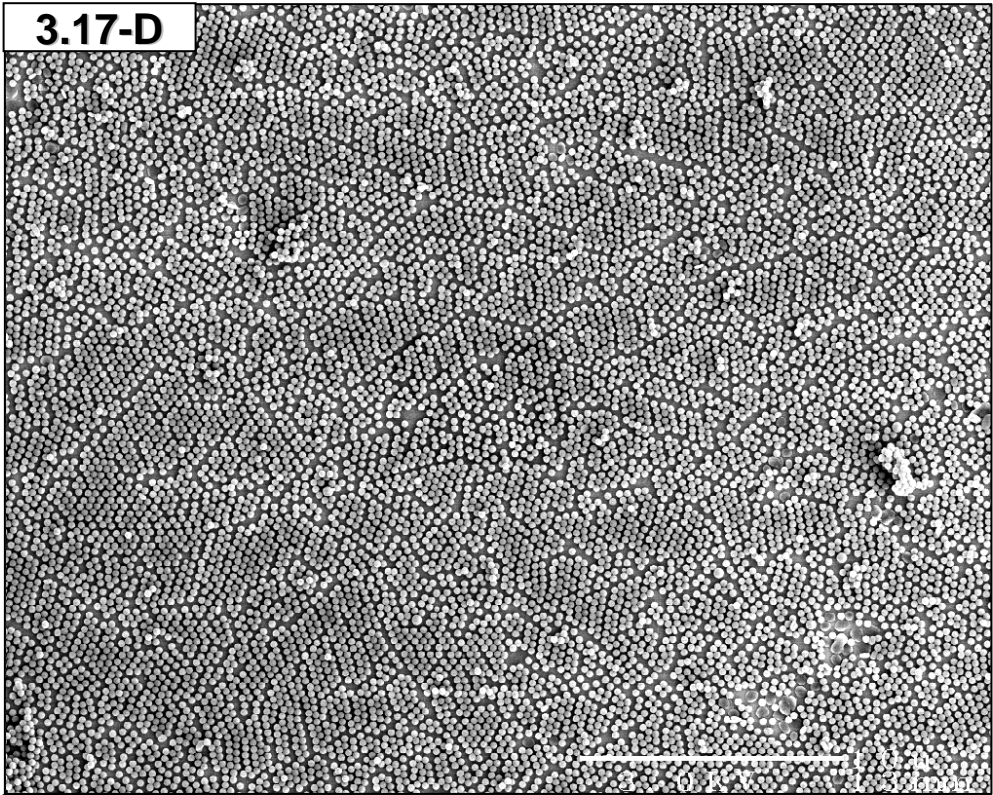
**Figure 3.17** *Native particle films of Imidazole 258 latex particles transferred by the LS method to mirror-finish stainless steel substrates on the first compression cycle. Transfers were performed at compression ratios of: (A) 0%, (B) 20%, (C) 40%, (D) 60%, and (E) 80%. Scale Bars: 1  $\mu$ m.*



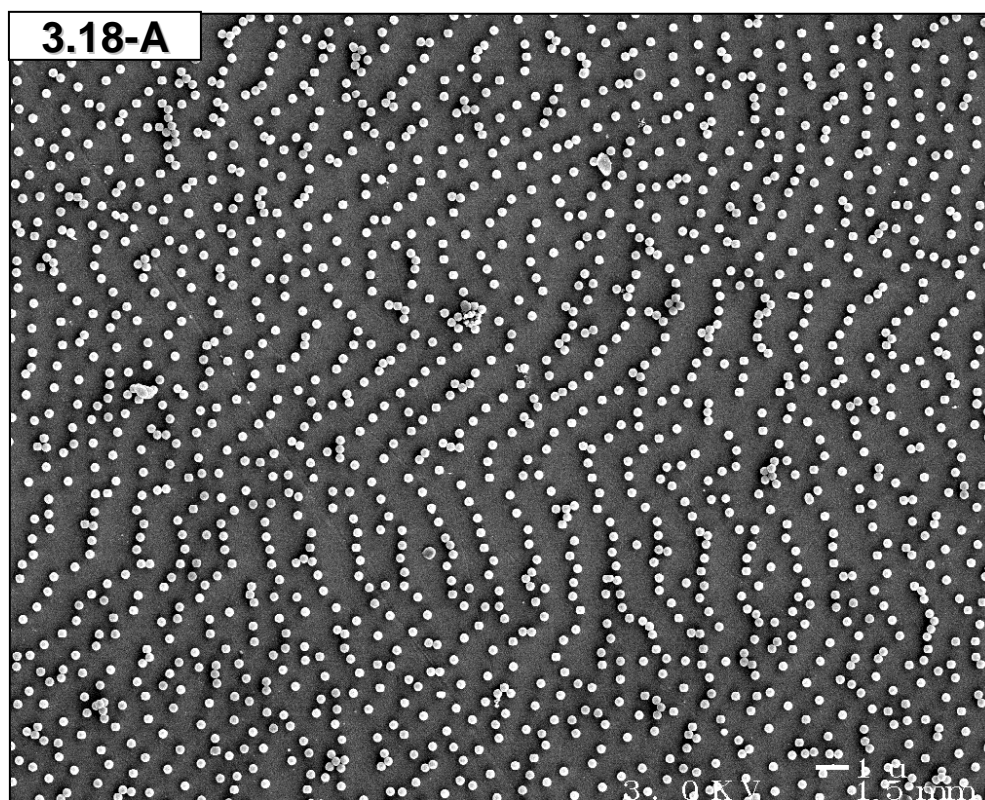


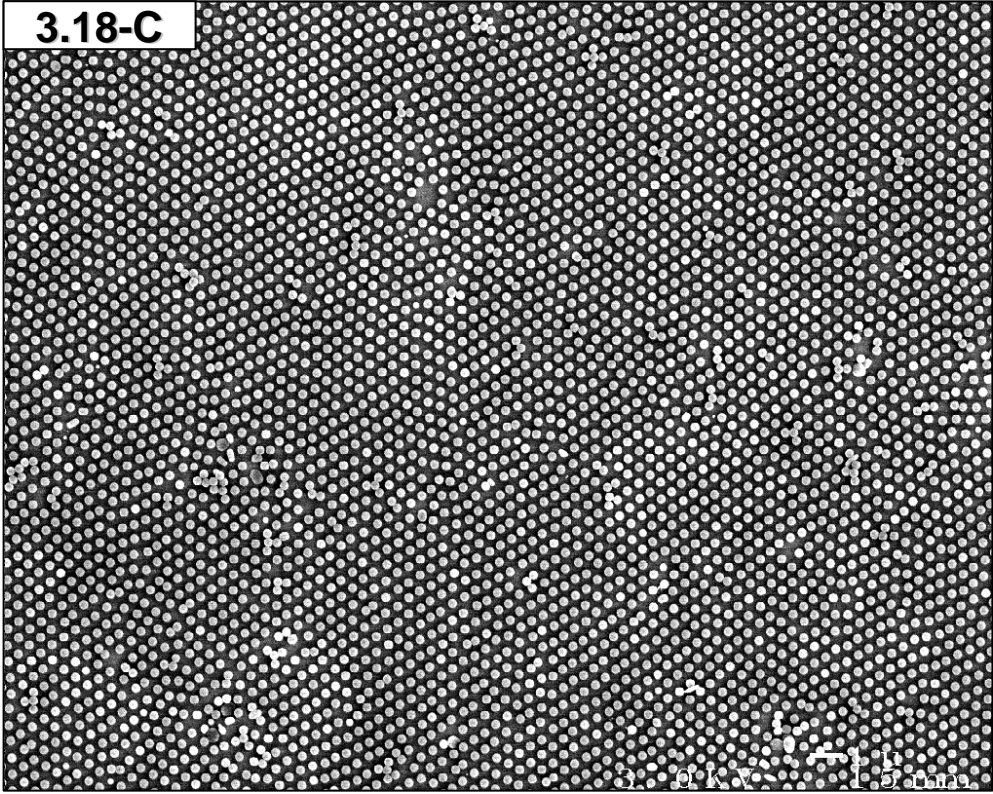
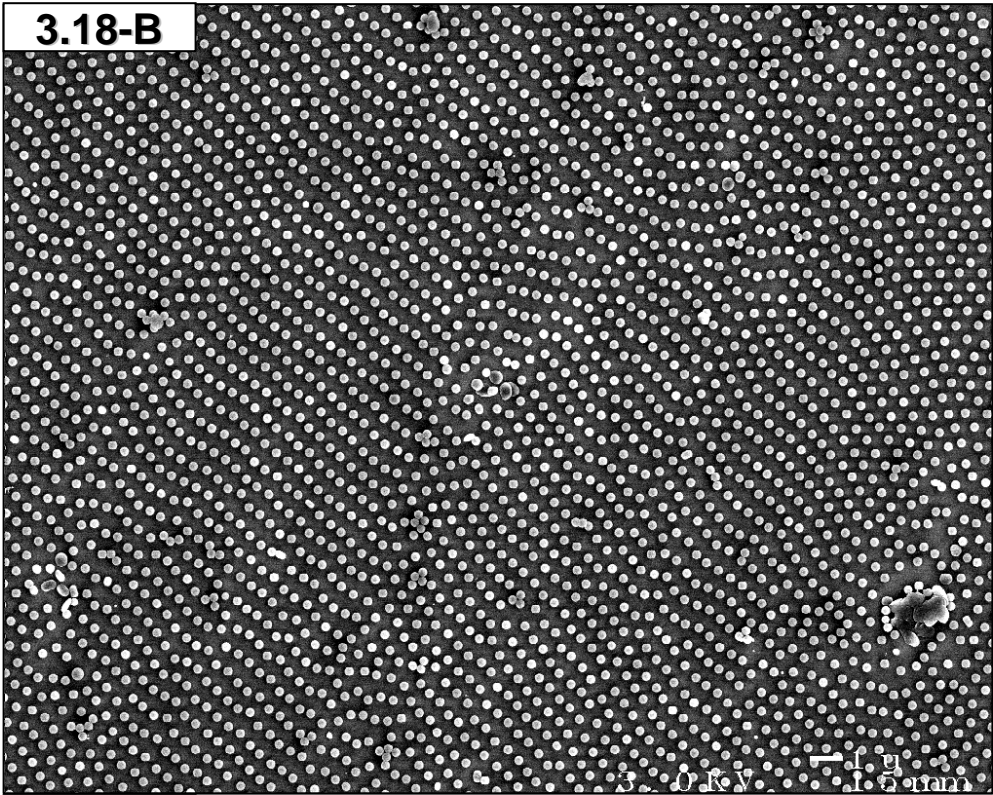




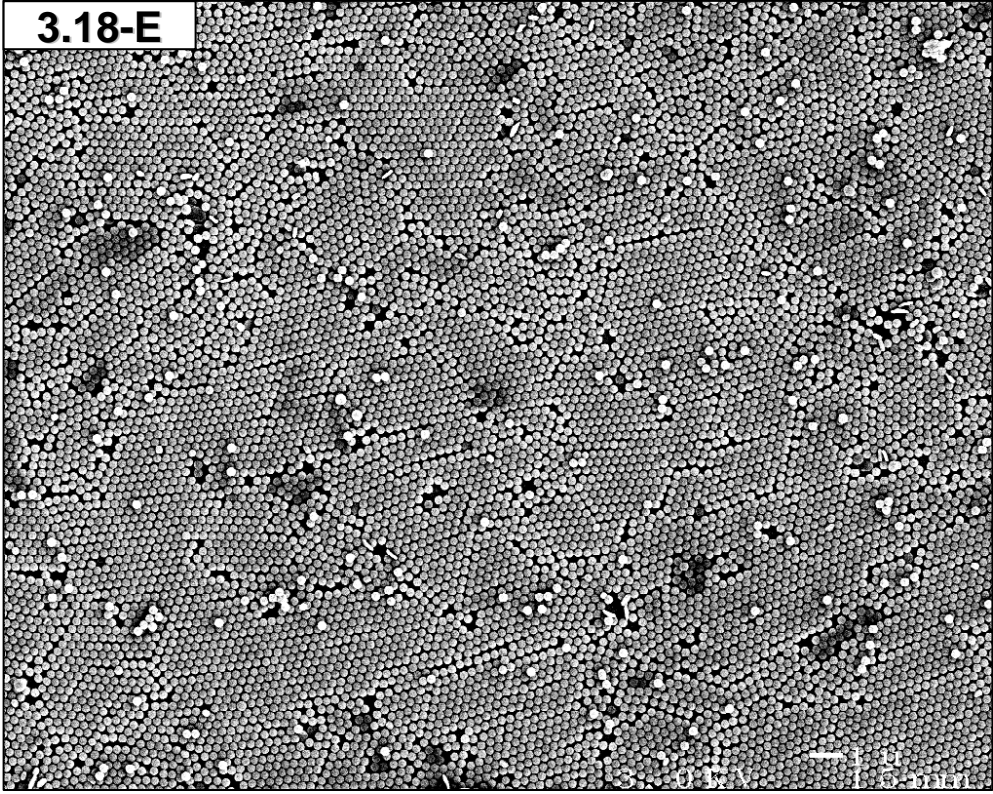
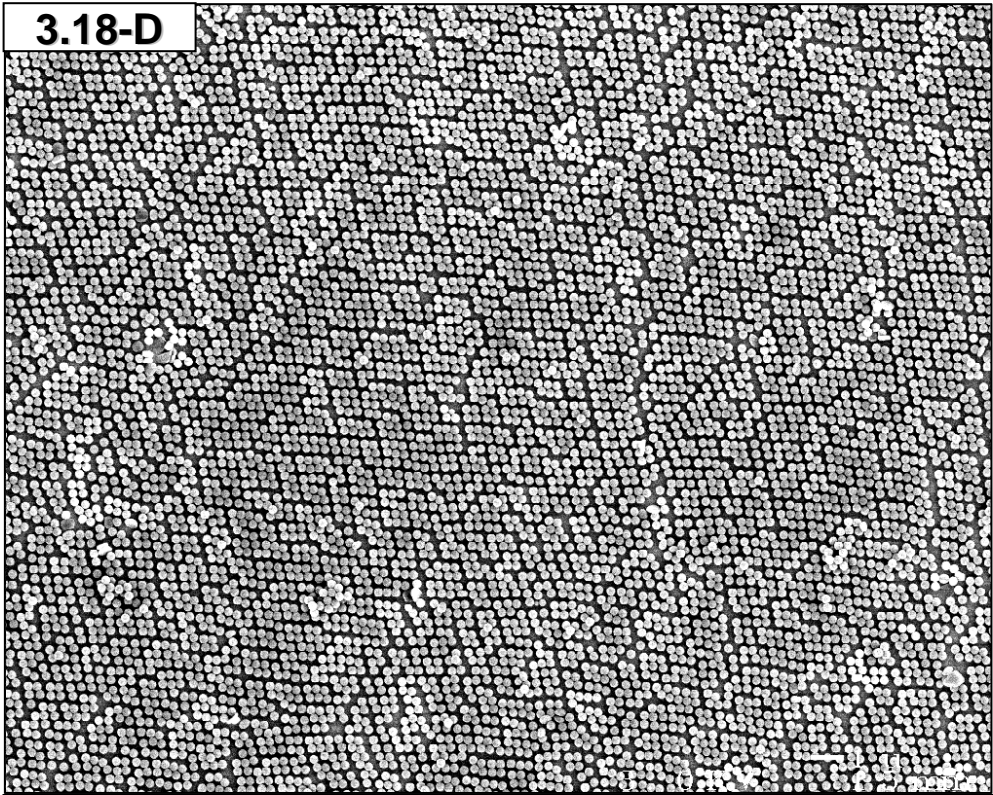


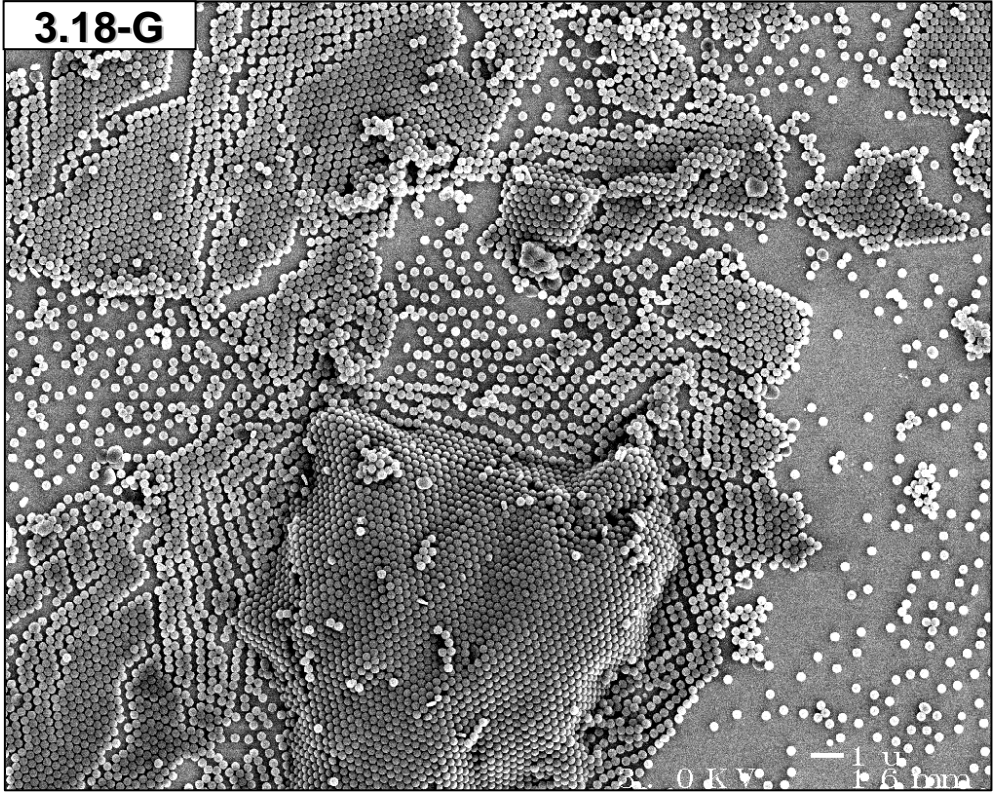
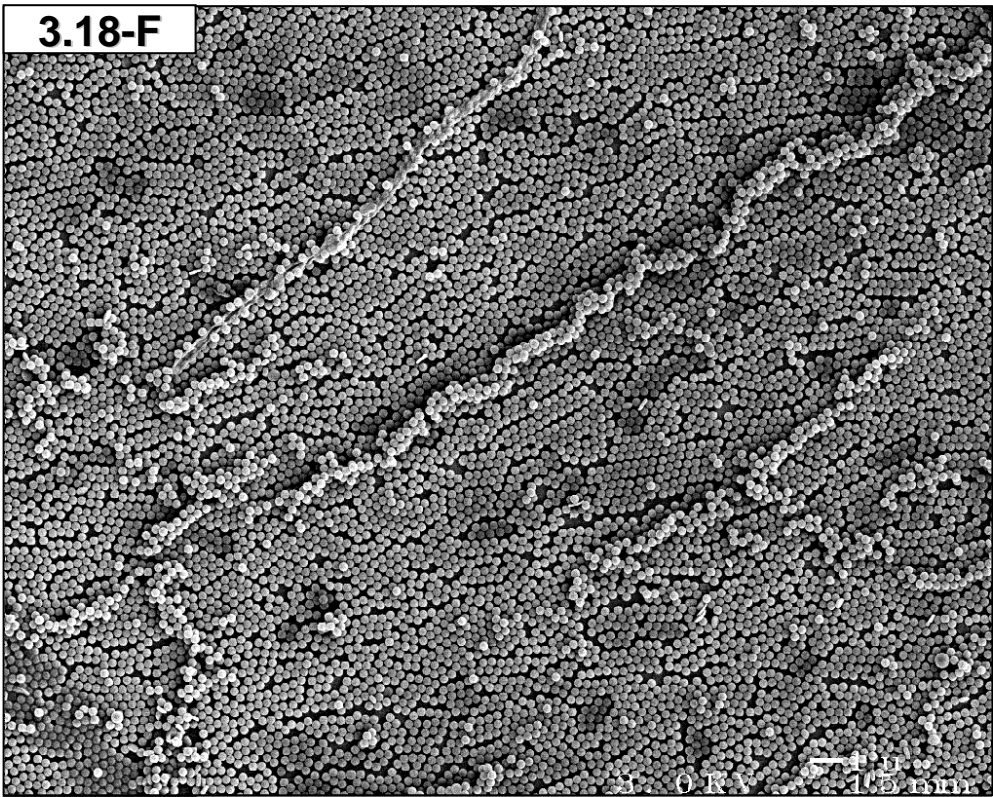
**Figure 3.18** *Native particle films of Imidazole 258 latex particles transferred by the LS method to mirror-finish stainless steel substrates on the second compression cycle. Transfers were performed at compression ratios of: (A) 0%, (B) 20%, (C) 40%, (D) 60%, (E) 80%, (F) 88%, and (G) cycle 3 at 40%. Scale Bars: 1  $\mu$ m.*







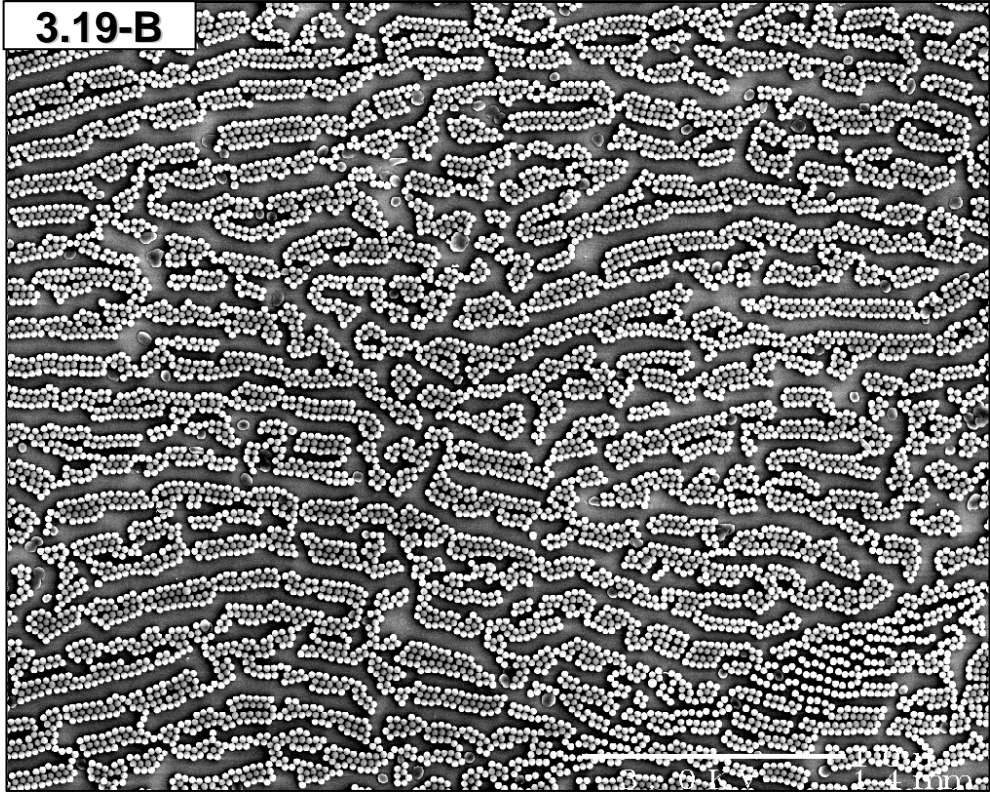
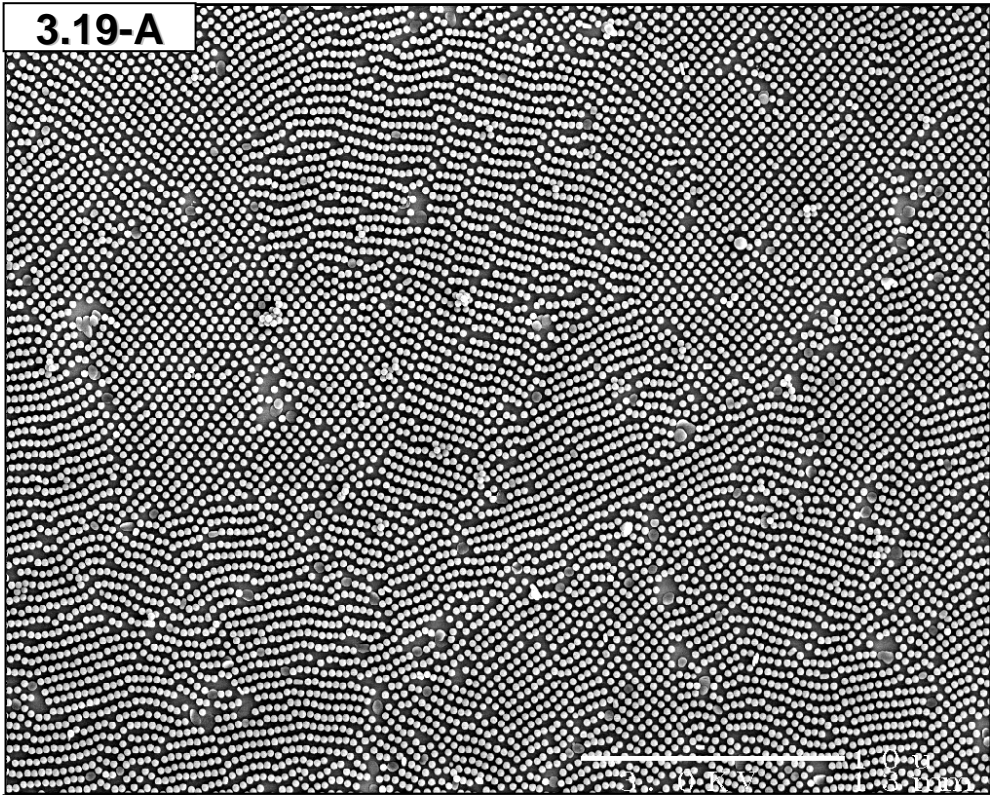




diffraction coloration. This macroscopic change in appearance was caused by a change in the microstructure of the transferred particle film. Both LB and LS transfers were performed to these substrates, and substrates bearing SAMs derived from SPTCS were used as a control. For the LB experiment, the vortex compression method was used with a sample of 0.2 wt % latex. The latex interface was refreshed before every deposition by sonicating for 1 s and vortexing for 5 s. Transfers were performed using the first-generation dipper at a rate of 11.8 mm/s. The strength of the particle-octadecylsiloxane interaction was insufficient to overcome the effect of lateral capillary forces during drying. In this manner, adjacent particle lines, like those observed on the SPTCS-treated control substrate, were squeezed together to form the thick-line patterns seen on the OTS-treated substrate in **Figure 3.19**. In addition, LS transfer experiments were performed using both OTS- and SPCTS-treated substrates with 0.2 wt % latex in the mechanical trough. A substrate holder was made so that two samples could be simultaneously brought into contact with the surface film in an LS geometry at a rate of 13.6 mm/s, using the second-generation mechanical dipper. Samples A and B, shown in **Figure 3.20**, were taken in tandem at a surface pressure of approximately 2.5 mN/m. Once again the particles rearranged to form small rafts of HCP monolayer separated by voids. Samples C and D were taken in tandem at a surface pressure of approximately 27 mN/m. When the transfer occurred at high surface pressure, the SPTCS and OTS samples appeared more alike because there was very little free area to allow the particles to rearrange. This set of experiments highlight the crucial role of the substrate surface charge in preserving the original ordered state of the particle array.

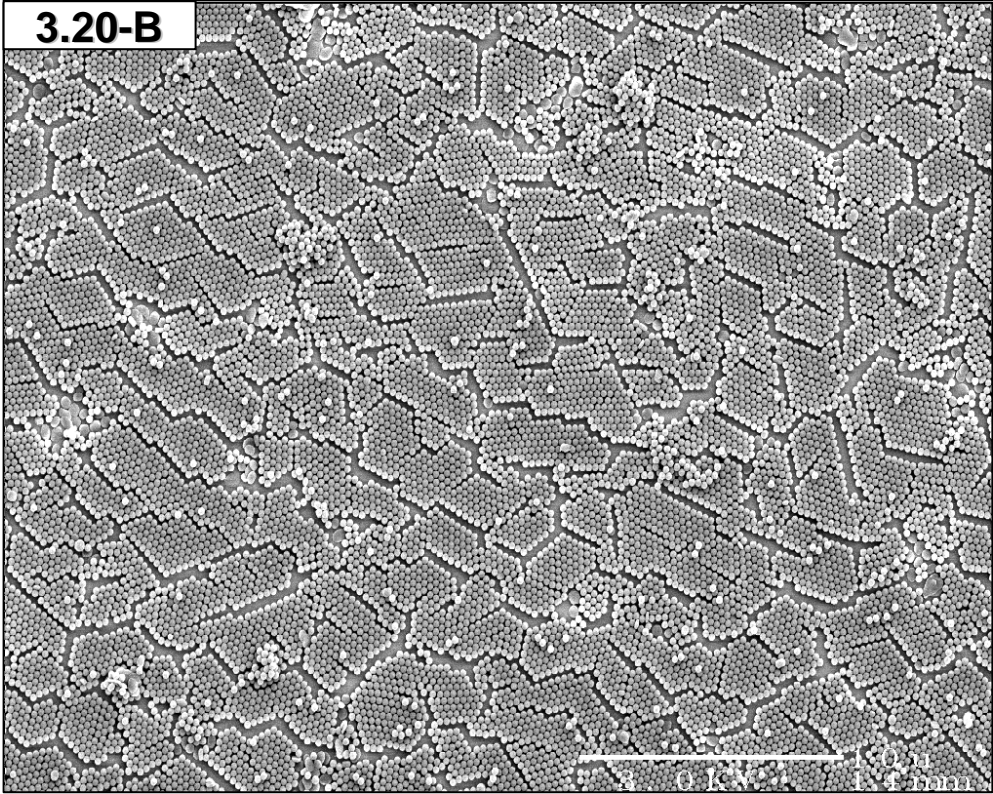
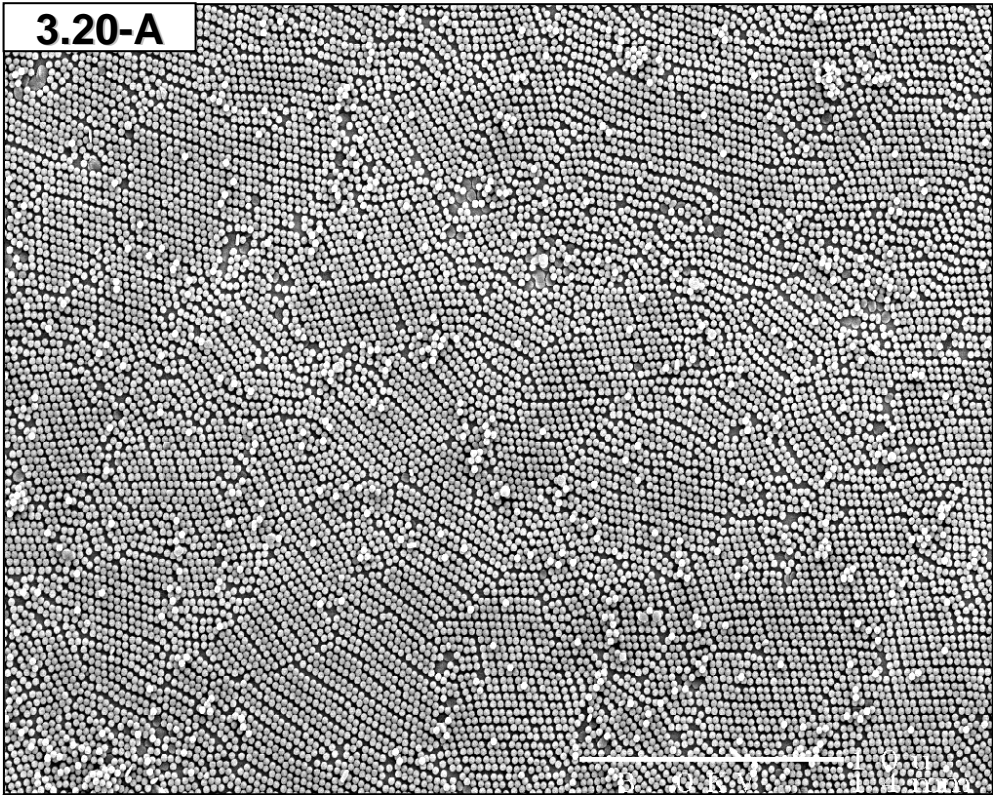
**Figure 3.19** *Substrate-dependent LB depositions.* Native particle film on a sample of 0.2 wt % Imidazole 258 latex prepared by the vortex compression method. Transfers were performed at a rate of 11.8 mm/s onto (A) negatively-charged SPTCS-treated and (B) non-charged OTS-treated SAM substrates. The OTS-treated surface allowed the particles to rearrange. Scale Bars: 10  $\mu\text{m}$ .

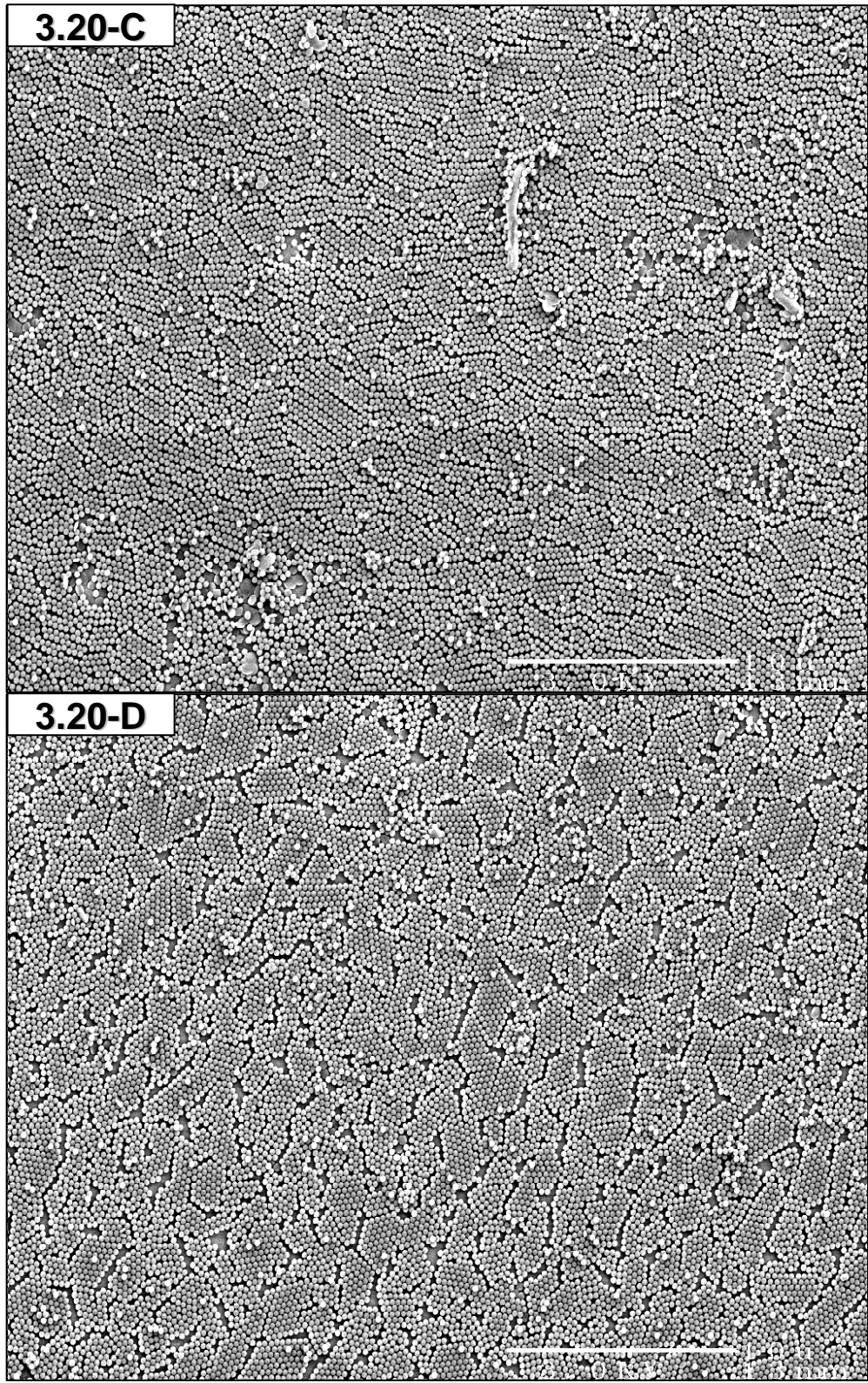






**Figure 3.20** *Surface-pressure- and substrate-dependent LS transfers. Samples were transferred at (A) 2.5 mN/m on a SPTCS-treated silicon substrate, (B) 2.5 mN/m on an OTS-treated silicon substrate, (C) 27 mN/m on a SPTCS-treated silicon substrate, (D) 27 mN/m on an OTS-treated silicon substrate. Scale Bars: 10  $\mu$ m.*





**3.3.2.6 Particle Films Exposed to Shear Flow.** Distortion of particle monolayers trapped at an air-water interface has previously been reported by Stancik et.al.<sup>43</sup> In these studies, 3- $\mu\text{m}$  polystyrene particles were placed at a water-decane interface, and the resulting HCP particle lattice was subjected to shear caused by two rotating belts in the plane of the interface. As a result, the crystal lattice between the belts deformed to accommodate particle motion. We have found that the LB transfer method also induces a crystal-lattice distortion of the interfacial particle array, resulting in a stretched appearance of the transferred pattern (i.e., **Figure 3.19-A**). The resulting particle pattern after LB transfer was heavily dependent on the original orientation of the precursor crystalline grains at the air-water interface with respect to the stretching direction. Although the patterns after LB transfer always had a similar appearance, it was difficult to distort the particle patterns in a quantitatively reproducible manner because of the limited individual crystalline grain size at the air-water interface. If the entire interface were covered by a single two-dimensional crystal, the orientation of the crystal could be measured non-destructively by laser diffraction, and the dipping direction could be reproducibly aligned. However, because the particle pattern at the air-water interface was polycrystalline, with many grains at various orientations, the resulting pattern after transfer always comprised a variety of different deposition modes. In an effort to gain a degree of control on the distortion procedure, the effect of varying both the transfer rate and angle were investigated.

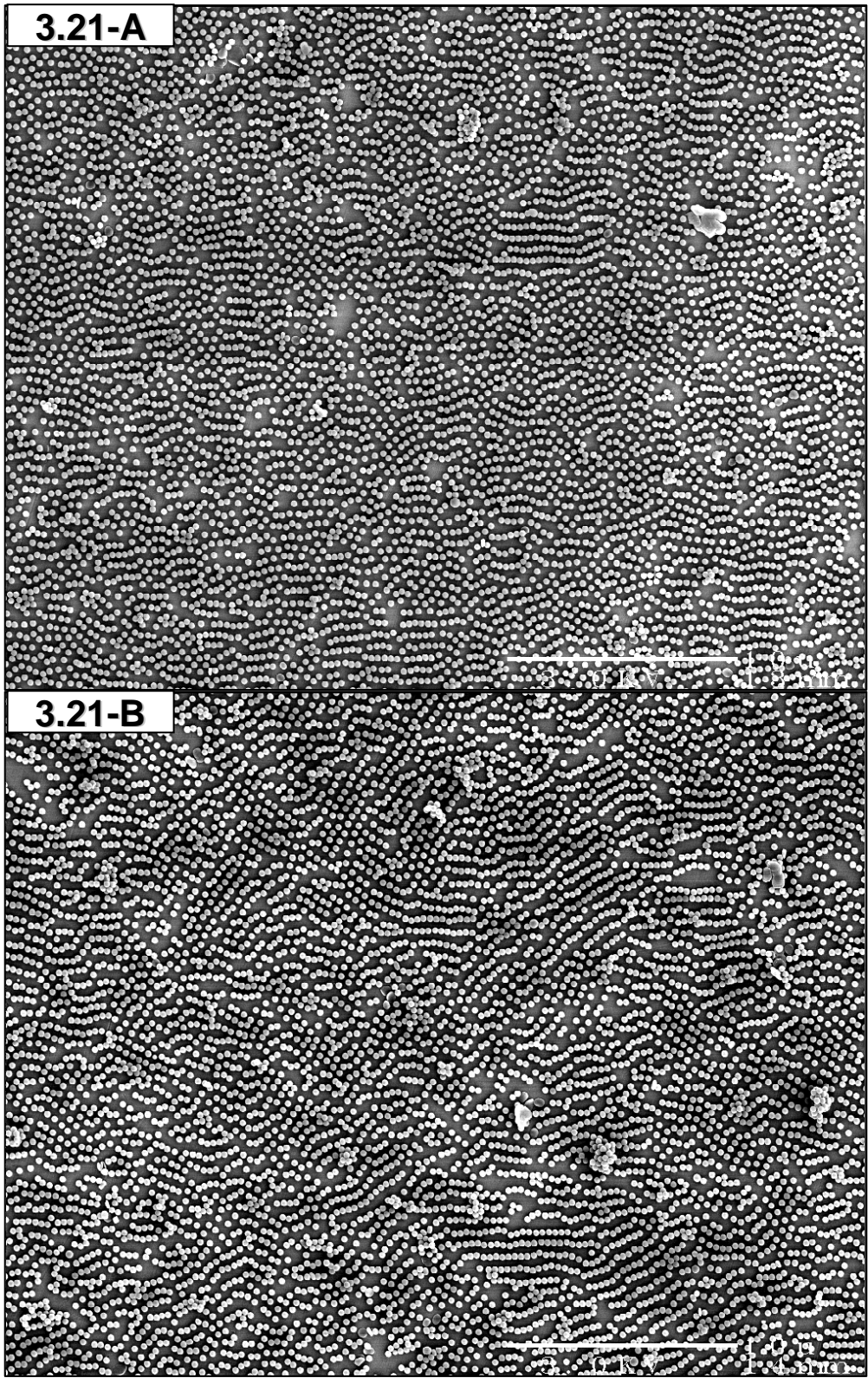
Several experiments were performed to investigate the effect of varying the dipping rate on the resulting pattern of transferred particles. Approximately 30 mL of

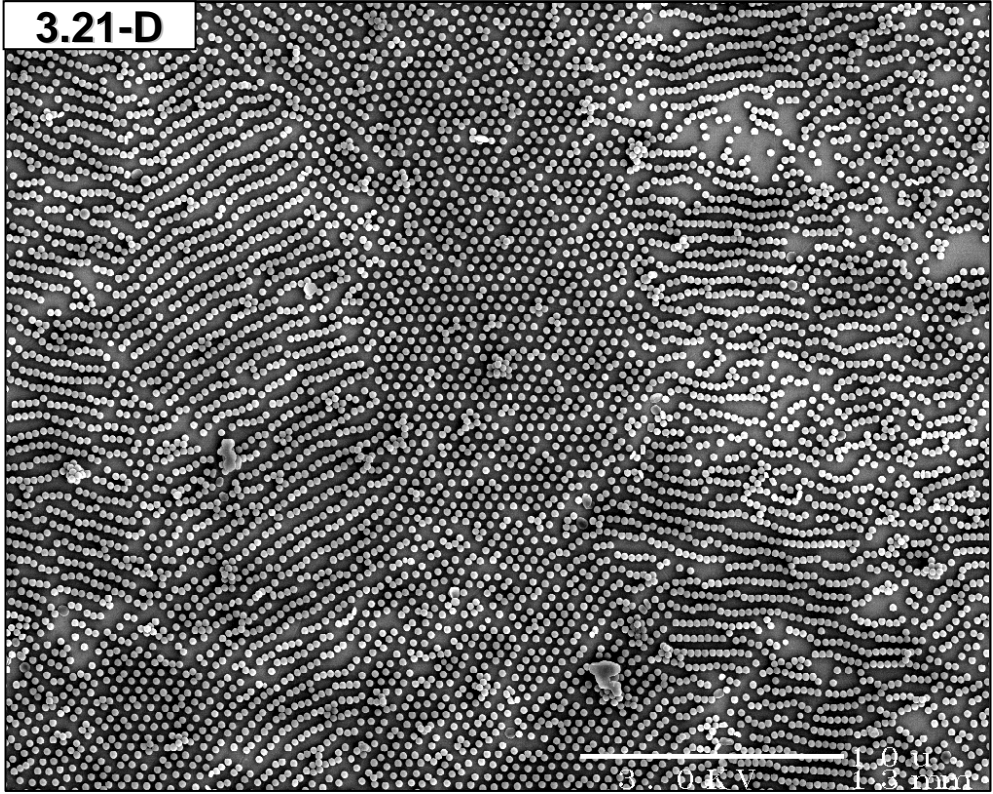
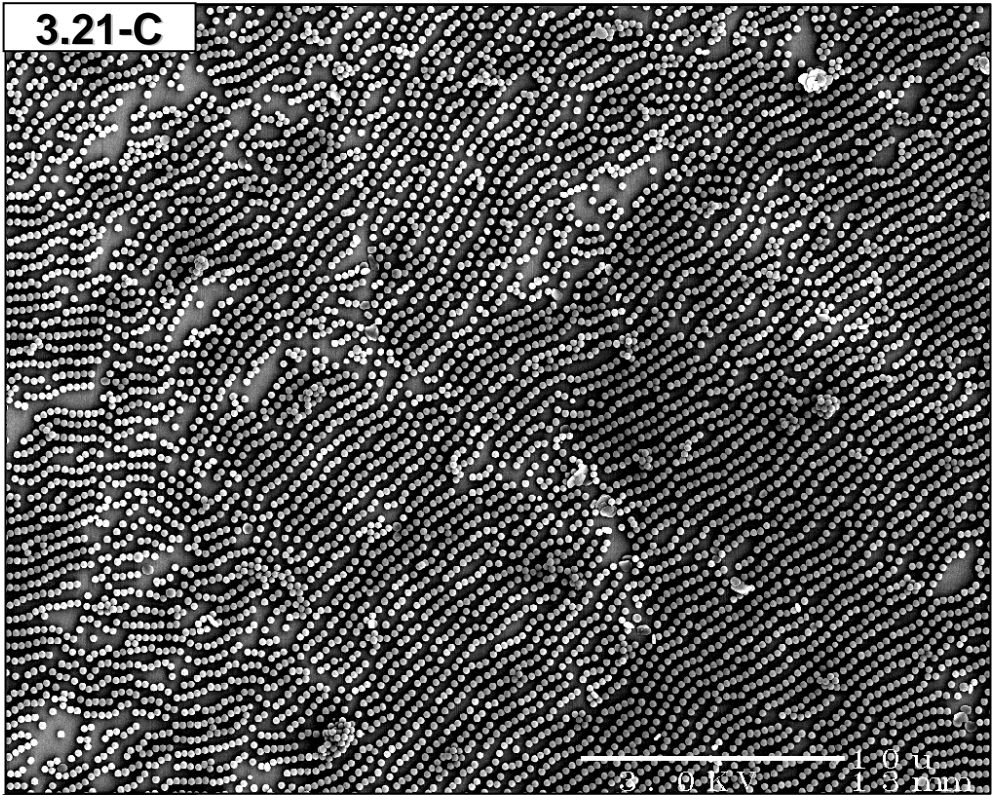
0.2 wt % Imidazole 258 latex were placed into the manually operated trough. The area of the native surface film was compressed by 60 and 80 % and LB transfers were performed onto stainless steel substrates at rates of 3.3 mm/s and 6.3 mm/s using the second-generation dipper. The grain-like patterns in **Figure 3.21-A** through **-D** are much more pronounced at the faster transfer rate for both compression ratios. The faster rate caused a higher degree of stretching along the dipping direction (the vertical axis of each micrograph). Additionally, it is evident that the higher compression ratio results in a more regular grain-like pattern, and that the most uniformly distorted patterns are likely formed from fully compressed HCP monolayers. In a partially disordered area of the 80%-6.3 mm/s transferred film, a section of HCP monolayer transferred intact while part of the same grain was stretched into a distorted pattern (**Figure 3.22**). This micrograph gives valuable insight into the pattern distortion mechanism. The {10} particle lines (see **Appendix B, Figure B.2**) in the original HCP array become separated and stretched apart in the dipping direction by forces during the LB-transfer process. The final pattern after transfer is highly dependent on the original orientation of the lattice with respect to the dipping (or stretching) direction.

Several experiments were also performed to investigate the effect of varying the dipping angle on the resulting pattern of transferred particles. The hypothesis was that decreasing the dipping angle would increase the degree of pattern distortion. The area of the native surface film on a sample of 0.2 wt % Imidazole 258 latex was compressed by 60 and 80 %, and samples were transferred to stainless steel substrates at an angle of incidence of 60° and a rate of 6.3 mm/s using the second-generation dipper. The

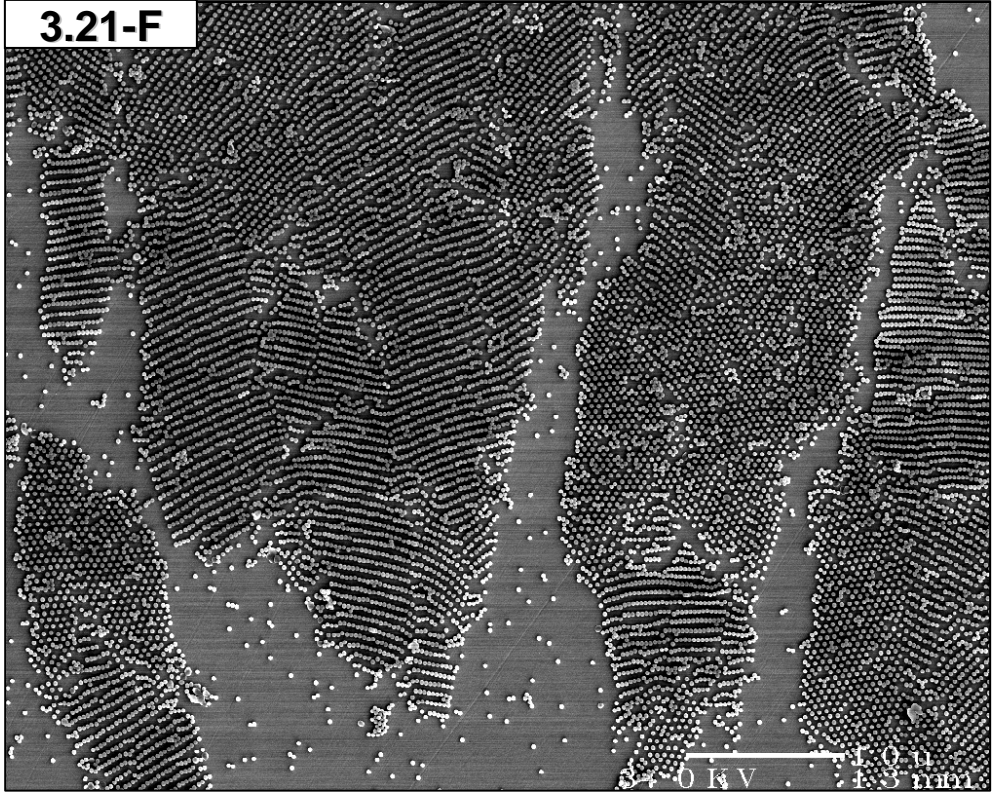
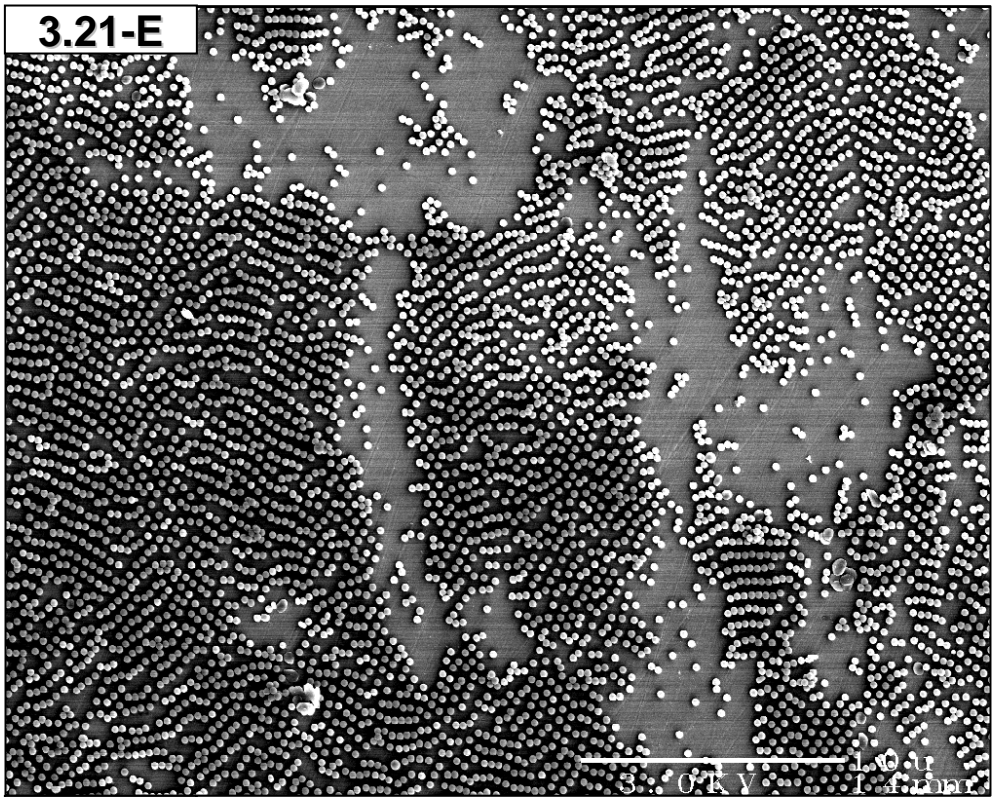
**Figure 3.21** *Angle- and rate-dependent transfer.* Native surface films on a sample of 0.2 wt % Imidazole 258 latex transferred to stainless steel substrates using the manual trough and the second generation-dipper. Parameters are given in the order of dipping angle, compression ratio, and dipping rate: (A) 90°, 60%, 3.3 mm/s; (B) 90°, 80%, 3.3 mm/s; (C) 90°, 60%, 6.3 mm/s; (D) 90°, 80%, 6.3 mm/s; (E) 60°, 60%, 6.3 mm/s; and (F) 60°, 80%, 6.3 mm/s; Scale Bars: 10  $\mu$ m.











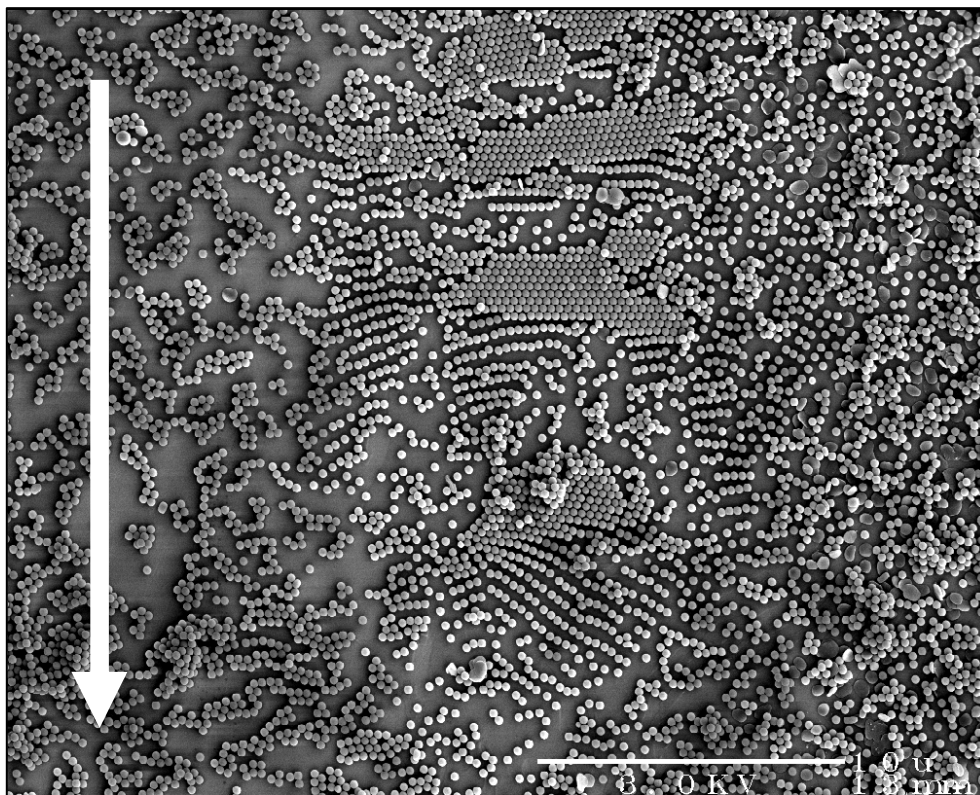


**Figure 3.22** *Region of HCP monolayer partially distorted during the LB deposition process. This SEM micrograph demonstrates how regions of HCP monolayer at the air-water interface are stretched into a distorted pattern. Langmuir-Blodgett transfer at an 80 % compression ratio onto a stainless steel substrate at 6.3 mm/s. The arrow denotes the dipping direction. Scale Bar: 10  $\mu\text{m}$ .*

resulting patterns are shown in **Figure 3.21-E** and **-F**. The 60° angle of entry caused some of the grains to separate at the grain boundaries leaving bare substrate in between. The effect was more pronounced at the 80% compression ratio when compared with the 60% compression ratio. Even though a higher degree of pattern distortion was achieved by decreasing the dipping angle to 60°, the slippage induced along the grain boundaries resulted in a loss, rather than a gain, in control over the patterning process.

**3.3.2.9 Native Particle Films on the Imidazole 391 Latex.** A series of experiments were carried out to investigate if native surface films on the Imidazole 391 latex could be successfully transferred to mirror finish stainless steel substrates. The system was expected to behave very similarly to the Imidazole 258 case because the surface chemistry of the particles was identical. Surface pressure-area isotherms of the native surface film on a sample of 0.2 wt % latex were collected using the manual trough (**Figure 3.23**). This system did not show a solid phase transition on the initial compression cycle, however, after surface film enrichment by bubbling nitrogen through the bulk latex, the transition was observed. Both LB and LS transfers were performed at various compression ratios. The LB transfers were performed using the first-generation dipper at a rate of  $22.1 \pm 0.5$  mm/s, and the LS transfers were performed manually. Surprisingly, only at compression ratios at or above 80% was any obvious ordering observed, and no significant difference was noted between the LB and LS cases. A micrograph of a region of the LS sample transferred at a compression ration of

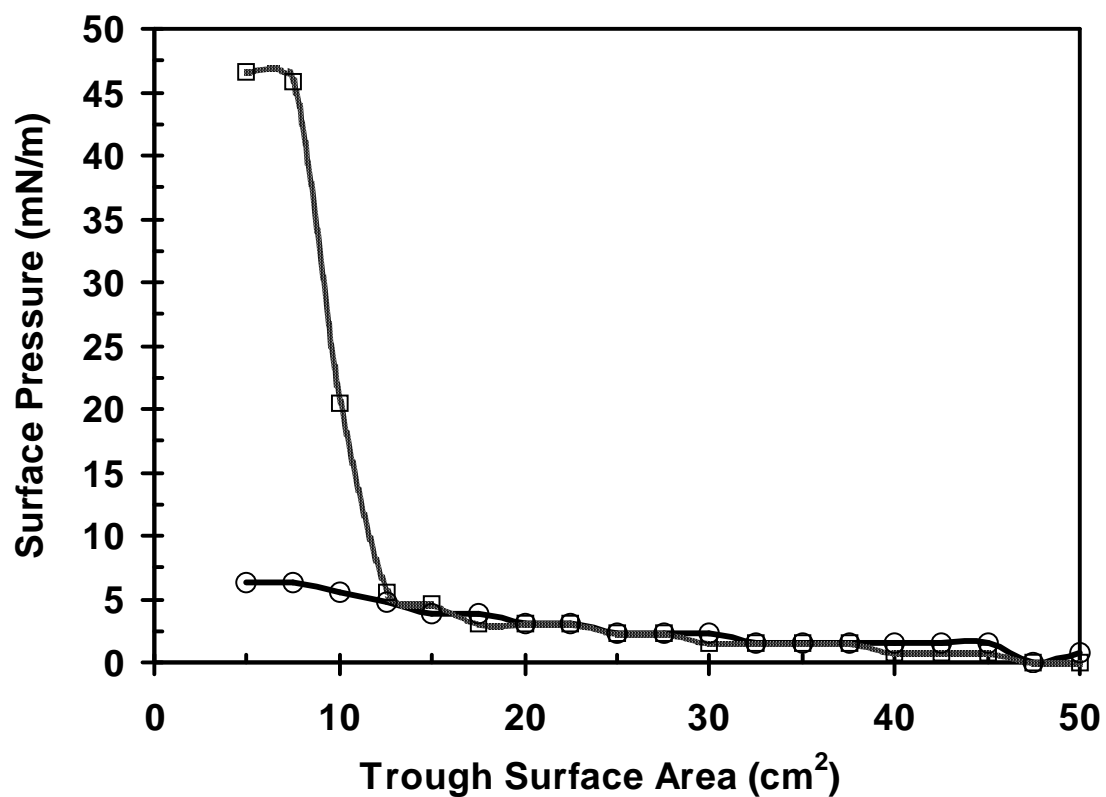


**Figure 3.23** *Surface pressure-area isotherms for the native surface film on a sample of 0.2 wt % Imidazole 391 latex. (○) Isotherm resulting from the compression of the native surface film. (□) Isotherm after surface film enrichment by bubbling nitrogen through the suspension. Data were collected using the manual trough.*

88% is shown in **Figure 3.24**. The native surface film on the Imidazole 391 latex was much less dense than that on the Imidazole 258 latex.

### **3.3.3 Problems with the Native Film System**

Pressure-area isotherms of native films on the Imidazole 258 latex were not reproducible. In spite of identical sample preparation and isotherm acquisition techniques, repetitive experimental trials always yielded unique isotherms. Even though the isotherms were typically superimposable by a shift in compression ratio, it was not possible during an experiment to predict where a solid transition would occur. As a result, performing reproducible pattern transfers proved to be difficult. The main problem with this system is that the number of particles at the interface is unknown and variable. After the isotherm was recorded, the number of particles that were at the surface can be calculated using the assumption that the solid transition occurs when the particles at the surface form a full HCP monolayer. However, since this is a destructive measurement technique, subsequent quantitative compression cycles and transfers cannot be performed.

Even though negatively charged sulfate latexes are stable in alcohol suspension, imidazole, amine, and pyridine functionalized latexes that are quite stable in aqueous media were not stable in alcohols. In fact, even if only a few percent of alcohol were added to the aqueous suspension, the Imidazole 258 latex coagulated and precipitated after several hours. For this reason, it was impossible to spread a known amount of the

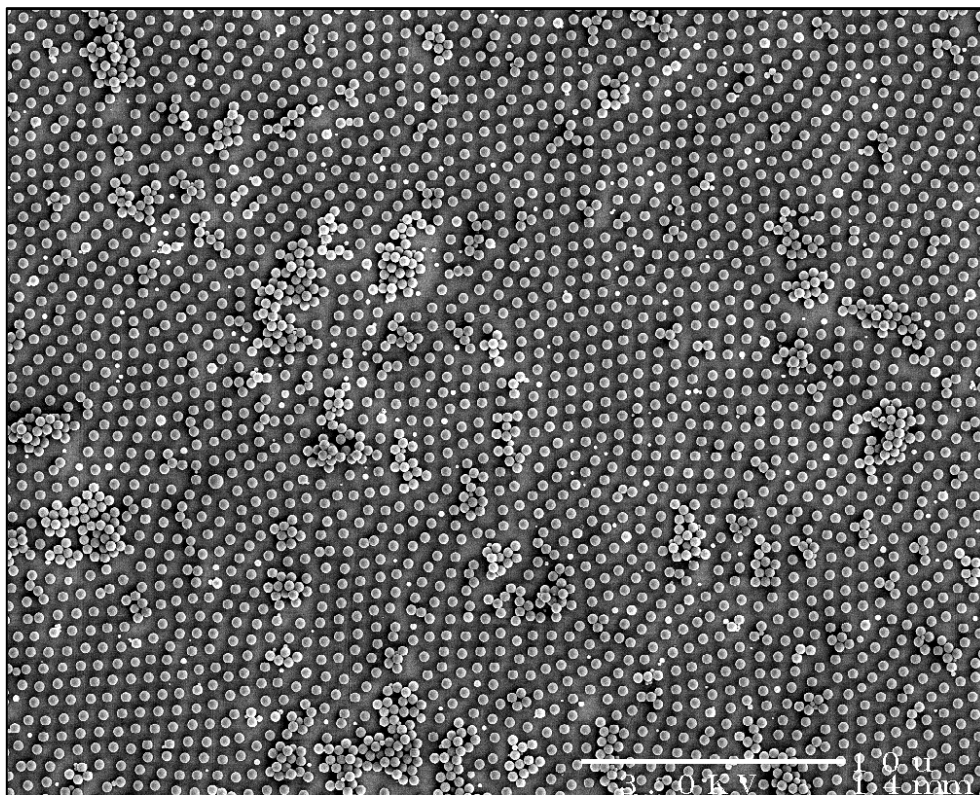


**Figure 3.24** *LS transfer of the native surface film on a sample of 0.2 wt. Imidazole 391 latex to a mirror finish stainless steel substrate. In spite of multiple clusters, the hexagonal motif is readily observable. Scale Bar: 10 μm.*

positive particles at a clean air-water interface in the traditional Langmuir-trough fashion.

Surface pressure-area isotherms for the negatively charged Sulfate 128 and 290 latexes were attempted, however no isotherm features were observed before or after the bubble enrichment process. These latexes, for some reason, have a low tendency to entrap native surface particle films. It may be that the particle-interface contact angles were very low and therefore the particles were able to move away from the surface during compression. These experiments underscore that some particles are much more highly surface active than others.<sup>15</sup>

#### **3.3.4 Deposited Particle Films**

As a result of the difficulties associated with the native particle film systems, the focus of our research shifted to the transfer of particle films deposited at a clean air-water interface. As mentioned in the background section, a variety of studies have previously investigated the interfacial behavior of negatively-charged sulfate functionalized latex particles at such interfaces. This literature provided a valuable starting point for continuing our research. Highly negatively-charged, sulfate-functionalized latex particles with an average diameter of 2.7  $\mu\text{m}$  (Sulfate 2700 latex), were purchased from Interfacial Dynamics Corporation. This latex was chosen because it is quite similar to several latexes used previously in the literature, thereby providing the ability to compare experimental results directly. One of the most important benefits of using sulfate-based latexes was the ability to use alcohols as spreading solvents. This

feature allowed the placement of precisely known amounts of particles at the interface. From the viewpoint of choosing an interface that allows optimal formation of non-continuous HCP particle arrays, the choice should be the oil-water interface as opposed to the air-water interface because charged particles have been shown to experience stronger electrostatic repulsions at the oil-water interface than at the air-water interface.<sup>12</sup> Unfortunately, all attempts to transfer particles at the *n*-octane-water interface to TDAC- or TBAC-modified silicon substrates failed, possibly because a layer of octane adsorbed to the substrate surface preventing the particle film from properly contacting the substrate. As a result, all further investigations were focused on finding a way to successfully use the air-water interface.

**3.3.4.1 Spreading Considerations.** The spreading of one liquid on another can be quite a turbulent process.<sup>44</sup> In the case of alcohol spreading at an air-water interface, local alcohol concentration variations, temperature fluctuations due to alcohol evaporation, and local changes in interfacial curvature all contribute to the observed interfacial turbulence. This behavior is an example of the Marangoni effect.<sup>45</sup> Initial experiments with the Sulfate 2700 latex were carried out by the drop wise addition of known amounts of particles suspended in isopropyl alcohol to a clean air-water interface. As soon as a drop would contact the interface, it would rapidly expand and compress the previously deposited surface film toward the perimeter of the trough. Particle multiplets and small clusters were likely formed during the compression resulting from this poorly controlled spreading. In order to test this hypothesis, the



spikes in surface pressure during these compressive events were measured. An 85-mm polystyrene Petri dish was filled half full with DI water, and the Wilhelmy plate surface pressure sensor was placed so that the plate was about 1 cm from the edge of the dish. Drops of 3.0 wt % Sulfate 2700 latex in IPA were added to the interface while measuring the resulting spikes in surface pressure. In a parallel control experiment, drops of pure IPA were added to the interface while monitoring the surface pressure. The drop-wise addition of pure IPA to the interface resulted in surface pressure spikes of 5 mN/m while addition of 3 % suspension in IPA resulted in pressure spikes in excess of 25 mN/m (**Figure 3.25**). In addition, it is likely that local areas of even higher surface pressure exist at the interface during spreading, which could easily account for the clusters observed at the interface after deposition by this method. To avoid this problem, the particle suspension was deposited at the air-water interface slowly *via* a syringe pump with the needle in contact with the interface. Although the surface pressure still slowly increases with the addition of more particles to the interface, the increase is quite smooth with no pressure spikes. A marked decrease in the number of clusters and multiplets at the interface was observed when using this deposition process. Since multiplets typically initiate pattern defects and grain boundaries, the overall order of the resulting patterns was greatly increased by using this deposition process.

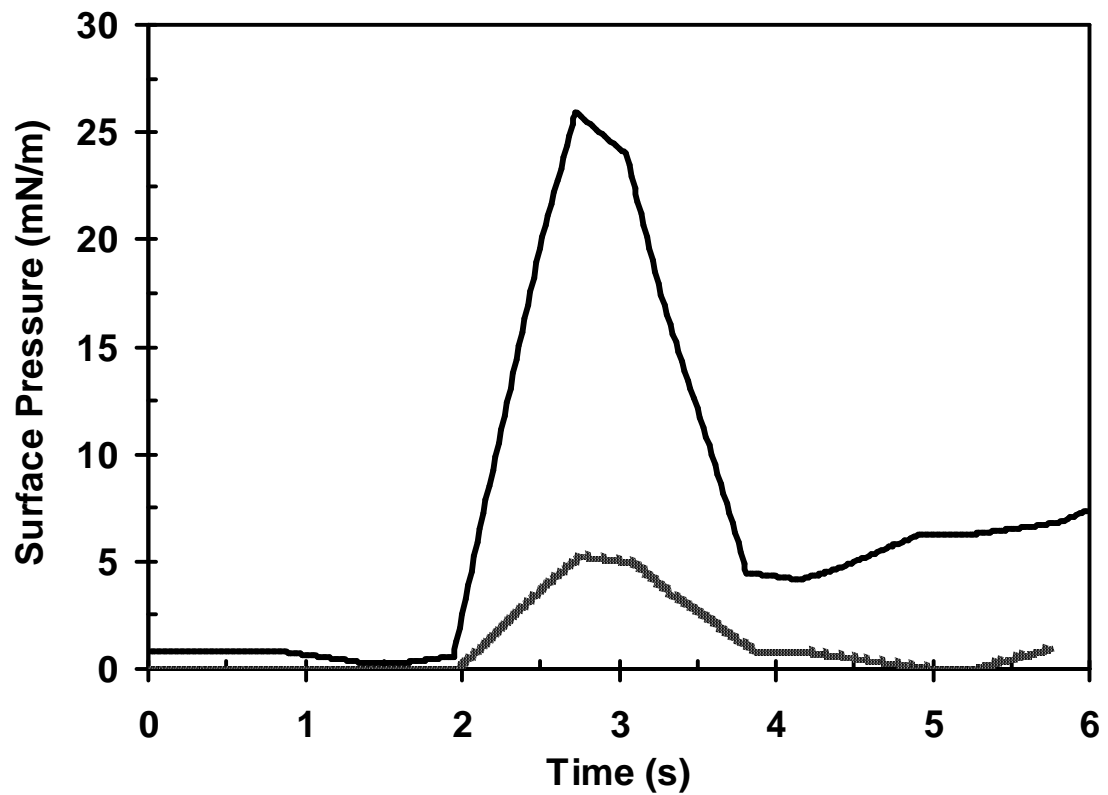


**Figure 3.25** *Increase in surface pressure upon drop-wise addition of IPA and suspensions in IPA. One drop of isopropyl alcohol (shaded) and one drop of a 3.0 wt % suspension Sulfate 2700 latex in isopropyl alcohol (solid) added at  $t = 2s$ . The particles had a pronounced effect on the initial spike in surface pressure.*

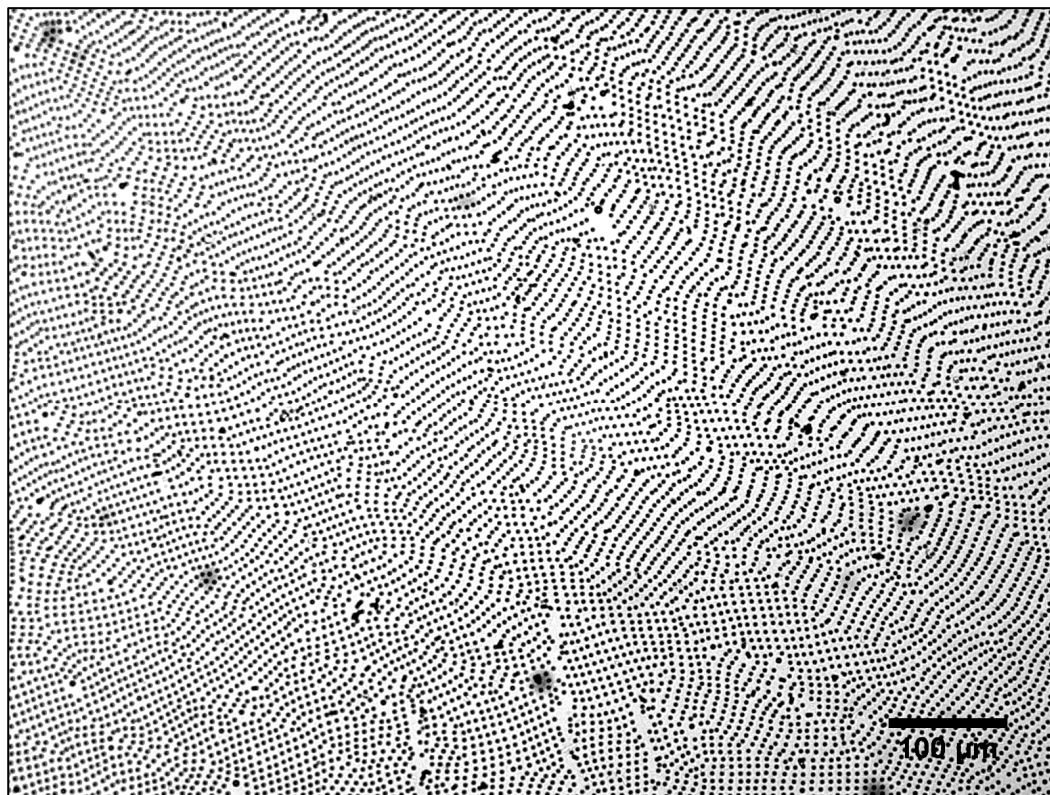
#### **3.3.4.2 Contact Angle Measurements at the Particle-(Air/Water) Interface.**

The particle-interface contact angle is a very important parameter for understanding and controlling the magnitude of particle interactions at an interface.<sup>12, 15, 46</sup> Qualitatively, the most highly ordered particle systems observed were those that had a nearly equatorial particle-interface contact line. Obviously, the magnitude of inter-particle repulsion is proportional to the amount of the particle surface exposed to the low dielectric medium. The highly ordered particle films discussed in **Section 3.3.4.6** were obtained from a system with a particle-interface contact angle of  $81 \pm 2^\circ$  (standard deviation, 11 measurements) as shown in **Figure 3.6**.

**3.3.4.3 Pattern Distortion Resulting from LB Transfers.** An 85-mm polystyrene Petri dish was half filled with deionized water, and 50  $\mu\text{L}$  of 3.0 wt % Sulfate 2700 latex in IPA was added to the interface *via* a syringe pump at a rate of 5  $\mu\text{L}/\text{min}$ . LB transfers were manually performed using TBAC-treated silicon substrates. Optical micrographs of the resulting patterns, shown in **Figure 3.26**, qualitatively appear quite similar to those of the Imidazole 258 latex patterns transferred by the LB method described in **Section 3.3.2.6** (above). The mechanism for pattern distortion discussed for the positive particles probably causes this pattern distortion as well.

#### **3.3.4.4 Composite Isotherm Construction Using the Mechanical Trough.**

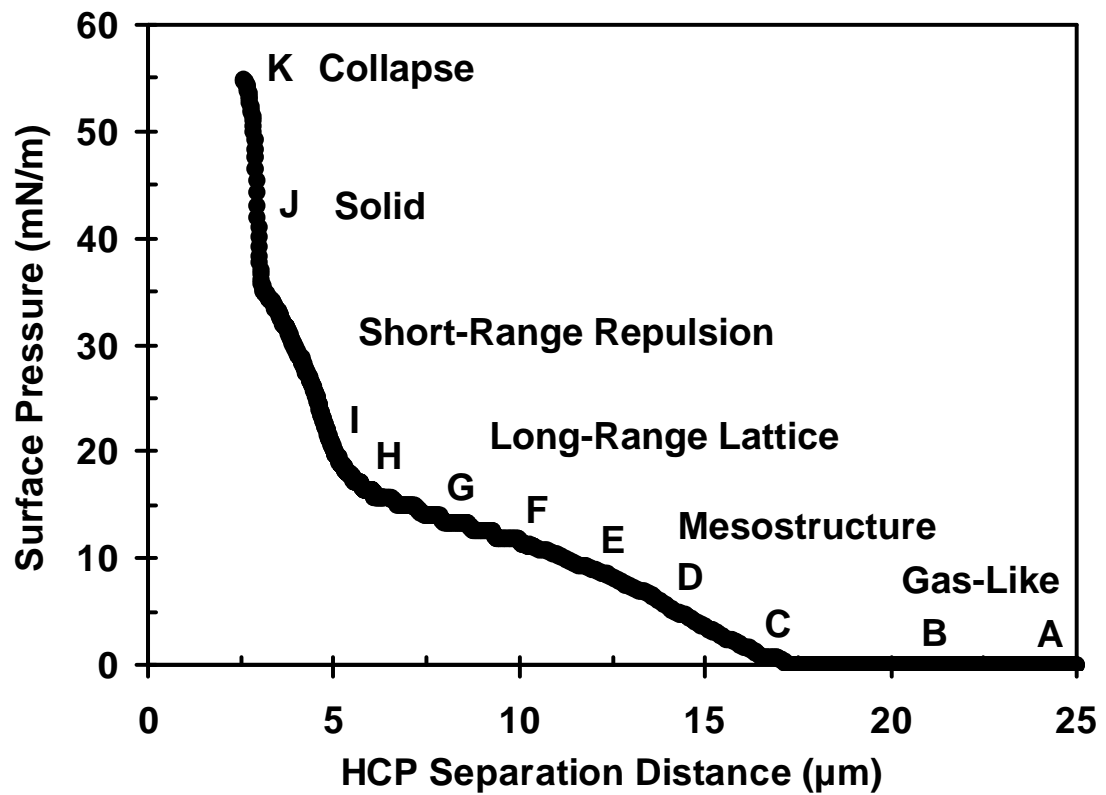
The maximum compression ratio for the mechanical trough was  $\sim 90\%$  because higher compression ratios interfered with the surface pressure-sensor. As a result, it was not



**Figure 3.26** *Optical micrograph of the distorted pattern that resulted from an LB transfer of a Sulfate 2700 latex film. The interfacial film was prepared by the constant-area compression method and was transferred manually to a TBAC-treated silicon substrate by the LB method. The resulting distorted pattern was quite similar to those observed with the Imidazole 258 latex system (i.e. **Figure 3.16-E** and **Figure 3.19-A**). Scale Bar: 100  $\mu\text{m}$ .*

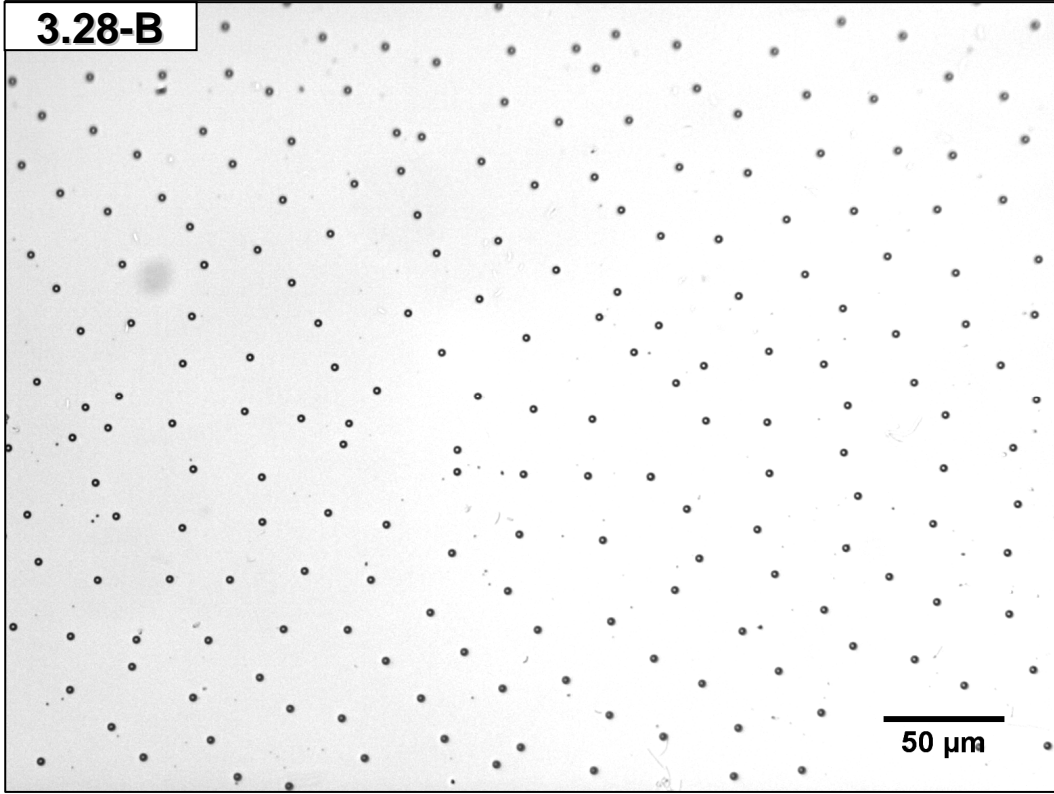
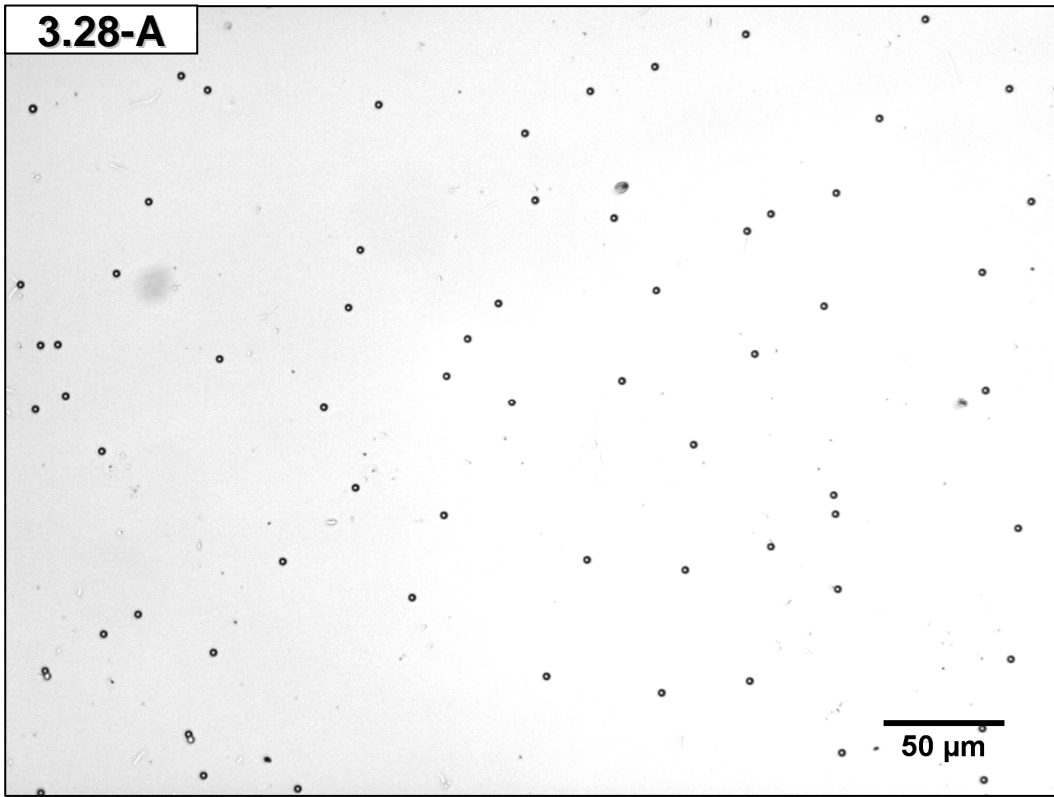
possible to record all of the two-dimensional phase transitions in a single compression cycle. In three separate experiments, 5, 20, and 80  $\mu\text{L}$  of 3.00 wt % Sulfate 2700 latex in IPA were deposited at a clean air-water interface at a rate of 5  $\mu\text{L}/\text{min}$  and the resulting interfacial films were compressed at a rate of 23  $\text{mm}^2/\text{s}$  (22.6 %/min). The resulting isotherms were overlaid by making small adjustments to the surface-pressure baseline for each plot. The complete surface pressure-area isotherm is shown in **Figure 3.27**. Each change in slope corresponds to a change in two-dimensional phase of the interfacial particle film. There are 6 main regions of the isotherm, the gas-like state, the mesostructure region, the long-range lattice region, the short-range repulsion region, solid close-packed monolayer, and the collapse region. The above procedure was repeated, and samples were taken by pausing the movable barrier and performing LS transfers to TDAC-treated silicon substrates at various positions on the isotherm.

**3.3.4.5 Isotherm Analysis.** The transferred patterns correlate nicely with the expected phase regions of the isotherm (**Figure 3.28**). All of the optical micrographs show the patterns after underwater LS transfers, as described in **Section 3.2.9.3**. Micrographs A and B demonstrate the typical surface structure in the gas-like region. Particles are randomly spread across the surface and do not interact with each other in a coordinated fashion. Micrograph C shows the surface structure at the gas-mesostructure phase transition, which could also be described as the *onset of interaction*, as this initial rise in the surface pressure marks the point at which the particles begin to interact in an organized fashion. A bit of disagreement is found in the literature concerning the

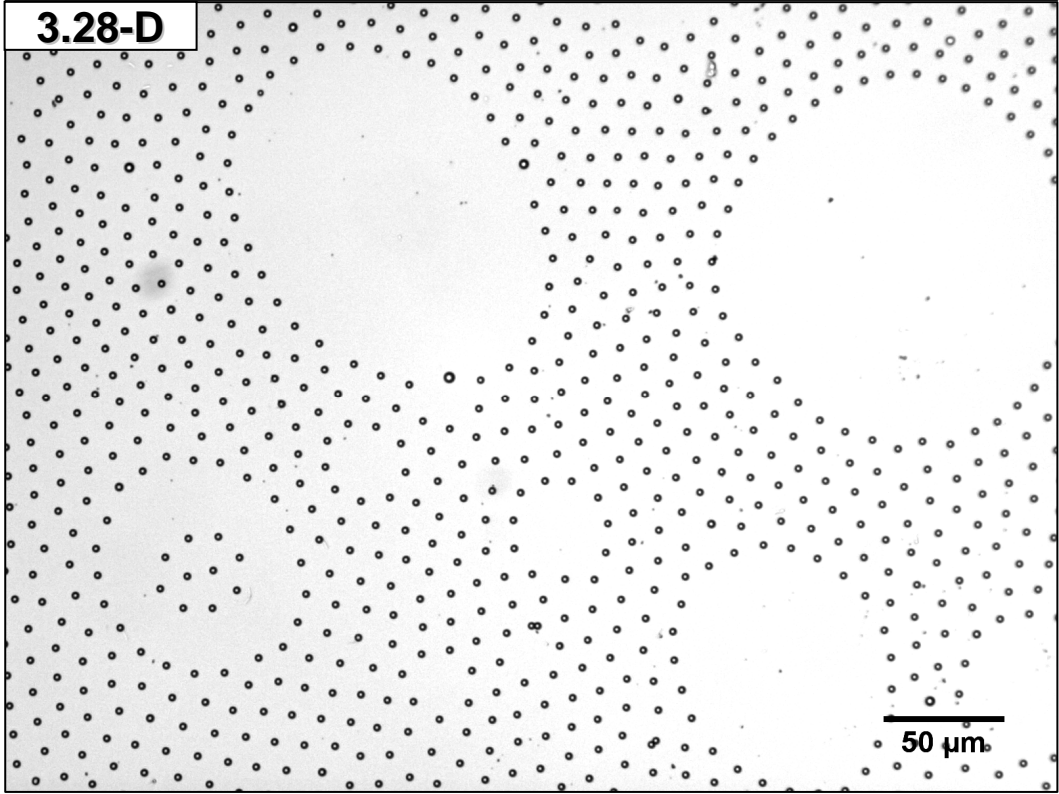
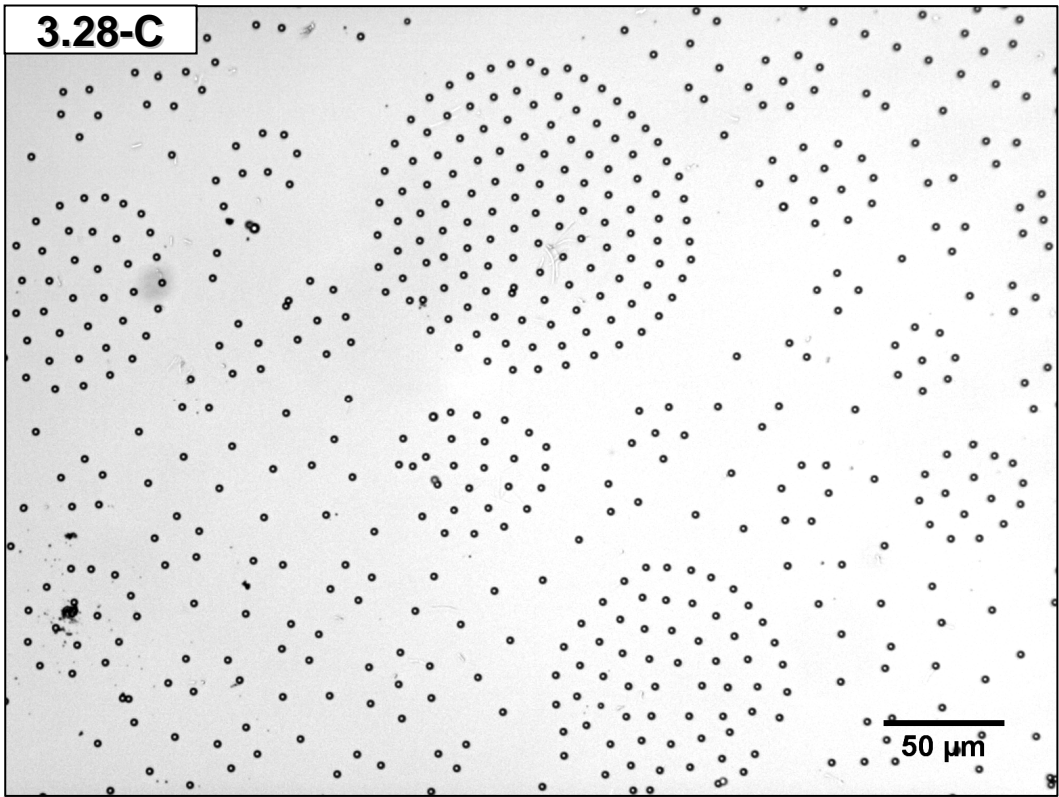


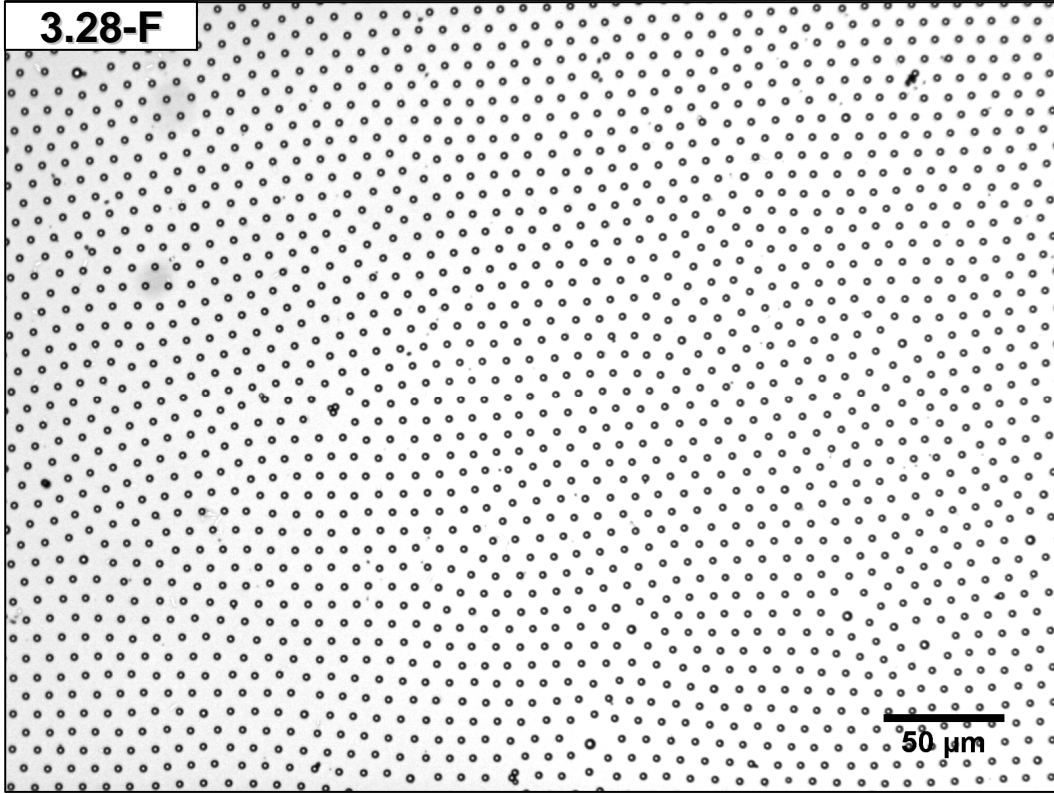
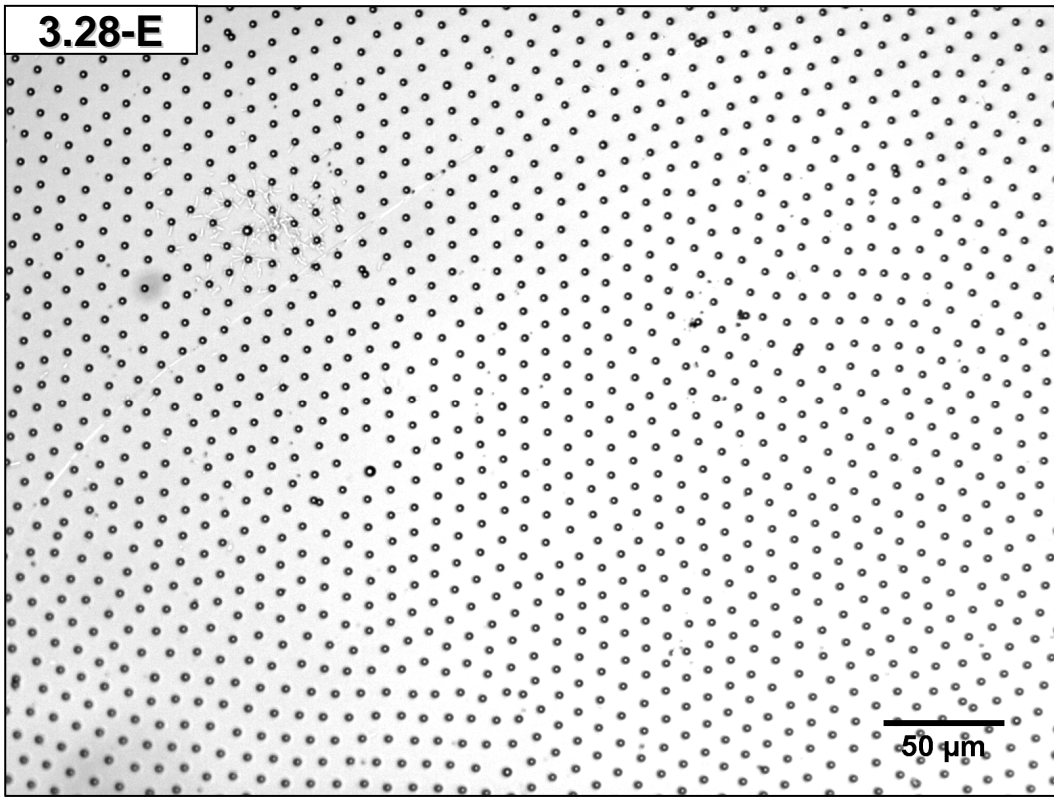
**Figure 3.27** *Surface pressure-distance isotherm for the Sulfate 2700 latex. The changes in isotherm slope correspond to changes in the two-dimensional phase of the film, as described in the text. The letters correspond to LS transfers that are shown in Figure 3.28.*

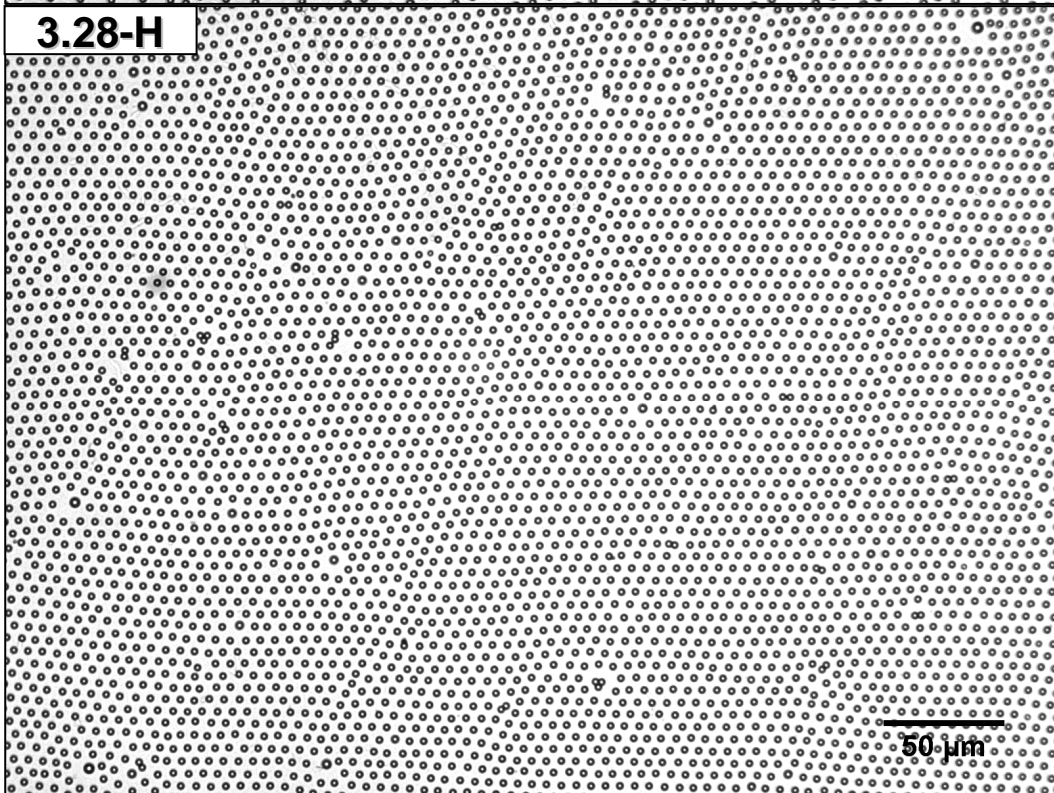
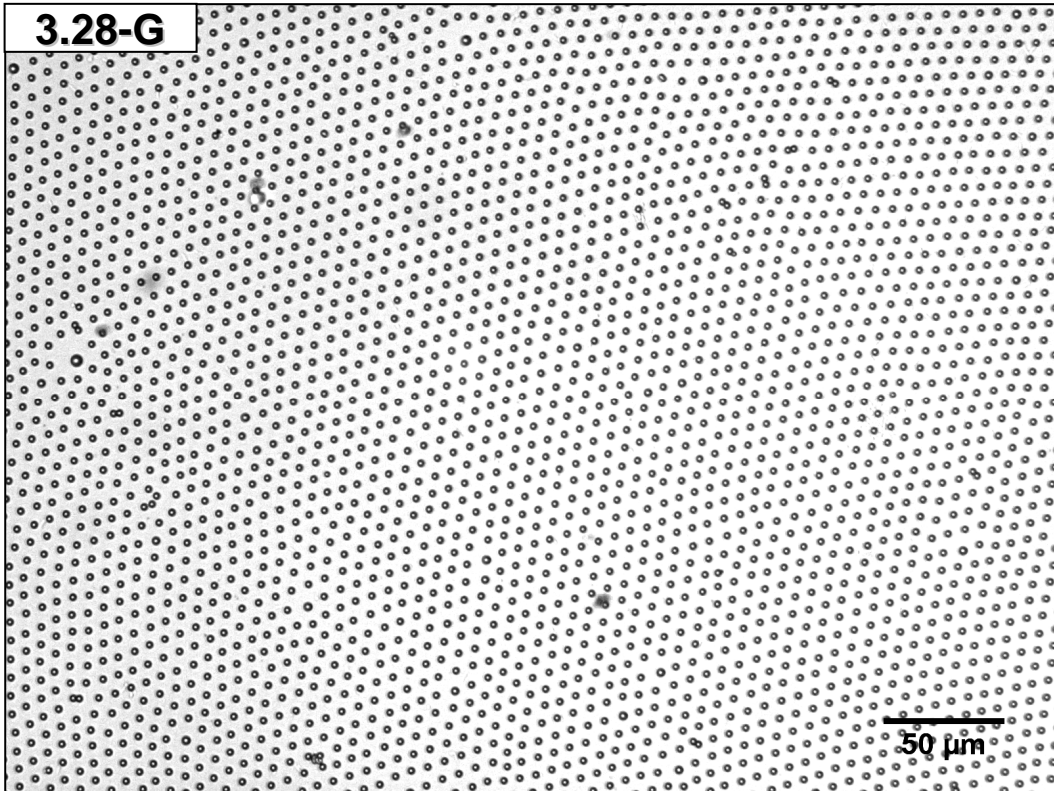
**Figure 3.28** *Isotherm-coordinated LS transfers.* The experiment from which the isotherm in **Figure 3.27** was produced was repeated, and manual LS transfers were performed using TDAC-treated silicon substrates at various stages. The transfers were performed at: (A) 0.0 mN/m, (B) 0.0 mN/m, (C) 0.7 mN/m, (D) 5.0 mN/m, (E) 9.0 mN/m, (F) 11.7 mN/m, (G) 14.0 mN/m, (H) 16.4 mN/m, (I) 17.6 mN/m, (J) 41.3 mN/m, and (K) 55.0 mN/m. The sample shown in micrograph (L) was transferred after re-expansion of the collapsed film. Scale Bars: 50  $\mu\text{m}$ .





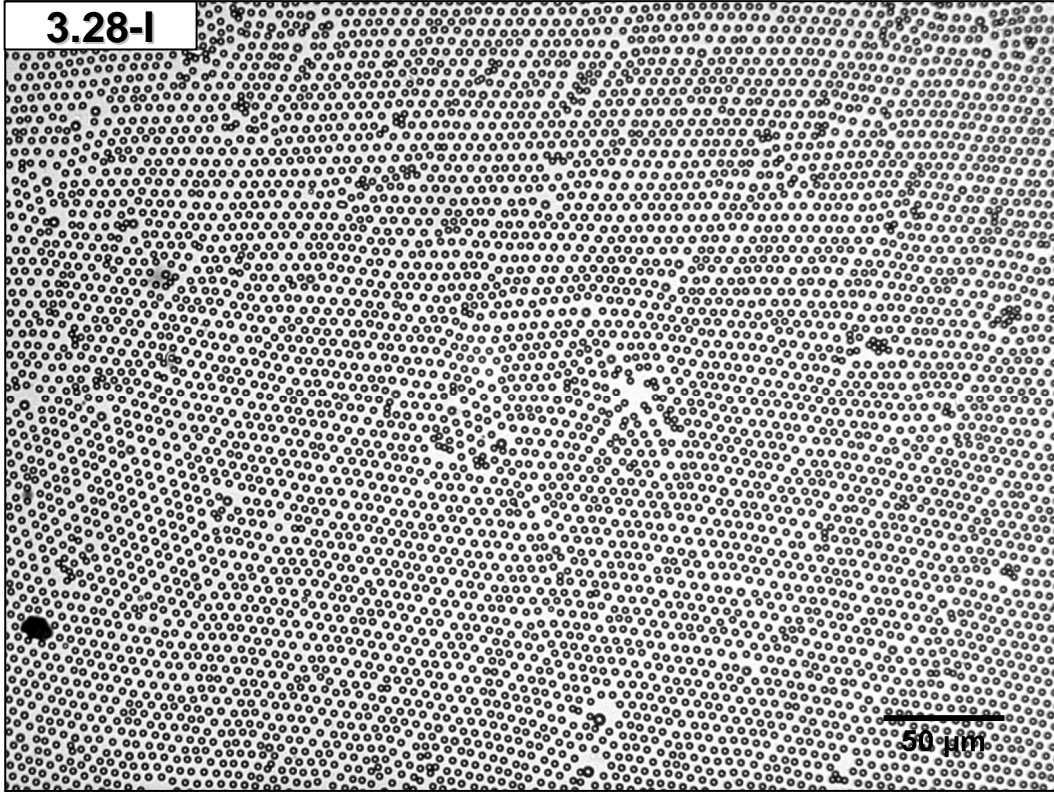




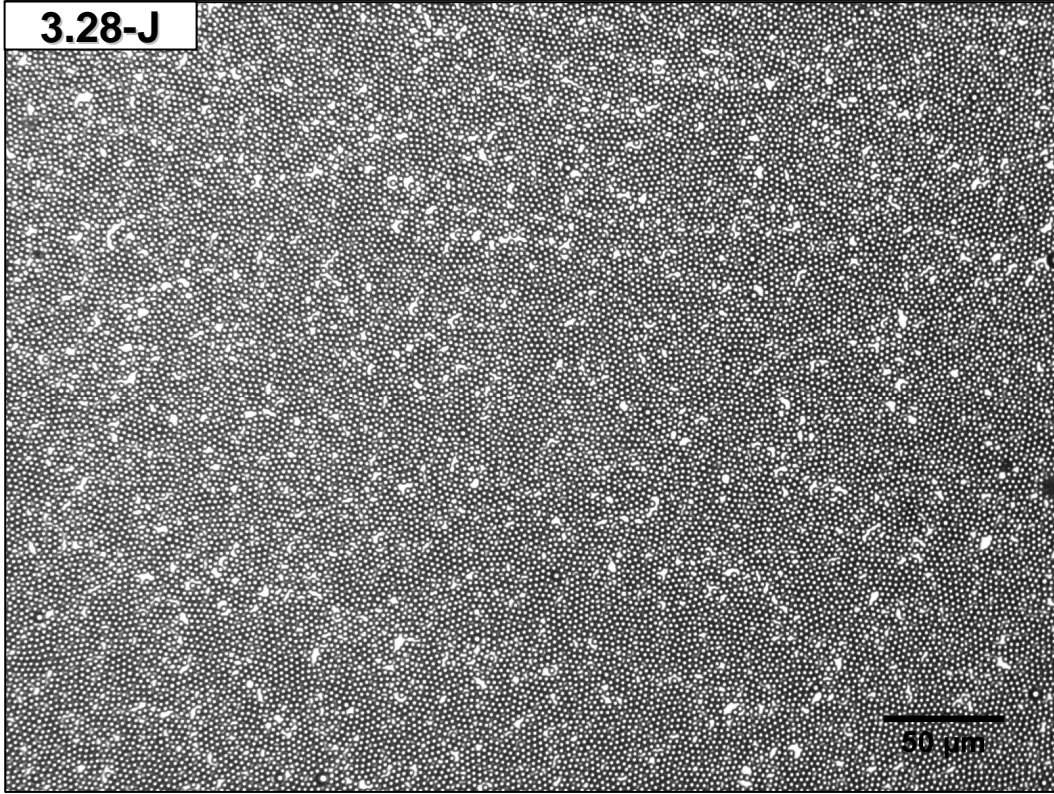


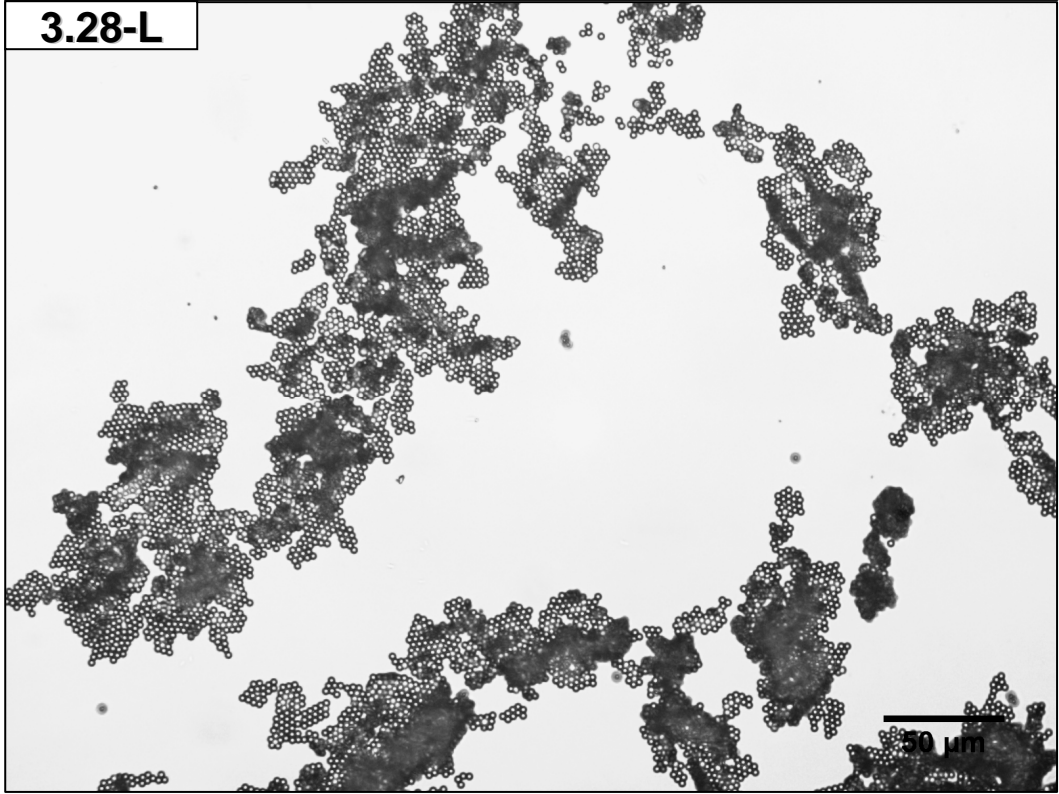
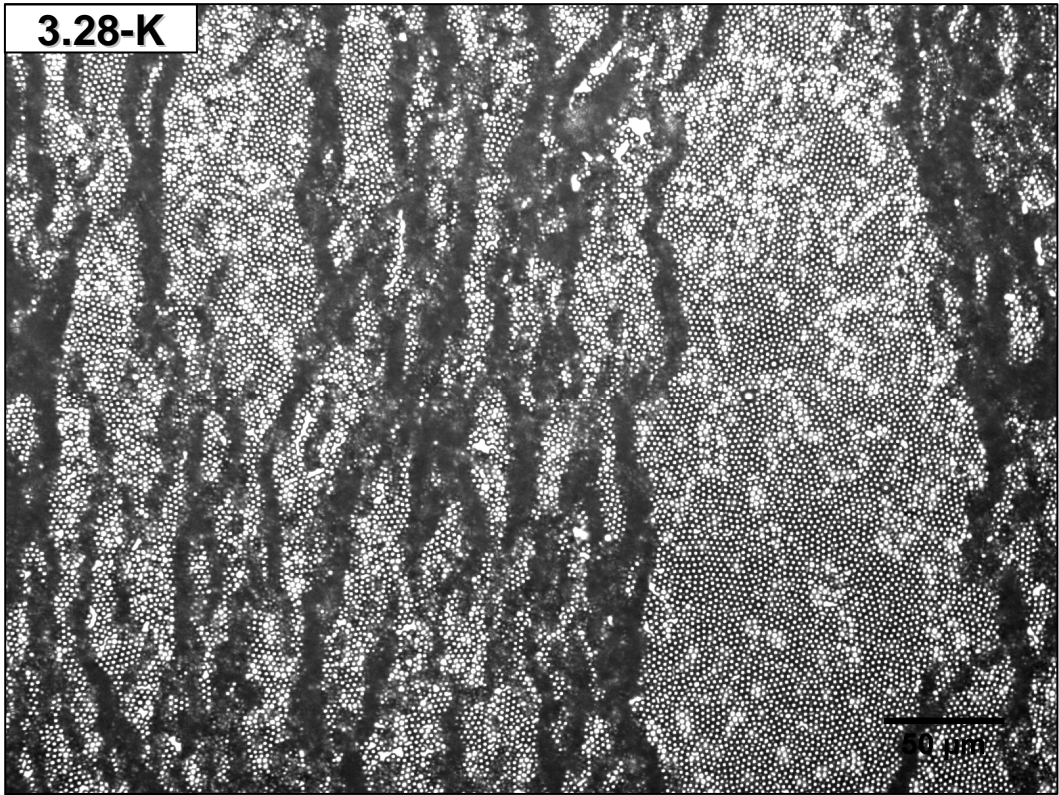


**3.28-I**



**3.28-J**





formation of these so-called mesostructures.<sup>16, 47</sup> Some references suggest that these structures are caused by impurities in the system,<sup>10</sup> or by residual spreading solvent at the interface.<sup>16</sup> These explanations seem unlikely in our case because the effects are totally removed upon further compression of the surface film. Other studies have concluded that these structures form as a result of the interplay between long-range attractive and repulsive interparticle forces, however, no unified theory exists on the origin of the long-range attractive force. Interestingly, nearest-neighbor analysis of micrograph C (**Figure 3.29**) produces a bimodal separation distance (with maxima at 11 and 15  $\mu\text{m}$  and similar peak widths), which suggests that an energy barrier may exist between the gas-like and mesostructure states. Several additional micrographs showing mesostructures are shown in **Figure 3.30**.

Micrograph D shows that upon further compression the mesostructures merge forming a continuous particle phase with islands of free space. As the compression continues, the free space was gradually eliminated, at which point the slope of the isotherm slightly changed upon moving into the long-range repulsion region. Micrographs E-I demonstrate how, in this region, further compression simply results in a uniform decrease in the lattice spacing of the hexagonal pattern across the entire lattice. In this region, long-range electrostatic repulsion through the low dielectric super-phase dominates particle interaction. The next change in isotherm slope likely occurs when the particles are close enough to experience double layer repulsion through the subphase. The added contribution of these forces is the likely cause of the observed sharp increase in slope when moving into the short-range repulsion region.

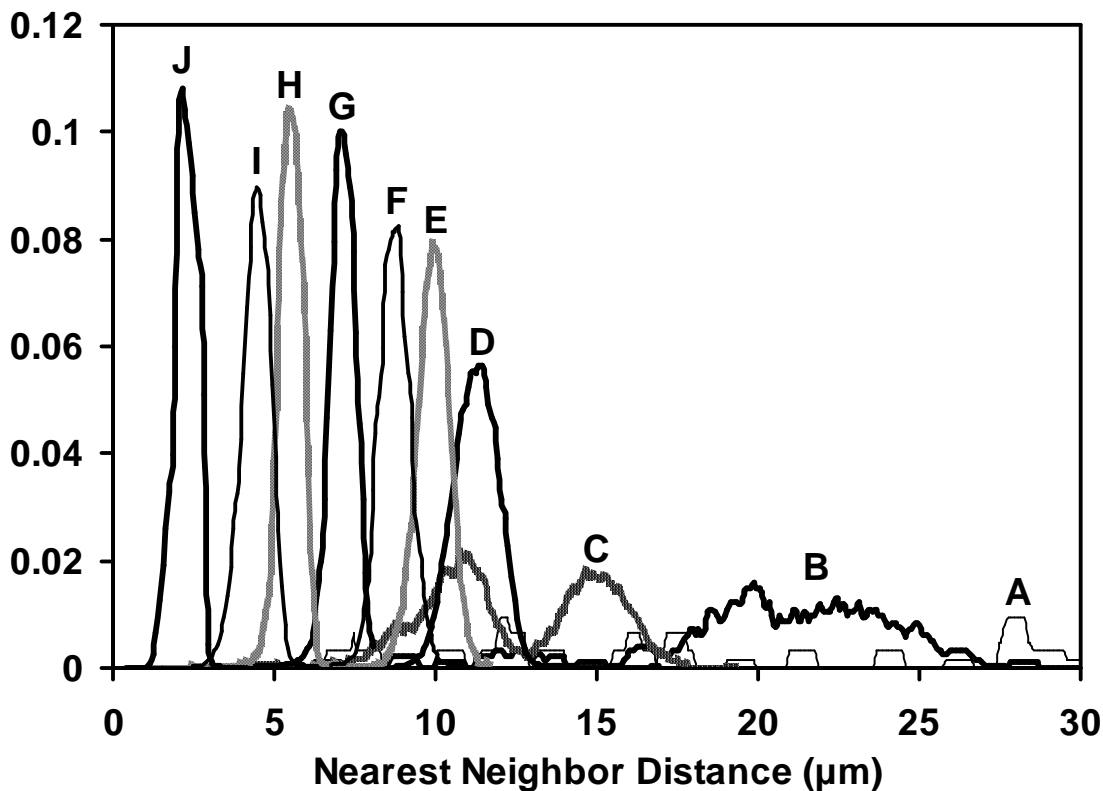
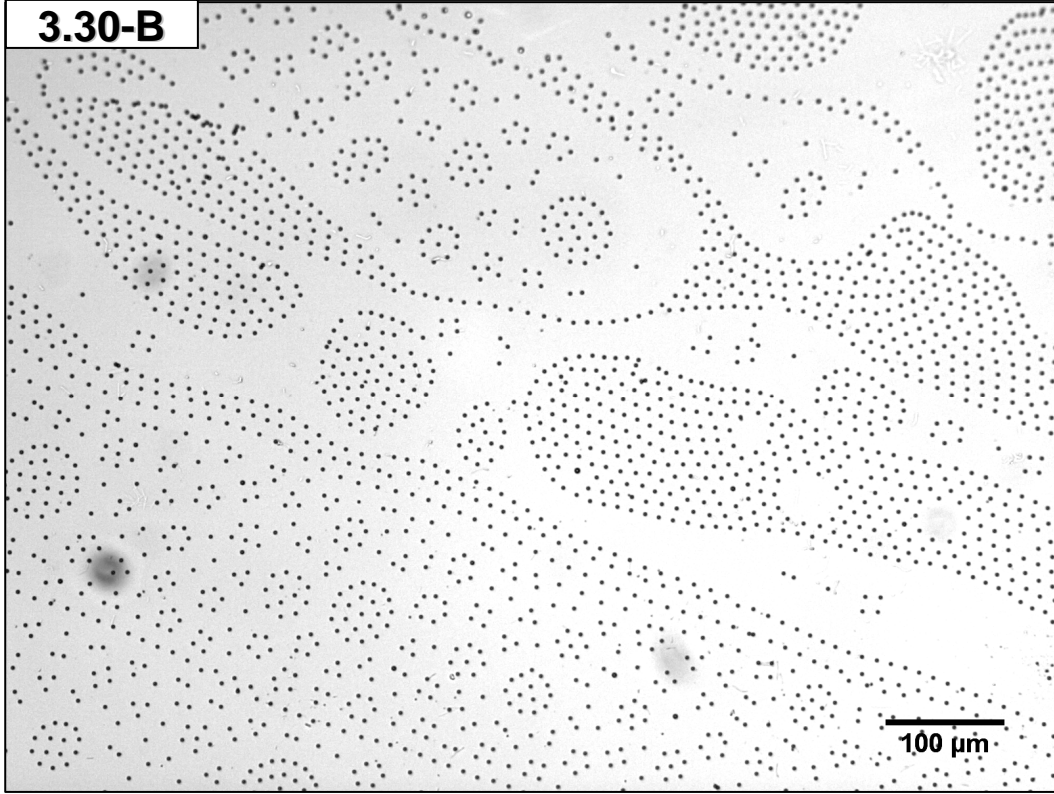
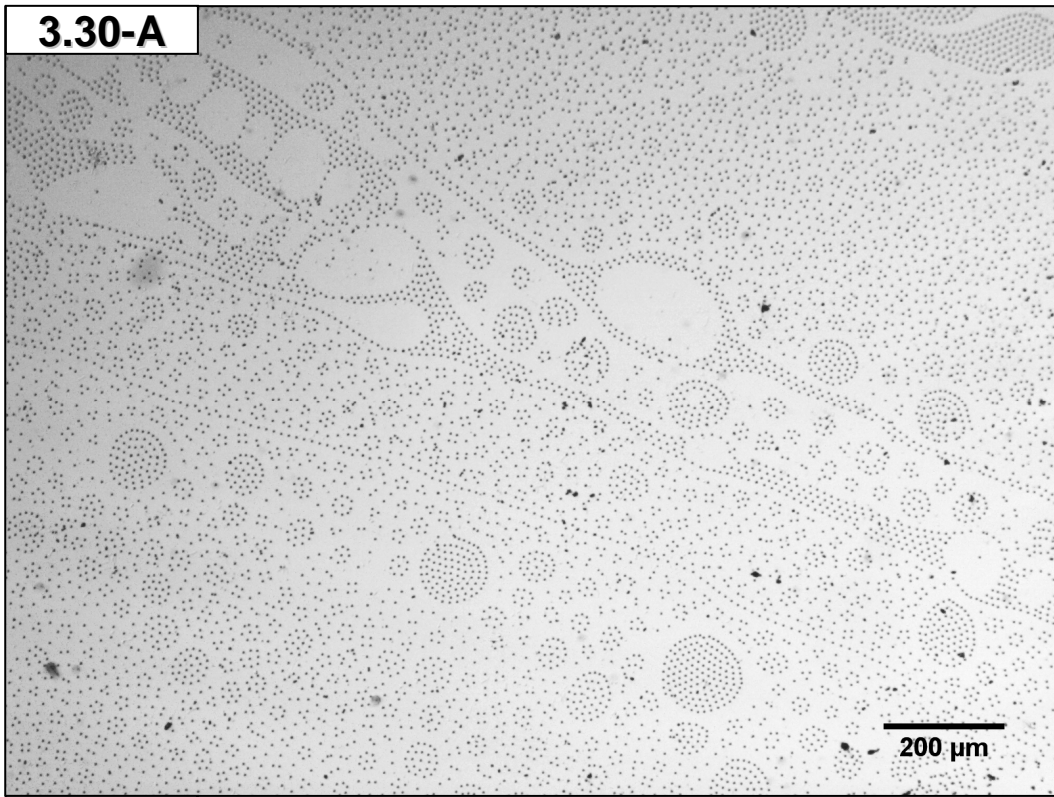


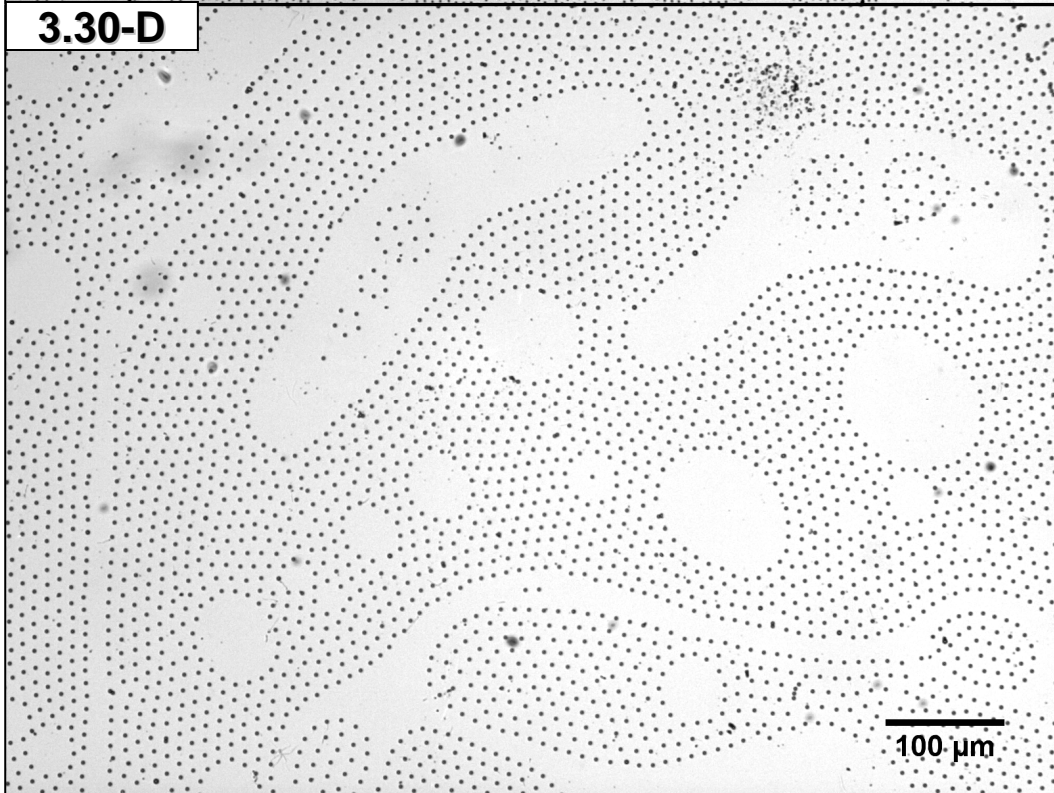
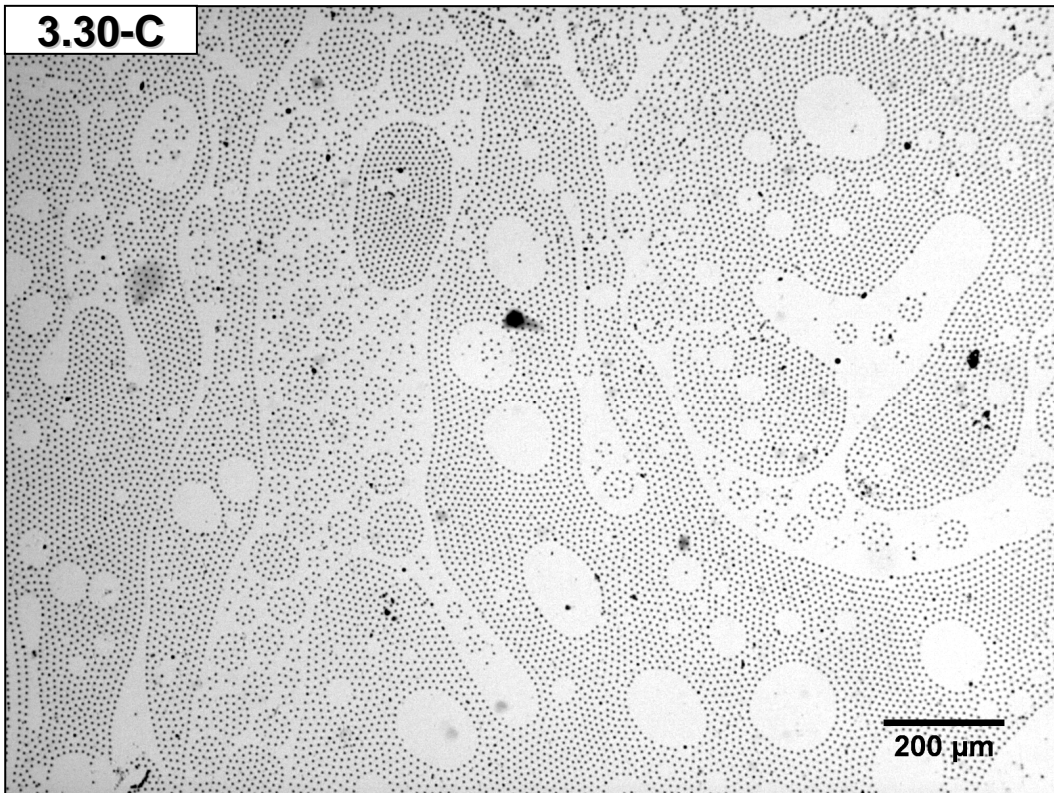
**Figure 3.29** *Nearest-neighbor analysis of the micrographs shown in Figure 3.28.*

*Nearest-neighbor analyses were performed and the curves were normalized, as described in Appendix B.2. Curve A shows a random distribution that extends to 60  $\mu\text{m}$ . Curve B shows a broad distribution centered at 22  $\mu\text{m}$ , demonstrating that a characteristic separation distance can emerge in the gas-like phase. Curve C shows a bimodal separation distance representing particles participating in mesostructures and those that are not. Curves D through J show the smooth decrease in particle separation distance with increased compression.*

**Figure 3.30** *Typical structures observed in the mesostructure region. Micrographs A and B show additional areas of the sample shown in **Figure 3.28-C**, and micrographs C and D show additional areas of the sample shown in **Figure 3.28-D**. Scale Bars: A and C, 200  $\mu\text{m}$ ; B and D, 100  $\mu\text{m}$ .*







When the particles finally touch each other at the solid-phase transition, as in micrograph J, the two-dimensional hard sphere packing limit is achieved, and the pressure rapidly increases upon further compression. Once the collapse pressure of the film is attained, the solid surface film buckles out of plane to form ridges and valleys that run parallel to the movable barrier (micrograph K). Upon re-expansion, a netlike interconnected aggregate is formed across the entire surface (micrograph L). As would be expected, subsequent compression cycles after collapse reveal an altered isotherm shape, underscoring that compression above the collapse pressure is an irreversible process.

Nearest-neighbor analysis was performed on the images shown in **Figure 3.29**, following the procedure outlined in **Appendix B.2**. The first nearest-neighbor measurements were plotted as a normalized histogram. The lack of order in curves A and B is evidenced by the distribution. Highly uniform particle spacings result in narrow distributions as seen in curves E through J.

### **3.3.5 Transfer Completion**

In a typical small-molecule LS transfer, the monolayer is simply allowed to dry in air on the substrate.<sup>48</sup> Unfortunately, transferred particle films became disordered after the substrate was lifted out of the water and allowed to dry. In fact, any time an air-water-substrate contact line swept across a patterned array of the Sulfate 2700 latex on any substrate, particles in the array were squeezed together into random particle clusters. This process was directly observed by optical microscopy. Patterns with

closely spaced particles were more highly disrupted than those separated by several particle diameters. Presumably, this disruption was caused by lateral capillary forces.<sup>49</sup> As a result of the limited particle-substrate contact area and the relatively large particle size, the magnitude of the lateral capillary force can exceed the adhesive force between the particles and the substrate and disrupt the array.

As a patterned particle array is of little use if it must be stored under water indefinitely, a method for *solvent-fixing* the particle array to the substrate was developed, as described in **Section 3.2.9.4**. A series of experiments were performed to investigate control of particle deformation at the interface using a fixing solvent. The exposure time was held constant at 30 s, and the composition of the fixing solvent was varied. Experiments were performed with acetone, diethyl ether, and mixtures of 1, 2, 5, 10, 20, and 30 vol % toluene in IPA. The results are shown in **Figure 3.31**. At 1 and 2 % toluene in IPA, destructive capillary forces were still observed upon drying the substrate; in fact, 1 % was still ineffective after a 15-minute exposure time. At 5 % toluene in IPA for 30 s, the appearance of the array was virtually unchanged while rendering the array resistant to capillary forces. Increasing degrees of deformation could be achieved using the higher toluene ratios, however, it was difficult to achieve uniform particle deformation across the entire substrate at or above 10% toluene in IPA, presumably due to toluene concentration gradients caused by water leaving the substrate after the cover slip was removed. This problem could be avoided by treatment with neat acetone or diethyl ether which produced increasing degrees of deformation uniformly over the entire substrate. The pattern was conserved after the solvent fixing

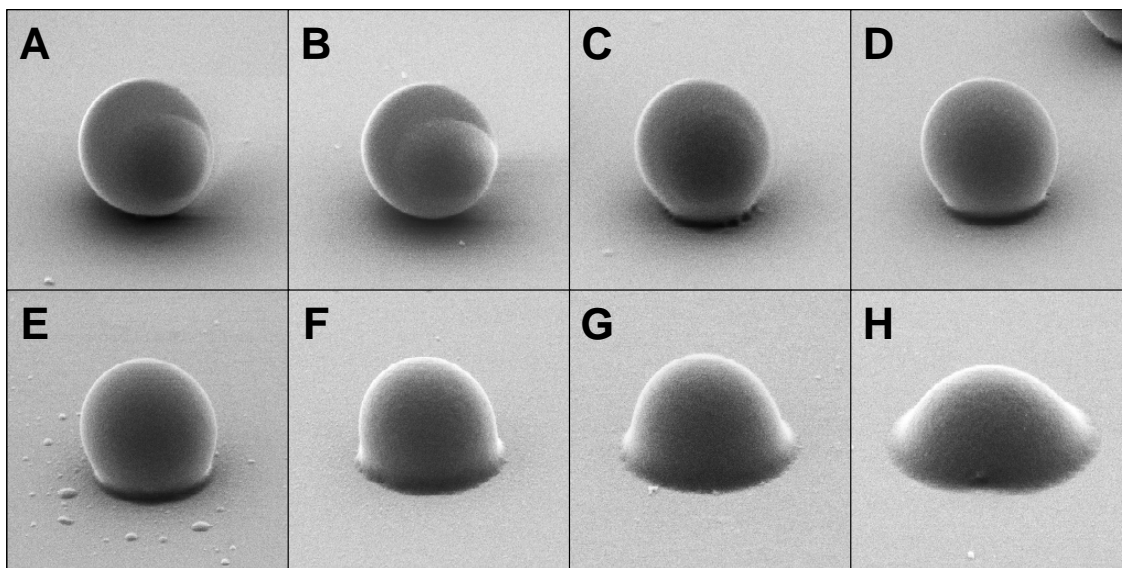


**Figure 3.31** *Particles after solvent-fixing as a function of solvent composition.*

*Micrograph A shows an untreated particle. Samples B-H were prepared for 30 seconds with the following solvents: (B) 5 vol % toluene in IPA, (C) 10 % toluene in IPA, (D) 10 % toluene in IPA, (E) 20 % toluene in IPA, (F) acetone (neat), (G) 30 % toluene in IPA, and (H) diethyl ether (neat). The wrinkle-like feature on the particle surface in A and B is a charging artifact. Each panel is approximately 5  $\mu\text{m}$  x 5  $\mu\text{m}$ .*

process (**Figure 3.32**). The solvent-fixing procedure had an additional use. Once a particle array had been deformed at the substrate surface, it could then function as a lithographic mask to etch the pattern into the substrate, as described in **Section 4.2.2.1**.

An additional method was developed to avoid destructive capillary forces during the drying process. Since the magnitude of the capillary force is proportional to the surface tension of the bridging liquid, the strength of the resulting capillary force can be greatly reduced by allowing the pattern to dry from ethanol ( $\gamma_{lv} = 22.39$  mN/m at 20 °C) instead of water ( $\gamma_{lv} = 72.94$  mN/m at 20 °C).<sup>50</sup> An 85-mm diameter polystyrene Petri dish was half filled with deionized water, and 20  $\mu$ L of 3.0 wt % Sulfate 2700 latex that had aged at 25 °C for 17 days in IPA was added to the interface *via* a syringe pump at a rate of 5  $\mu$ L/min. Then LS transfers were performed by the *underwater* method onto TBAC-treated silicon substrates. The transfer was completed using the fluid-exchange process with ethanol. An optical micrograph of the resulting pattern is shown in **Figure 3.33**. The surface was highly ordered and exhibited large individual grain sizes, on the order of mm<sup>2</sup>.

### 3.3.6 Comparison of Methods for Pattern Analysis

Three methods of analysis were routinely used to characterize the particle patterns, nearest neighbor (NN), laser diffraction (LD), and fast Fourier transform (FFT). All three of these methods produced remarkably similar results. To test the internal consistency of these methods, the HCP pattern of Sulfate 2700 latex particles

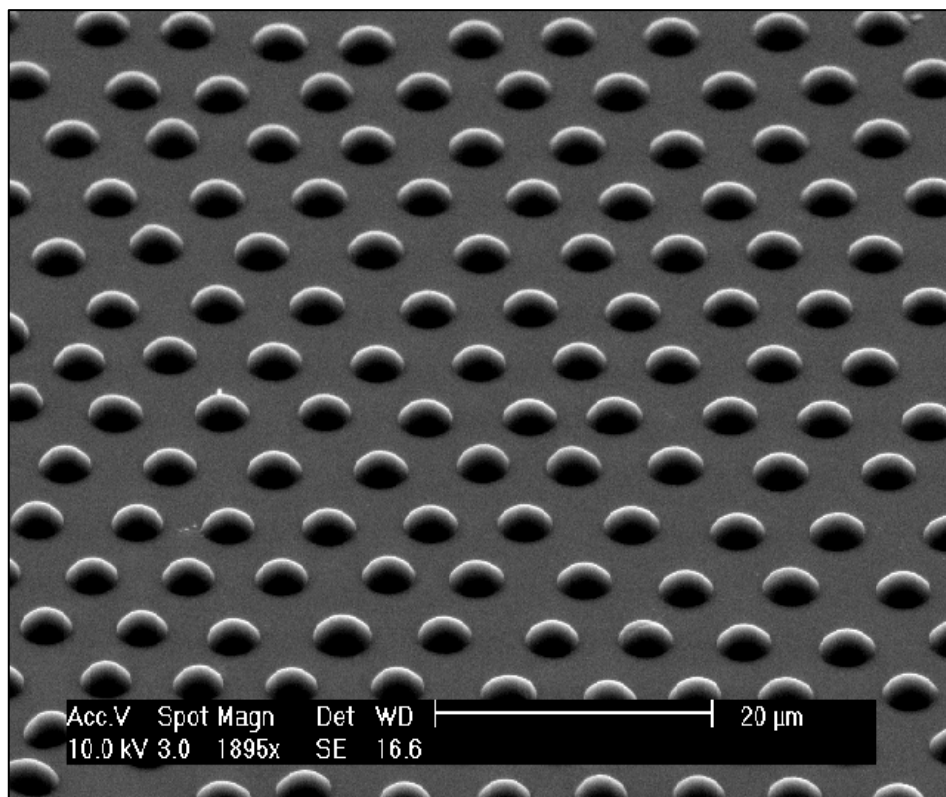


**Figure 3.32** *Particle array after solvent-fixing with acetone for 30 s. The pattern was conserved after the solvent-fixing process.*

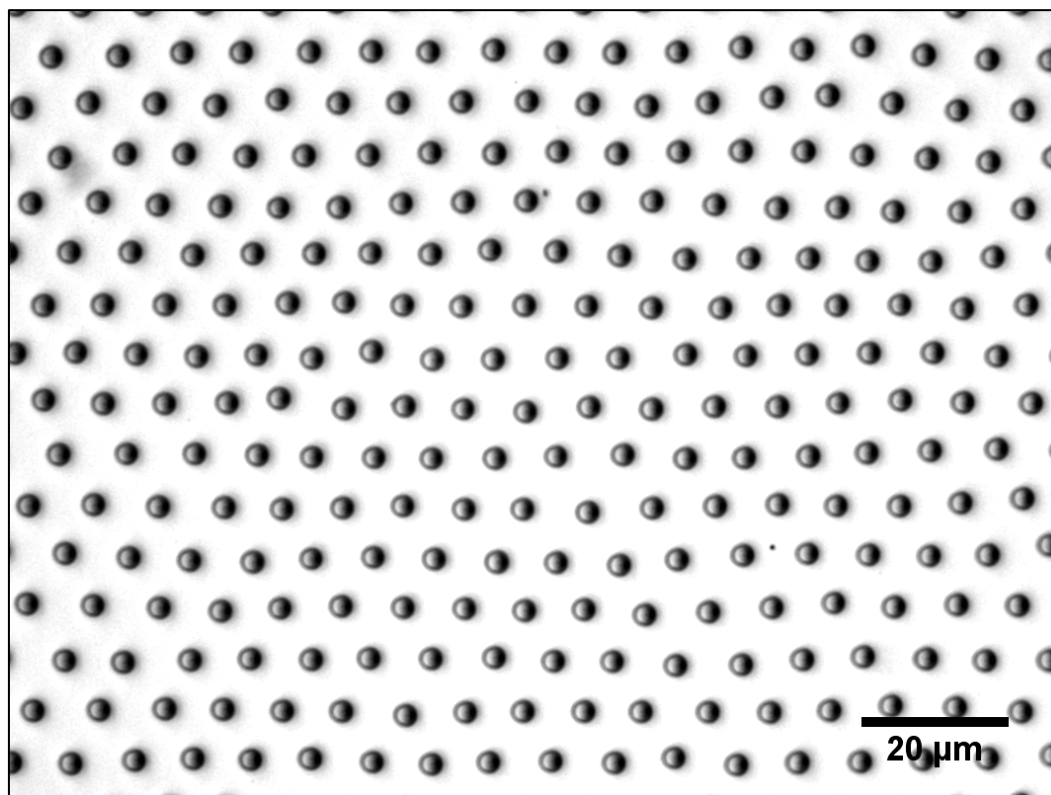


**Figure 3.33** *Optical micrograph of a hexagonal pattern of Sulfate 2700 latex particles. Sample was prepared by the constant-area dish compression method, and was transferred to a TBAC-treated silicon substrate by the underwater-LS method, and was allowed to air dry after being submerged in ethanol. By rinsing the sample with a low surface-tension liquid, destructive capillary forces could be lessened during the drying process. Scale Bar: 20 μm.*



shown in **Figure 3.33** was analyzed by all three methods. The optical micrograph of the pattern was used to calculate the NN and the FFT separation distances. The first, second, and third nearest neighbors were averaged together and produced a spacing of  $7.89 \pm 0.33 \mu\text{m}$  (standard deviation, 1121 measurements). The original transferred pattern on silicon was used to generate an LD pattern in reflection mode at a projection length of 10 cm. The diffraction pattern, shown in **Figure 3.34**, was contrast-corrected to compensate for the higher intensity of the inner points. The LD and FFT (**Figure 3.35**) patterns were analyzed in an identical fashion. Diffraction points caused by the  $\{10\}$ ,  $\{11\}$ ,  $\{21\}$ , and  $\{31\}$  particle lines were used to calculate 60 independent measurements of the particle spacing. The LD analysis produced an average spacing of  $8.05 \pm 0.28 \mu\text{m}$ , and the FFT analysis gave an average spacing of  $7.93 \pm 0.32 \mu\text{m}$ . Additionally, the data from all three analyses were plotted as normalized histograms, 5-point moving averaged, and fitted with Gaussian distributions as shown in **Figure 3.36**. The three methods produced very similar distributions. The NN measurements were only capable of taking into account three of the six nearest neighbor distances for each particle in the micrograph. As a result, interparticle spacings measured by the NN method were systematically less than the LD and FFT methods.

### **3.3.7 Particle Surface Reconstruction**

The properties of deposited surface films of freshly prepared Sulfate 2700 latex in IPA greatly differed from films deposited after the suspension had aged. Initially, for a latex sample freshly suspended in IPA, a high degree of transfer to the bulk subphase

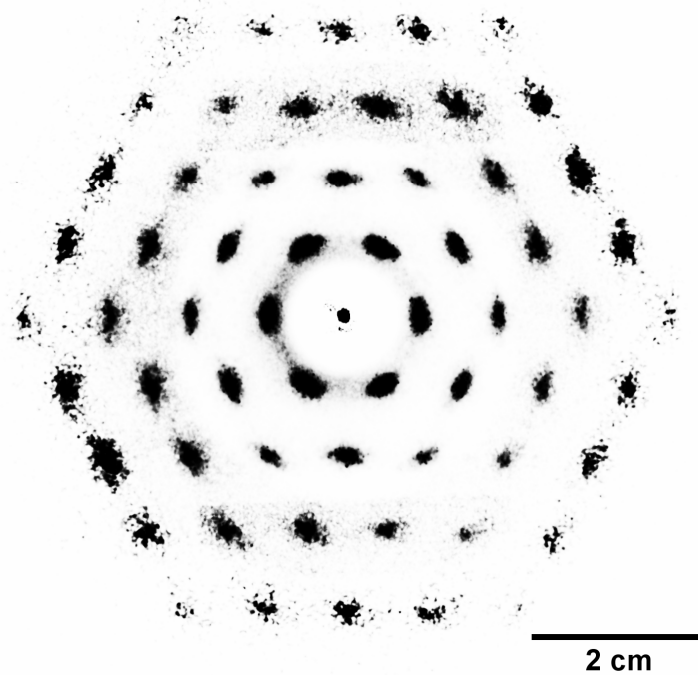


**Figure 3.34** *Laser diffraction pattern of a particle array with an 8- $\mu\text{m}$  spacing. The same array shown in **Figure 3.33** was used to produce this diffraction pattern. The pattern was obtained in reflection mode at a projection length of 10 cm. The diffraction spots are indexed according to the hexagonal system. Analysis of the 60 points comprising the pattern yields an average particle spacing of  $8.05 \pm 0.28 \mu\text{m}$ . The diffraction pattern was contrast-corrected to make all points of similar intensity.*

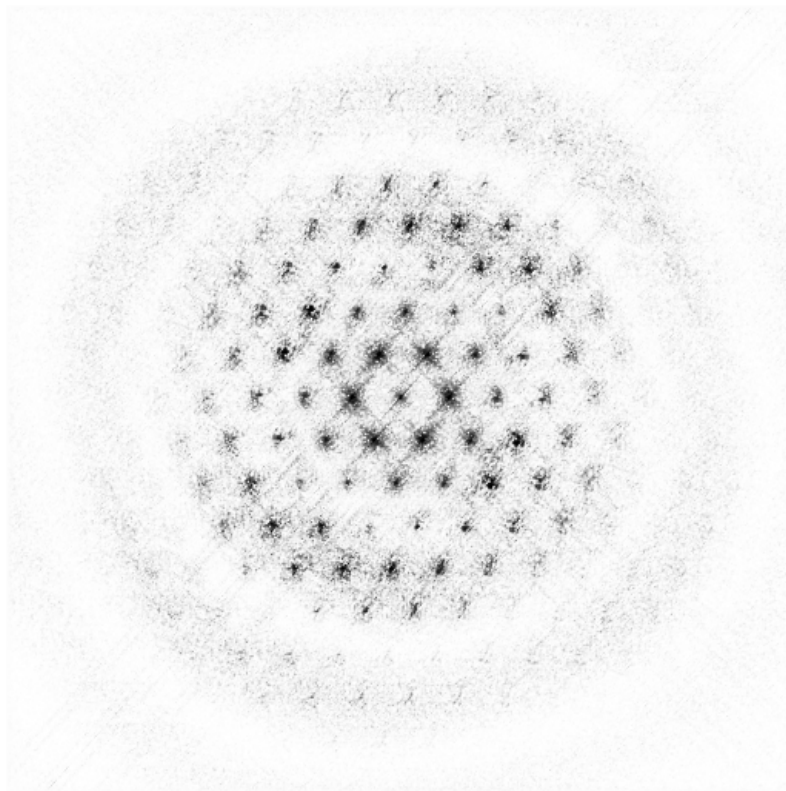


**Figure 3.35** *Pattern resulting from a fast Fourier transform of the image in Figure 3.33. There is a marked similarity between the FFT and the LD pattern. The pattern was rotated by 45° and contrast-corrected for clarity. The FFT pattern was analyzed in a similar fashion to the LD pattern and yielded an average particle spacing of  $7.93 \pm 0.32 \mu\text{m}$  (standard deviation, 60 measurements). Only the central region of the transformed image is shown.*

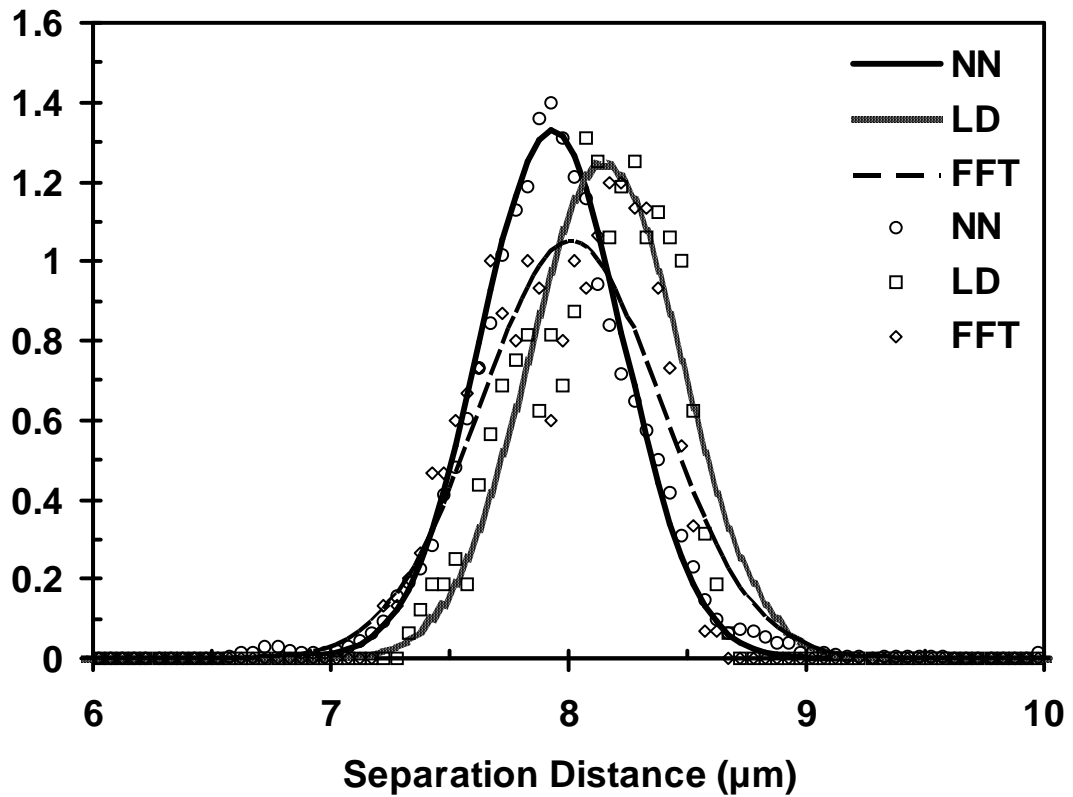


**Figure 3.36** *Comparison of methods of analysis for the pattern shown in Figure 3.33. All three methods show good agreement. The distribution shown is mostly due to the real distribution of particle spacings in the pattern. The Gaussian curve fits returned mean values of  $7.93 \pm 0.29 \mu\text{m}$  for the NN,  $8.15 \pm 0.31 \mu\text{m}$  for the LD, and  $8.02 \pm 0.37 \mu\text{m}$  for the FFT analysis.*

was visually observed. This was likely due to a low initial particle-interface contact angle. After allowing the suspension in IPA to age, transfer to the subphase greatly decreased until finally almost no transfer was observed. Additionally, superior particle patterns formed after the latex was allowed to age for approximately 20 days at 25 °C with occasional sonication. If the latex was aged for a month or longer, the resistance to cluster formation during deposition slowly degraded, but the particles still remained resistant to transfer to the subphase.

The particle-interface contact angle was measured as a function of the time the particles had been in contact with IPA before spreading at the interface (**Figure 3.37**). From these measurements, it was evident that the contact angle started at approximately 25° or less for a latex sample recently suspended in IPA, and increased toward a limiting value of approximately 90°, which is also the equilibrium contact angle value for bulk polystyrene.<sup>51, 52</sup> This increase in contact angle resulted in the higher efficiency of interfacial entrapment.<sup>15</sup> The percent surface area above the interface as a function of contact angle is shown in **Figure 3.38**. When the contact angle was 25°, only 4.7 % of the particle surface was exposed while at 90°, 50 % was exposed. In agreement with current theory,<sup>20</sup> the increase in exposed surface area would correspond to an increase in the magnitude of the inter-particle repulsion, and thus the observed improvement in long range ordering.

A similar trend was observed in the onset of interparticle repulsion (**Figure 3.39**). For this experiment, the initial rise in surface pressure (known as the interaction onset) was extrapolated to the baseline, as shown in the inset of **Figure 3.39**, and the x-

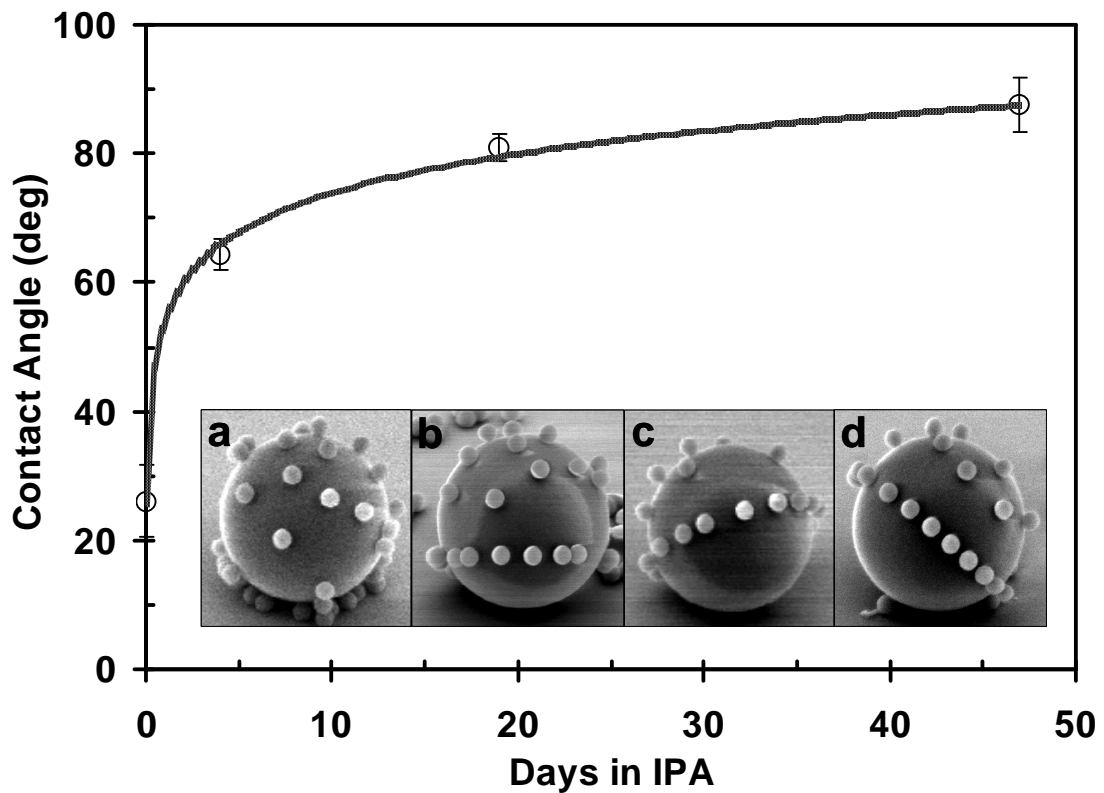


**Figure 3.37** *Particle-(air-water) interface contact angle as a function of aging time in IPA. (a) The contact angle at the particle-interface for Sulfate 2700 latex particles recently suspended in IPA and spread at an air-water interface was less than 25°. (b) After aging for 4 days, the contact angle increased to 64°. (c) After aging for 19 days, it increased to 81°. (d) After aging for 47 days, it increased to 88°. Each inset panel is approximately 3  $\mu\text{m}$  x 3  $\mu\text{m}$ .*

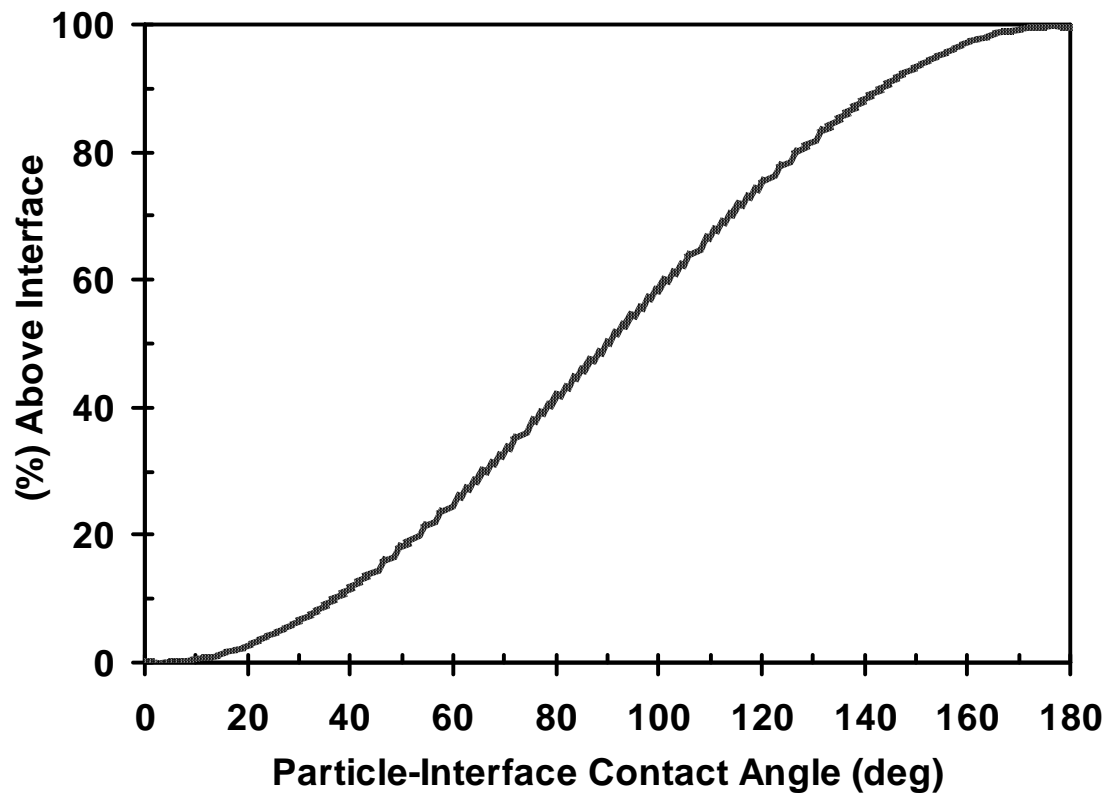


**Figure 3.38** *Calculated amount of particle surface exposed as a function of particle-interface contact angle. For contact angles less than 20°, only a small fraction of the particle surface is exposed to the low dielectric medium, resulting in weak inter-particle repulsion at long distances, and lower resistance to transfer to the subphase. As the contact angle approaches 90°, a high degree of long range inter-particle repulsion is observed, and the particles are quite resistant to transfer to the subphase.*

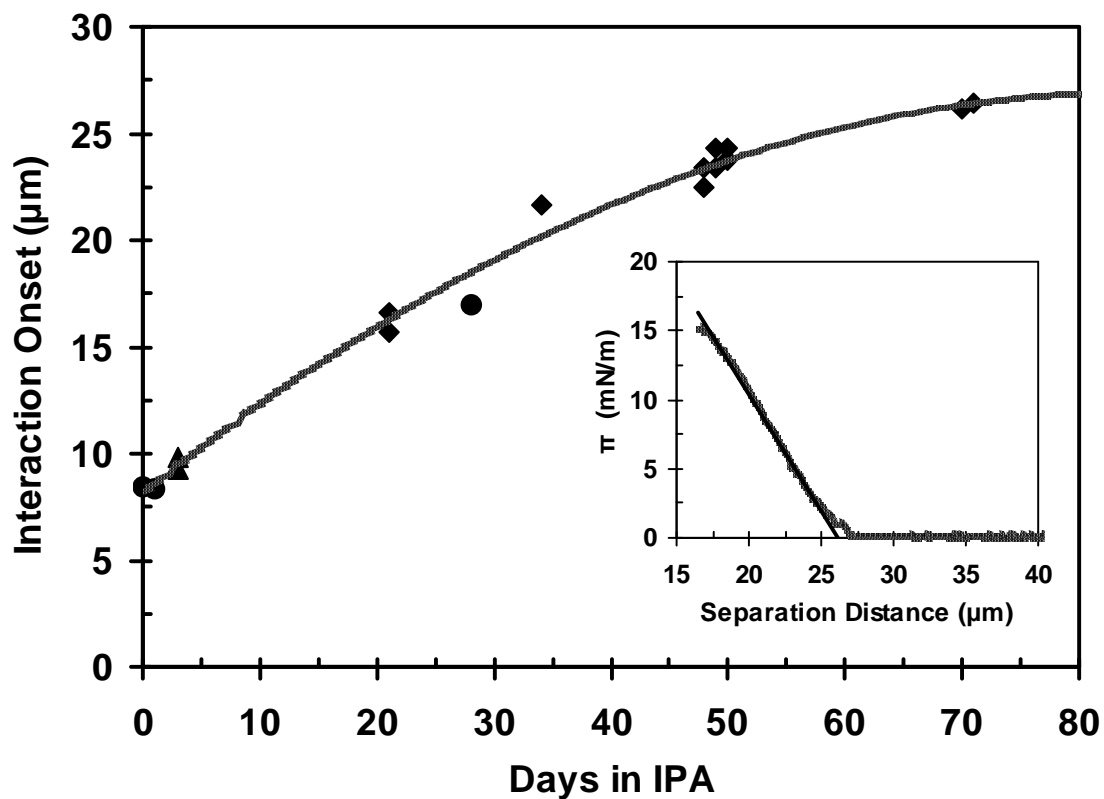


**Figure 3.39** *Interaction onset as a function of particle aging time in IPA. The interaction onset is measured by extrapolating the initial rise in the isotherm to the baseline and recording the x-intercept, as shown in the inset above. This value was highly dependent on the time a Sulfate 2700 latex sample was in contact with IPA. The different symbols represent separate runs.*



intercept was recorded. This measurement accounts for both the efficiency of surface capture during the deposition process and the degree of inter-particle repulsion. The interaction onset represents the theoretical particle separation distance at which the isotherm deviates from the baseline if all of the deposited particles were trapped at the interface. As this is not true for non-aged suspensions, due to transfer to the subphase, this value should be considered as a goodness value and not the literal particle separation distance. A clear trend exists as a function of particle age in IPA, with the interaction onset increasing toward a limiting value.

This observed change in particle behavior upon aging in IPA could be due to frustrated surface reconstruction of the polar functional groups at the particle surface. High-energy groups have a tendency to bury into the surface of even glassy polymers over time.<sup>53, 54, 55</sup> Even though IPA is a non-solvent for polystyrene, it is likely able to plasticize the particle surface to some extent. In addition, because of the polar initiators used, the particle surface in water becomes enriched with the polar chain ends which inherently have higher mobility. The concentration of polar surface functional groups may have decreased as a function of time against IPA, resulting in the observed increase in particle-interface contact angle due to the increased hydrophobicity of the particle surface. This idea is consistent with the observed limit in contact angle at the value for bulk polystyrene. Even though the total number of charged surface groups presumably decreased, the observed inter-particle repulsion could still increase if the total number of charges above the interface increased. As stated earlier, the particles behaved the best after aging 20 days, before reaching the limiting contact angle. After reaching this

maximum in particle repulsion it was noted that at longer ages, even though they didn't transfer to the bulk, the particles had a higher tendency to aggregate once at the interface. This result also fits with the frustrated surface reconstruction hypothesis because fewer and fewer stabilizing charge groups would be available with time. Further investigation into this topic was not pursued, as it was beyond the scope of the project, but this seems to be a plausible explanation of the experimental data.

### **3.4 Conclusions**

Patterned, sub-monolayer latex-particle films trapped at an air-water interface were successfully transferred to solid substrates. Suitable transfer substrates were easily prepared with various surface functional groups with commercially available organosilicon compounds. By choosing a silane with complementary surface functionality to that of the latex particles comprising the surface film, rapid adhesion and transfer was achieved with a minimum amount of pattern distortion. The transferred array could then be solvent-fixed before drying to prevent disorganization during the drying process, caused by lateral capillary forces. In contrast to previously reported examples in the literature, highly organized particle films were prepared at an air-water interface by simply allowing the latex suspension to age in contact with IPA before deposition. The aging process, possibly caused by frustrated surface reconstruction, caused an increase in both the particle-interface contact angle and the maximum distance over which particles were capable of interacting.

### 3.5 References and Notes

---

- <sup>1</sup> Langmuir Blodgett Systems Operating Manual, 3<sup>rd</sup> Ed.; F. Grunfeld, Ed.; Nima Technology Ltd.: Coventry, England, 1992; pp 20-22.
- <sup>2</sup> Maurer-Mathison, D. *The Ultimate Marbling Handbook: A Guide to Basic and Advanced Techniques for Marbling Paper and Fabric*; Watson-Guption: New York, NY. 1999; pp 18.
- <sup>3</sup> Pockels, A. *Nature*, **1891**, 43, 437.
- <sup>4</sup> Langmuir, I. *The Collected Works of Irving Langmuir; With Contributions in Memoriam, Including a Complete Bibliography of His Works*; Suits, C. G.; Way, H. E. Eds.; Pergamon Press: New York, NY, 1960-1962; Vol. 1-12.
- <sup>5</sup> Blodgett, K. B.; Langmuir, I. *Phys. Rev.* **1937**, 51, 964-982.
- <sup>6</sup> Langmuir, I.; Schaefer, V. J. *J. Am. Chem. Soc.* **1938**, 60, 1351-60.
- <sup>7</sup> Schuller H. *Kolloid-Z.* **1967**, 380, 216-217.
- <sup>8</sup> Sheppard, E.; Tchekrekdjian, N. *J. Colloid Interface Sci.* **1968**, 28, 481-486.
- <sup>9</sup> Pieranski, P. *Phys. Rev. Lett.* **1980**, 45, 569-572.
- <sup>10</sup> Armstrong, A.J., Mockler, R.C.; O'Sullivan, W.J. *J. Phys. Condens. Matter*, **1989**, 1, 1707-1730.
- <sup>11</sup> Doroszkowski, A.; Lambourne, R. *J. Polymer Sci. C*, **1971**, 34, 253.
- <sup>12</sup> Aveyard R.; Clint, J.H.; Nees, D.; Paunov, V.N. *Langmuir*, **2000**, 16, 1969-1979.
- <sup>13</sup> Aveyard, R.; Clint, J.H.; Nees, D.; Quirke, N. *Langmuir*, **2000**, 16, 8820-8828.
- <sup>14</sup> Goodwin J.W.; Ottewill, R.H.; Dorentich, A. *J. Phys. Chem.* **1980**, 84, 1580-1586.

- 
- <sup>15</sup> Binks, B.P. *Curr. Opin. Colloid Interface Sci.* **2002**, 7, 21-41.
- <sup>16</sup> Ghezzi, F.; Earnshaw, J.C.; Finnis, M.; McCluney, M. *J. Colloid Interface Sci.* **2001**, 238, 433-446.
- <sup>17</sup> Nikolaides, M.G.; Bausch, A.R.; Hsu, M.F.; Dinsmore, A.D.; Brenner, M.P.; Gay C.; Weitz, D.A. *Nature*, **2002**, 420, 299-301.
- <sup>18</sup> Hurd, A.J. *J Phys A: Math Gen.* **1985**, 18, L1055-L1060.
- <sup>19</sup> Robinson, D.J.; Earnshaw, J.C. *Langmuir*, **1993**, 9, 1436-1438.
- <sup>20</sup> Aveyard, R.; Binks, B.; Clint, J.H.; Fletcher, P.D.I.; Horozov, T.S.; Neumann, B.; Paunov, V.N.; Annesley, J.; Botchway, S.W.; Nees, D.; Parker, A.W.; Ward, A.D.; Burgess, A.N. *Phys. Rev. Lett.* **2002**, 88, 246102-1—246102-4.
- <sup>21</sup> Megens, M.; Aizenberg, J. *Nature*, **2003**, 424, 1014.
- <sup>22</sup> Lenzmann, F.; et al. *Chem. Mater.* **1994**, 6, 156-159.
- <sup>23</sup> Bardosova, M.; et al. *Thin Solid Films*, **2003**, 437, 276-279.
- <sup>24</sup> Goldenberg, L.M.; et al. *Langmuir*, **2002**, 18, 5627-5629.
- <sup>25</sup> Fulda, K.U.; Tieke, B. *Supramol. Sci.* **1997**, 4, 265-273.
- <sup>26</sup> Kumaki, J. *Macromolecules*, **1986**, 19, 2258-2263.
- <sup>27</sup> Kumaki, J. *Macromolecules*, **1988**, 21, 749-755.
- <sup>28</sup> Fulda, K. U.; Tieke, B. *Supramol. Sci.* **1997**, 4, 265-273.
- <sup>29</sup> Tieke, B.; Fulda, K.U.; Kampes, A. in *Nano-Surface Chemistry*, **2002**, 213-243.
- <sup>30</sup> Rouse, J.H.; Ferguson, G.S. *J. Am. Chem. Soc.* **2003**, 125, 15529-15536.

- 
- <sup>31</sup> Sacco, H.; C.; Iamamoto, Y.; Smith, J. R. L. *J.Chem. Soc., Perkin Trans.* **2001**, 2, 181-190.
- <sup>32</sup> Garcia-Sanchez, R.; Bettmer, J.; Ebdon, L. *Microchem. J.* **2004**, 76, 161-171.
- <sup>33</sup> Riepe, H. G.; Gomez, M.; Camara, C.; Bettmer, J. *J. Mass. Spectrom.* **2000**, 35, 891-896.
- <sup>34</sup> Yamamoto, S.; Ejaz, M.; Tsujii, Y.; Fukuda, T. *Macromolecules*, **2000**, 33, 5608-5612.
- <sup>35</sup> Ulrich, J.; del Campo, A.; Kruger, C.; Glasser, G.; Boos, D. *PNAS*, **2002**, 8, 5034-5039.
- <sup>36</sup> Kruger, C.; Jonas, U. *J. Colloid Interface Sci.* **2002**, 252, 331-338.
- <sup>37</sup> Special thanks are owed to Jeff Spirko for useful discussions about how to develop a method to extract quantitative particle-interface contact angle data, irrespective of individual particle halo tilt angles, from SEM micrographs.
- <sup>38</sup> ImageJ analysis software is available free of charge at <http://rsb.info.nih.gov/ij/>.
- <sup>39</sup> Spatial Analysis Utilities is available free of charge at <http://www.archeogr.unisi.it/infapp/sau/>.
- <sup>40</sup> WSxM is available free of charge at <http://www.nanotec.es/>.
- <sup>41</sup> Ulman, A. *Chem. Rev.* **1996**, 96, 1533-1554.
- <sup>42</sup> Thomas, I. L.; McCorkle, K. H. *J. Colloid Interface Sci.* **1971**, 36, 110-118.

- 
- <sup>43</sup> Stancik, E.J.; Gavranovic, G. T.; Widenbrant, M. J. O.; Lasckitsch, A. T.; Vermant, J.; Fuller, G. G. *Faraday Discuss.* **2003**, 123, 145-156.; Stancik, E. J.; Hawkinson, A. L.; Vermant, J.; Fuller, G. G. *J. Rehol.* **2004**, 48, 159-173.
- <sup>44</sup> Santiago-Rosanne, M.; Vignes-Adler, M.; Velarde, M. G. *J. Colloid Interface Sci.* **1997**, 191, 65-80.; Walters, D. A. *Langmuir*, **1990**, 6, 991-994.; Santiago-Rosanne, M.; Vignes-Adler, M.; Velarde, M. G. *J. Colloid Interface Sci.* **2001**, 234, 375-383.; Chowdhury, D.; Sarkar, S. P.; Kalita, D.; Sarma, T. K.; Paul, A.; Chattopadhyay, A. *Langmuir*, **2004**, 20, 1251-1257.
- <sup>45</sup> Adamson, A.W.; Gast, A. P. *Physical Chemistry of Surfaces*, 6<sup>th</sup> Edition; Wiley: New York, NY, 1997, pp 111-112.
- <sup>46</sup> Danov, K.D.; Kralchevsky, P.A.; Boneva, M.P. *Langmuir*, 2006, 2653-2667.
- <sup>47</sup> Ghezzi, F.; Earnshaw, J. C. *Il Nuovo Cimento*, **1998**, 20, 2243-2250.
- <sup>48</sup> Petty, M. C. *Langmuir-Blodgett Films: An Introduction*; Cambridge: New York, NY, 1996.
- <sup>49</sup> Kralchevsky, P.A.; Nagayama, K. *Langmuir*, **1994**, 10, 23-36.
- <sup>50</sup> Adamson, A.W.; Gast, A. P. *Physical Chemistry of Surfaces*, 6<sup>th</sup> Edition; Wiley: New York, NY, 1997, pp 36-37.
- <sup>51</sup> Sciutto, A.; Garbassi, F.; Meda, L.; Po, R.; Pozzi, L. *Appl. Surf. Sci.*, **1998**, 125, 287-292.
- <sup>52</sup> Idage, S. B.; Badrinarayanan, S. *Langmuir*, **1998**, 14, 2780-2785.
- <sup>53</sup> Rouse, J. H.; Twaddle, P. L.; Ferguson, G. S. *Macromolecules*, **1999**, 32, 1665-1671.

---

<sup>54</sup> Dupont-Gillain, C. C.; Adriaensen, Y.; Derclaye, S.; Rouxhet, P. G. *Langmuir*, **2000**, 16, 8194-8200.

<sup>55</sup> Clement, F.; Held, B.; Soulem, N.; Martinez, H. *Eur. Phys. J. AP*, **2003**, 21, 59-66.

## Chapter 4

### Hierarchical Structures and Patterns

#### 4.1 Introduction

A number of proof-of-concept experiments were performed to investigate possible variations and applications of particle self-assembly to form patterned surfaces. The patterned particle arrays described in Chapters 2 and 3 were used as a scaffolding to build increased complexity into the self-assembled systems. After thermal or solvent annealing, the particle arrays could function as lithographic masks, resulting in the pattern being etched into the substrate. By electrostatically adsorbing colloidal silica onto an array, and then calcining at high temperature, the polymer cores were burnt away leaving behind a patterned array of hollow spheres. Particle patterns were also embedded into PDMS elastomer and removed from the original substrate. The resulting stretchable particle array exhibited interesting optical properties. These examples demonstrate the versatility of particle patterns in the context of bottom-up approaches to self-assembly, and provide potential directions for future work in this area.

#### 4.2 Experimental Results and Discussion

(Each sub-section describes a set of proof-of-concept experiments, giving relevant background material, experimental methods, results, and discussion.)



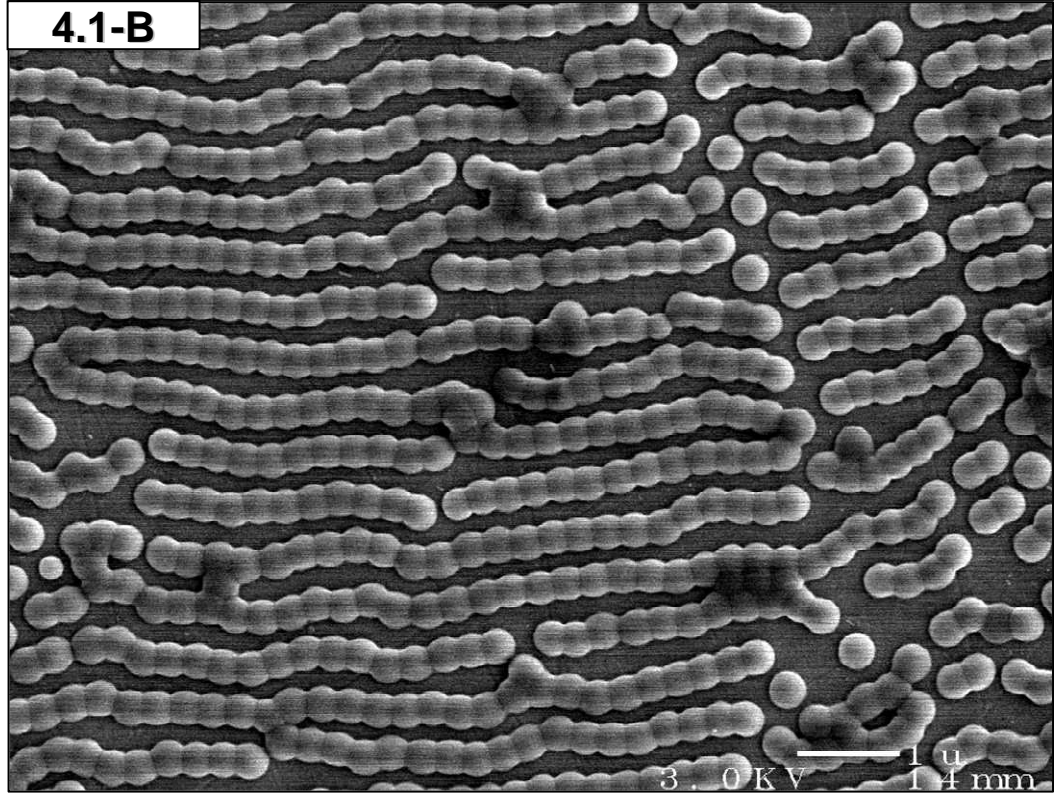
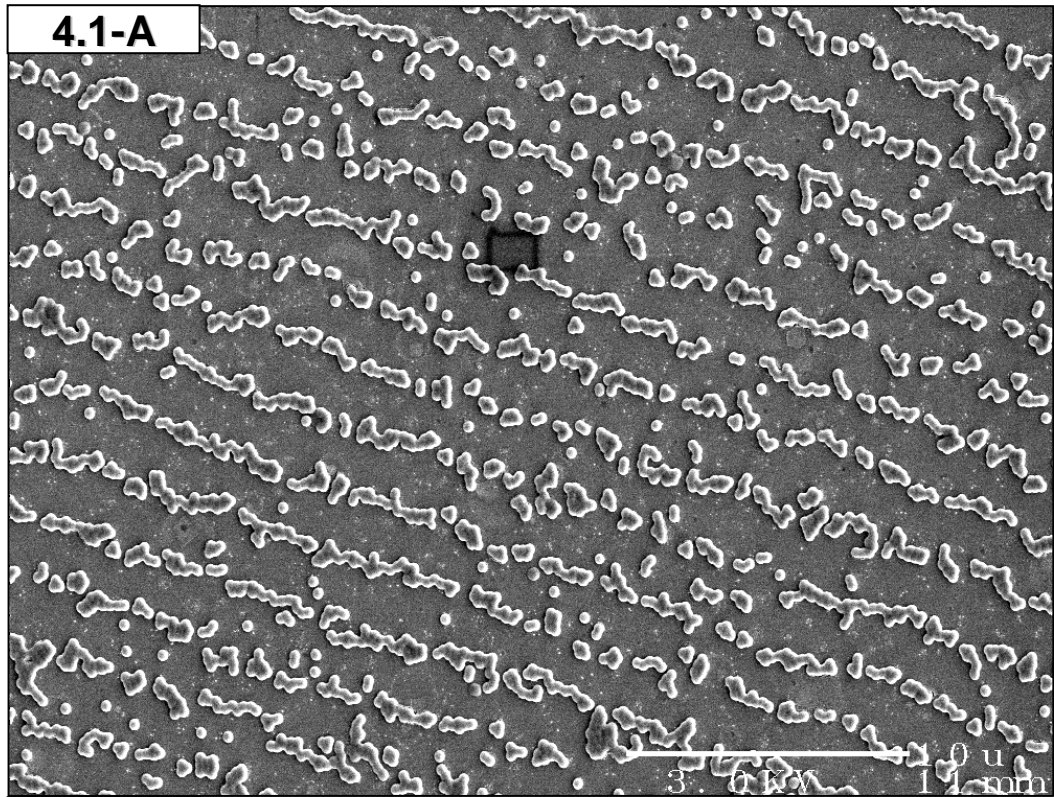
### 4.2.1 Thermal Annealing

Thermal annealing is a common method for producing continuous films from polymer latexes.<sup>1</sup> For the linear patterns discussed in **Chapter 2**, heating the array above the particle  $T_g$  at 110 °C for several hours resulted in the individual spherical particles flattening out onto the substrate surface and forming polymer lines that were more continuous, as shown in **Figure 4.1-A**. By increasing the line-width before annealing, completely continuous polymer lines could likely be produced by this method. It may also be possible to create continuous particle lines by using a suspension of polymer particles with a bi- or tri- modal size distribution to form the linear pattern. The particles with the largest diameter would likely define the line spacing, and the smaller ones could fill in the interstitial space between the larger ones. This strategy has been successfully demonstrated in latex films to achieve a higher degree of film clarity by decreasing light scattering by interstitial voids.<sup>2,3</sup> Similarly, an LB pattern of Imidazole 258 latex particles prepared on a stainless steel substrate as described in **Chapter 3** was annealed to give results quite similar to those from the solvent-fixing procedure discussed in **Section 3.3.5 (Figure 4.1-B)**.

### 4.2.2 Substrate Etching

Substrate etching is a method typically employed in conjunction with a top-down patterning approach such as optical lithography. As a result of the progress in the semiconductor industry, a wide variety of well-controlled silicon etching techniques exist. These methods can also be used in conjunction with patterns prepared with a

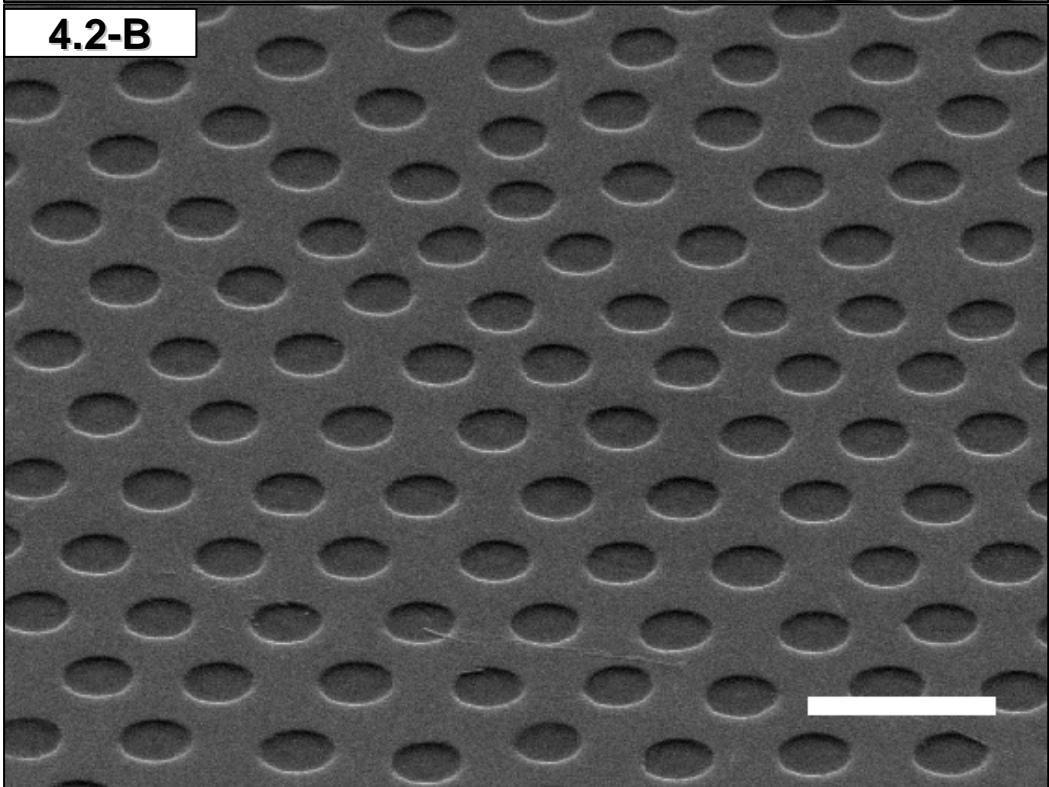
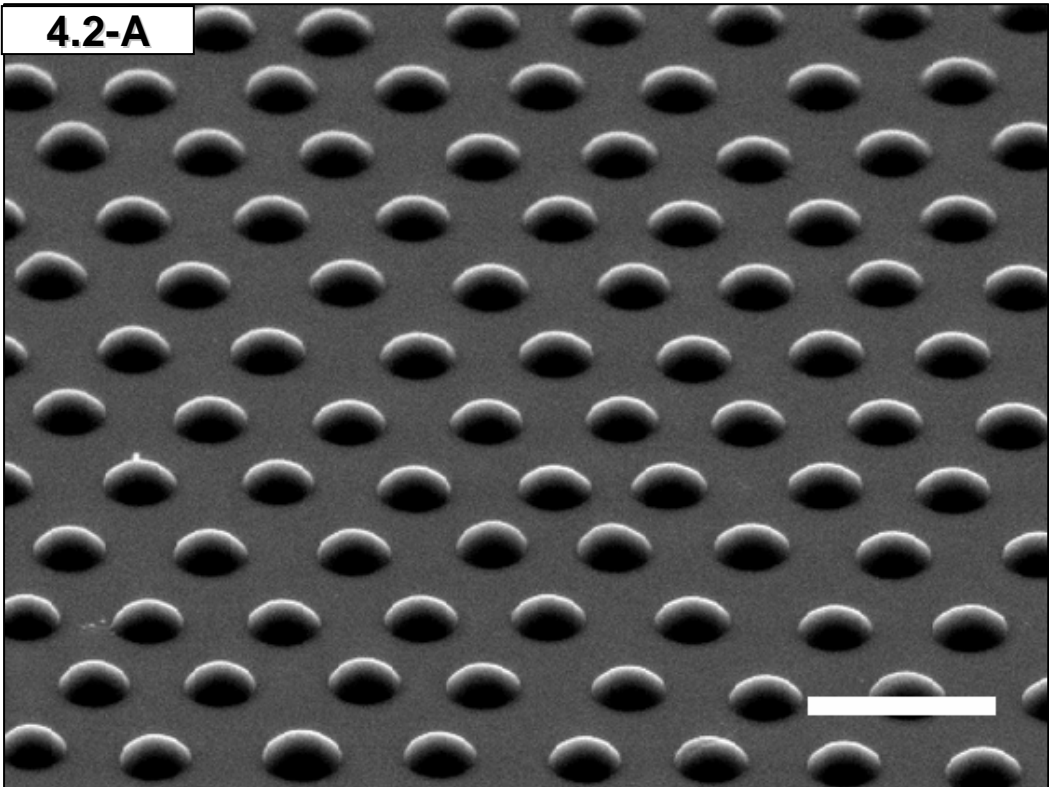
**Figure 4.1** *Imidazole 258 particle patterns after thermal annealing. Micrograph A shows a linear pattern on glass, and micrograph B shows an LB pattern on a stainless steel substrate, both after being annealed at 110 °C for several hours. Individual particles comprising the pattern partially coalesced, forming more continuous pattern features. Scale Bars: 10 and 1  $\mu\text{m}$ , respectively.*



bottom-up approach such as particle self-assembly.<sup>4,5</sup> Although the resulting patterns typically have a higher instance of defects than their top-down counterparts, the results are likely good enough to find usable applications.

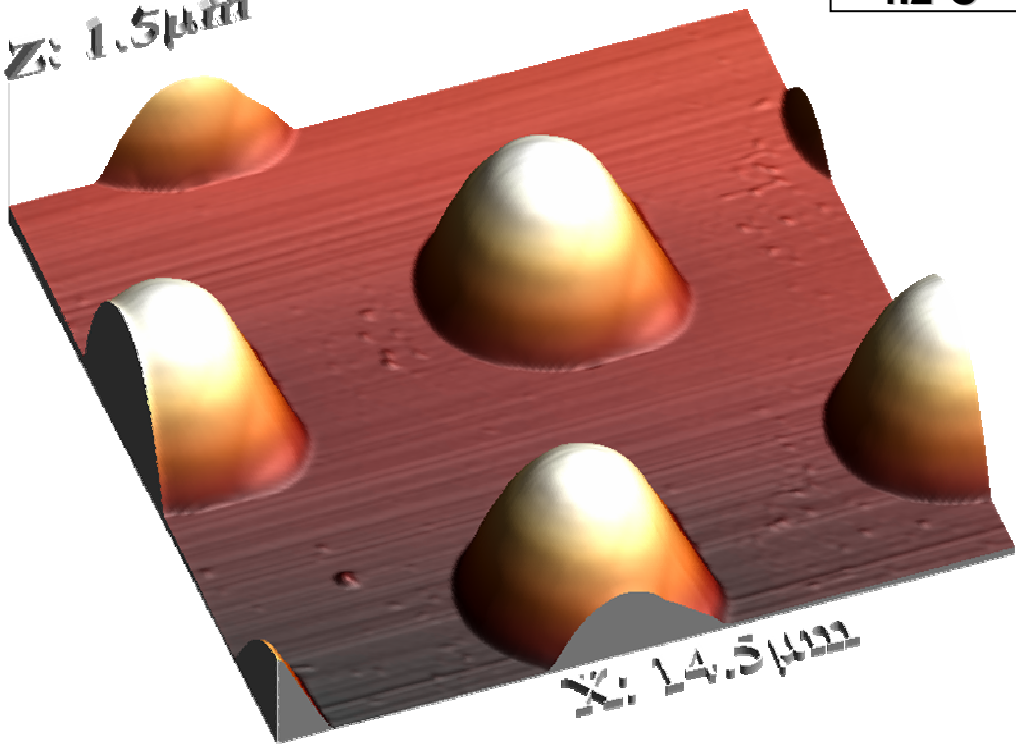
**4.2.2.1 Negative-KOH Etching.** Solvent-fixed patterns transferred by the LS method with the Sulfate 2700 latex were used as masks for selective etching of the native oxide on silicon with KOH. A monolayer derived from TDAC provided a degree of etch-resistance to the bare substrate. Surprisingly, the solvent fixed particles disrupt the etch resistance of the SAM directly beneath them. The polymer particles rapidly dissolved in the basic etchant solution exposing the compromised SAM to the etchant. At times less than 3 min, etching occurred almost exclusively where the particles had been, creating a patterned array of divots in the substrate. The diameter of the divots ( $3.9 \pm 0.1 \mu\text{m}$ , 25 measurements, **Figure 4.2-A**) was approximately equal to or slightly smaller than the diameter of the deformed particle masks ( $4.1 \pm 0.1 \mu\text{m}$ , 25 measurements, **Figure 4.2-B**). The heights of the polystyrene mounds were approximately  $1.5 \mu\text{m}$ , measured by atomic force microscopy (AFM, **Figure 4.2-C**). The depths of the divots were measured by AFM and found to be approximately 200 nm (**Figure 4.2-D**). At exposure times longer than 5 min, etching occurred across the entire surface, resulting in slow degradation of the pattern. Since the particle spacing can be precisely controlled, and the particle-interface contact area can be varied using different solvent fixing conditions, the system is able to be tuned to produce a range of results.

**Figure 4.2** *Negative etching using a particle pattern mask.* (A) SEM micrograph of an array of Sulfate 2700 latex particles after LS transfer to a TDAC-treated silicon substrate and solvent fixing with acetone. Scale Bar: 10  $\mu\text{m}$ . (B) SEM micrograph of the resulting divots in the substrate after etching. Scale Bar: 10  $\mu\text{m}$ . (C) AFM micrograph of the particle mask. (D) AFM micrograph of the resulting divots. (E-F) Optical micrographs showing an expanded view of the etched array. Scale Bars: 20 and 10  $\mu\text{m}$  respectively.



Z: 1.5  $\mu\text{m}$

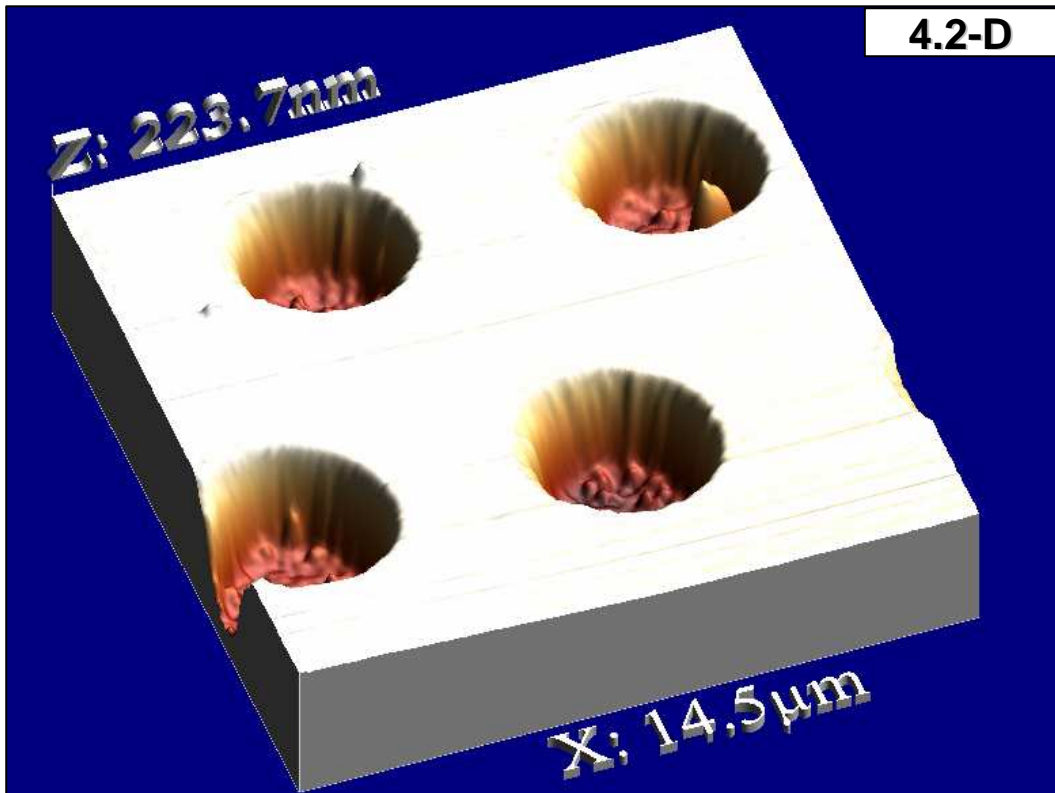
4.2-C



X: 14.5  $\mu\text{m}$

Z: 223.7 nm

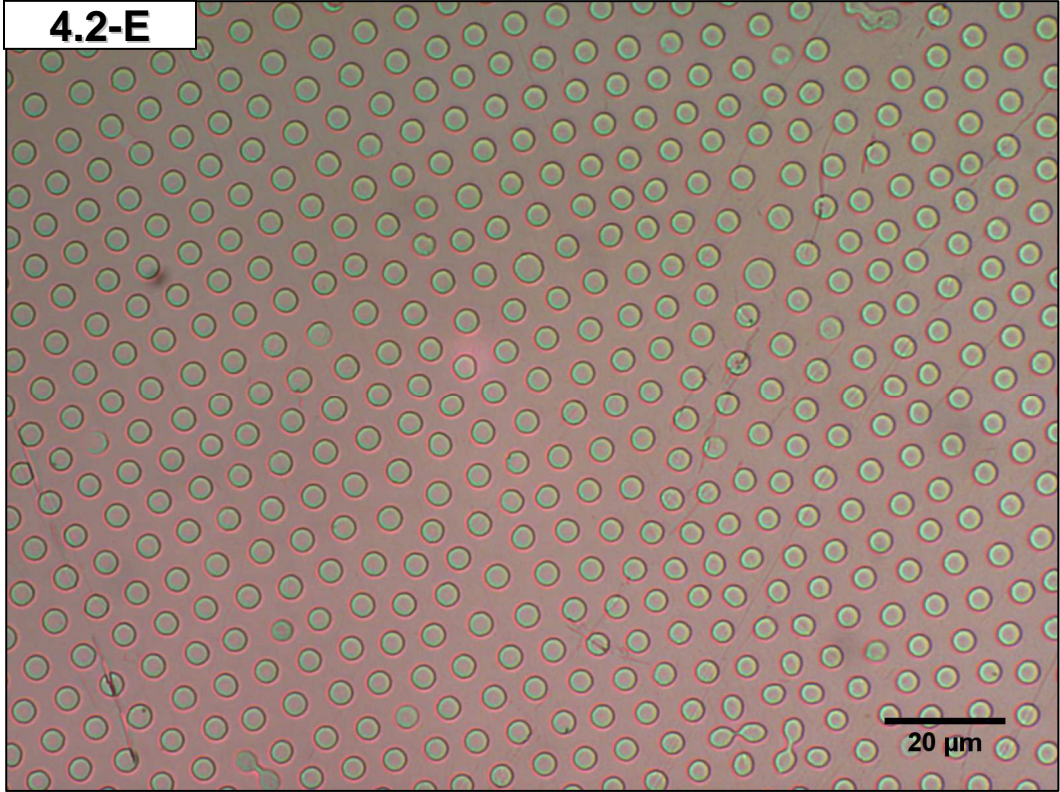
4.2-D



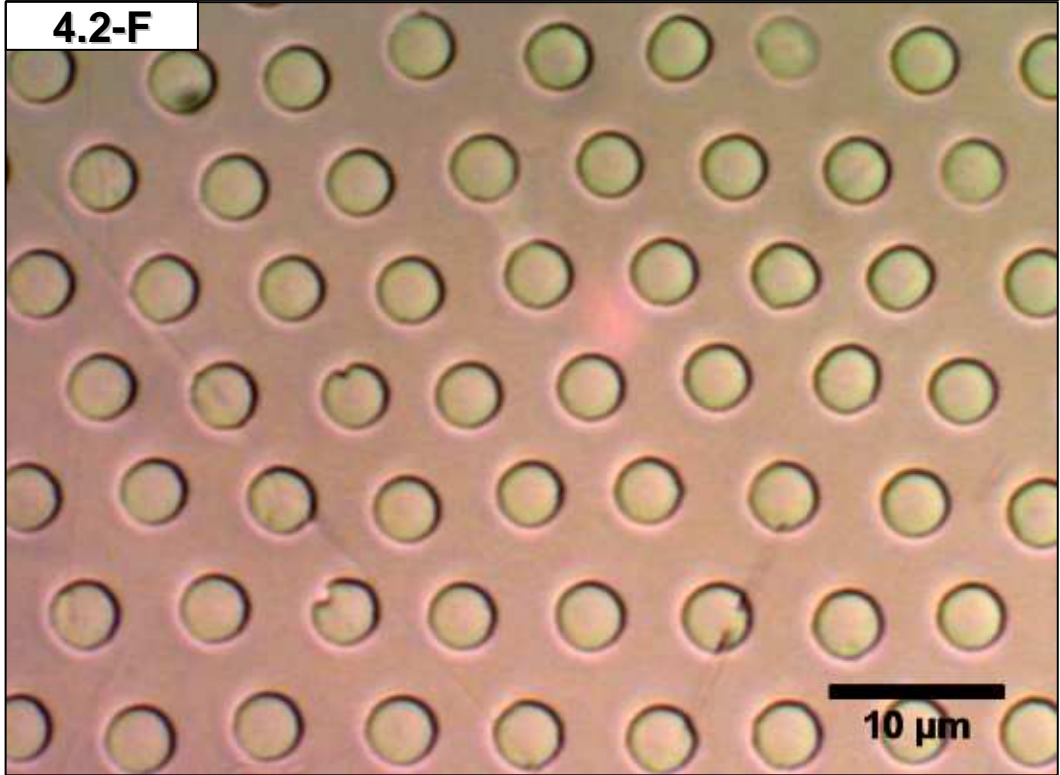
X: 14.5  $\mu\text{m}$



4.2-E



4.2-F



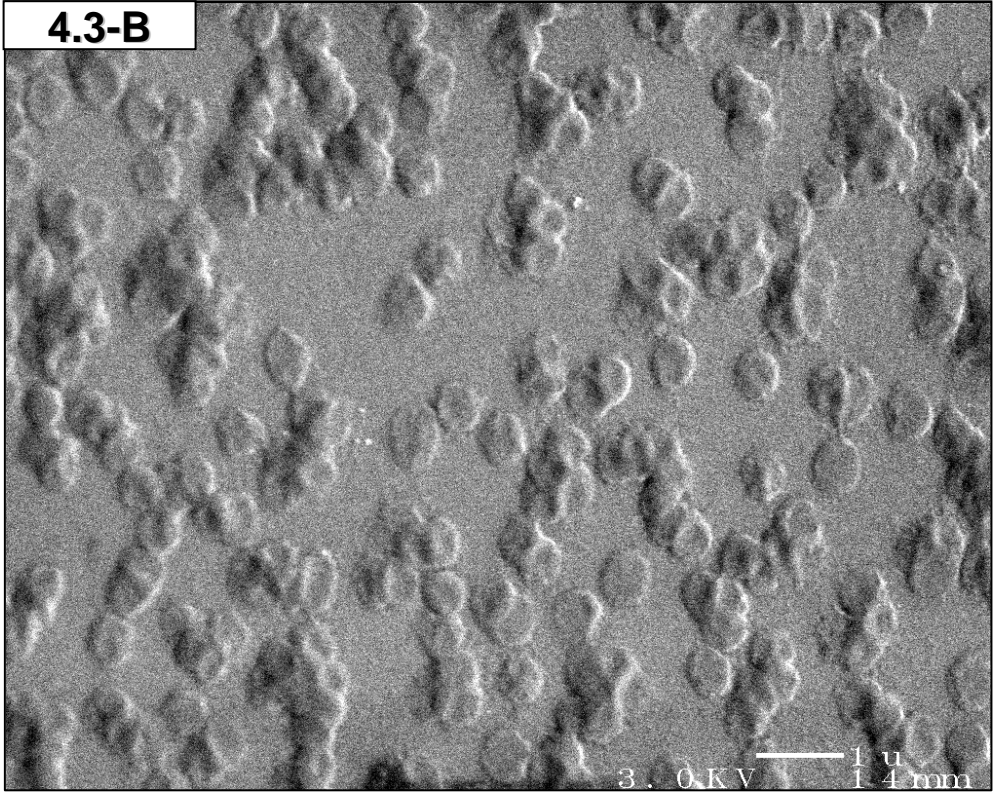
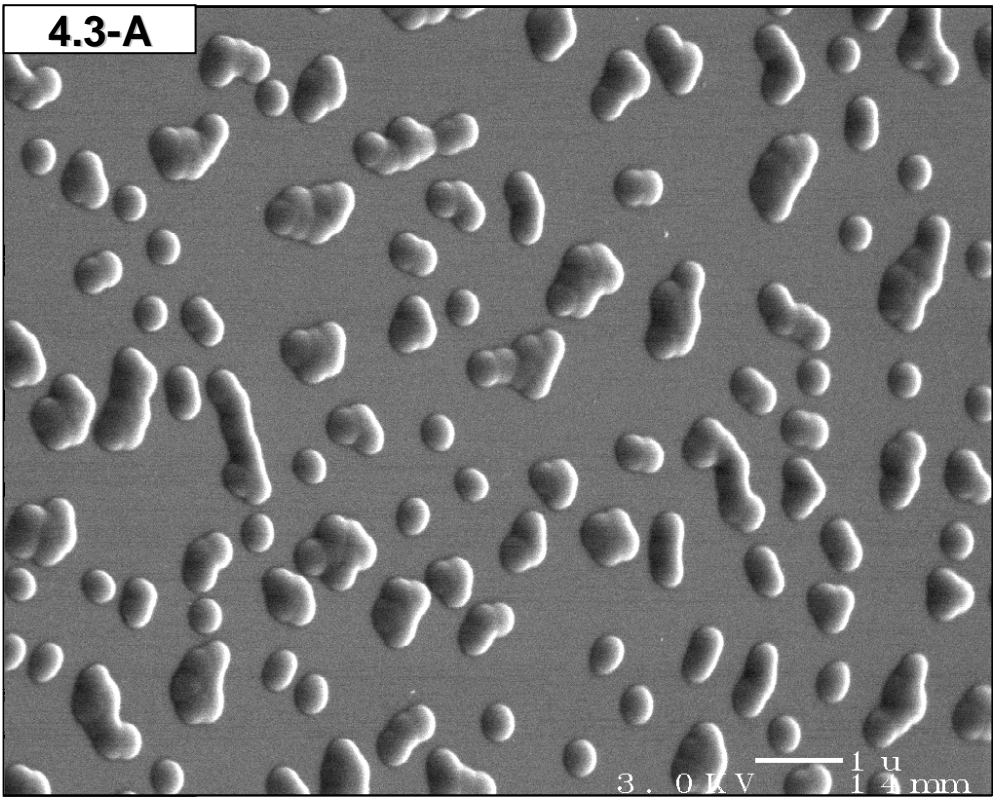


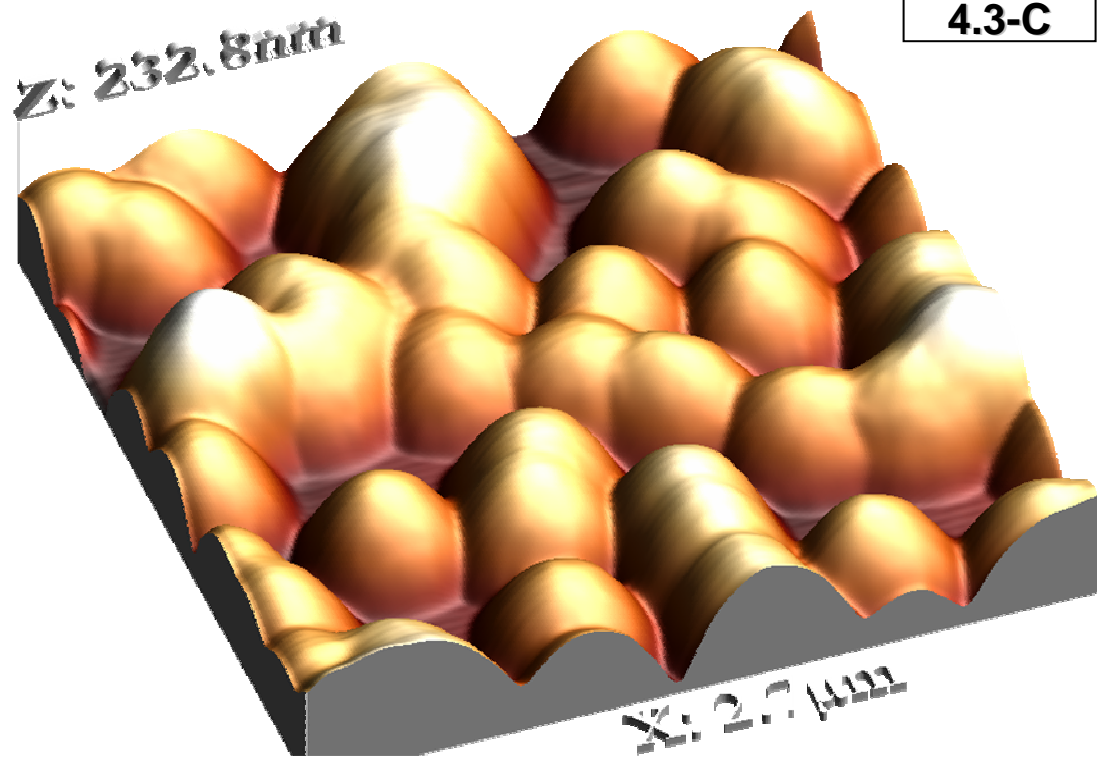
**Negative-Etching Procedure.** After solvent-fixing on TDAC-treated substrates, the pattern (shown in **Figure 4.2-A**) was etched into the silicon wafer substrate. The etchant consisted of 20 wt % KOH in a 4:1 solution of DI water and IPA. Patterned, solvent fixed, substrates were placed in the etchant solution at 60 °C for 3 min. The reaction caused bubbling at the surface of the substrate due to the production of hydrogen gas.<sup>6</sup> The substrates were then removed, rinsed sequentially with IPA, Toluene, IPA, DI water, and then blown dry with a nitrogen jet. The resulting array of divots is shown in **Figure 4.2-B**.

**4.2.2.2 Positive-HF Etching.** Hydrofluoric acid is a strong etchant for SiO<sub>2</sub>, but has little effect on polymeric materials. As a result, areas of a substrate underneath a particle mask were protected, and the HF etched around the polymer mounds into the substrate. The depth of the etch was controllable by the exposure time, however, long exposure times resulted in a loss of resolution. The HF partially etched under the edge of the particle mask, causing the features to become irregular.

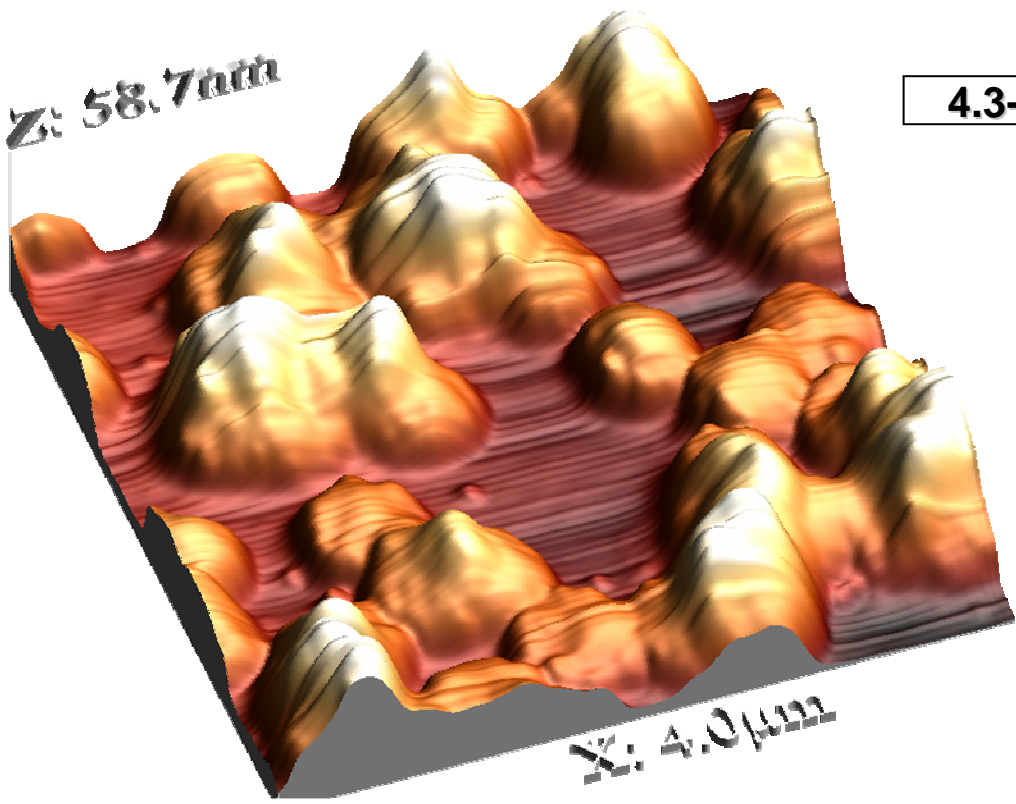
**Positive-Etching Procedure.** In this experiment, a randomly adsorbed particle layer was used. A clean silicon substrate was placed vertically into 0.2 wt-% Imidazole 258 latex for one min, after which it was removed, rinsed with deionized water, and blown dry with a nitrogen jet. The substrate was then heated at 115 °C for 19 h in a covered Petri dish. The resulting annealed particle array is shown in **Figure 4.3-A**. The substrate was then immersed into 5 wt % HF for 15 s, followed by a rinse with deionized water, toluene, deionized water, and finally was blown dry with a nitrogen

**Figure 4.3** *Positive etching using a particle mask. (A) SEM micrograph of the random particle array after thermal annealing. (B) SEM micrograph of the array after etching. (C) AFM micrograph of the annealed particle mask. (D) AFM micrograph of the array etched into the silicon substrate.*





4.3-C



4.3-D

jet. The configuration of the particles in the array was etched into the silicon substrate, as seen in **Figure 4.3-B**.

### **4.2.3 Gold Nanoparticle Adsorption**

Patterned particle arrays provide an attractive and potentially useful scaffolding for the deposition of additional materials onto the particle surfaces. Since the substrate surface typically bears an opposite charge than the particles for the patterns created in this research, nanoparticles can be selectively adsorbed onto the particles or the substrate. Gold nanoparticles were synthesized according to a known procedure.<sup>7</sup> The surface of the nanoparticles were functionalized with a difunctional thiol-carboxylic acid. The thiol group binds to the gold particle's surface allowing the ionizable carboxylic acid functional group to extend into solution giving Coulombic stability to the particle system at high pH.

**4.2.3.1 Gold Nanoparticle Synthesis.** A  $5.739 \times 10^{-3}$ -M solution of  $\text{HAuCl}_4$  was prepared by dissolving 0.2260 g of  $\text{HAuCl}_4 \cdot 3\text{H}_2\text{O}$  (Aldrich) in 100.0 mL of distilled water. A 0.1699-M solution of trisodium citrate (Aldrich) was prepared by dissolving 4.998 g of trisodium citrate dihydrate in 100.0 mL of distilled water. A  $3.63 \times 10^{-2}$  M solution of sodium 3-mercaptopropionate was prepared by dissolving 0.39 g of 3-mercaptopropionic acid (Aldrich) in 25.0 mL of distilled water then adding 25.0 mL of 0.145 M NaOH (1 eq.) and diluting the final solution to 100.0 mL. 250. mL of distilled water was heated to reflux in a 500-mL round-bottom flask fitted with a reflux

condenser. A 25.0 mL aliquot of the  $\text{HAuCl}_4$  stock solution was added, and the resulting solution was heated to boiling. A 10.0 mL aliquot of the trisodium citrate stock solution, and 0.40 mL of 3-mercaptopropionic acid sodium salt stock solution was then injected into the reaction vessel. The reaction was allowed to reflux for 5 h during which the solution turned from colorless to dark red. The particles were then analyzed by TEM, revealing an average diameter of 15 nm (**Figure 4.4**).

**4.2.3.2 Adsorption Procedure.** A substrate bearing a striped pattern of Imidazole 258 latex particles was placed vertically into the gold nanoparticle solution for 4 hours. The sample was then rinsed with deionized water and blown dry with a nitrogen jet. The patterned region of the substrate had a slight red tint after particle adsorption. The negatively-charged gold particles adsorbed onto the positively-charged latex particles as shown in **Figure 4.5**.

#### **4.2.4 $\text{SiO}_2$ Nanoparticle Adsorption**

Silica particles with an average diameter of 6 nm were synthesized according to a published procedure.<sup>8</sup> Silica particles typically bear a negative charge in suspension, and thus it was possible to adsorb a full layer of  $\text{SiO}_2$  particles onto the positively charged latex surface by Columbic interactions.

**4.2.4.1 Synthesis of Silica Particles.** Silica nanoparticles (*Batch A Silica*) with an average diameter of  $6 \pm 1$  nm (30 measurements, TEM) were synthesized as follows:

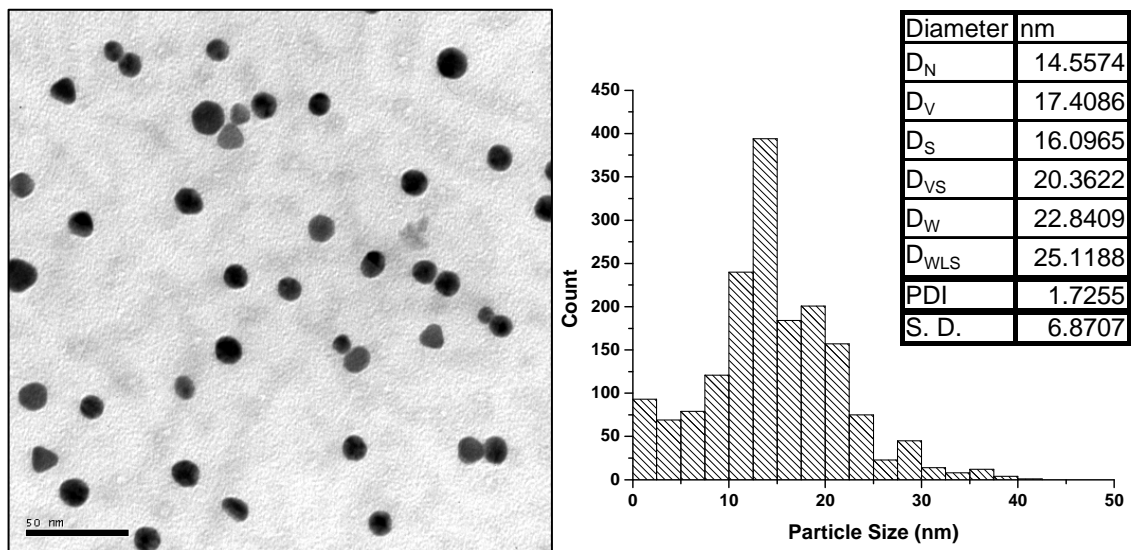


**Figure 4.4** *Particle size distribution analysis for the 15 nm diameter gold nanoparticles. The TEM micrograph shows a sample of the gold nanoparticles synthesized as described in the text. Scale Bar: 50 nm.*

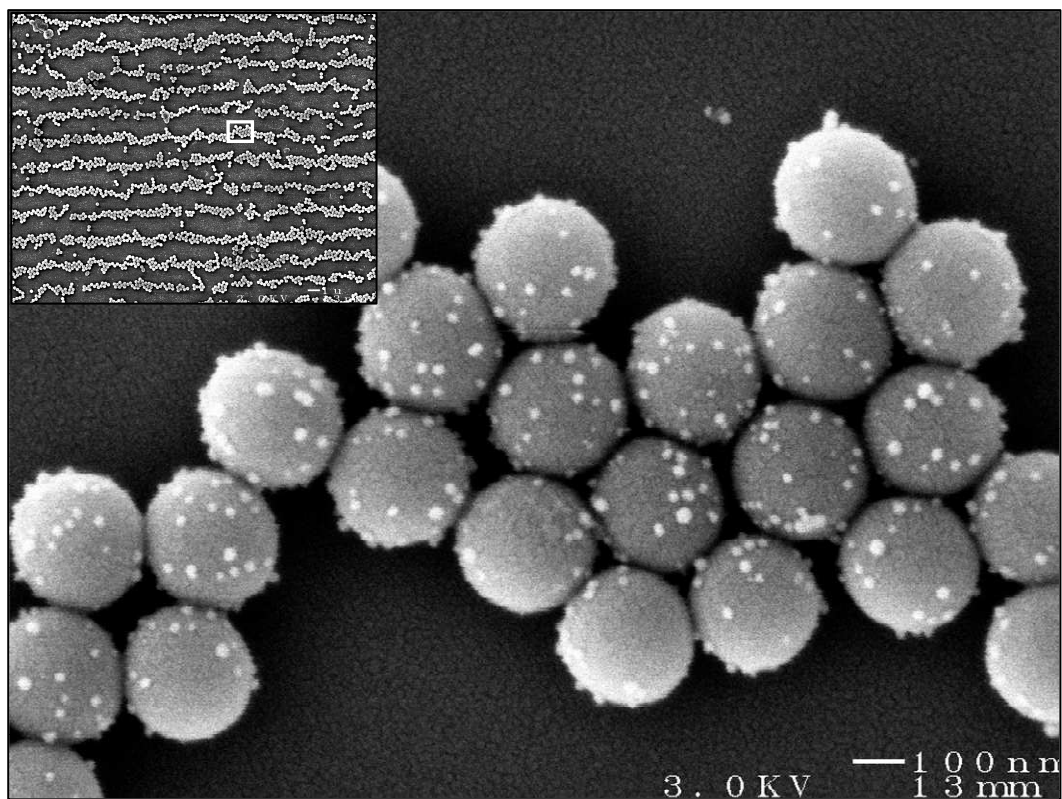


**Figure 4.5** *Gold nanoparticles adsorbed onto a striped pattern of Imidazole 258 latex particles. Scale Bar: 100 nm. The inset (24  $\mu\text{m}$  x 30  $\mu\text{m}$ ) shows an expanded view of the striped pattern, and the white box outlines the magnified region.*

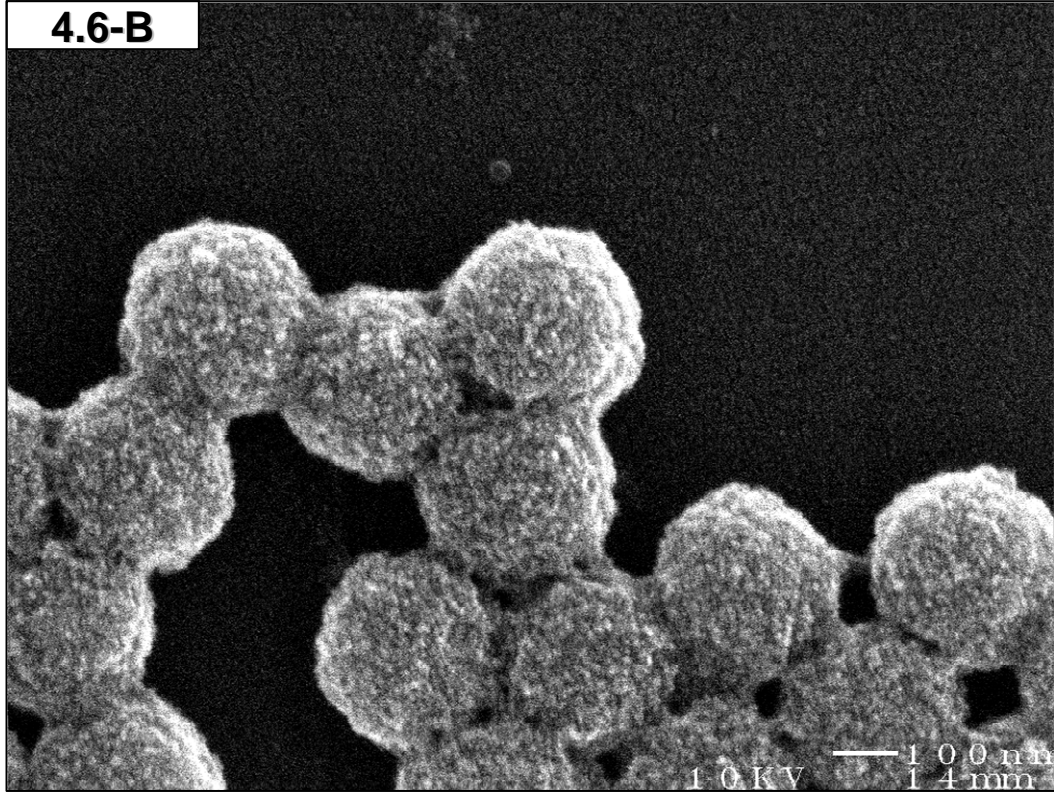
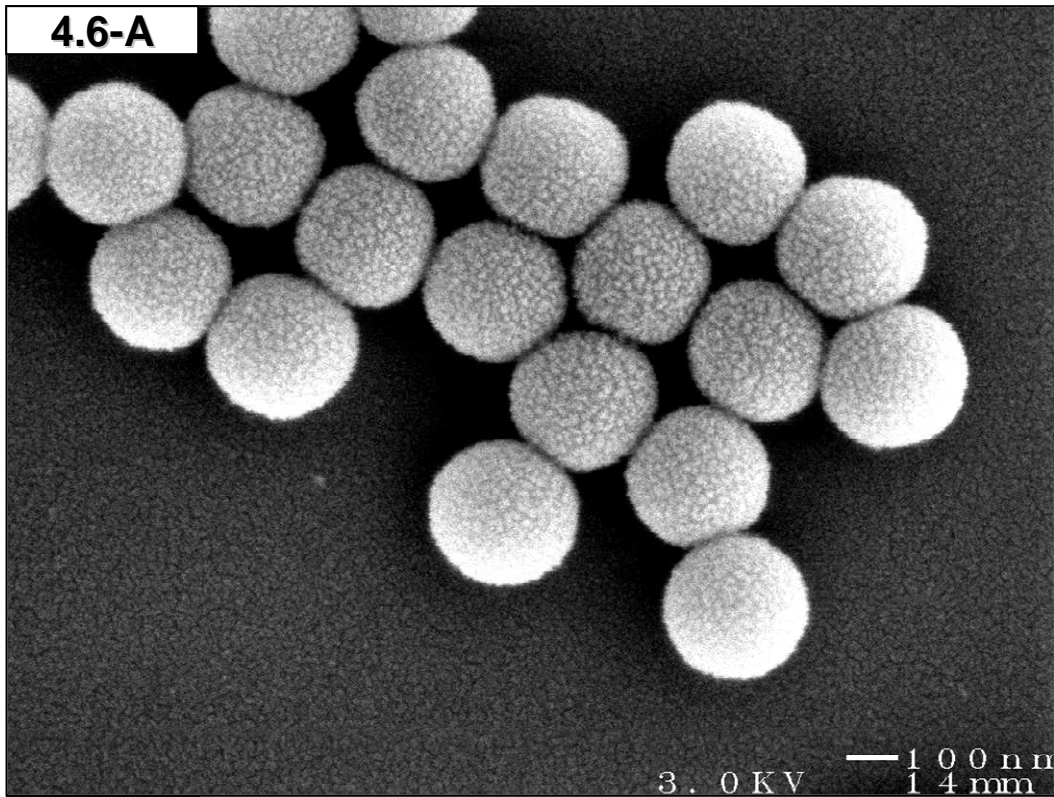


0.21 g of TEOS (tetraethylorthosilicate, Aldrich, 0.0010 mol) was added to 100.0 mL of deionized water with stirring at room temperature. After stirring for 2 hours, 0.46 mL of 0.50 mg/mL NaOH ( $5.8 \times 10^{-6}$  mol) was added. The TEOS:NaOH ratio was 174:1 and produced a 0.060 wt % suspension of SiO<sub>2</sub> particles. The suspension was allowed to stir for 30 days before use.

A more concentrated batch of SiO<sub>2</sub> nanoparticles (*Batch B Silica*) was also prepared: 0.93 g of TEOS (0.0045 mol) was added to 100.0 mL of deionized water with stirring at room temperature. After stirring for 2 hours, 0.50 mL of 0.50 mg/mL NaOH ( $6.3 \times 10^{-6}$  mol) was added. The TEOS:NaOH ratio was 714:1 and produced a 0.26 wt % suspension of SiO<sub>2</sub> particles. The suspension was allowed to stir for 30 days before use.

**4.2.4.2 Adsorption of Silica Particles.** Substrates bearing linear patterns of Imidazole 258 or 391 latex particles were vertically suspended in a sample of SiO<sub>2</sub> suspension for 2-3 hours. The substrates were then removed, rinsed with DI water and blown dry with a nitrogen jet. The thickness of the resulting SiO<sub>2</sub> shell could be controlled by varying the concentration of the suspension or the exposure time. **Figure 4.6-A** shows Imidazole 258 latex particles encapsulated with *Batch A Silica* and **Figure 4.6-B** shows encapsulation with *Batch B*. The textured appearance of the substrate surface is not the result of SiO<sub>2</sub> adsorption, but rather is caused from AuPd sputter coating during the SEM sample preparation procedure.

**Figure 4.6** *Linear patterns of the Imidazole 258 latex after adsorption of SiO<sub>2</sub> nanoparticles. Micrograph A shows a pattern after adsorption of Batch A Silica, and micrograph B shows a pattern after adsorption of Batch B Silica. Scale Bars: 100 nm.*



#### 4.2.5 Formation of Silica Shells

Hollow silica particles can be synthesized by templating inorganic precursor molecules or particles against polymer latex particles and then burning or dissolving away the polymer core.<sup>9, 10</sup> If such an approach is performed using a three-dimensional HCP particle lattice, the resulting material can exhibit nonlinear optical effects.<sup>11, 12</sup> This method was used to transform patterned particle arrays of the Imidazole latexes into arrays of empty silica spheres. The SiO<sub>2</sub> shells, prepared as described above, could be calcined by heating the patterned array at 500 °C for 3 hours. This treatment had two effects on the patterned array: The individual SiO<sub>2</sub> particles were annealed into a continuous shell and the polymer core was oxidized away and effectively burned out of the interior leaving an array of hollow inorganic shells (**Figure 4.7** and **Figure 4.8**).

For striped patterns of the Imidazole 391 latex, a significant amount of SiO<sub>2</sub> adsorbed to the substrate between the particle lines (**Figure 4.7-B**). Surprisingly, SiO<sub>2</sub> did not significantly adsorb to the substrate within approximately 250 nm of a particle line. This phenomenon can be explained by the presence of water soluble polyvinylimidazole (PVI) homopolymer in the original suspension of 0.02 wt % Imidazole 391 latex during the linear patterning process. Immediately after deposition, when the particle lines were still bridged by the wetting film, the dissolved PVI was electrostatically repelled by the like-charged particle lines, and deposited on the substrate upon drying while maintaining a fixed perimeter from the particle lines. Silica was then adsorbed onto these positively-charged regions, as well as the latex particles.

**Figure 4.7** *Linear patterns of the (A) Imidazole 258 and (B) Imiazole 391 latex after adsorbing Batch-A Silica followed by calcination. Encapsulated particles in linear patterns were calcined at 400 °C for 40 min, followed by 2 h at 500 °C. The initial heating step, below the decomposition temperature of the polymer, allows the individual silica particles to crosslink partially before the polymer support is removed. Scale Bars: 1 μm.*

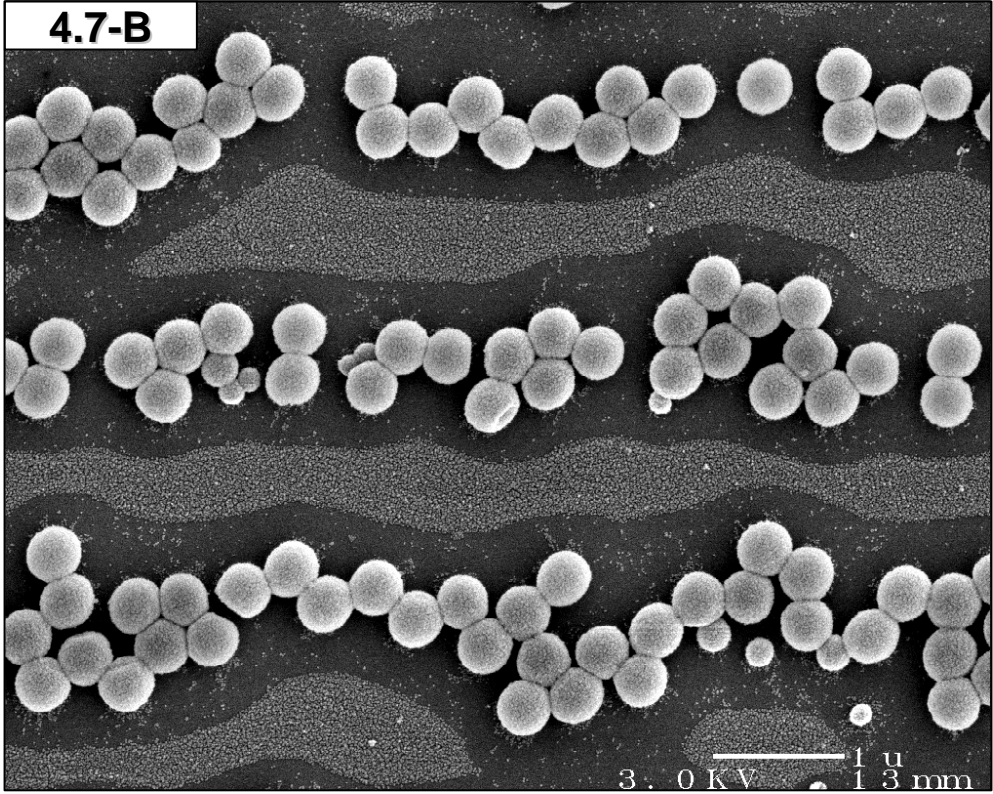
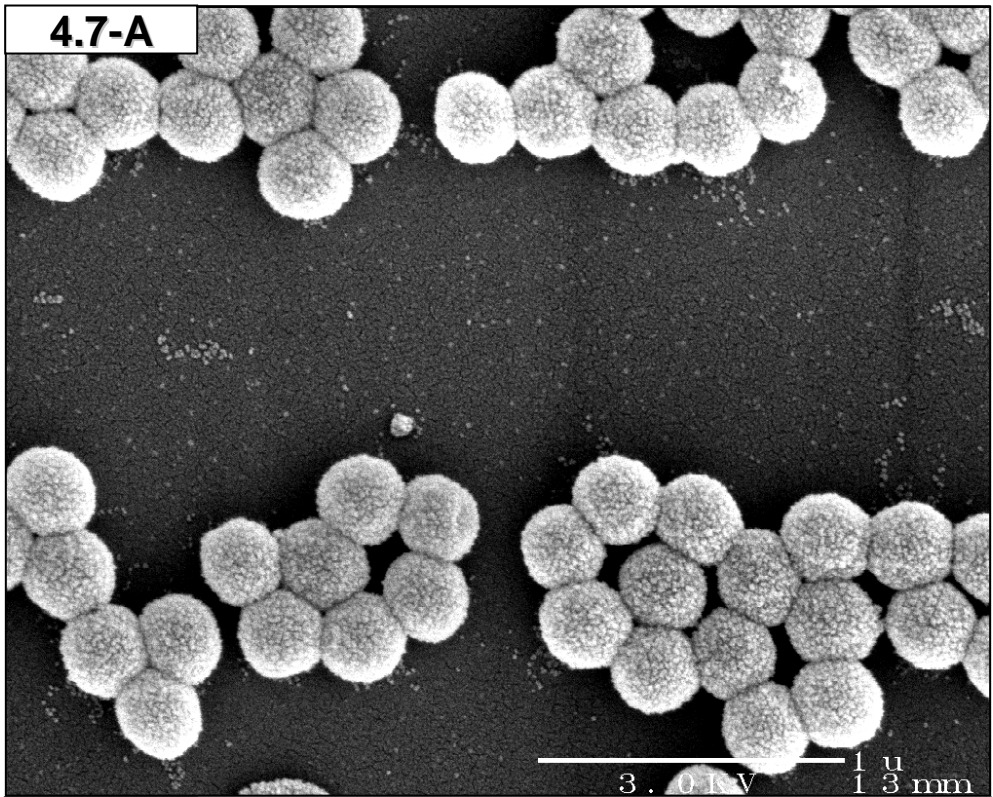
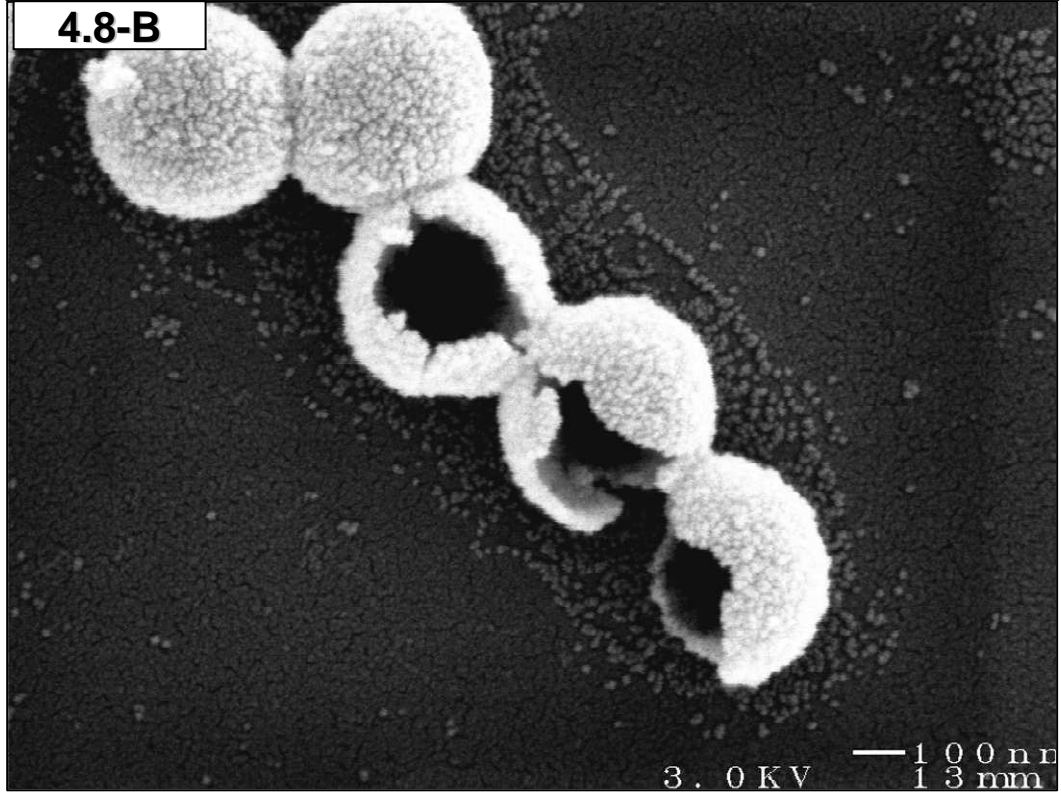
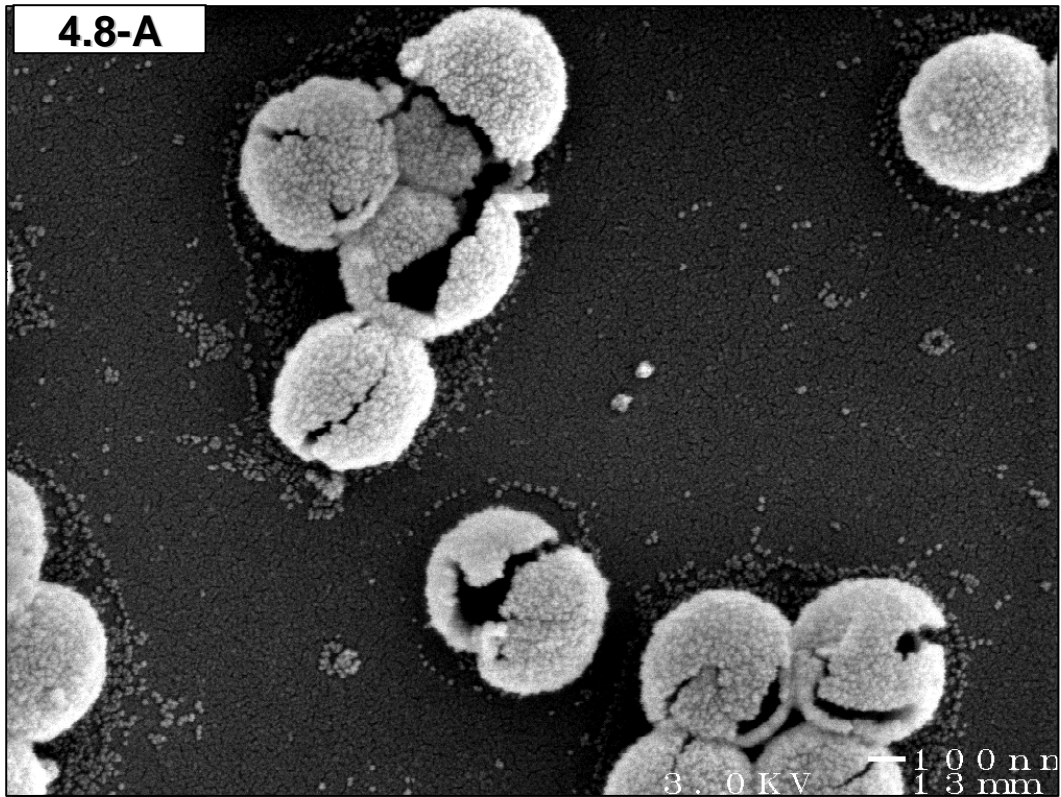


**Figure 4.8** *Partially crushed calcined-silica nanoshells.* These micrographs of shells templated from Imidazole 391 latex particles show the area where the substrate was grasped with tweezers, revealing broken shells. These images allow the void and the shell thickness to be observed directly. Scale Bars: 100 nm.





The Imidazole 258 latex was more rigorously cleaned than the Imidazole 391 latex, which explains why this effect was much less pronounced in **Figure 4.7-A**.

**4.2.5.1 Thermal Properties of the Imidazole 391 Latex.** The decomposition temperature of the Imidazole 391 latex particles was measured using thermogravimetric analysis (TA Instruments TGA). The latex was cleaned by repeated centrifugation-redispersion cycles and then dried under vacuum. Approximately 13 mg of the latex was loaded into the TGA sample pan and heated from room temperature at a rate of 20 °C per minute to 600 °C. The onset of decomposition occurred at approximately 350 °C with a derivative weight-loss peak at 440 °C (**Figure 4.9**).

**4.2.5.2 Calcination Procedure.** Samples were heated using a Barnstead Thermolyne 1500 Series muffle furnace. The heating profile had an effect on the shape of the resulting hollow nanoshells. To allow the silica particles to form a cohesive shell before burning out the polymer core, the samples were heated according to the following profile: 25 to 400 °C in 12 minutes; 400 °C for 40 minutes; and 500 °C for 2 hours. The furnace was then allowed to cool to room temperature overnight. Interestingly, some of the particles developed a small opening near the top of the shell presumably necessary to allow the exit of the gaseous products during polymer decomposition (**Figure 4.10**).

If a faster temperature ramp was used, such as 25 to 500 °C in 12 minutes, and then sustaining 500 °C for 3 hours followed by a cool down to RT overnight, the silica

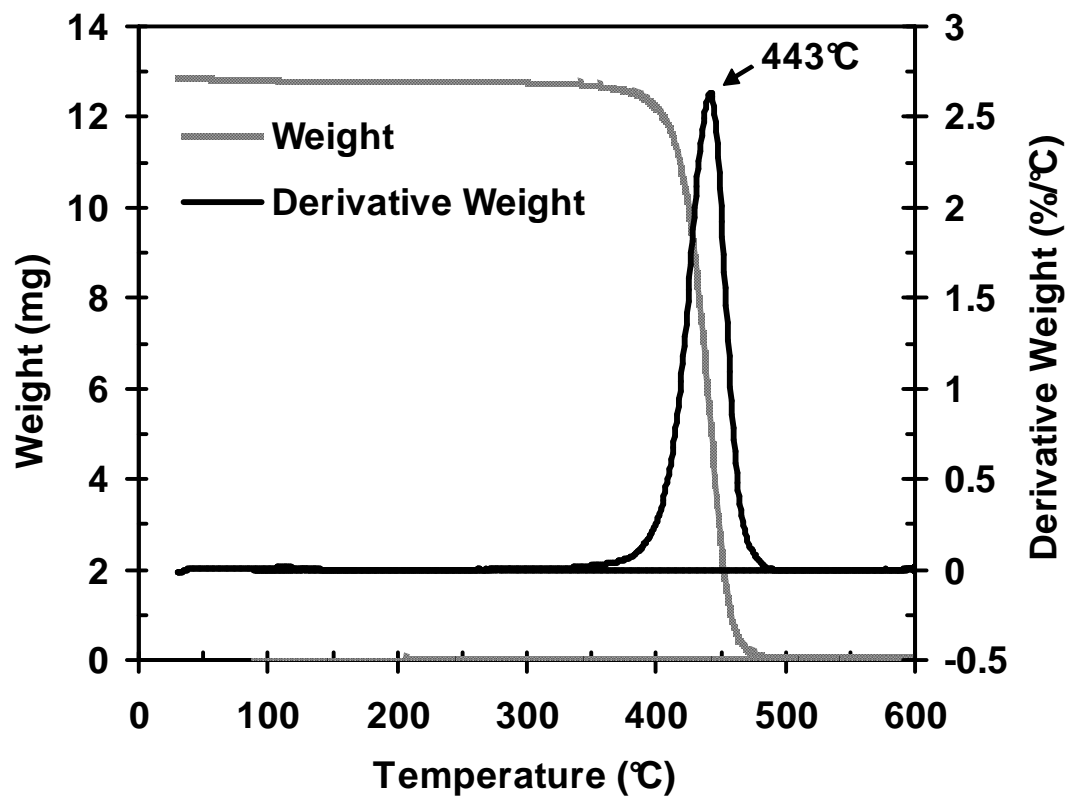


**Figure 4.9** *Thermogravimetric Analysis (TGA) of the Imidazole 391 latex. A 12.9 mg sample of cleaned, vacuumed dried latex was thermally ramped at a rate of 20 °C/min to 600 °C. The decomposition temperature for the Imidazole 391 latex was 443 °C.*

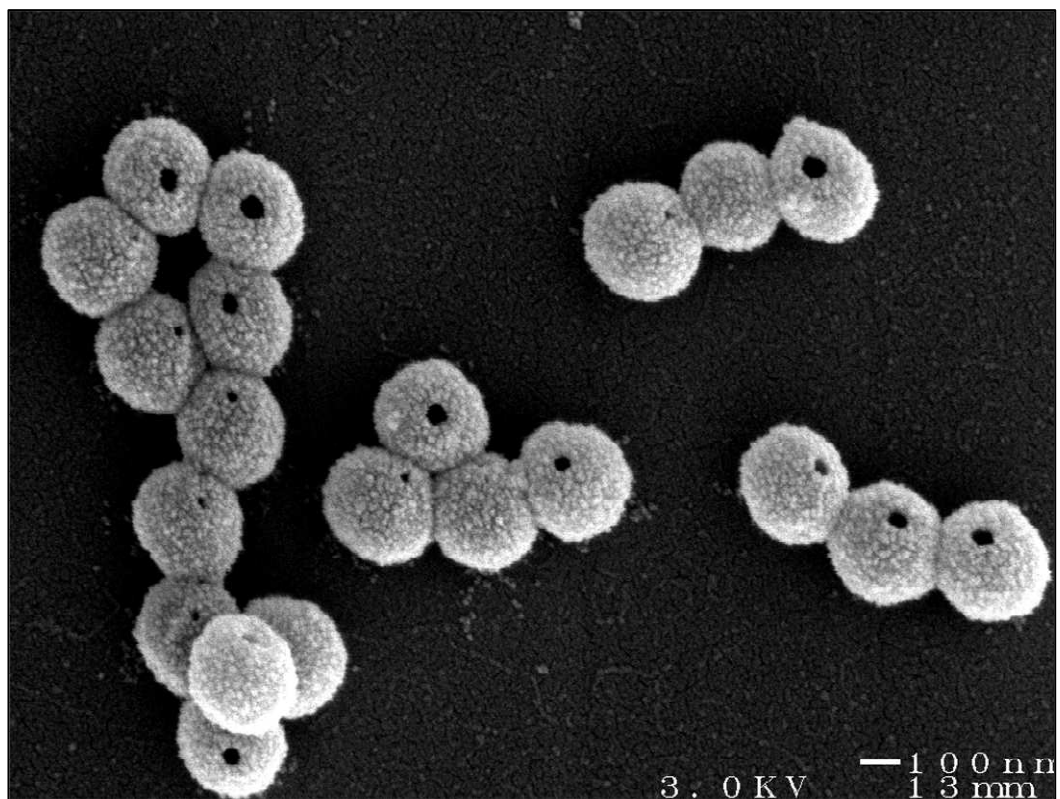


**Figure 4.10** *Silica shells with a chimney.* On the calcined Imidazole 258 substrate (see **Figure 4.7-A**), some regions of the substrate showed particles with small holes. These holes presumably formed as the polymer decomposition products were escaping from the shell, suggesting that the shells are nonporous. Scale Bar: 100 nm.

shells apparently did not have time to sufficiently crosslink before the polymer core burned away and the shells had a deflated appearance (**Figure 4.11**).

#### **4.2.6 Embedding Particle Arrays in PDMS**

Interfacial particle films have previously been embedded into polydimethylsiloxane (PDMS) elastomer following a gel-transfer process.<sup>13</sup> In this method, latex particles were deposited at an interface between *n*-decane and aqueous. After the agarose gelled, the *n*-decane was replaced by PDMS and the particle layer was removed intact along with the elastomer after curing.

A simpler method was developed to embed linear patterns or transferred interfacial particle patterns created in this research work, using Dow Corning Sylgard 184 Silicone Elastomer. This material was supplied as a base silicone oil and a curing agent that was mixed in a 10:1 ratio before use. The patterned arrays of polymer particles on silicon, glass, or stainless steel substrates were placed face up in the bottom of a Petri dish. Several grams of the premixed silicone precursor were then poured into the Petri dish on top of the samples. The Petri dish was then placed uncovered into a desiccator and a vacuum was pulled on the samples for 30 minutes. This process removed the air bubbles that were introduced into the sample during the mixing process. After the bubbling subsided, the surface became very smooth and quiescent. The dish was then removed and placed into an oven at 100-110 °C overnight. The elastomer was then cut around the perimeter of the substrates and removed from the Petri dish still in contact with the substrate. Because the void between the bottom of the substrates and

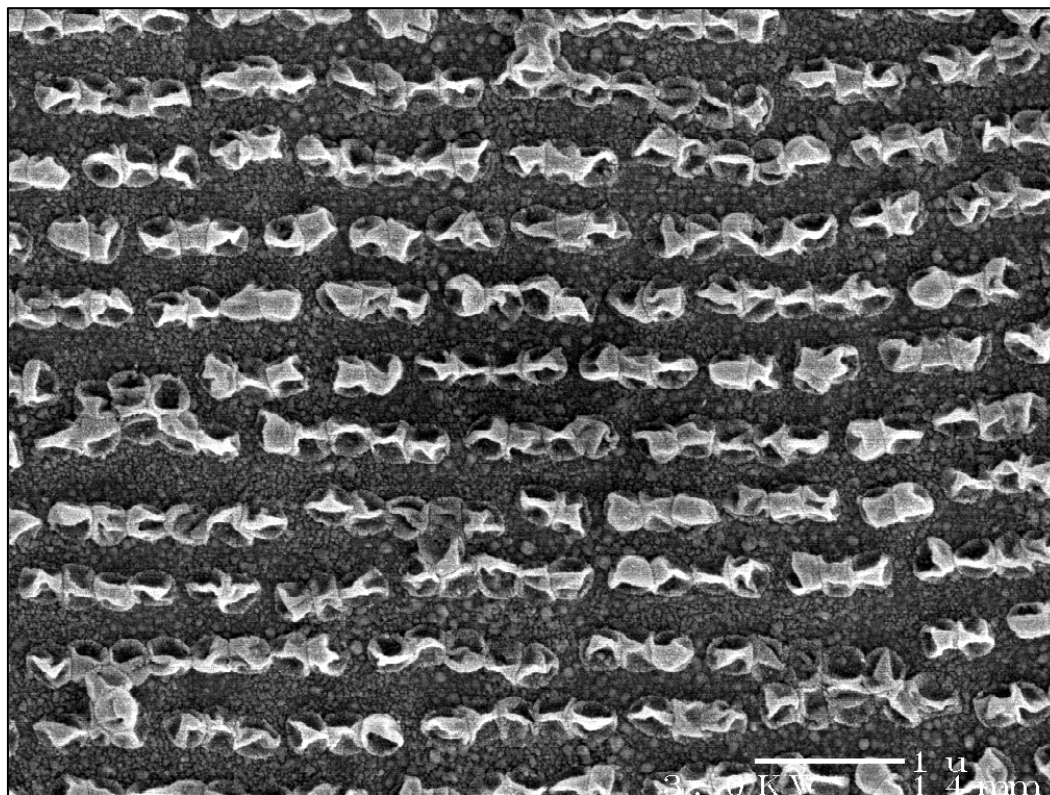
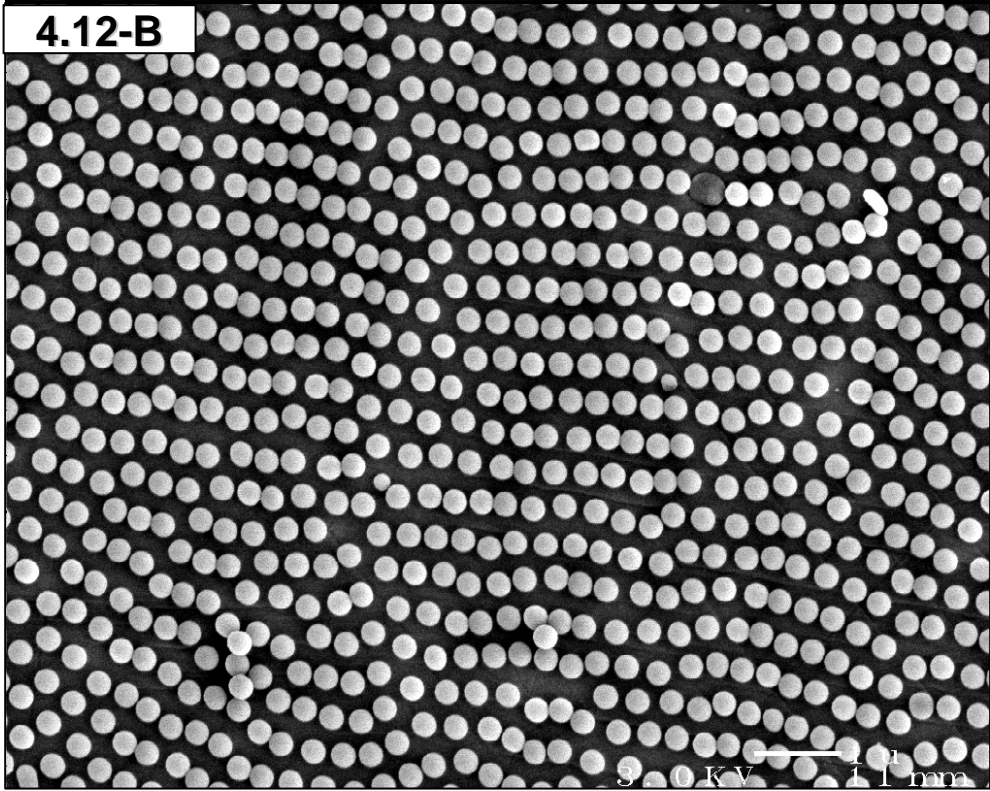
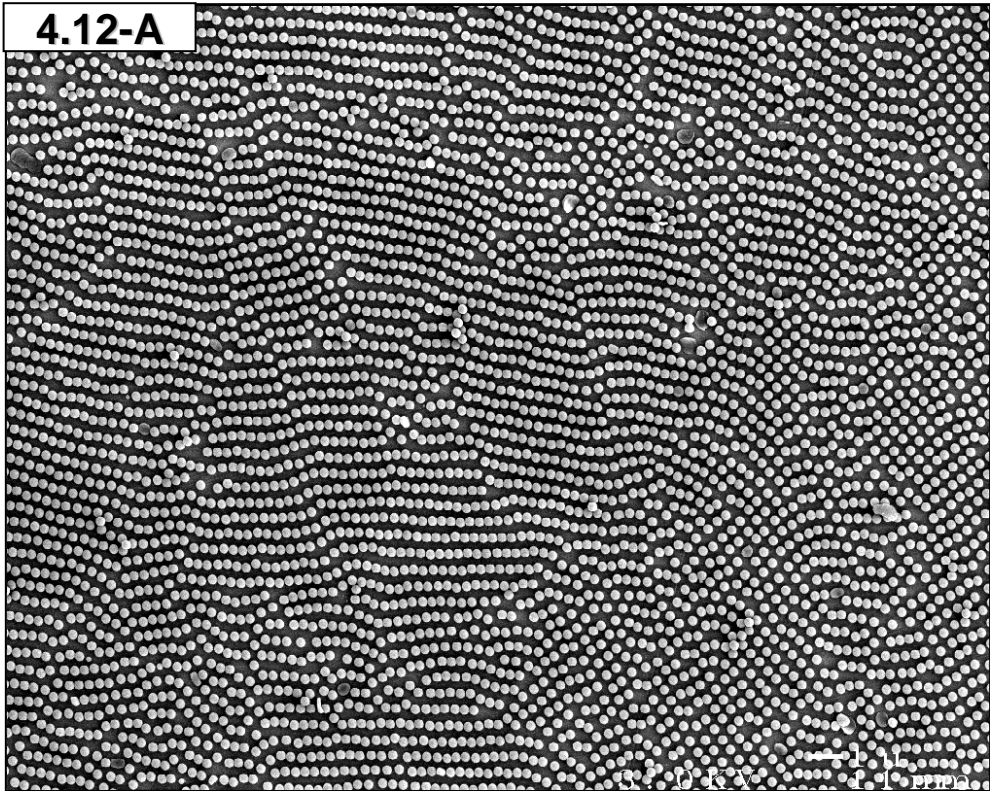


**Figure 4.11** *SiO<sub>2</sub> shells created on stainless steel. An LB pattern of the Imidazole 258 latex was coated with Batch-A Silica and calcined at 500 °C for 3 hours. Omitting the initial heating step at 400° resulted in collapse of the shells. In addition, the substrate surface roughened, presumably by the growth of metal oxides. Macroscopically, the color of the substrate turned brown after the calcination procedure. Scale Bar: 1 μm.*

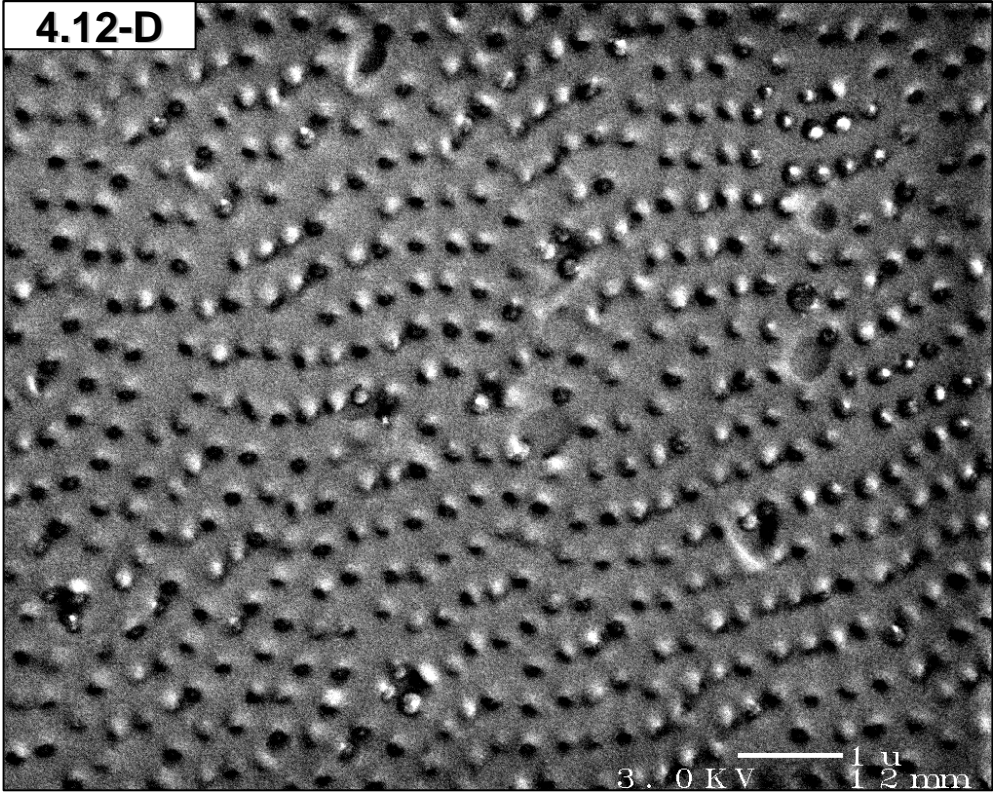
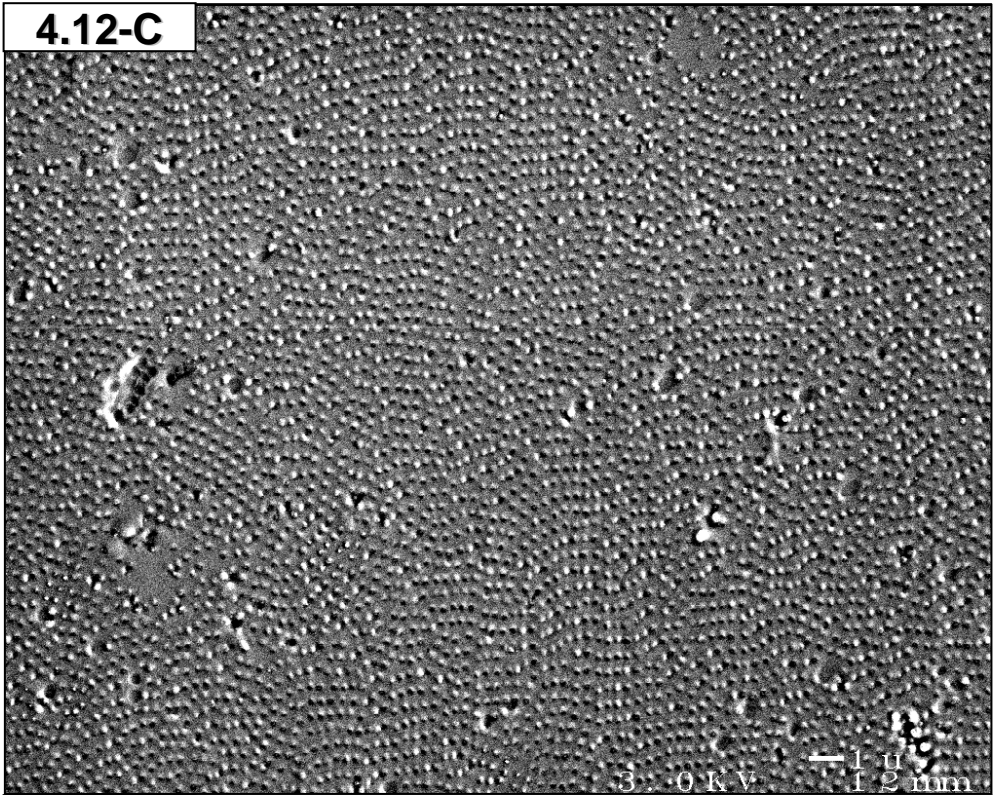
the Petri dish became filled with the elastomer during the evacuation process, it was difficult to remove the substrates from the dish. After the samples were removed, the elastomer was carefully peeled away from the substrate taking the particle pattern with it. Scanning electron micrographs of an LB pattern of Imidazole 258 latex particles transferred by the vortex method to stainless-steel substrates, before (**A** and **B**), and after (**C** and **D**), embedding in PDMS, are shown in **Figure 4.12**.

**4.2.6.2 Stretchable Diffraction Grating.** An Imidazole 258 LB pattern was embedded in PDMS by the procedure outlined above. The embedded array shown in **Figure 4.12-C** and **-D** was prepared in the same batch as the one used for this experiment. The film was stretched along the dipping direction of the original substrate. When placed into a beam of white light, uniform diffraction color was observed across the entire substrate at a shallow viewing angle. The color of the diffracted light could be varied at constant viewing angle and distance (approximately  $15^\circ$  and 30 cm respectively) by stretching the film. In fact, it was possible to vary the color from violet completely through the spectrum to red by this method. In this way, the diffraction conditions for the grating were changed by physically varying the grating spacing instead of varying the viewing angle, as with a conventional grating. The stretchable particle array behaved like a spectroscopic strain gauge.

**Figure 4.12** *Patterned array of Imidazole 258 latex particles embedded in PDMS Elastomer. Macrographs A and B show an interfacial pattern transferred to a stainless-steel substrate by the LB-vortex method. Micrographs C and D show pattern prepared by the same process after being embedded in PDMS elastomer and then being peeled from the substrate surface. The particles cleanly transfer from the substrate leaving no visible residue. Scale Bars: 1  $\mu\text{m}$ .*



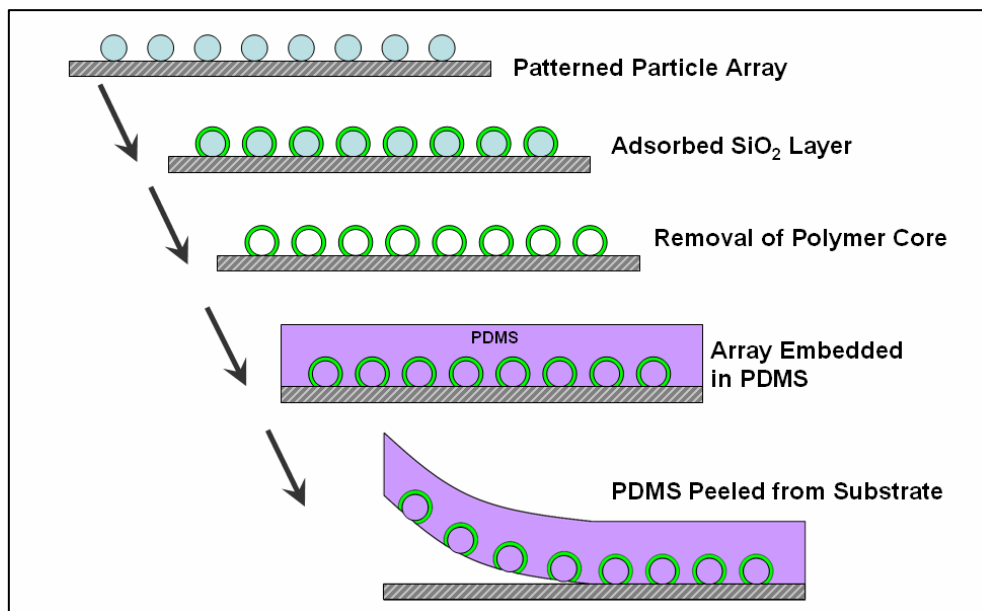




#### 4.2.7 Nanopore Synthesis

By combining the formation and embedding procedures, an attempt was made to construct a PDMS surface with silica-lined pores. Such a material would be interesting because functionalized silane monolayers could be selectively placed onto the interior surface of the pores. Unfortunately, these pores became filled with PDMS during the procedure. The process is represented schematically in **Figure 4.13**.

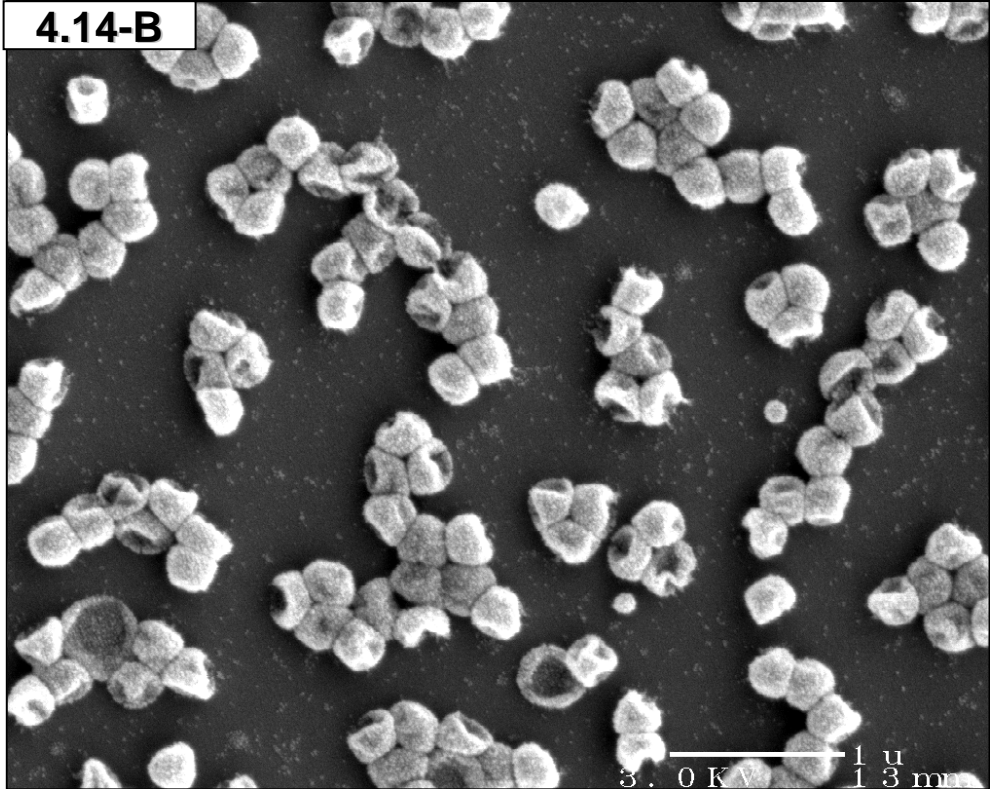
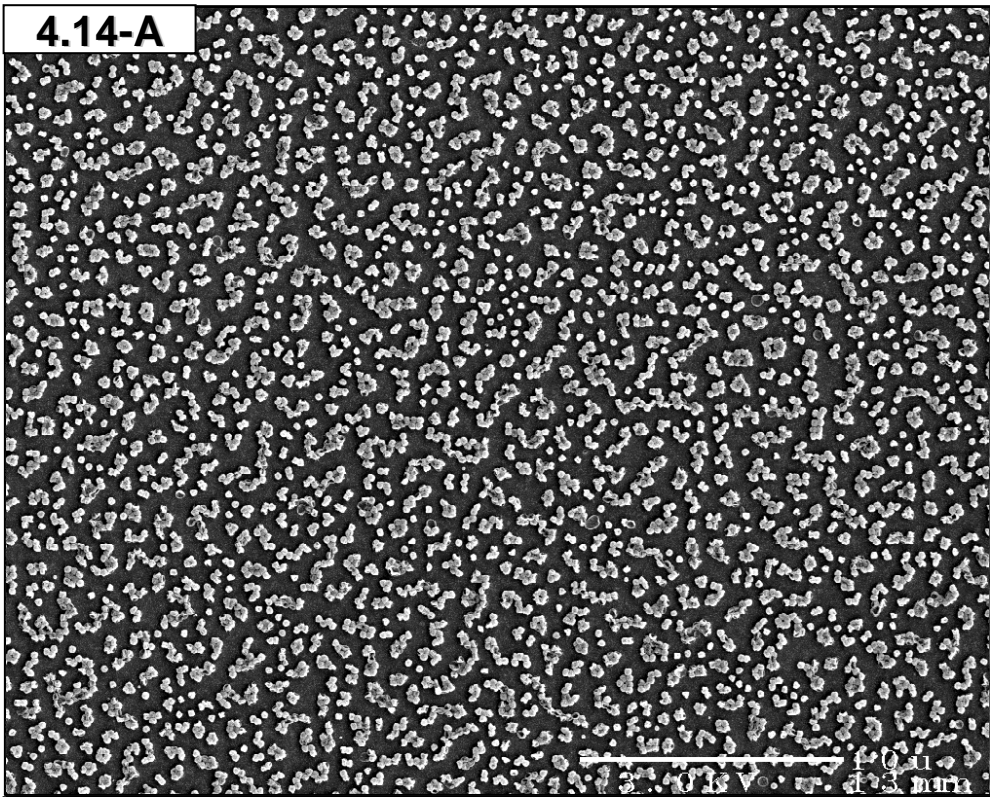
**4.2.7.1 Experimental Procedure.** The process was performed using a randomly adsorbed layer of Imidazole 258 latex particles on clean glass. The substrates were first placed vertically into 0.2 wt % latex for 30 minutes, rinsed with deionized water, and blown dry with a nitrogen jet. The substrates were then placed vertically into a sample of Batch-A Silica for 2 hours, rinsed with deionized water, and blown dry with a nitrogen jet. The samples were calcined as outlined in **Section 4.2.5.2**. **Figure 4.14-A** and **-B** show the resulting layer of silica shells. The shells were then embedded in PDMS elastomer as described above. It was difficult to remove the PDMS film from the glass substrate. Although the shells fractured, leaving the majority of the shell embedded in the PDMS film (**Figure 4.14-C** and **-D**), the PDMS film also cohesively failed near the base of the shells leaving behind small deposits on the glass surface (**Figure 4.14-E** and **-F**). In addition, the broken shells appeared to be filled with the elastomer, which likely occurred during the degassing step of the PDMS preparation.

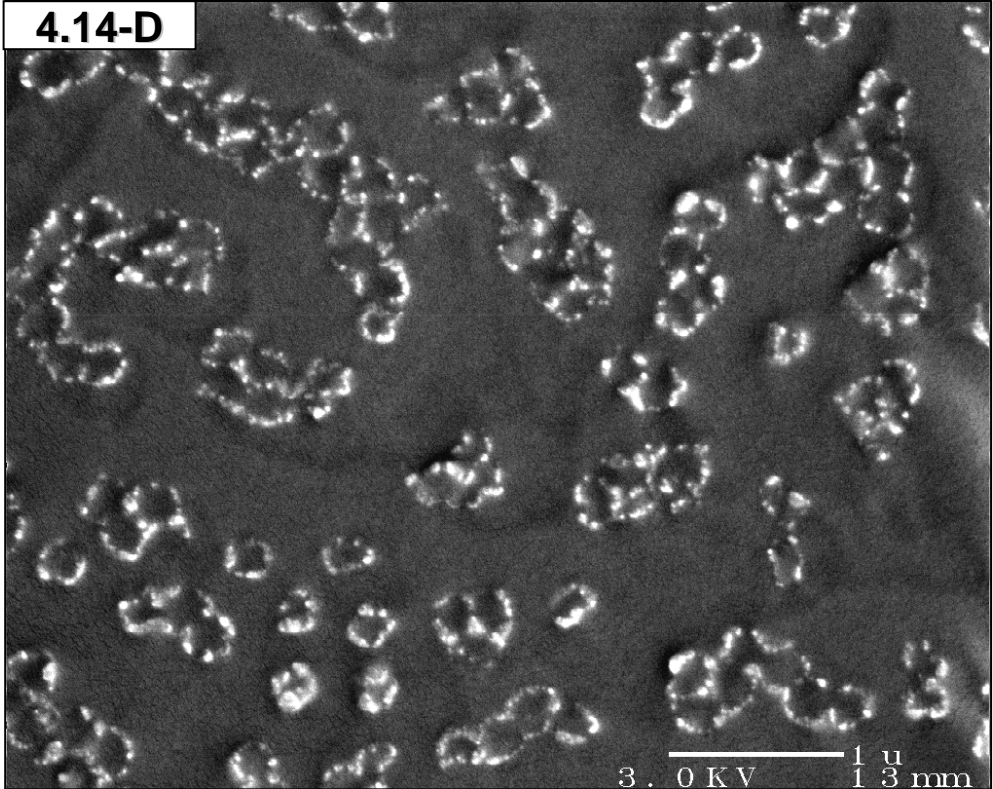
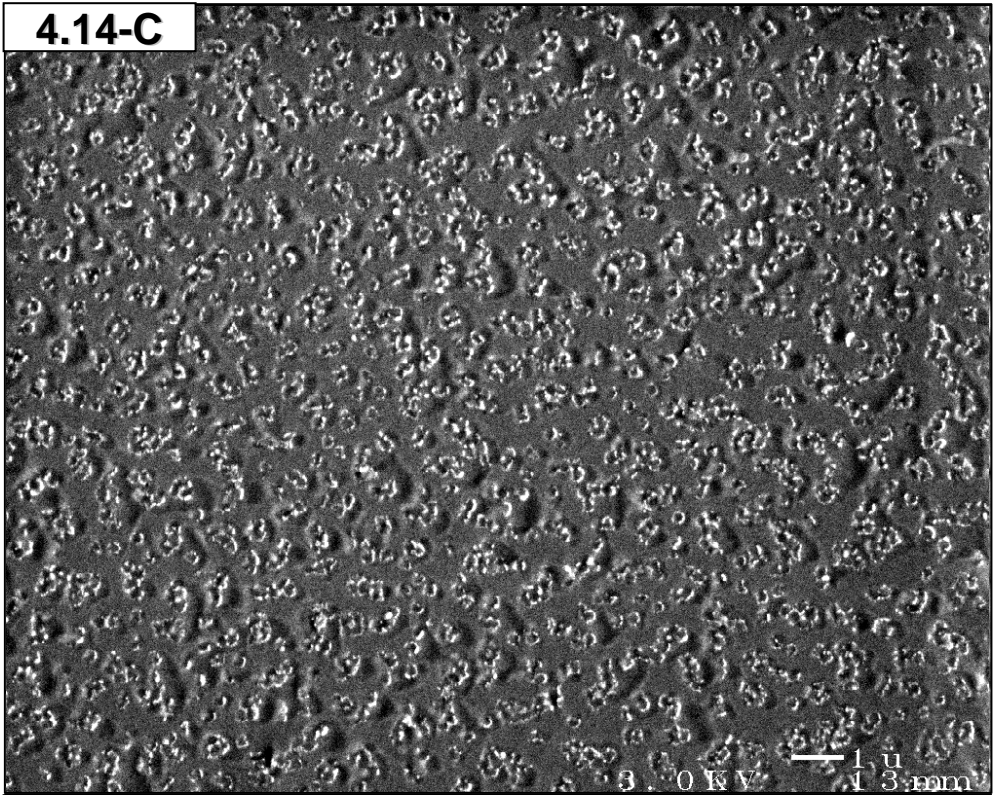


**Figure 4.13** *Attempt to produce patterned SiO<sub>2</sub> nanopores embedded in PDMS.*

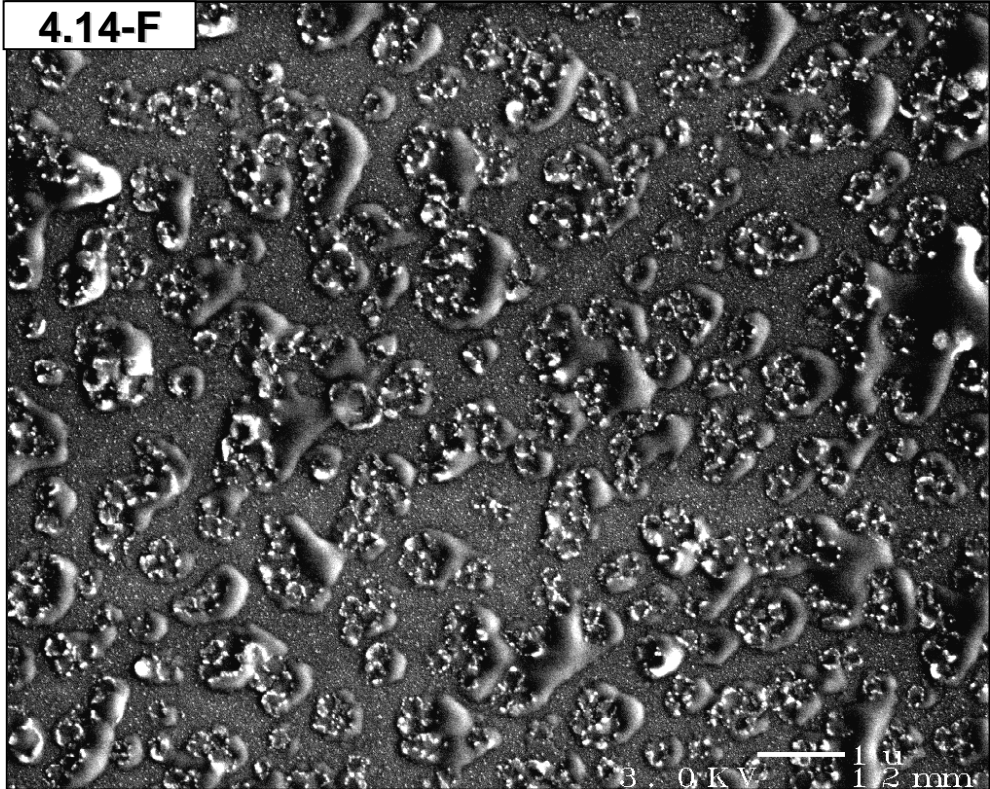
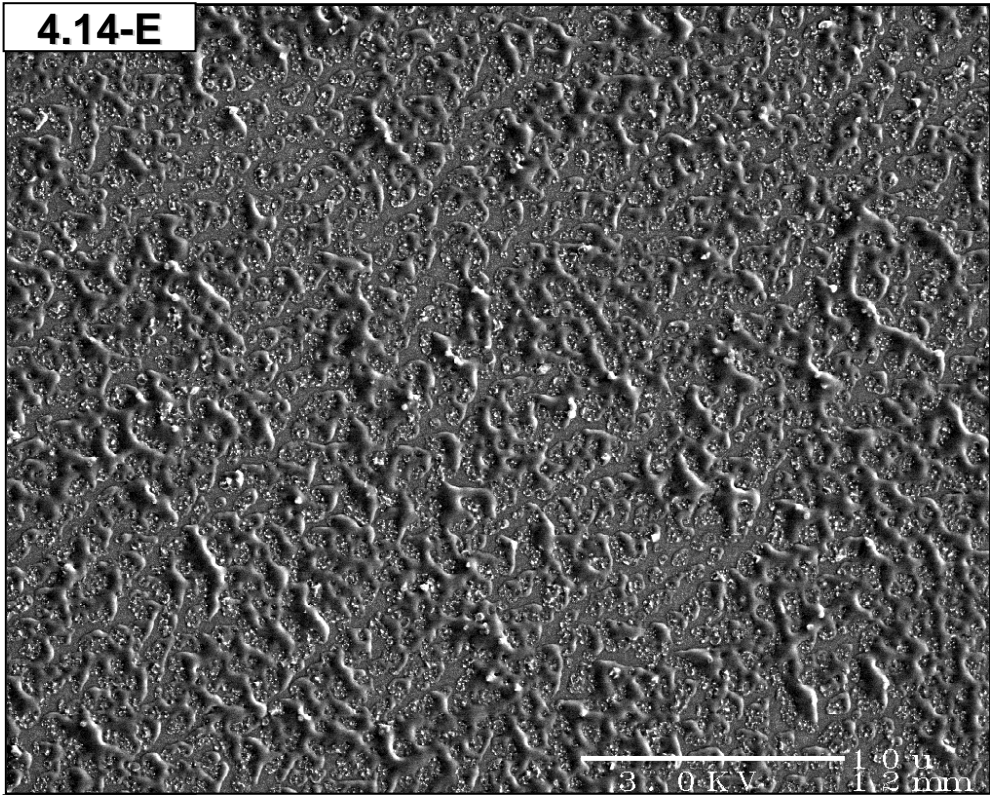
*Experimental results are shown in Figure 4.14.*

**Figure 4.14** *Experimental results of the nanopore synthesis. Macrographs A and B show calcined SiO<sub>2</sub> shells using a randomly adsorbed layer of Imidazole 258 latex particles on clean glass as a template. Micrographs C and D show the shells after being embedded into PDMS elastomer and peeled from the glass surface. Micrographs E and F show the residual SiO<sub>2</sub> and PDMS left on the substrate. The shells are firmly fixed to the substrate after the calcinations process. As can be seen, fracture occurred above the point of contact with the substrate.*









#### 4.2.8 Deposition onto Patterned Substrates

The following approach combines top-down substrate patterning with bottom-up particle patterning. A significant amount of work has been done in the area of colloidal particle adsorption onto a substrate that has been chemically patterned.<sup>14, 15, 16, 17</sup> In these processes, a substrate surface is patterned with PDMS stamp inked with an appropriate silane or polyelectrolyte. By then placing the chemically heterogeneous surface in contact with a suspension of colloidal particles, selective adsorption occurs at the substrate regions that bear the opposite surface charge and the particles are repelled by the substrate regions bearing the same charge. Even though the particle array takes on the pattern stamped onto the substrate, the particles sequentially deposit onto the substrate by random adsorption. As a result, there is no high degree of order *within* a patterned region.<sup>14</sup> By combining the stamping method with the LB or LS transfer method described in **Chapter 3**, the particles may be put into an ordered state and then selectively transferred to the substrate regions bearing complimentary surface chemistry (**Figure 4.15**). The following proof-of-concept experiment was performed to investigate this possibility.

**4.2.8.1 Experimental Procedure.** A patterned PDMS stamp was obtained through collaboration with another research group.<sup>18</sup> Approximately 2 drops of SPCTS stock solution (2-(4-chlorosulfonylphenyl)-ethyltrichlorosilane, Gelest, 50 wt % solution in toluene) was added to 10.0 mL of anhydrous toluene in a Petri dish. The patterned PDMS stamp was placed into the solution for 10 seconds, removed, and



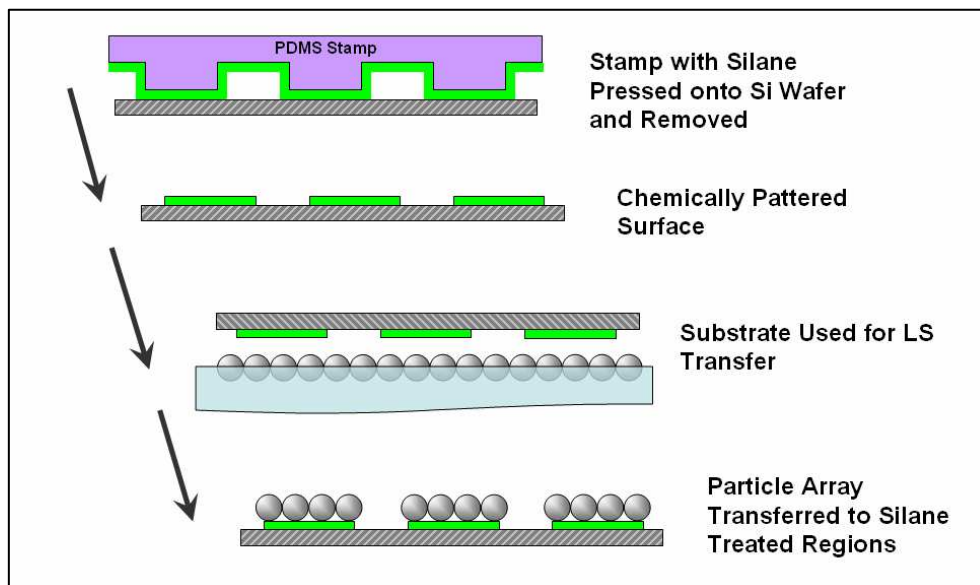


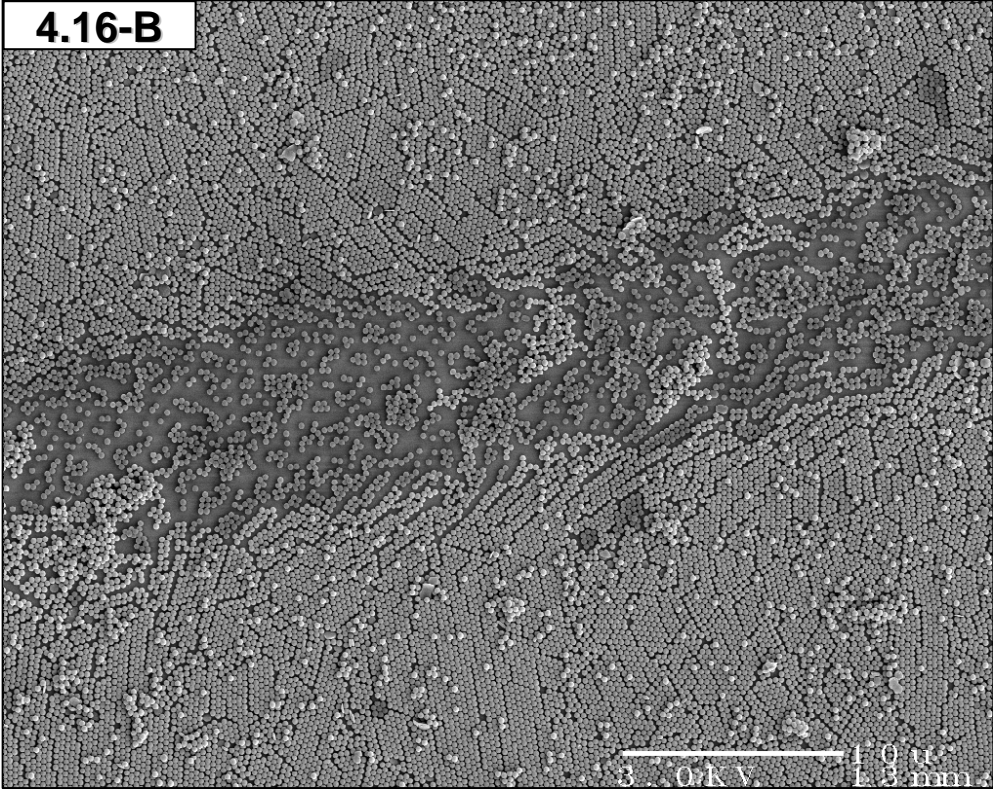
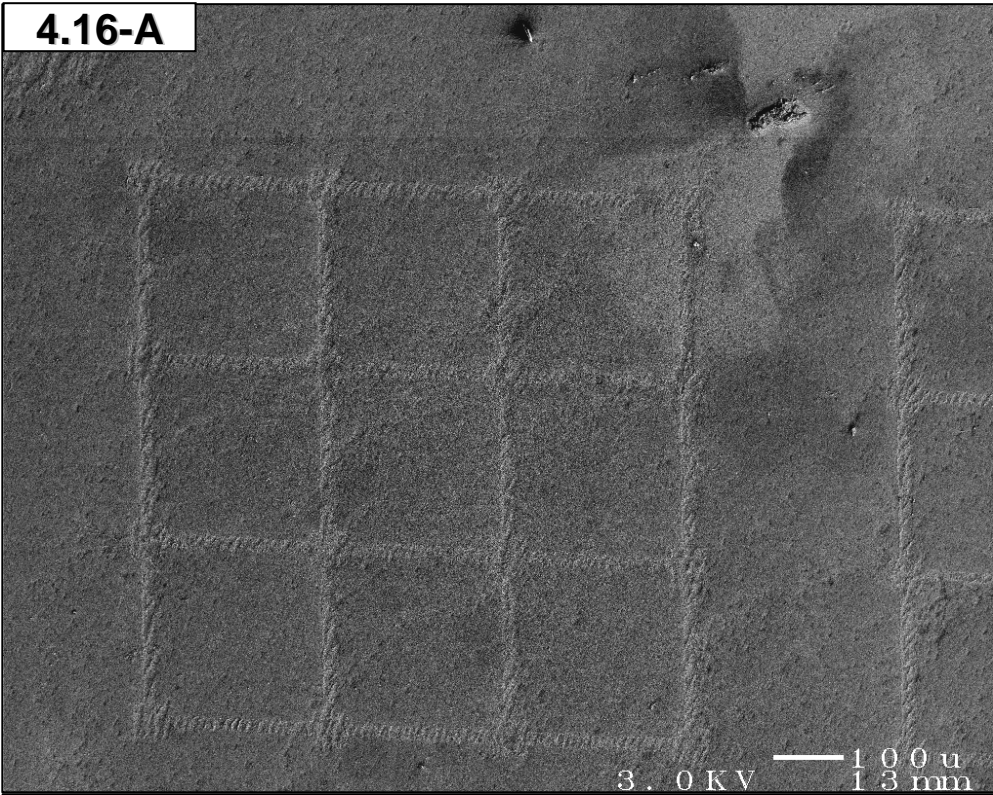
**Figure 4.15** *Schematic illustration of LS deposition onto patterned substrates. The LS transfer substrate was functionalized with a patterned SAM using a PDMS stamp. The substrate was then used to perform an LS transfer, resulting in particle adhesion to the patterned regions.*

blown dry with a nitrogen jet. The stamp was then rinsed with methanol and toluene to remove any aggregates and allowed to dry in air for approximately 30 minutes. The stamp was then pressed onto a clean silicon wafer substrate for 5 seconds and removed. The native surface film on a sample of 0.2 wt % Imidazole 258 latex was then compressed to a surface pressure of 20 mN/m using the mechanical trough. The patterned substrate was used to perform a manual LS transfer. The transferred particle film was then rinsed with DI water and blown dry with a nitrogen jet. The resulting patterned array is shown in **Figure 4.16**. The bare silicon substrate and the SPCTS-treated regions both bear a negative charge. As a result, some particles still adsorbed onto the bare substrate. The particle ordering within a chemically functionalized region of the substrate was superior to examples found in the literature,<sup>16, 17, 18, 19</sup> however, the selectivity was not as good due to random adsorption to the regions of bare silicon. This experiment demonstrates that by combining substrate stamping with Langmuir transfer processes, patterns with a higher degree of complexity could be attained.

#### **4.2.9 Microscopy and Analysis.**

Scanning electron microscopy was performed using a JEOL 6300f or a Phillips XL-30 SEM. All of the SEM samples were sputter-coated with a thin layer of gold palladium alloy (Polaron E5100 SEM coating unit) to make the surface conductive. Optical microscopy was performed using an Olympus BH2 optical microscope, fitted with a PAX-it CCD camera imaging system. Optical and scanning electron micrographs were analyzed using ImageJ<sup>19</sup> version 1.34s. Atomic force microscopy was performed

**Figure 4.16** *SEM Micrographs of an LS transfer onto a pre-patterned, chemically heterogeneous substrate. (A) The squares of the grid are SPTCS-treated, while the grid lines are untreated silicon. (B) Grid-line region at higher magnification. The ordered Imidazole 258 latex particle film transferred to the SPTCS-treated region, while the bare silicon randomly adsorbed particles. Scale Bars: 100 and 10  $\mu\text{m}$ .*



using a Digital Instruments Nanoscope E, LFM-2, and AFM Images were processed using WSxM<sup>20</sup> version 4.0 develop 8.6.

### **4.3 Conclusions**

A variety of methods to increase the complexity and potential usefulness of the self-assembled particle arrays created in this research project were investigated. Although not entirely successful, these experiments represent possible future directions if this work were to be continued. In most of the examples presented, only a few experiments were performed to see if a particular method was feasible for further development. Many of the attempted methods produced results that would merit further investigation.

## 4.4 References and Notes

- 
- <sup>1</sup> Lovell, P.A. and El-Asser, M.S., Eds. *Emulsion Polymerization and Emulsion Polymers*; Wiley: West Sussex, England, 1997, pp 209.
- <sup>2</sup> Fitch, R. M. *Polymer Colloids: A Comprehensive Introduction*; Academic Press: San Diego, CA, 1997, pp 337.
- <sup>3</sup> Special thanks are owed to E. David Sudol for valuable discussions on this topic.
- <sup>4</sup> Burmeister, F.; Badowsky, W.; Braun, T.; Wieprich, S.; Boneberg, J.; Leiderer, P. *Appl. Surf. Sci.* **1999**, 144-145, 461-466.
- <sup>5</sup> Hanarp, P.; Sutherland, D. S.; Gold, J.; Kasemo, B. *Colloids and Surfaces A.* **2003**, 214, 23-36.
- <sup>6</sup> Seidel, H.; Csepregi, L.; Heuberger, A.; Baumqartel, H. *J. Electrochem. Soc.* **1990**, 137, 3612-3626.
- <sup>7</sup> Yonezawa, T.; Sutoh, M.; Kunitake, T. *Chem. Lett.* **1997**, 619-620.
- <sup>8</sup> Rouse, J.H.; Ferguson, G.S. *J. Am. Chem. Soc.* **2003**, 125, 15529-15536.
- <sup>9</sup> Ding, X.; Yu, K.; Jiang, Y.; Bala, H.; Zhang, H.; Wang, Z. *Mater. Lett.* **2004**, 58, 3618-3621.
- <sup>10</sup> Xia, Y.; Gates, B.; Yin, Y.; Lu, Y. *Adv. Mater.* **2000**, 12, 693-713.
- <sup>11</sup> Lopez, C. *Adv. Mater.* **2003**, 15, 1679-1704.
- <sup>12</sup> Manoharan, V. N.; Imhof, A.; Thorne, J. D.; Pine, D. J. *Adv. Mater.* **2001**, 13, 447-450.

- 
- <sup>13</sup> Cayre, O. J.; Paunov, V. N. *J. Mater. Chem.* **2004**, 14, 3300-3302.
- <sup>14</sup> Chen, K. M.; Jiang, X.; Kimerling, L. C.; Hammond, P. T. *Langmuir*, **2000**, 16, 7825-7834.
- <sup>15</sup> Zheng, H.; Rubner, M. F.; Hammond, P. T. *Langmuir*, **2002**, 18, 4505-4510.
- <sup>16</sup> Aizenberg, J.; Braun, P. V.; Wiltzius, P. *Phys. Rev. Lett.* **2000**, 84, 2997-3000.
- <sup>17</sup> Lyles, B. L.; Terrot, M. S.; Hammond, P. T.; Gast, A. P. *Langmuir*, **2004**, 20, 3028-3031.
- <sup>18</sup> Special thanks are owed to **J. Labukas** of the Ferguson research group for kindly donating a PDMS stamp.
- <sup>19</sup> ImageJ analysis software is available free of charge at <http://rsb.info.nih.gov/ij/>.
- <sup>20</sup> WSxM is available free of charge at <http://www.nanotec.es/>.

## Appendix A

### Langmuir Trough Construction and Isotherm Data Processing

#### A.1 First Generation Dipping Apparatus

Parts from a discarded Isco Foxy Fraction Collector (Serial # 121255) were used to construct the dipping apparatus. The right-and-left carriage assembly, which moved along two steel rods and was driven by a DC motor connected to a toothed belt drive, was removed and adapted for up and down motion. A simple driver circuit was designed and constructed to drive the unit. A linear scale was placed on the side of the unit to allow recording of exact start and stop positions. A magnet was placed on the side of the movable carriage to hold a pair of self-locking tweezers in a vertical position. The unit was fixed to a brick for stability as shown in **Figure A.1**. In spite of the crude design, the unit functioned surprisingly well. The dipping rates were calibrated by measuring the amount of time the carriage took to traverse known distances using a stopwatch. The dipping rates could be set by varying the resistance in the controller circuit.





**Figure A.1** *Manual trough and the first generation dipper. This picture shows the typical geometry for the manual trough experiments. The scale on the side of the trough is in cm.*

## **A.2 25 mL Manual Trough**

A 25-mL manually operated Langmuir trough (**Figure A.1**) was milled from a 1"x 3"x 5" Virgin Electrical Grade Teflon Rectangular Bar (McMaster Carr, #8735 K72). Simple drawings drafted to describe the dimensions of the trough and movable barriers were given to the Lehigh Physics Department Machine Shop, where the Teflon milling was performed.<sup>1</sup> A Wilhelmy plate surface tension transducer (NIMA, Type PS3) connected to a NIMA tensiometer display unit was used to collect surface pressure measurements. Voltages from the display unit were routed from the plotter port into an analog to digital converter (Vernier Serial Box Interface) connected to a PC. The sensor was calibrated and data were logged using Vernier Logger Pro Software Version 2.2. Data points were collected at regular distance intervals while manually advancing or retracting the barrier. Surface pressure-area isotherms collected by this trough were crude, however, this trough produced some valuable data and was a significant stepping stone toward understanding the particle self-assembly systems.

## **A.3 Wilhelmy Plate Theory and Operation**

Central to the study of the behavior of interfacial films is the ability to measure the surface pressure of the interface accurately. A number of methods have been devised for doing this, but perhaps the simplest involves a Wilhelmy plate attached to a microbalance. The Wilhelmy plate is partially submerged through an interface and changes in downward force are measured by the microbalance. Wilhelmy plates can be

made from a variety of materials such as platinum, ceramic, or paper. The condition is that the liquid must make a stable and known contact angle with the plate. For this reason, chromatography paper is widely used as a Wilhelmy plate material because it is inexpensive, highly porous, and since water completely wets the surface, has a contact angle of  $0^\circ$ . This also simplifies the math, as the angle term drops out. Surface tension arises from the summation of the unbalanced intermolecular forces of molecules comprising an interface. Surface tension is defined as the work required to expand an interface per unit area at constant temperature, i.e. isothermally. The SI unit for work (N·m or J), and the corresponding unit of surface tension is  $\text{N}\cdot\text{m}/\text{m}^2$  which simplifies to N/m. Because the magnitude of the work involved is relatively small, measurements are typically recorded in mN/m. The cgs unit, dynes/cm, is equivalent to mN/m because 1 dyne is equal to  $10^{-5}$  N such that  $1 \text{ mN}/\text{m} = 1 \text{ dyne}\cdot\text{cm}/\text{cm}^2 = 1 \text{ dyne}/\text{cm}$ . Assuming the thickness of the Wilhelmy plate is negligible compared with the width, the change in surface tension,  $\Delta\gamma$ , is equal to,

$$\Delta\gamma = \frac{\Delta F}{2w} \quad (\text{A.1})$$

in which  $\Delta F$  is the change in force measured by the microbalance and  $w$  is the width of the Wilhelmy plate.<sup>2</sup> Impurities, such as surfactants at an interface, decrease the surface tension of the native interface. Surface pressure is defined as the decrease in surface tension from that of a clean interface. For example, if the surface tension of a particular surface film on water were 52 mN/m, that would correspond to a surface pressure of  $\sim 20$  mN/m since water has a surface tension of 72.13 mN/m at 25 °C.<sup>3</sup> In this way, an

increase in the concentration of surface active agents at the interface results in an increase in the surface pressure.

#### **A.4 Second Generation Dipping Apparatus.**

A stepper motor with a 50:1 gear ratio (Nippon Pulse America Inc., PF35T-48C1G1/50-M) was used to drive a linear belt on which a pair of self-locking tweezers was fixed. The dipping unit was supported by a 3-knuckle adjustable arm (Bogen), which allowed the apparatus to be held in any desired position. The unit was interfaced using a stepper motor controller board (BiStep A06, Peter Norberg Consulting) interfaced with a PC. Simple software routines were written in Microsoft Visual Basic 6 and Microsoft Quick Basic 4.5 to control the dipping apparatus.

#### **A.5 Mechanical Langmuir Trough Construction**

Some of the concepts used in the design of this trough (**Figure A.2** and **Figure A.3**) were patterned after a description given in one of Aveyard's publications,<sup>4</sup> and by studying commercial troughs manufactured by NIMA.<sup>5</sup> The drawings shown in **Figure A.4**, along with most of the needed materials, were given to the Physics Department Machine Shop. The body of the trough was milled from a solid 1 x 3 x 7" bar of virgin electrical grade PTFE (McMaster Carr, #8735 K721). The inner trough was 140 mm in length, 50 mm in width, and 6 mm in height. A 28-mm diameter hole was drilled in the center of the trough which was able to accommodate a plug, well, or window,

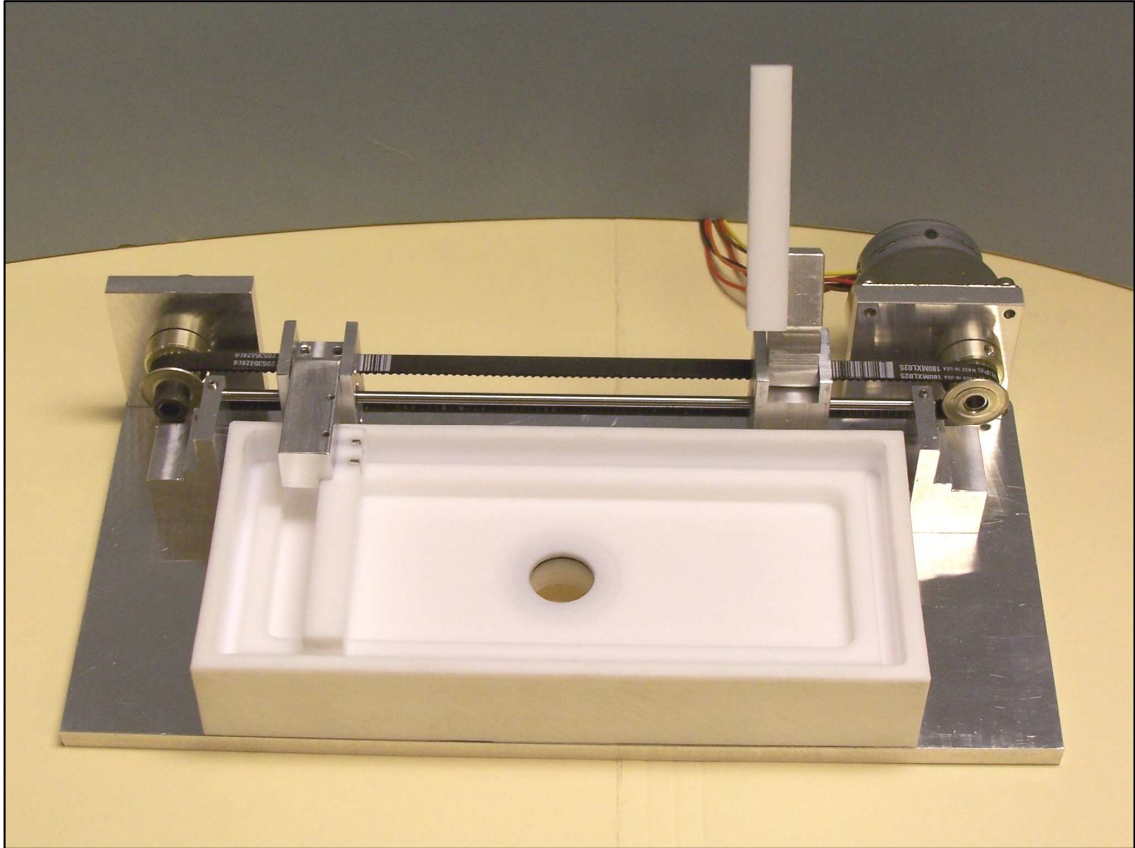


**Figure A.2** *The mechanical trough. This picture shows the mechanical trough with the central window installed. The window can be replaced with a plug or dipping well.*

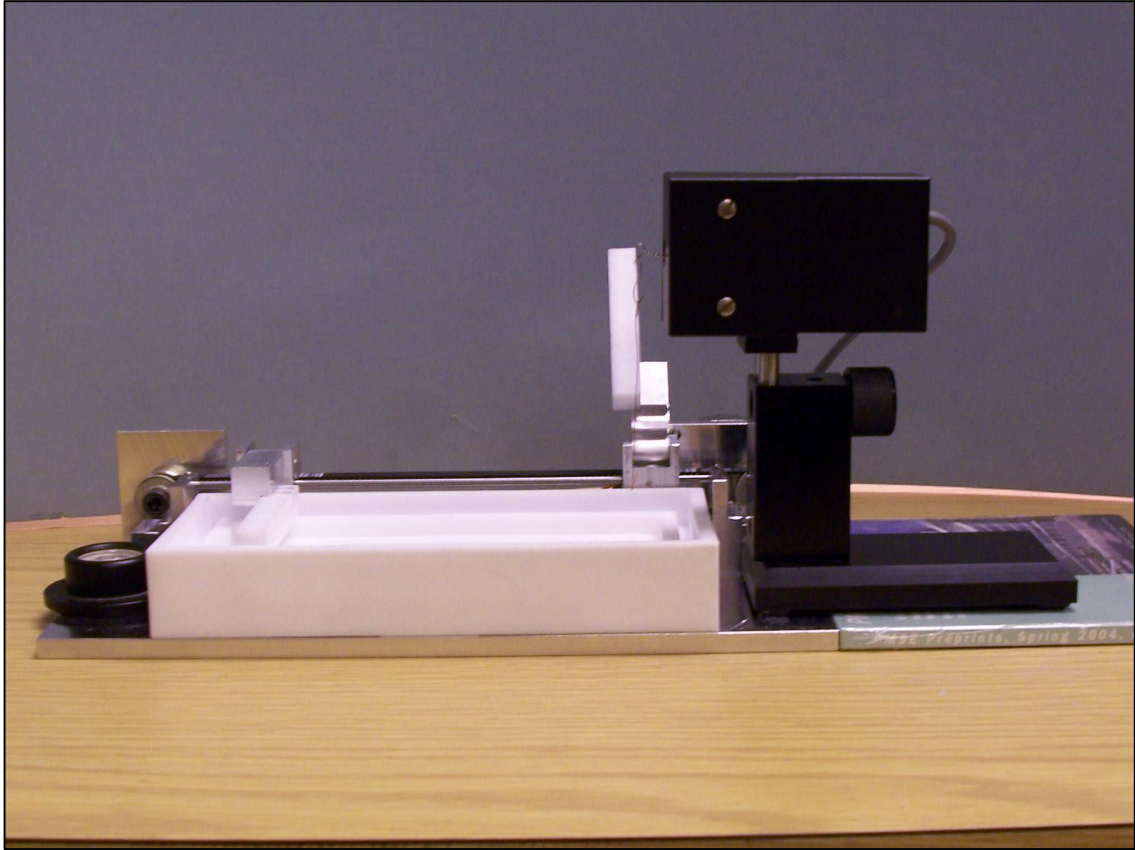
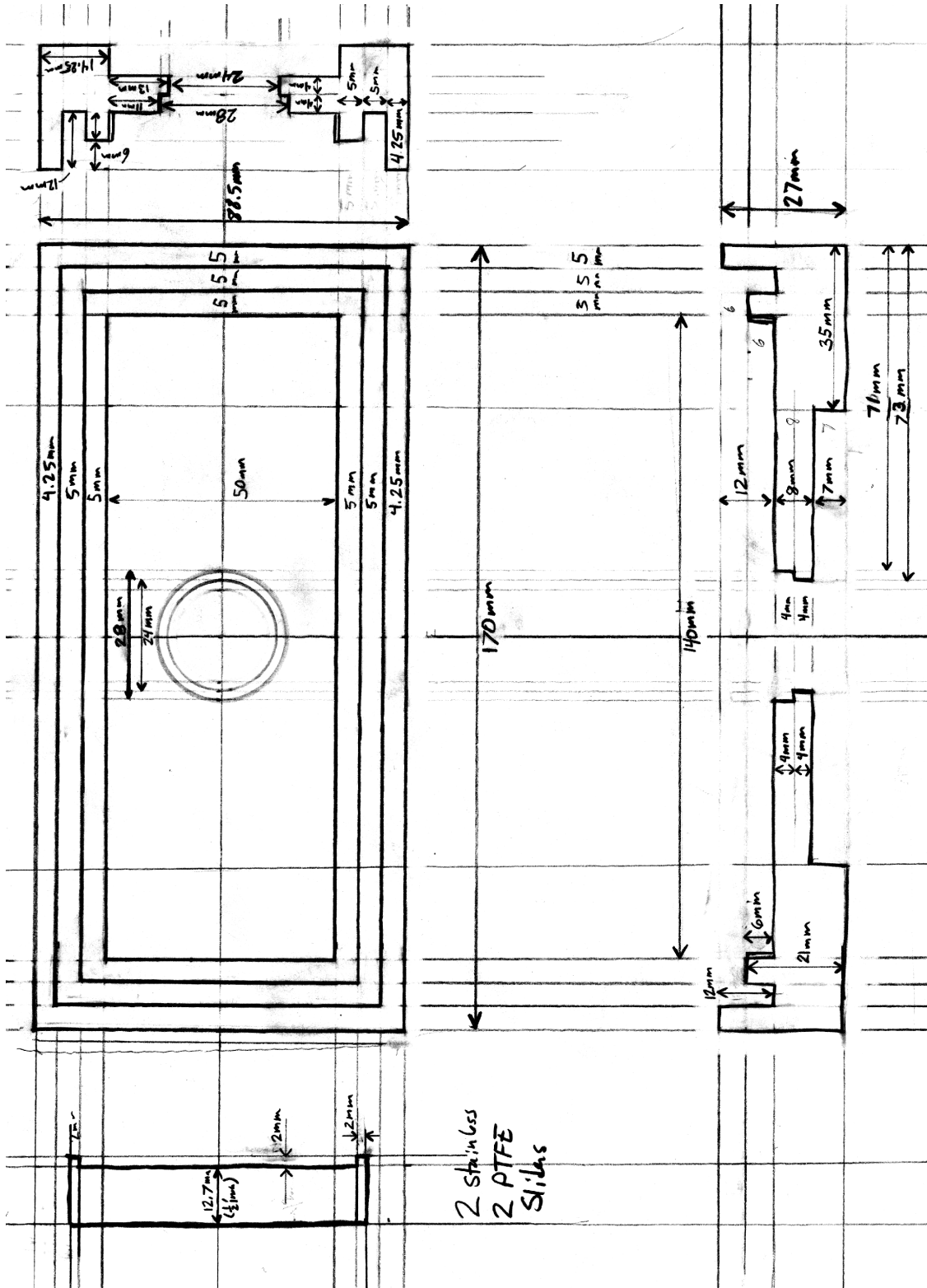


**Figure A.3** *Mechanical trough with the surface pressure transducer. This picture shows the typical geometry used for performing experiments with the mechanical trough. The trough was usually operated in single barrier mode.*

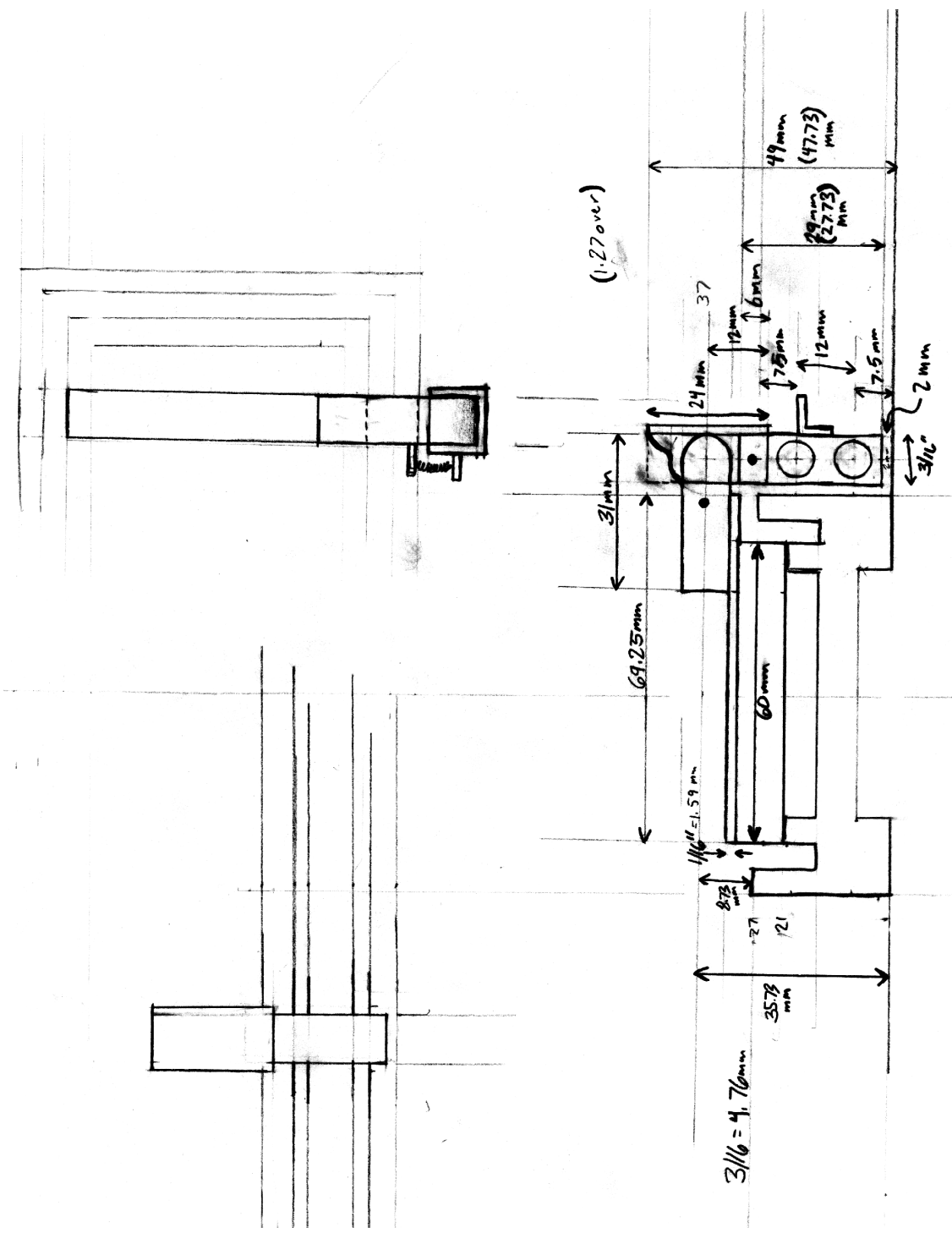
**Figure A.4** *Drawings used for the fabrication of the mechanical trough. The following set of drawings show the precise measurements of the trough.*

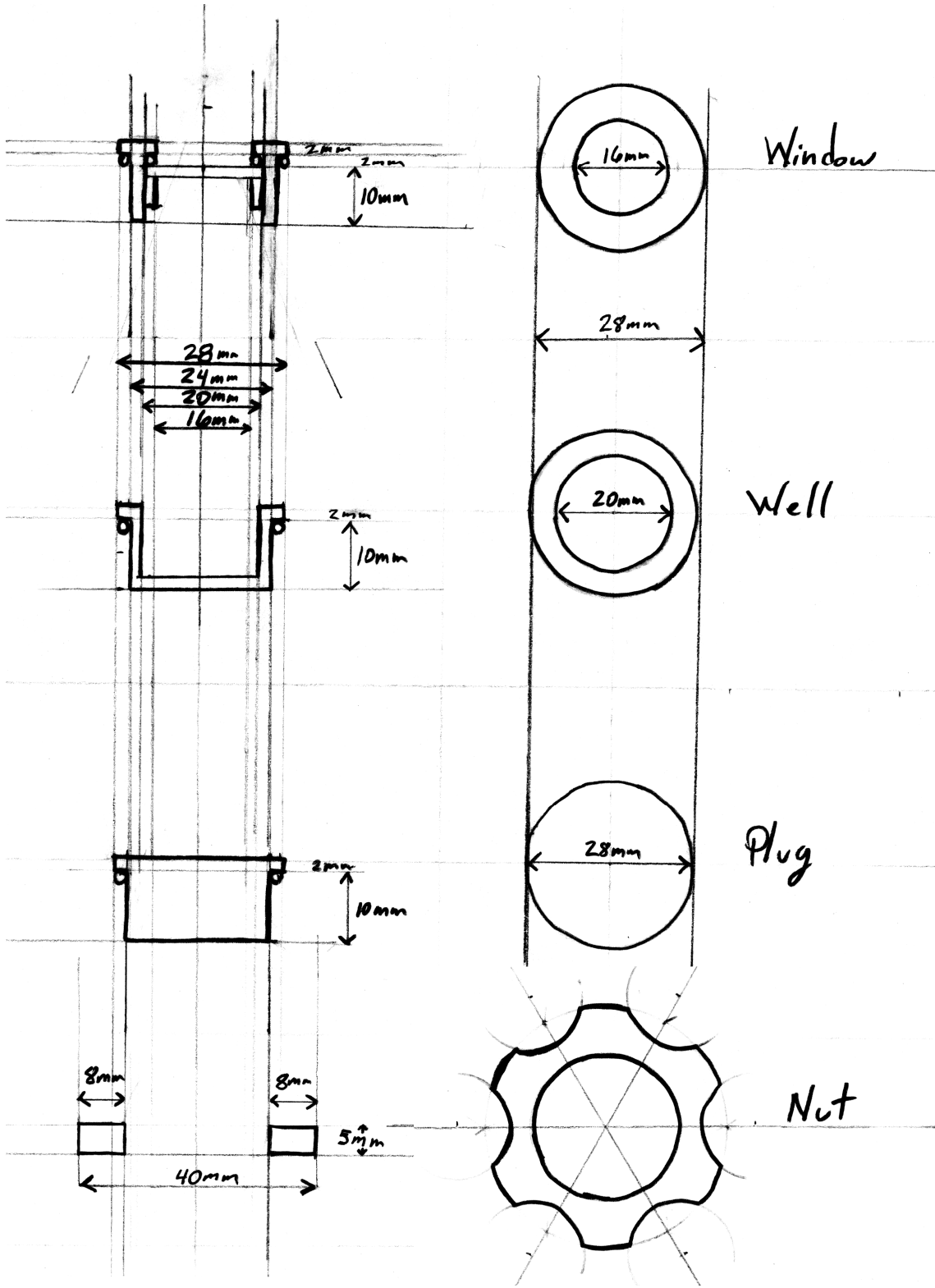


2 stainless  
2 PTFE  
Slabs









depending on the desired function and application of the experiment to be run. The body of the plug, well, and window were constructed from a 1-1/8" diameter virgin electrical grade PTFE rod of 1' length (McMaster Carr, #8546 K265). Two sets of trough barriers were constructed. The first was made from a square 3/8" thick 1' long bar of virgin electrical grade PTFE (McMaster Carr, #8737 K15) and the second was made from a square 3/8" thick 1' long bar of type 303 stainless steel (McMaster Carr, #8986 K141). The trough was mounted on a 1/4 inch thick aluminum base plate. A dual linear rail assembly was constructed from a 3-mm (OD) hardened precision metric steel shaft, (400 mm length, McMaster Carr, #6112 K11), upon which the two barrier carriages moved. The barrier carriages were constructed from two 0.5" square aluminum bars and four 3-mm (ID) fixed alignment linear steel ball bearing assemblies, (McMaster Carr, #61205 K31). The trough was powered by a stepper motor with a 70:1 gear ratio (Nippon Pulse America Inc., PF35T-48C1G1/75-M). The head of the stepper motor was fitted with a miniature MXL series aluminum timing-belt pulley with a 0.685" (OD) and 20 teeth (McMaster Carr, #1375 K39) and an identical belt pulley was used at the opposite end of the trough to keep tension. An MXL series neoprene rubber timing belt with a 0.08" pitch, an 18" outer circle, and a 1/4" width (McMaster Carr, #7887 K9) was used to transfer motion from the motor to the barriers.

A stepper motor controller board from a 5.25" floppy drive was adapted to run the main barrier drive stepper motor. These boards can be conveniently controlled *via* a computer parallel port with an easy to construct interface cable. A commercial Wilhelmy plate film balance (Nima, model #PS3) was used.

## **A.6 Software Development**

Software programs were written in Microsoft QuickBASIC and Visual Basic 6.0. The role of this software was to provide a suitable interface for controlling the stepper motors, interfacing the Wilhelmy plate transducer, and logging simultaneous barrier position and surface pressure data. The signal voltage from the Wilhelmy plate transducer was converted with a Vernier Serial Box Interface (SBI) analog to digital converter. A collection of software helps called the SBI Toolbox was downloaded from the Vernier website.<sup>6</sup> Useful subroutines from this collection were utilized in the interface software.

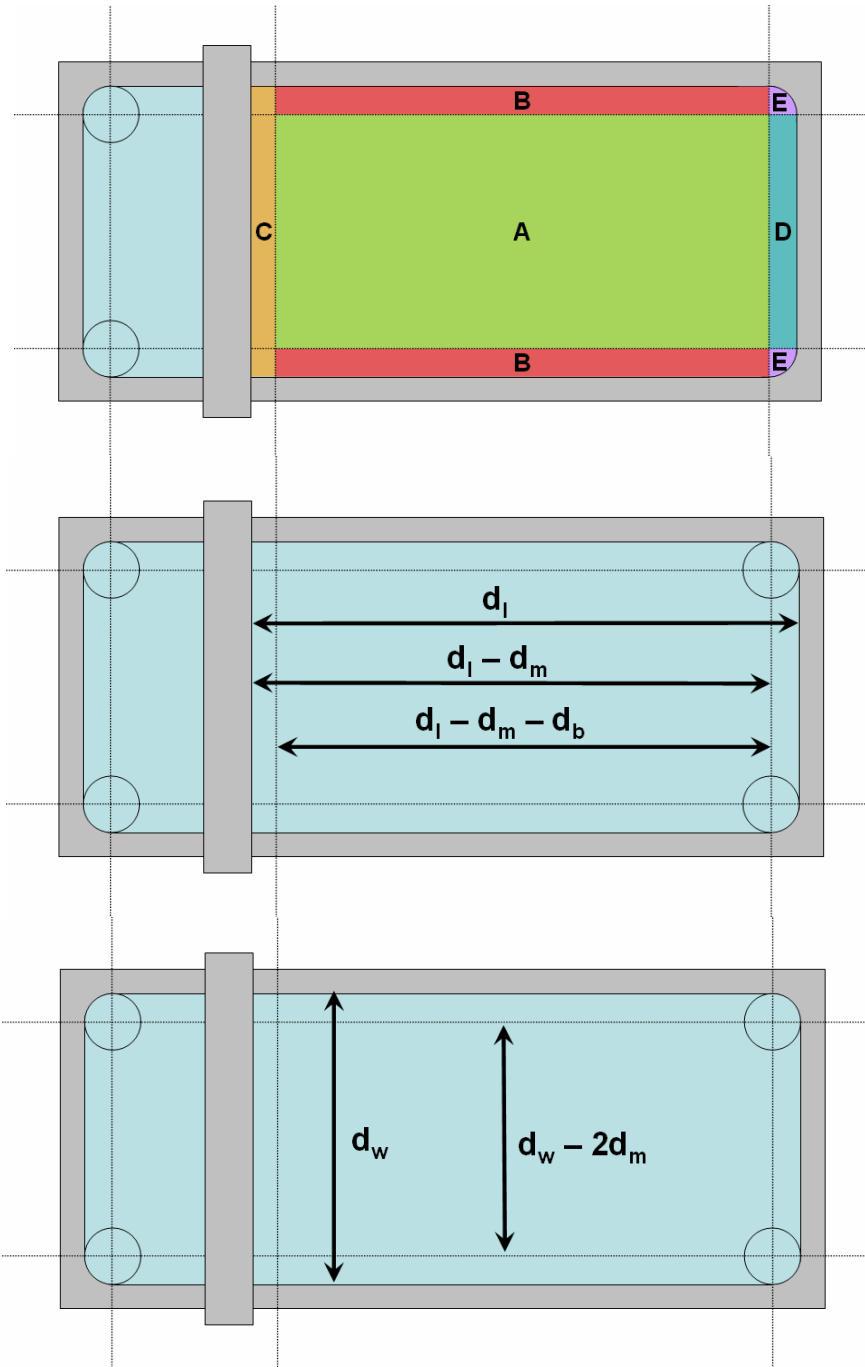
## **A.7 Barrier Modification**

The trough was designed to have two sets of movable barriers with different wetting characteristics to be switched when appropriate. Unfortunately, neither the Teflon or stainless steel barriers were effective at preventing barrier leakage with the 2.7- $\mu\text{m}$  particle films. Leakage occurred at the intersection of the barrier with the trough edges. Leakage would occur when surface pressures exceeded 20 mN/m. The stainless steel barrier was modified by first enclosing it with wet dialysis tubing and then wrapping both edges with Teflon tape. The bottom edge of the Teflon tape met flush with the trough edge. The resulting composite barrier proved to have superior leakage suppression, as no detectable leakage was observed.

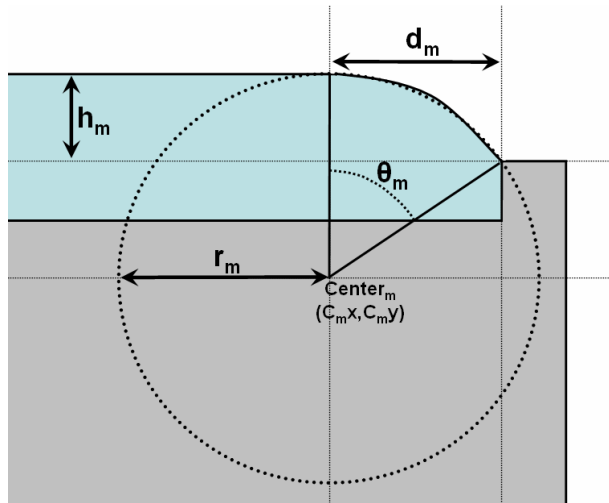
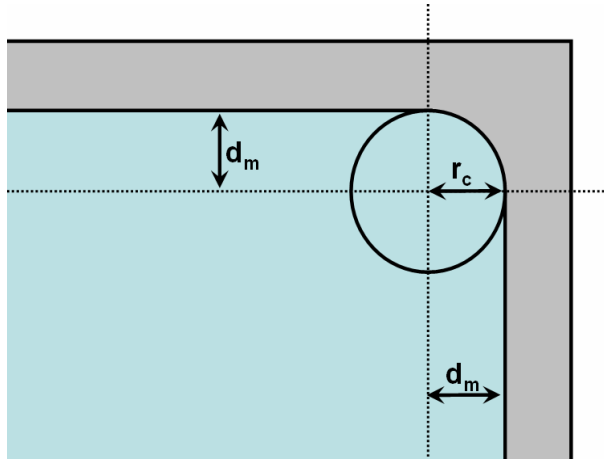
## A.8 Accurate Surface Area Determination.

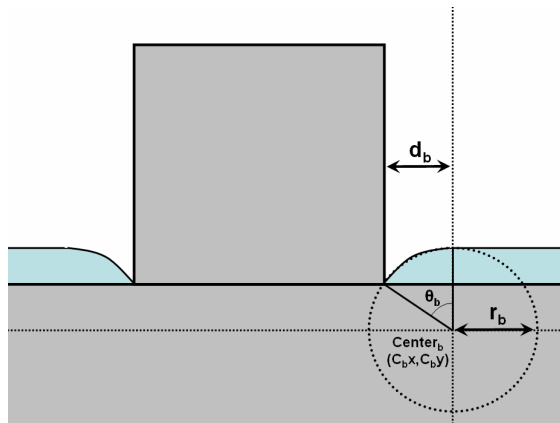
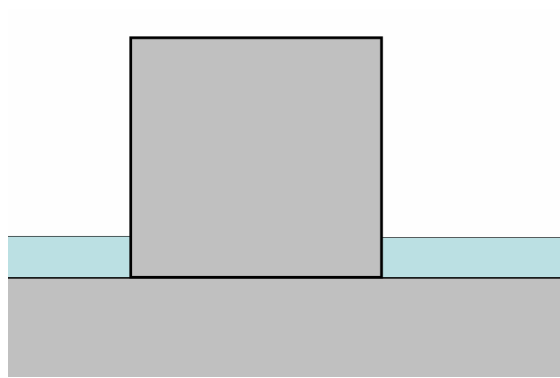
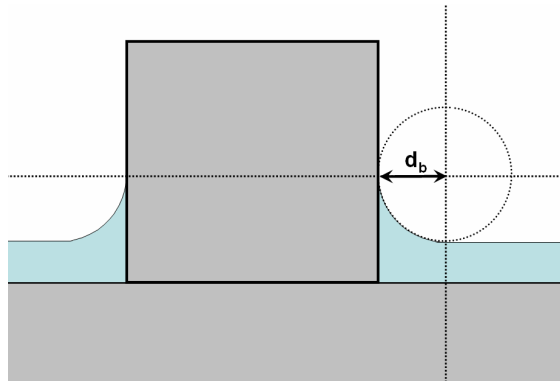
Because the volume and surface area of the trough were so small, measurements were susceptible to error introduction *via* edge effects that are considered insignificant for larger troughs. Because the Langmuir troughs are typically slightly overfilled, the true surface area of the air-water interface is larger than the surface area of the trough rim. In order to calculate the true surface area of the air-water interface, the surface area of the curved regions where the interface contacts the trough rim must be approximated (**Figure A.5**). The surface was divided into several regions. For a meniscus height of  $h_m$  above the trough edge, the area of region A is the most simple to calculate since this region is planar and equal to  $(d_l - d_m - d_b) \cdot (d_w - 2d_m)$ . The area of region B can be approximated by assuming it is a subset of a cylinder with a center  $(C_{mx}, C_{my})$ , a radius  $r_m$ , a sweep angle of  $\theta_m$ , and a length of  $2(d_l - d_m - d_b)$ . The distance  $d_m$  describes the distance from the edge of the trough over which the surface is non-planar and is equal to  $r_m \cdot \sin(\theta_m)$ . The area of region C depends on the wetting characteristic of the barrier that is installed. For a hydrophilic barrier with a very low contact angle such as the composite cellulose PTFE barrier, the surface area can be approximated as a quarter cylinder with a radius of  $d_b$  and a length of  $d_w$ . For a barrier with a contact angle near  $90^\circ$ , such as the stainless steel barrier,  $d_b = 0$  and the area of region C is included in regions A and B. For a hydrophobic barrier such as PTFE, the area of region C can be approximated as a subset of a cylinder with a center  $(C_{bx}, C_{by})$ , a radius  $r_b$ , a sweep angle of  $\theta_b$ , and a length of  $d_w$ . In this case, the distance  $d_b$  is equal to  $r_b \cdot \sin(\theta_b)$ . The surface area of region D can be calculated using the same

**Figure A.5** *Surface area determination.* The following set of figures show the parameters used to calculate the surface area of the curved liquid interface of the overfilled trough.









approximation used for region B except using a cylinder length of  $(d_w - 2d_m)$ . Region E is the most difficult to calculate because it has a complex curvature in two axis. This region can be calculated by assuming its area can be approximated as a surface of rotation. The radius of curvature of the corners of the trough,  $r_c$ , is constant and equal to 5 mm. This curvature may be defined to lie in the x-y plane. The curvature in the x-z and y-z plane can be described by the equation,

$$F = \sqrt{y^2 - x^2} - r \quad (\text{A.1})$$

The surface area, SA, of region E can therefore be calculated as,

$$SA = \pi \int_0^5 x \sqrt{1 - \left(\frac{dF}{dx}\right)^2} dx \quad (\text{A.2})$$

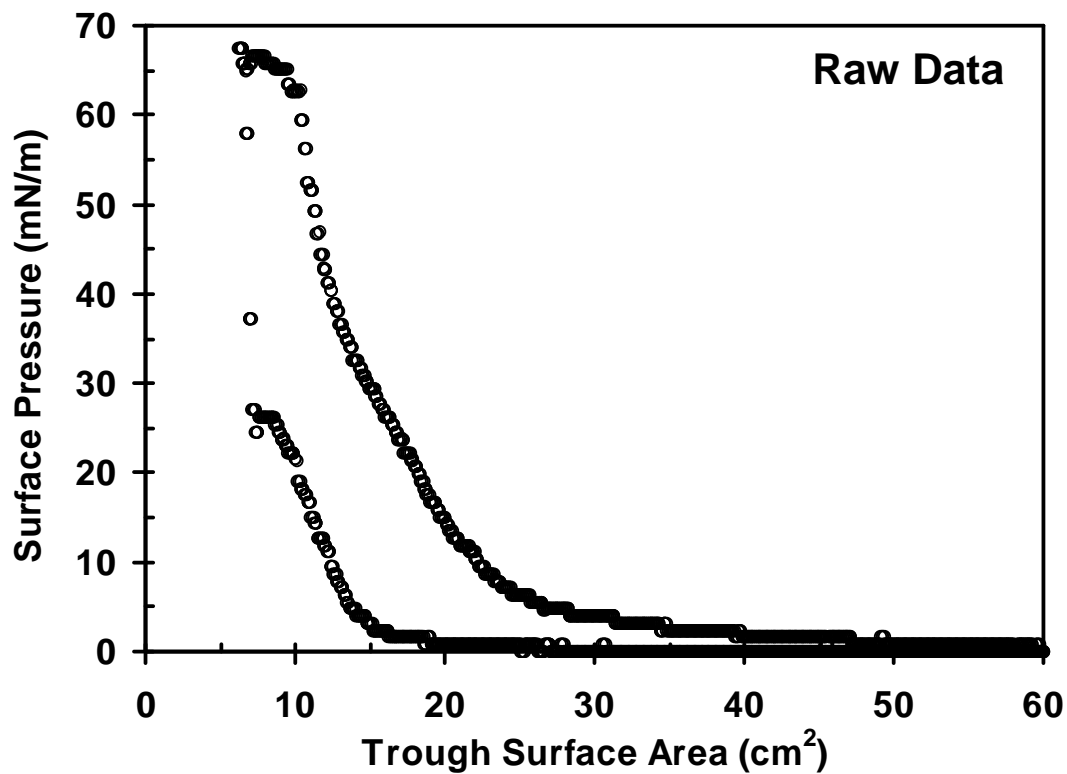
which accounts for both E regions. This approximation for E provides a continuous surface between regions B and D.

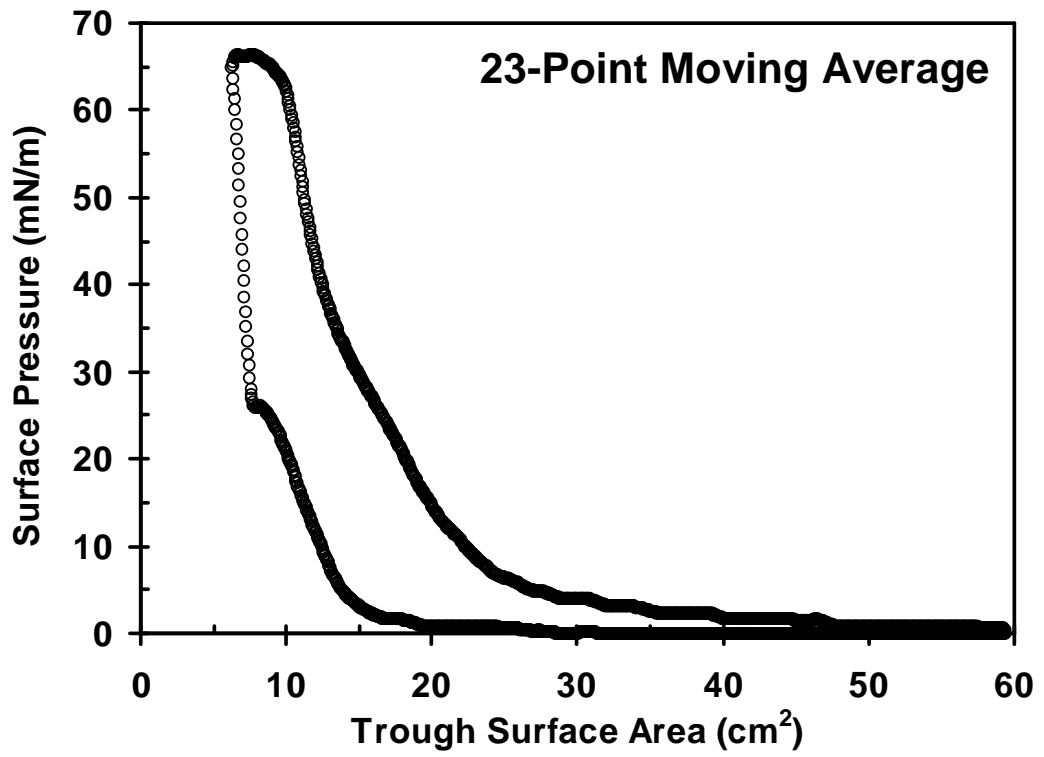
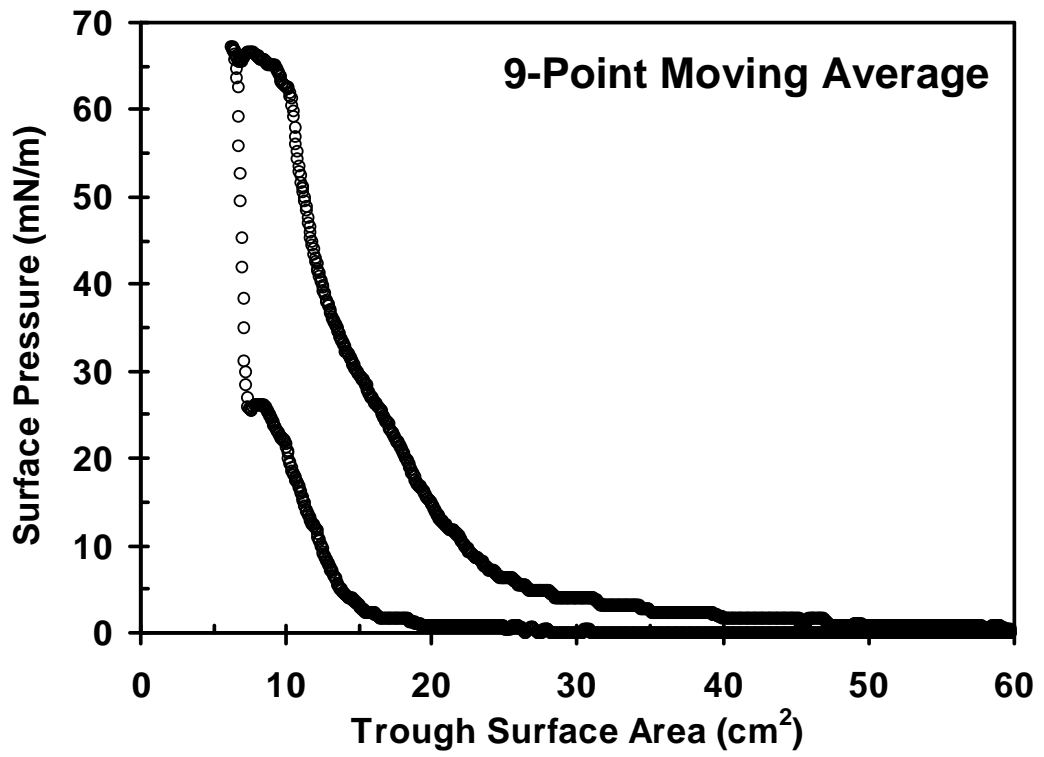
For example, if the stainless steel barrier was installed and the trough filled to a meniscus height of 3 mm, the regions would have the following areas: A = 4600.0 mm<sup>2</sup>, B = 1407.8 mm<sup>2</sup>, C = 0 mm<sup>2</sup> (because the barrier contact angle is 90°, the area of region C is included in A and B), D = 244.8 mm<sup>2</sup>, and E = 53.4 mm<sup>2</sup>, for a total trough area of 6306.0 mm<sup>2</sup>. If the nominal operational trough area (6000 mm<sup>2</sup>) were used, it would have introduced up to 5 % error into the isotherm measurements.

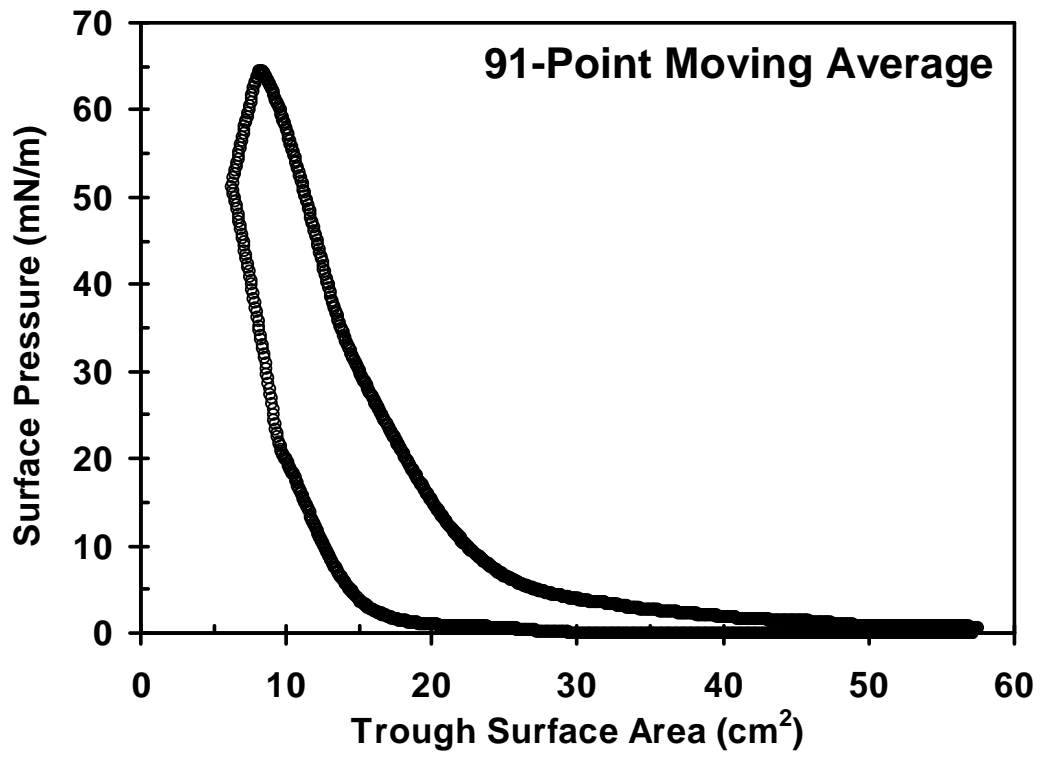
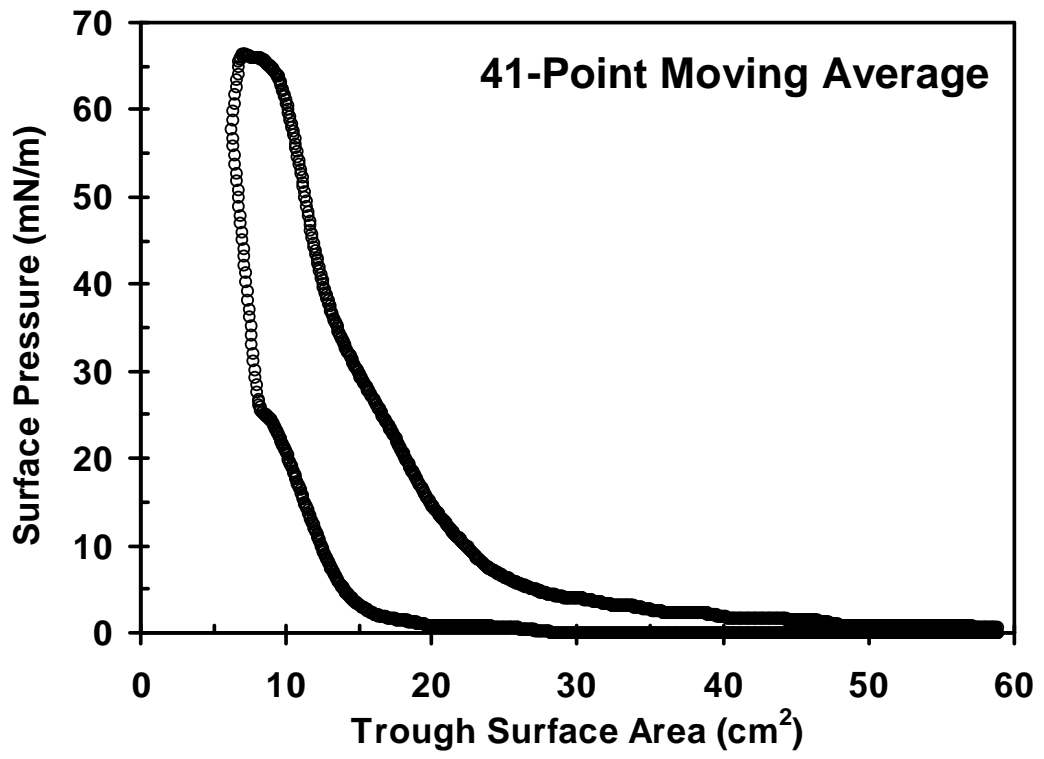
## A.9 Isotherm Data Treatment

The Vernier Serial Box Interface analog to digital converter has 12-bit resolution. Since only a small portion of the full range is used, the logged data takes on a blocky appearance. A moving average was performed to overcome these artifacts. The moving average was performed by averaging an odd number of sequential data points and recording the mean value as the central point in the averaged data set. The process was then repeated for every point in the data set. A moving average causes  $(n-1)/2$  data points to be omitted from the beginning and end of the data set, and can broaden or remove small features in the data set. To minimize these undesired effects, the number of points used in the moving average should be set to the minimum value necessary to achieve acceptable results. Most of the data sets in this research were processed using a 9-point moving average. Several stearic acid isotherms processed by increasingly wider ranges are shown in **Figure A.6**. Each apparent data point in the raw data set is actually a superposition of multiple data points. As a result of this artifact, the total number of data points appear to increase in the averaged data sets.

**Figure A.6** *Surface pressure-area isotherm data treatment.* This sequence of figures show the effect of using an increasingly wider data range for the moving average of the isotherm data. The isotherm shown is stearic acid at an air-water interface. As the range widens, the resolution of the data is lost.







## A.10 References and Notes

---

<sup>1</sup> Special thanks are owed to **Joseph Zelinski**, who does excellent work in the Lehigh University Physics Department Machine Shop.

<sup>2</sup> Petty, M. C. *Langmuir-Blodgett Films: An Introduction*; Cambridge: New York, NY. 1996; pp 54.

<sup>3</sup> Adamson, A.W.; Gast, A.P. *Physical Chemistry of Surfaces*, 6<sup>th</sup> Edition; Wiley: New York, NY, 1997; pp 36-37.

<sup>4</sup> Aveyard, R.; Clint, J. H.; Nees, D.; Quirke, N. *Langmuir*, **2000**, 16, 8820-8828.

<sup>5</sup> <http://www.nima.co.uk/>

<sup>6</sup> <http://www.vernier.com/>



## Appendix B

### Additional Details of Data Analysis

#### B.1 Particle Size Characterization.

This section describes the method used to characterize particle size by scanning electron microscopy. The latex was first diluted with DI water. A drop of the diluted latex was then placed onto a clean silicon or glass substrate. The sample was allowed to dry or the droplet was wicked away from the surface using the edge of a Kimwipe® depending on the degree surface coverage desired. Naturally, allowing the entire droplet to dry on the surface would create a concentrated sample that would likely have large clusters depending on the concentration of the diluted drop. The proper sample preparation scheme was therefore adjusted on a per-sample basis to achieve accurate results. In order to perform particle size analysis, a sample with a high coverage of well-isolated and -spaced particles is desirable. After the latex was placed on the substrate surface, it was sputter-coated with a thin layer of gold-palladium alloy to render the surface conductive, using a Polaron E5100 SEM sputter coating unit. A 15-second exposure at ~25 mA gave the desired minimal surface coating. If this step was not performed, the surface of the electrically insulating polymer and silicon surfaces charged up once in the SEM and subjected to the electron beam, thus making the image blurry and impossible to be focus. Several images of each sample were taken at the

same magnification. For particles with diameters in the range of 200-500 nm, a magnification of approximately 10 to 20 k was appropriate for measurements of particle size. The goal is to maximize the number of well-separated particles in the image while keeping the individual particle size in the image large enough to obtain an accurate measurement. Once the images were captured and saved as .tif files, they were analyzed using Image J version 1.34s.<sup>1</sup> Even though .tif files take up more space than a compressed image file such as a .jpg, the .tif gave a superior quality image with no loss of data due to compression.

Using this software, the scale bar region of the micrograph was magnified and the line tool was used to draw a straight line with the same length as the scale bar. Then, by using the *Set Scale* routine in the *Analyze* menu, the software is calibrated to the image scale. The image was then converted to a 8-bit image (the image must be in this format for subsequent processing) using the *Image > Type > 8-Bit* Routine. The Image was then converted to a binary black and white image using the *Threshold* routine found in the *Image > Adjust* menu. The threshold contrast was adjusted until only the particles were totally masked in red, after applying the mask, a black and white image resulted. If the background had specks comprised of four pixels or less, the *Despeckle* routine found in the *Process > Noise* menu was used. If some particles in the micrograph were touching, they would be counted as a single larger particle. To avoid this misassignment, the *Watershed* routine was run, found in the *Process > Binary* menu. This routine separates the particles in the neck region with a thin white line. After performing the above steps, the image was analyzed.

Using the *Set Measurements* routine in the *Analyze* menu, the following methods were selected to be used to measure the particle diameter: *Area*, *Bounding Rectangle*, *Fit Ellipse*, *Perimeter*, *Feret's Diameter*. *Area* gives a measurement of the area of each individual particle measured. The diameter can be easily calculated from the area in MS-Excel using the simple equation  $D = 2 \cdot \sqrt{A/\pi}$ . The *Bounding Rectangle* fits a rectangle around each particle and outputs the coordinates of the upper left-hand corner, (*BX*, *BY*), and the *Width* and *Height* of the rectangle. For a spherical particle, both the *Width* and *Height* provide a measure of particle diameter. The fitting rectangle is always oriented parallel to the vertical and horizontal dimension of the image. The *Fit Ellipse* places a best fit ellipse around each particle and returns the *Major* and *Minor* axis length of the ellipse, as well as the *Angle* the major axis makes with the bottom edge (x-axis) of the image. For a spherical particle, the *Major* and *Minor* axis lengths provide a measure of particle diameter as well. The *Perimeter* measurement can also be used to measure the particle diameter in MS-Excel using the equation  $D = P/\pi$ . This measurement always seemed to give a value that was much higher than the total average particle diameter, which may be an artifact due to the pixilated edge of the particle, and for that reason was not routinely used. The effect was minimized by imaging at higher magnification, so that each particle is represented by a larger number of pixels. The final measurement, the *Feret's Diameter*, also called the caliper length, is a measurement of the longest distance between two points on the perimeter of the particle. This method also typically gives values much larger than the total average particle diameter, again likely due to the pixilated edge of the particle.

This method gives accurate measurements of particle diameter only for very clean well-imaged micrographs. For these reasons, the *Feret's Diameter* was also not routinely used.

For a typical measurement of particle size, the following method was employed. The *Set Measurements* routine was typically set to *Area, Bounding Rectangle, and Fit Ellipse*. This provided 5 independent diameter measurements for each particle. The *Analyze Particles* routine was then selected in the *Analyze* menu. The *Max* and *Min* size were set so that only particles in the desired gross size range were measured (i.e., noise from background texture and particle clusters were excluded). The *Show* option was set to *Outlines* or *Masks* to show which particles were included in the measurement. The *Display Results, Clear Results, Exclude on Edges, and Flood Fill* check boxes were checked. After clicking *OK*, the image was analyzed and the results window displayed 9 columns of output data: *Count* (unlabeled), *Area, BX, BY, Width, Height, Major, Minor, and Angle*. Using the *Copy All* command in the *Edit* menu of the *Results* window, the data were copied and pasted into a MS-Excel spreadsheet.

This process was repeated for each micrograph to be included in the measurement, each time adding the data to the same spreadsheet. Once all of the images were analyzed, the diameter was calculated from the area measurements and placed into a column entitled *Area Diameter*. The columns of interest (*Width, Height, Major, Minor, Area Diameter*) were averaged and the standard deviation calculated. For measurement of complex distributions,, a Particle Size macro for MS-Excel (Available from the Emulsion Polymer Institute at Lehigh University) was used. The

columns of interest were copied and pasted into the *Data Points* page. The data columns were arranged into a single column labeled *Diameter*, sorted into ascending order using the *Data > Sort* Routine, and indexed (1, 2, 3, ...) in the adjacent column. The particle-size distributions were then calculated by pressing the *Process Data* button on the *Summary* page of the macro. The formulas used for the different distribution measurements are given in **Appendix C**. The size distribution can then be graphed by plotting the values in the Diameter column as a histogram in MS-Excel or Microcal Origin.

## **B.2 Nearest-Neighbor Analysis**

Nearest-neighbor analysis was performed with Spatial Analysis Utilities<sup>2</sup> and ImageJ. The micrograph was first opened and calibrated in ImageJ. In order to obtain precise measurements and separation-distance distributions, the image was always calibrated in nm. The image was then converted to an 8-bit grayscale image and thresholded as described in the previous section. This routine in ImageJ allowed the software to differentiate between particles and background. This process involves changing the image to a 2-bit black-and-white image and adjusting the gray value threshold below which a pixel will be black and above which it will be white. After applying the threshold routine, additional steps were taken if necessary to clean up the image as described in the previous section. If a large number of specks smaller than 4 pixels existed in the image, the *Despeckle* routine was run. If some of the particles appeared to be hollow rings after the threshold procedure (a common focusing artifact

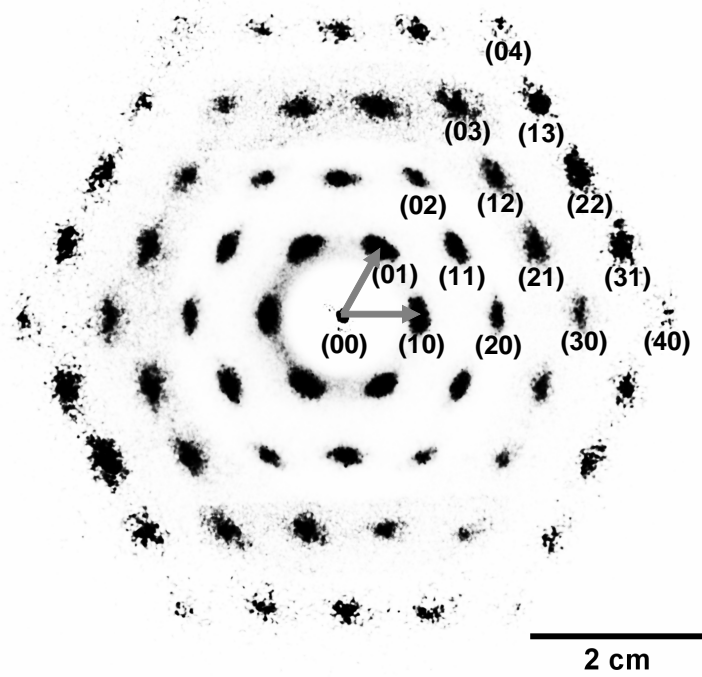
seen with optical micrographs) the *Fill Holes* procedure was run. If any particles were touching one another, the *Watershed* procedure was run to separate the particles. After an acceptable 2-bit image was produced, the analysis was continued. First in the *Set Measurements* routine, the *Centroid* option was selected and all others were deselected. The *Analyze Particles* routine was run and the upper and lower limits were set above and below the area in pixels of the desired particles. These numbers were adjusted to include all of the desired particles while excluding gross particle clusters and small particles or noise. The Analyze Particles output was saved as a text file and opened in MS-Excel. The first column showed the particle number index. This column was deleted, and the remaining two columns were shifted to the left. Then column labels in row 1 were then deleted and the data was shifted up by one row (the data must be put in this format to be accepted by Spatial Analysis Utilities). The file was then saved as a text file. The text file contained the x and y coordinates (in nm) of the center of mass of every particle in the original image. A new nearest-neighbor analysis was started using Spatial Analysis Utilities. The text file was Imported, Displayed, and Processed and the data was output using the data log button (4<sup>th</sup> from left) using a bin size of 100 nm. The histogram data was saved and copied into MS-Excel where multiple runs were plotted on the same graph. This process was followed for all the nearest-neighbor data in Chapter 3.

### B.3 Assignment of Miller Indices to an HCP Array

The diffraction pattern used for the measurement reported in **Figure 3.32** is shown in **Figure B.1**. The distance between each diffraction spot and the main beam (00) were measured. Diffraction angles were calculated using the ratio of this distance and the projection length, which was 10 cm. The inter-particle spacing,  $D$ , in the original image was calculated using the equation,

$$D = \frac{m \cdot \lambda}{\sin(\theta) \cdot \sin(\varphi)} \quad (\text{B.1})$$

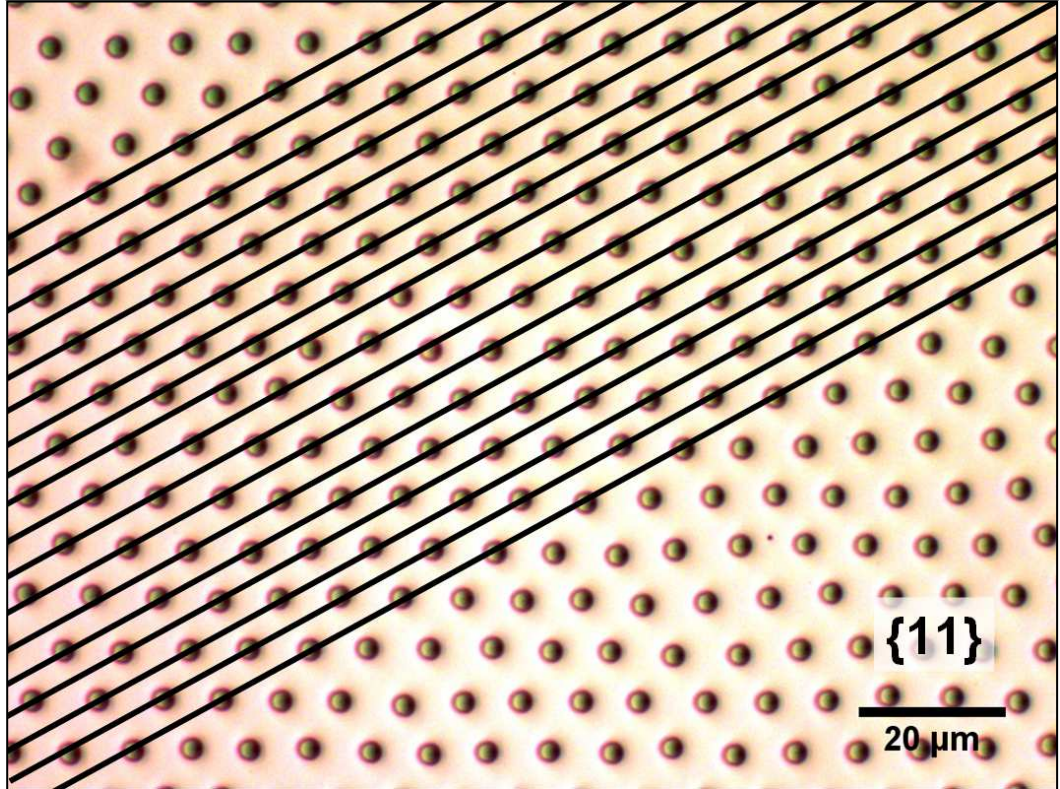
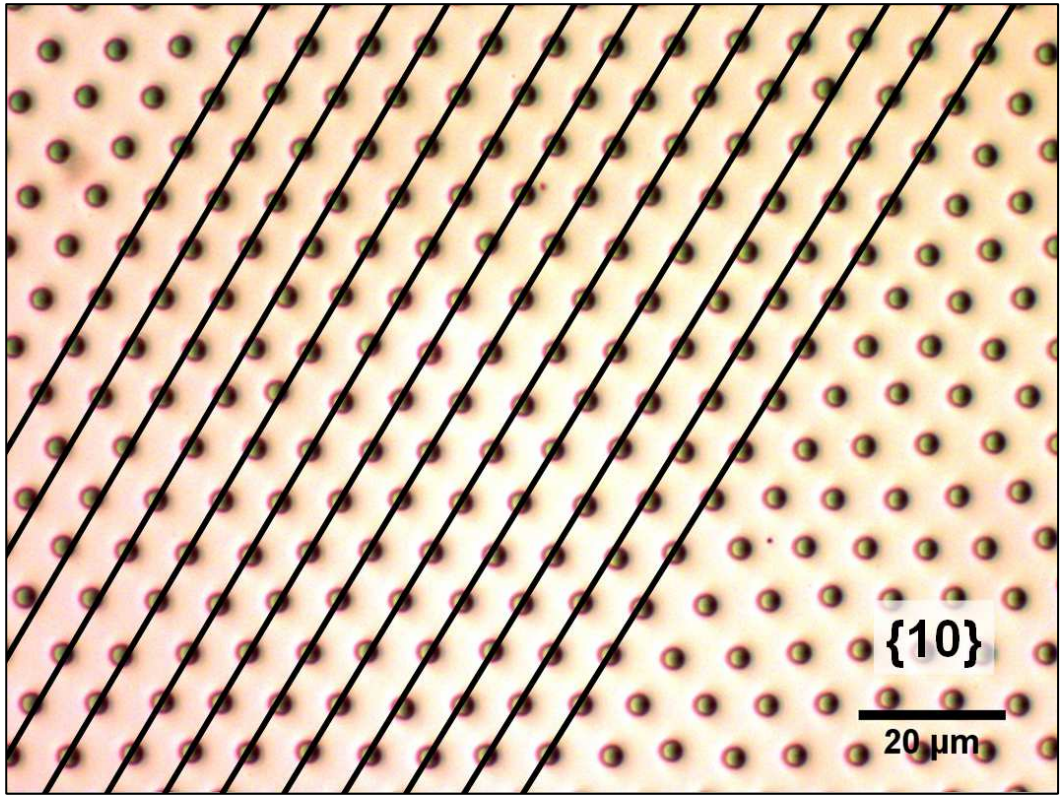
in which  $m$  is the order of the diffraction spot (i.e. for the (20) spot,  $m = 2$ ),  $\lambda$  is the wavelength of the incident laser (633 nm),  $\theta$  is equal to the diffraction angle, and  $\varphi$  is equal to  $60^\circ$  for the {10} lines,  $45^\circ$  for the {11} lines,  $20^\circ$  for the {21} lines, and  $15^\circ$  for the {31} lines. **Figure B.2** shows the families of particle lines responsible for the different diffraction spots.



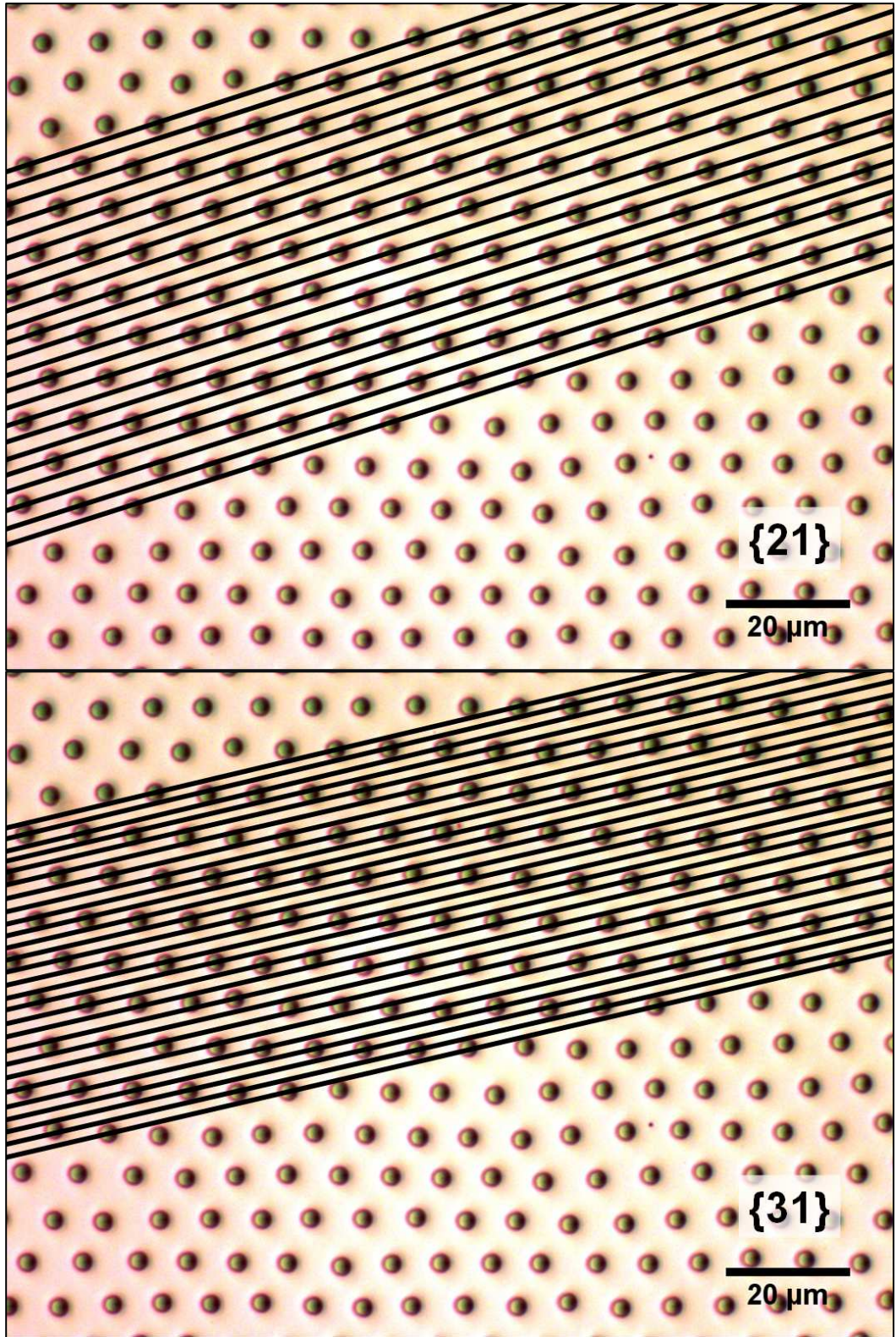
**Figure B.1** *Indexed particle array laser diffraction pattern. 2-D Miller indices are given.*



**Figure B.2** *Families of particle lines responsible for producing the diffraction spots.*







## **B.4 References and Notes**

---

<sup>1</sup> ImageJ analysis software is available free of charge at <http://rsb.info.nih.gov/ij/>.

<sup>2</sup> Spatial Analysis Utilities is available free of charge at  
<http://www.archeogr.unisi.it/infapp/sau/>.

## Appendix C

### Useful Equations and Conversions

$$\frac{\mu\text{C}}{\text{cm}^2} = \frac{1602}{\left(\frac{\text{\AA}^2}{\text{charge}}\right)}$$

$$\frac{\text{\AA}^2}{\text{charge}} = \frac{1602}{\left(\frac{\mu\text{C}}{\text{cm}^2}\right)}$$

$$\frac{\text{\AA}^2}{\text{charge}} = \frac{9.444 \times 10^5}{\left(\frac{\mu\text{Eq}}{\text{g}}\right) \cdot D_{(nm)}}$$

$$\frac{\mu\text{Eq}}{\text{g}} = \frac{9.444 \times 10^5}{\left(\frac{\text{\AA}^2}{\text{charge}}\right) \cdot D_{(nm)}}$$

$$\frac{\text{cm}^2}{\text{g}} = \frac{5.687 \times 10^7}{D_{(nm)}} \quad \text{for polystyrene}$$

$$\frac{\text{particles}}{\text{mL}} = \frac{6 \cdot \left(\frac{\text{wt.}\%}{100}\right)}{\pi \cdot \rho \cdot D_{(\mu\text{m})}}$$

$$\frac{\text{particles}}{\text{mL}} = \frac{1.803 \times 10^{12} \cdot \left(\frac{\text{wt.}\%}{100}\right)}{D_{(\mu\text{m})}} \quad \text{for polystyrene}$$

## For Gaussian Distributions

$$\bar{x} = \frac{1}{N} \sum_{i=1}^N x_i$$

$$\sigma = \sqrt{\frac{1}{N} \sum_{i=1}^N (x_i - \bar{x})^2}$$

$$CV = \frac{\sigma}{D_N} = \frac{\sigma}{M_N} = \sqrt{\frac{M_w}{M_N} - 1} = \sqrt{PDI - 1}$$

$$PDI = \frac{M_w}{M_N} = CV^2 + 1$$

$\sigma$  = Standard Deviation

CV = Coefficient of Variation

PDI = Polydispersity Index

$D_N$  = Number Average Particle Diameter

$M_N$  = Number Average Particle Size or Molecular Weight

$M_w$  = Weight Average Particle Size or Molecular Weight

## Particle Size Distributions

$$D_N = \frac{\sum_i n_i \cdot d_i}{\sum_i n_i}$$

$$D_S = \left( \frac{\sum_i n_i \cdot (d_i)^2}{\sum_i n_i} \right)^{\frac{1}{2}}$$

$$D_V = \left( \frac{\sum_i n_i \cdot (d_i)^3}{\sum_i n_i} \right)^{\frac{1}{3}}$$

$$D_{VS} = \frac{\sum_i n_i \cdot (d_i)^3}{\sum_i n_i \cdot (d_i)^2} = \frac{D_V^3}{D_S^2}$$

$$D_W = \frac{\sum_i n_i \cdot (d_i)^4}{\sum_i n_i \cdot (d_i)^3}$$

$$D_{WLS} = \left( \frac{\sum_i n_i \cdot (d_i)^6}{\sum_i n_i \cdot (d_i)^3} \right)^{\frac{1}{3}}$$

$$D_N < D_S < D_V < D_{VS} < D_W < D_{WLS}$$

$$PDI = \frac{D_{WLS}}{D_N}$$

# Biography

## EDUCATION

- Lehigh University (2001-2007), Ph.D. in Chemistry
- Lehigh University (2001-2004), M.S. in Chemistry
- Bob Jones University (1997-2001), B.S. in Chemistry, Minor: Physics (*magna cum laude*)

## AFFILIATIONS

- Sigma Xi
- American Chemical Society
- Emulsion Polymers Institute, Lehigh University

## PUBLICATIONS

- Ray, M.A.; Kim, H.; Jia, L. "Dynamic Self-Assembly of Polymer Colloids To Form Linear Patterns." *Langmuir*, 2005, 21, 4786-4789.



## PRESENTATIONS

- Ray, M.A.; Kim, H.; Jia, L. “Dynamic Self-Assembly of Polymer Colloids To Form Linear Patterns.” 230<sup>th</sup> ACS National Meeting, Washington, DC, Aug. 28-Sept. 1, 2005, COLL-415.
- Ray, M.A.; Kim, H.; Jia, L. “Dynamic Self-Assembly of Polymer Colloids To Form Linear Patterns.” Gordon Research Conference on Polymer Colloids, Tilton, NH, July 3-8, 2005.
- Ray, M.A.; Jia, L. “Patterning of Functionalized Polymer Colloids by Self-Assembly.” 228<sup>th</sup> ACS National Meeting, Philadelphia, PA, Aug. 22-26, 2004, COLL-151.
- Ray, M.A.; Jia, L. “Bottom-Up Surface Self-Assembly of Polymer Colloids to Form Patterned Arrays.” 37<sup>th</sup> Annual Short Course, Emulsion Polymers Institute, Bethlehem, PA, June 5-9, 2006.
- Ray, M.A.; Jia, L. “Bottom-Up Surface Self-Assembly of Polymer Colloids to Form Patterned Arrays.” Annual Review Meeting, Emulsion Polymers Institute, Bethlehem, PA, March 22-23, 2006.
- Ray, M.A.; Jia, L. “Dynamic Self-Assembly of Latex Particles to Form Linear Patterns.” 36<sup>th</sup> Annual Short Course, Emulsion Polymers Institute, Bethlehem, PA, June 6-10, 2005.
- Ray, M.A.; Jia, L. “Dynamic Self-Assembly of Latex Particles to Form Linear Patterns.” Annual Review Meeting, Emulsion Polymers Institute, Bethlehem, PA, March 16-17, 2005.
- Ray, M.A.; Jia, L. “Self-Assembly of Colloidal Particles.” 35<sup>th</sup> Annual Short Course, Emulsion Polymers Institute, Bethlehem, PA, June 7-11, 2004.
- Ray, M.A.; Jia, L. “Self-Assembly of Colloidal Particles.” Annual Review Meeting, Emulsion Polymers Institute, Bethlehem, PA, March 17-18, 2004.

## HONORS

- Ticona Award (2005), awarded for excellence in polymer research.
- Chemistry Department Fellowship (2005-2006), awarded for academic performance.
- Edward D. Amstutz Fellowship (2004-2005), awarded for academic performance.
- Emulsion Polymers Institute’s Industrial Liaison Program’s 1<sup>st</sup> Prize Poster (2005).
- Emulsion Polymers Institute’s Industrial Liaison Program’s 2<sup>nd</sup> Prize Poster (2006).
- American Chemical Society Outstanding Senior Chemistry Major (2001).
- American Institute of Chemists Foundation Student Award (2001).